

1225-0767(ISSN Print)
2287-6715(ISSN Online)
한국연구재단 우수등재학술지

Journal of Ocean Engineering and Technology

Vol. 34, No. 6 (Serial Number 157)

December 2020

한국해양공학회지



www.joet.org



The Korean Society of Ocean Engineers

Editorial Board

■ Editor-in-Chief

Joonmo Choung Inha University, Korea

■ Manuscript Editors

Hyeungsik Choi Korea Maritime and Ocean University, Korea

Joon-Young Kim Korea Maritime and Ocean University, Korea

Seokhwan Ahn Jungwon University, Korea

Sungwon Shin Hanyang University, Korea

Woo Dong Lee Gyeongsang National University, Korea

■ Editorial Board Members

Ahmet Ergin Istanbul Technical University, Turkey

Atila Incecik University of Strathclyde, UK

Beom-Seon Jang Seoul National University, Korea

Bo Woo Nam Seoul National University, Korea

Chang Yong Song Mokpo National University, Korea

Chong Hyun Lee Jeju National University, Korea

Do Kyun Kim Newcastle University, UK

Dongho Jung Korea Research Institute of Ships & Ocean Engineering, Korea

Erkan Oterkus University of Strathclyde, UK

Geoffrey Lyons BPP-TECH, UK

Gökhan Tansel Tayyar Istanbul Technical University, Turkey

Gyung Cho Tongmyong University, Korea

Hee Jin Kang Korea Research Institute of Ships & Ocean Engineering, Korea

Hooi-Siang Kang Universiti Teknologi Malaysia, Malaysia

Hyeon Kyu Yoon Changwon National University, Korea

Hyun-Sik Kim Tongmyong University, Korea

Jinwhan Kim Korea Advanced Institute of Science and Technology, Korea

Jong Chun Park Pusan National University, Korea

Kangsu Lee Korea Research Institute of Ships & Ocean Engineering, Korea

Kookhyun Kim Tongmyong University, Korea

Kwang-Jun Paik Inha University, Korea

Masashi Kashiwagi Osaka University, Japan

Moo Hyun Kim Texas A&M University, USA

Narakorn Srini Newcastle University, UK

Norimi Mizutani Nagoya University, Japan

Se-Min Jeong Chosun University, Korea

Seongim Choi Virginia Tech, USA

Seung Min Park Hyein Engineering & Construction, Co., Ltd., Korea

Soonchul Kwon Pusan National University, Korea

Sungnam Hong Gyeongsang National University, Korea

Sung-Woong Choi Gyeongsang National University, Korea

Taemin Ha Kangwon National University, Korea

TaeSeong Kim Loughborough University, UK

TaeSoon Kang GeoSystem Research Corp., Korea

Tak Kee Lee Gyeongsang National University, Korea

Weoncheol Koo Inha University, Korea

Yeon-Joong Kim Inje University, Korea

Yong Uk Ryu Chonnam National University, Korea

Younghun Kim Kyungnam University, Korea

Youngsub Lim Seoul National University, Korea

Research Ethics Board

■ Chief

Sung-Bu Suh Dongeui University, Korea

■ Research Ethics Board Members

Han Koo Jeong Kunsan National University, Korea

Jinwhan Kim Korea Advanced Institute of Science and Technology, Korea

Yong Uk Ryu Chonnam National University, Korea

Published on December 31, 2020

Published by The Korean Society of Ocean Engineers (KSOE)

Room1302, 13, Jungang-daero 180beon-gil, Dong-gu, Busan, 48821, Korea

TEL: +82-51-759-0656 FAX: +82-51-759-0657 E-mail: ksoehj@ksoe.or.kr URL: http://www.ksoe.or.kr

Printed by Hanrimwon Co., Ltd., Seoul, Korea E-mail: hanrim@hanrimwon.co.kr

ISSN(print) 1225-0767 **ISSN(online)** 2287-6715

This journal was supported by the Korean Federation of Science and Technology Societies (KOFST) grant funded by the Korean government.

© 2020 by The Korean Society of Ocean Engineers (KSOE)

This is an open access article distributed under the terms of the creative commons attribution non-commercial license (<http://creativecommons.org/licenses/by-nc/4.0>) which permits unrestricted non-commercial use, distribution, and reproduction in any medium, provided the original work is properly cited.

CONTENTS

Volume 34, Number 6

December, 2020

<Original Research Articles>

- Discussions on Availability of Weather Information Data and Painting Effect of Existing 8,600 TEU Container Ship Using Ship Performance Analysis Program
Myung-Soo Shin, Min Suk Ki, Gyeong Joong Lee, Beom Jin Park, Yeong Yeon Lee, Yeongseon Kim and Sang Bong Lee 377
- Numerical Study on the Extrapolation Method for Predicting the Full-scale Resistance of a Ship with an Air Lubrication System
Dong-Young Kim, Ji-Yeon Ha and Kwang-Jun Paik 387
- Development of Ice Load Generation Module to Evaluate Station-Keeping Performance for Arctic Floating Structures in Time Domain
Hyun Hwa Kang, Dae-Soo Lee, Ji-Su Lim, Seung Jae Lee, Jinho Jang, Kwang Hyo Jung and Jaeyong Lee ... 394
- Higher-order Spectral Method for Regular and Irregular Wave Simulations
Seunghoon Oh, Jae-Hwan Jung and Seok-Kyu Cho 406
- Study on PIV-Based Pressure Estimation Method of Wave Loading under a Fixed Deck
Gang Nam Lee, Tien Trung Duong, Kwang Hyo Jung, Sung Bu Suh and Jae Yong Lee 419
- Energetics of In-plane Motions in Coupled Plate Structures
Young-Ho Park and Chang Hyun Park 428
- Impact Assessment of Beach Erosion from Construction of Artificial Coastal Structures Using Parabolic Bay Shape Equation
Changbin Lim, Sahong Lee, Seung-Min Park and Jung Lyul Lee 436
- Single Image-based Enhancement Techniques for Underwater Optical Imaging
Do Gyun Kim and Soo Mee Kim 442
- Response Analysis of MW-Class Floating Offshore Wind Power System using International Standard IEC61400-3-2
Youngjae Yu and Hyunkyung Shin 454
- Trend Analysis on Korea's National R&D in Logistics
Jae Yun Jeong, Gyusung Cho and Jieon Yoon 461
- Study on Modularization of Components for Cost Reduction of Sail Yacht Steering System
Young-Hun Kim 469

<Technical Articles>

- Study on Unmanned Hybrid Unmanned Surface Vehicle and Unmanned Underwater Vehicle System
Han-Sol Jin, Hyunjoon Cho, Ji-Hyeong Lee, Huang Jiafeng, Myung-Jun Kim, Ji-Youn Oh and Hyeung-Sik Choi 475
- Material Property-Estimate Technique Based on Natural Frequency for Updating Finite Element Model of Orthotropic Beams
Kookhyun Kim, Sungju Park, Sangjoong Lee, Seongjun Hwang, Sumin Kim and Yonghee Lee 481

GENERAL INFORMATION

“Journal of Ocean Engineering and Technology” is the official journal published by “The Korean Society of Ocean Engineers (KSOE)”. The ISO abbreviation is “J. Ocean Eng. Technol.” and acronym is “**JOET**”. It was launched in 1987. It is published bimonthly in February, April, June, August, October, and December each year. Supplement numbers are published at times.

Journal of Ocean Engineering and Technology (JOET) is a medium for the publication of original research and development work in the field of ocean engineering. JOET covers the entire range of issues and technologies related to the following topics:

Ships and offshore platforms: Design of marine structures; Resistance and propulsion; Seakeeping and maneuvering; Experimental and computational fluid dynamics; Ocean wave mechanics; Fatigue strength; Plasticity; Optimization and reliability; Arctic technology and extreme mechanics; Noise, vibration, and acoustics; Concrete engineering; Thermodynamics and heat transfer; Hydraulics and pneumatics;
Coastal civil engineering: Coastal structures; Port and harbor structures; Soil mechanics; Drilling and exploration; Hydraulics of estuary; Seismic engineering; Coastal disaster prevention engineering;
Ocean renewable energy platforms: Offshore wind turbines; Wave energy platforms; Tidal current energy platforms; Floating photovoltaic energy platforms;
Marine robots: Robot sensor system; Autonomous navigation; Robot equipments; Spatial information and communications; Underwater network; Design of underwater vehicles;
Multidisciplinary areas: Design for safety; IT-based design; IT-based production engineering; Welding mechanics; Control engineering; GPS and GIS; Inspection and sensor; Port and logistics; Leisure boat and deep sea water; Offshore process systems engineering; Marine metallic materials; Marine organic materials; Marine Composite materials; Materials properties; Corrosion and Anti-corrosion; Tribology;

It contains original research articles, case reports, brief communications and reviews on technical issues. Conference papers, research papers, diploma papers and academic articles can be submitted.

All of the manuscripts are peer-reviewed. **JOET** has a system where two or more peer reviewers must review each submitted paper and it is operated very strictly.

JOET is an open access journal distributed under the terms of the creative commons attribution non-commercial license (<http://creativecommons.org/licenses/by-nc/4.0>). Therefore, all ocean engineers and researchers around the world can easily access all journal articles via the journal homepage (<http://www.joet.org>) and download the PDF-based original texts or view the web-based XML texts for free.

JOET is being indexed in some prominent database such as Korean Citation Index (KCI), Google Scholar, Science Central, Korea Science and Directory of Open Access Journals (DOAJ).

For correspondences concerning business matters, author needs to contact KSOE Secretariat by email or phone (e-mail: ksoehj@ksoe.or.kr or Tel: +82 51 759 0656). Correspondences for publication matters can be asked via email to the Editor-in-Chief (email: heroeswise2@gmail.com).

Discussions on Availability of Weather Information Data and Painting Effect of Existing 8,600 TEU Container Ship Using Ship Performance Analysis Program

Myung-Soo Shin¹, Min Suk Ki², Gyeong Joong Lee¹, Beom Jin Park²,
Yeong Yeon Lee¹, Yeongseon Kim³ and Sang Bong Lee⁴

¹Principal Researcher, Korea Research Institute of Ships & Ocean Engineering, Daejeon, Korea

²Senior Researcher, Korea Research Institute of Ships & Ocean Engineering, Daejeon, Korea

³Head of R&D Team, HMM Co., LTD, Busan, Korea

⁴CEO, LAB021, Busan, Korea

KEY WORDS: Speed-power analysis, Painting effect, Weather information, Wave radar, Wind resistance, Wave resistance, 8,600 TEU Container

ABSTRACT: This paper discusses the effectiveness of onboard measurements and data extracted from weather information for speed-power analysis. Furthermore, validation results of hull and propeller cleaning and painting during dry-docking are discussed. Wind and wave information can be obtained from onboard measurements or weather information from the National Oceanic and Atmospheric Administration (NOAA). The weather information of a specified position and time is extracted from NOAA weather data and compared with onboard measurements. In addition, to validate the effects of hull cleaning and painting during dry-docking, speed-power analysis results of before and after dry-docking are compared. The results show that both onboard measurements and weather information show acceptable reliability when added resistance and speed-power analysis results are compared with each other. Moreover, the ship performance analysis (SPA) software clearly shows the effects of hull cleaning and painting, and it can provide reliable analysis results with either onboard measurements or weather information. In conclusion, it is confirmed that the analysis method and SPA software used in this study are effective in analyzing the ship's speed-power performance.

Nomenclature

A_{XV}	Transverse projected area above the waterline	V_{WTrref}	True wind velocity at the reference height
C_{AA}	Wind resistance coef. ($C_{AA}(0)$ means head wind)	Z_a	Vertical height of anemometer
TM	Draught at midships (m)	Z_{ref}	Reference height for the wind resistance
R_{AA}	Resistance increase due to relative wind in newtons	α	Angle between ship's heading and component waves
R_{AW}	Resistance increase in short crested irregular waves	ΔR	Total resistance increase
R_{WAVE}	Resistance increase in regular waves	ρ_A	Mass density of air (kg/m^3)
UTC	Coordinated Universal Time	ψ	Ship's heading in degrees
V_G	Ship's speed over ground	ψ_{WR}	Relative wind direction at the height of anemometer
V_S	Ship's speed through the water	ψ_{WRef}	Relative wind direction at reference height
V_{WR}	Relative wind velocity at the height of anemometer	ψ_{WT}	True wind direction at the height of anemometer
V_{WRef}	Relative wind velocity at the reference height		
V_{WT}	True wind velocity at the height of anemometer		

1. Introduction

Global warming by greenhouse gases (GHGs) is a critical issue, and the International Maritime Organization (IMO) has been continuously

Received 5 October 2020, revised 20 October 2020, accepted 23 October 2020

Corresponding author Beom Jin Park: +82-42-866-3416, bjpark@kriso.re.kr

© 2020, The Korean Society of Ocean Engineers

This is an open access article distributed under the terms of the creative commons attribution non-commercial license (<http://creativecommons.org/licenses/by-nc/4.0>) which permits unrestricted non-commercial use, distribution, and reproduction in any medium, provided the original work is properly cited.

discussing regulations to reduce GHG emissions. The energy efficiency design index (EEDI) has been applied to new ships, whereas the energy efficiency existing ship index (EEXI) for regulating existing ships is under discussion (IMO, 2014; IMO, 2019).

To reduce GHG emissions from new ships, many technologies have been developed, primarily for shipyards. To reduce GHG emissions from existing ships and improve their operating efficiency, shipping companies are focusing on securing eco-friendly operating technology with fuel-saving benefits, such as low-speed operations, partial modifications of ship hull, and installation of energy-saving devices (ESDs).

Existing ships are periodically docked for the sanding, cleaning, and painting of the hull and propeller. These restore their resistance and propulsion performance. Recently, divers or robots also clean the hull and propeller of ships while they are moored in ports (Lysklett, 2018; Noordstrand, 2018). However, no precise method were available for verifying the fuel-saving effect of such activities.

To verify such activities, technology that can accurately identify the fuel consumption which emits GHGs during operation is necessary. The fuel consumption of an existing ship is the sum of the fuel for sailing at the speed through water (V_S) on a calm sea, and the additional fuel to respond to the added resistance due to wind and waves, and the resistance increase due to water temperature deviation caused by the marine environment. If the fuel consumption of each item can be identified, then the eco-friendly operating technologies applicable to shipping companies can be evaluated precisely; hence, plans for eco-friendly operations can be established.

European shipping companies are attempting to measure the thrust at propeller shaft in addition to the torque in order to evaluate the resistance and propulsion performance of existing ships. Once highly accurate thrust measurements are available, then the aging effect of the hull can be estimated separately from the aging degree of the propeller. In addition, the verification of the effect of the retrofitting of bulbous bow and the modification of propeller boss cap fin has been attempted; however, it was difficult to obtain quantitative and clear results. (Paereli et al., 2016; Balleghooijen et al., 2017).

The authors of this study developed a ship performance analysis (SPA) software program for operating ships based on the calculation procedure of the International Organization for Standardization (ISO) standard (ISO15016:2015)(ISO, 2015), which calculate the reference speed in calm seas included in the EEDI regulated by the IMO.

The analysis method and the software have been described by Park et al. (2019). Lee et al. (2019). Shin et al. (2020) verified the validity of the SPA software program and analysis method by conducting the speed-power analysis of a 176 K bulk carrier and an 8,600 TEU container ship in operation. The authors constructed the mean stowage diagram of containers by analyzing the operating condition and obtained onboard measurement data by improving the data transmission system owned by the shipping company. The authors confirmed that a comparison between the speed-power line in calm seas obtained as the analysis result and the model test speed-power line

clearly showed an increase in the delivered horse power (DHP) due to hull and propeller fouling and aging.

For the speed-power analysis of an existing ship, the location, speed, weight of cargo, and DHP of the ship as well as ocean climate environments information such as wind, wave, and sea water temperature are required. The ocean climate environments can be obtained through onboard measurements or by extracting data based on the time and position of the ship from the weather information of the National Oceanic and Atmospheric Administration (NOAA). In particular, for the analysis of added resistance due to wave, the values of the wave height, direction, and period are required for the sea wave and swell. These values can be obtained onboard from the observation of sailors or measurements using wave radar. However, it is extremely difficult for sailors to continuously observe waves, and wave radar is rarely installed on existing ships. Therefore, it is practical to extract data from weather information; however, studies that validate the accuracy of the information are nearly absent.

To verify the weather information in this study, the onboard measurements of the wave height, direction, and period obtained by installing wave radar in an existing ship were compared with data extracted from the weather information. In addition, the added resistance due to waves analyzed using the values obtained by each method were compared along with the speed-power analysis result applying each method. Furthermore, a study on wind speed and direction were also conducted with the same principle and the results were compared. Consequently, it was confirmed that both data obtaining method showed valid analysis results.

Existing ships are typically dry-docked every five years for inspection and maintenance. During dry-docking, the hull surface and propeller are cleaned and painted, and the verification of the effect of such activities is critical to shipping companies. In this study, the docking effect was quantitatively verified by analyzing the powering performance before and after docking using SPA software.

The results of this study show that the precise powering performance of an existing ship as well as the added DHP due to the resistance increase from wind and waves, as well as sea water temperature deviations can be calculated. In addition, this study on the effects of hull and propeller cleaning and painting performed during dry-docking and the GHG reduction by retrofitted ESDs is expected to be applied for green shipping.

2. 8,600 TEU Container Ship Overview

The target ship of this study is an 8,600 TEU container ship. Fig. 1 shows a photograph of the target ship, and Table 1 lists its principal particulars. The ship is identical to the target ship of Shin et al. (2020), and its main route includes South Korea, China, Singapore, the Middle East, and Europe. The standard operating conditions were determined by analyzing the operating profile of the shipping company and summarized in Table 1.



Fig. 1 Photograph of 8,600 TEU container ship (Shin et al., 2020)

Table 1 Standard operating condition for the speed-power analysis (Shin et al., 2020)

	TM 12.5 (Head haul)	TM 13.6 (Back haul)
Length between perpendiculars, Breadth (m)	322.6, 45.6	
Displacement (t)	109,961.5	122,954.4
Volume (m ³)	107118.5	119784.0
Wetted surface area (m ²)	16125.4	17178.3
Draught aft, draught forward (m)	12.5, 12.5	13.7, 13.5
TM (Draught at midship, m)	12.5	13.6
Reference speed (kn)	18.5 (9.5 m/s)	15.3 (7.9 m/s)
Speed range (kn)	12.5-22 (6.4-11.3 m/s)	
Transverse projected area (m ²)	1754.6	1704.5
Anemometer height from base line (m)	46.5	45.4
Measurement range of draught	TM: 11-13 m	TM: 13-15 m

The target ship is equipped with an energy efficiency monitoring system. This system collects various operating data in real time and transmits them to land. It collects more than 80 types of data, such as the DHP, fuel consumption, water temperature, wind speed, and wind direction, which further include more than 40 types of data, such as course, heading, and ballast water (Shin et al., 2020).

3. Wind and Wave Data Extraction from Weather Information

As for the ocean weather information used in this study, the values are calculated using a high-performance computer based on numerical weather prediction models. For the numerical weather prediction models, the meteorological modeling of the Earth’s weather system was performed using physical equations that governed the state and motion of the atmosphere.

For the speed-power analysis, the weather information of wind, waves, tidal currents, water temperature, air temperature, and atmospheric pressure in the waters of the ship operation was required as input data. Such information was collected from various numerical weather prediction models, as shown in Table 2.

Table 2 Ocean weather information for ship performance analysis

Weather type	Product	Model	Grid
Wave	Total wave height	NWW3 (NOAA Wave Watch 3)	0.5°
	Total wave direction		0.5°
	Total wave period		0.5°
	Wind wave height		0.5°
	Wind wave direction		0.5°
	Wind wave period		0.5°
	Swell wave height		0.5°
Wind	Swell wave direction	GFS (Global forecast system)	0.5°
	Swell wave period		0.5°
	Wind speed		0.5°
Air	Wind direction	RTOFS (Real time ocean forecast system)	0.5°
	Air temp’		0.5°
	Air pressure		0.5°
Sea surface	Sea water temp’		0.5°
	Current speed		0.5°
	Current direction		0.5°

The global ocean weather information was provided by the NOAA and the European Centre for Medium Range Weather Forecasts. In this study, weather information from the NOAA, which has been widely used for oceanic studies, was adopted.

The NOAA provides ocean weather information every three hours, eight times a day. The information is provided in a data format referred to as gridded binary (Grib). Because Grib files are not in a format that can be directly used for data analysis, the files must be stored in a database after they are decoded; subsequently, the data are to be extracted for the desired position and date. Weather data are provided at 0.5° latitude and longitude intervals eight times a day. The amount of data is approximately 30 million, a size that is difficult to process in a typical relational database. To secure fast performance, the data were stored and processed in a distributed database.

The ocean weather information was prepared in the form of predefined latitude and longitude grids. Fig. 2 shows an example of

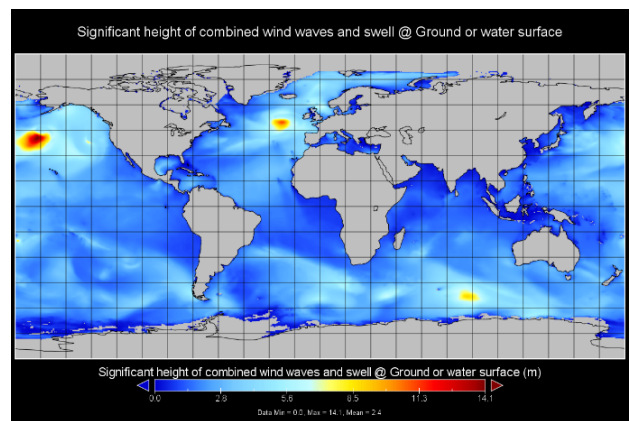


Fig. 2 Visualization of wave height information using NWW3 (NOAA Wave Watch 3) model.

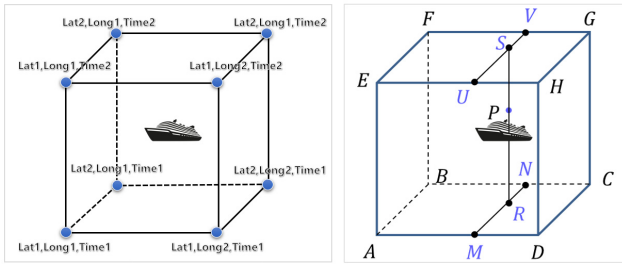


Fig. 3 Trilinear interpolation diagram based on ship position and time

such information on waves in grid form. To obtain accurate weather information for a specific ship position based on this form, the weather information must be interpolated.

Because the weather information used in this study was provided at 0.5° latitude and longitude intervals every three hours, spatio-temporal interpolation was required. Hence, the data values were interpolated for the sides and for an arbitrary internal point of a hexahedron with eight vertices in a three-dimensional (3D) space. Trilinear interpolation, a 3D interpolation method, was applied under the assumption that the values on each side were linear. In the trilinear interpolation method, the interpolated values at M and N were obtained first, and the value at R was interpolated from them to obtain P , which is the value of the current position and time of the ship, as shown in Fig. 3. The value at S was interpolated using the same method, and the final P value was obtained from S and R .

4. Speed-Power Analysis Results

4.1 Comparison of Wind Resistance between Onboard Measurements and Weather Information

To calculate the added resistance due to the ocean environment for the speed-power analysis of an existing ship, the accuracy and reliability of the input data must be reviewed first. In this section, the analysis results obtained based on onboard measurements (Shin et al., 2020) using an ultrasonic anemometer installed for accuracy improvement are compared with those obtained using the data extracted from the NOAA weather information based on the ship position and time to discuss the accuracy and availability of the data.

The onboard measurements of the relative wind speed and direction were converted to true wind speeds and directions using Eqs. (1) and (2). Here, the relative wind direction is the clockwise angle from the head, and the head wind is 0° .

$$V_{WT} = \sqrt{V^{2wr} + V_G^2 - 2V_{WR}V_G\cos\psi_{WR}} \quad (1)$$

$$\psi_{WT} = \tan^{-1} \left\{ \frac{V_{WR}\sin(\psi_{WR} + \psi) - V_G\sin(\psi)}{V_{WR}\cos(\psi_{WR} + \psi) - V_G\cos(\psi)} \right\} \quad (2)$$

for $V_{WR}\cos(\psi_{WR} + \psi) - V_G\cos(\psi) \geq 0$

$$\psi_{WT} = \tan^{-1} \left\{ \frac{V_{WR}\sin(\psi_{WR} + \psi) - V_G\sin(\psi)}{V_{WR}\cos(\psi_{WR} + \psi) - V_G\cos(\psi)} \right\} + 180$$

for $V_{WR}\cos(\psi_{WR} + \psi) - V_G\cos(\psi) < 0$

The converted wind speed (V_{WT}) and wind direction (ψ_{WT}) are the true wind speed and true wind direction at the anemometer height, respectively. According to ISO15016:2015, wind blowing toward a ship can be classified into two categories. One is the wind resistance due to the speed of advance of the ship. This wind is the head wind and is a uniform flow. This resistance is not treated as added resistance due to wind. The other is natural wind, which is a shear flow whose speed increases with altitude. As the true wind speed obtained using Eqs. (1) and (2) is the speed at the height of the anemometer installed on the ship, it is converted to the true wind speed at the reference height using Eq. (3).

$$V_{WTref} = V_{WT} \left(\frac{Z_{ref}}{Z_a} \right)^{\frac{1}{7}} \quad (3)$$

In Eq. (3), it is assumed that the shear flow profile based on the height from the ground follows the 1/7-squared profile, which is adopted by ISO15016:2015. In this study, a typical reference height value of 10 m was used, which is consistent with the weather information. The wind speed and direction measured using the anemometer installed on the ship were converted to the true wind velocity (V_{WTref}) and true wind direction (ψ_{WTref}) at the reference height using Eqs. (1), (2), and (3). These values were converted to the relative wind speed (V_{WRef}) and relative wind direction (ψ_{WRef}) using Eqs. (4) and (5), respectively, and the added resistance due to wind was calculated using Eq. (6).

Because the values extracted from the aforementioned weather information were the absolute wind speed (V_{WTref}) and absolute wind direction (ψ_{WT}) at the reference height of 10 m, they were directly converted to the relative wind speed and direction at the reference height using Eqs. (4) and (5) without using Eqs. (1), (2), and (3); furthermore, the added resistance due to wind was calculated using Eq. (6). The resistance due to the uniform flow caused by speed of advance (V_G) was not considered as added resistance, and only the added resistance caused by the speed and direction of natural wind was considered.

$$V_{WRef} = \sqrt{V^{2wref} + V_G^2 - 2V_{WTref}V_G\cos(\psi_{WT} - \psi)} \quad (4)$$

$$\psi_{WRef} = \tan^{-1} \left\{ \frac{V_{WTref}\sin(\psi_{WT} - \psi)}{V_G + V_{WTref}\cos(\psi_{WT} - \psi)} \right\} \quad (5)$$

$$\text{for } V_G + V_{WTref}\cos(\psi_{WT} - \psi) \geq 0$$

$$\psi_{WRef} = \tan^{-1} \left\{ \frac{V_{WTref}\sin(\psi_{WT} - \psi)}{V_G + V_{WTref}\cos(\psi_{WT} - \psi)} \right\} + 180$$

$$\text{for } V_G + V_{WTref}\cos(\psi_{WT} - \psi) < 0$$

$$R_{AA} = \frac{1}{2}\rho_A \cdot C_{AA}(\psi_{WRef}) \cdot A_{XV} \cdot V_{WRef}^2 - \frac{1}{2}\rho_A \cdot C_{AA}(0) \cdot A_{XV} \cdot V_G^2 \quad (6)$$

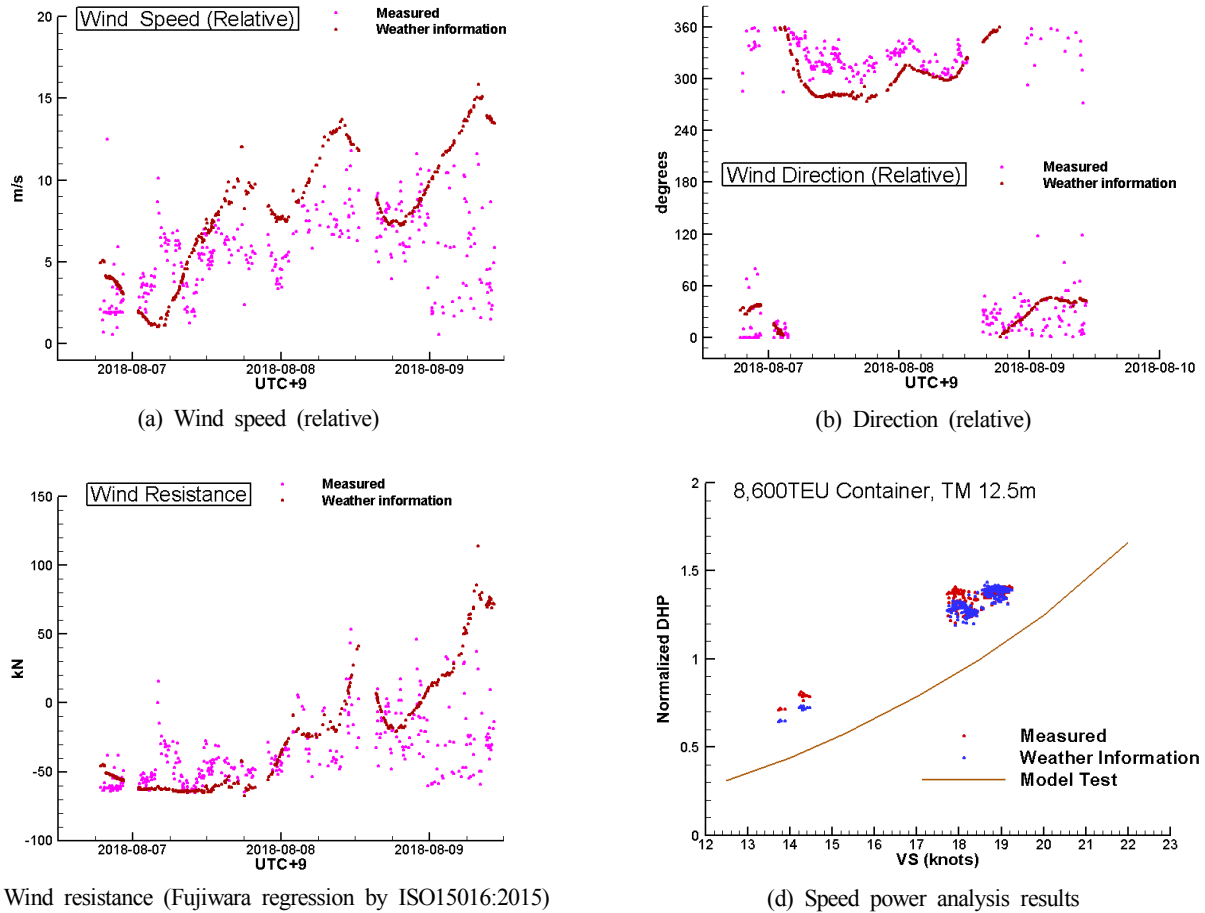


Fig. 4 Comparisons of wind speed, direction at reference height, resistance, and analysis results between onboard measured and weather information data (*TM* 12.5 m, Singapore → China)

Fig. 4 shows comparisons of the wind data and analysis results between onboard measured and weather information data. The operating route was from Singapore to China in August 2018. The displacement condition of the ship was standard operating condition *TM* 12.5 m in Table 1. In Figs. 4(a) and (b), the x-axis is UTC+9 (Korean local time) and the y-axes are the relative wind speed and relative wind direction at the reference height, respectively. As for the relative wind speed, the measured wind speed was generally lower compared with the weather information, except for some sections on August 7th. The relative wind direction results were consistent within the range of $\pm 20^\circ$. The wind resistance calculated using the Fujiwara regression formula of ISO15016:2015 (as shown in Fig. 4(c)) was generally low, similar to the wind speed. Fig. 4(d) shows the speed-power analysis results obtained by analyzing the wave resistance using the empirical correction method with frequency response function (hereafter, STAWAVE-2) of ISO15016:2015. The y-axis represents the normalized DHP based on the tank test results of 18.5 kn (9.5 m/s), which is the reference speed of *TM* 12.5 m in Table 1. The aforementioned tendency was reflected; however, a significant difference was not observed.

Fig. 5 shows comparisons of the wind data and analysis results between onboard measured and weather information data. Ship

operating route was from Malaysia to India in September 2018. Standard operating condition *TM* 13.6 m in Table 1 was applied. Figs. 5(a) and 5(b) show that the measured wind speed was generally lower compared with the weather information, except for some sections, as shown in Figs. 4(a) and 4(b); additionally, the relative wind direction results agreed well. As shown in Fig. 5(c), the wind resistance was generally low, similar to the wind speed. The speed-power analysis results in Fig. 5(d), however, exhibited no significant difference. The DHP was analyzed and normalized using the same methods as those used to obtain Fig. 4.

In this section, the onboard measurements and the values of the NOAA weather information that were used as input data as well as the wind resistance and speed-power analysis results of the existing ship are compared. The wind direction results indicated good agreement. As for the wind speed, the onboard measurements tended to be lower compared with the weather information. The wind resistance showed the same tendency, and the wind resistance from the measured data was lower. However, the speed-power analysis results exhibited no significant difference. Both the added resistance due to wind by the onboard anemometer measurements and that by the wind speed and direction values extracted from the weather information provided reliable accuracy, indicating that any of the two methods can be used

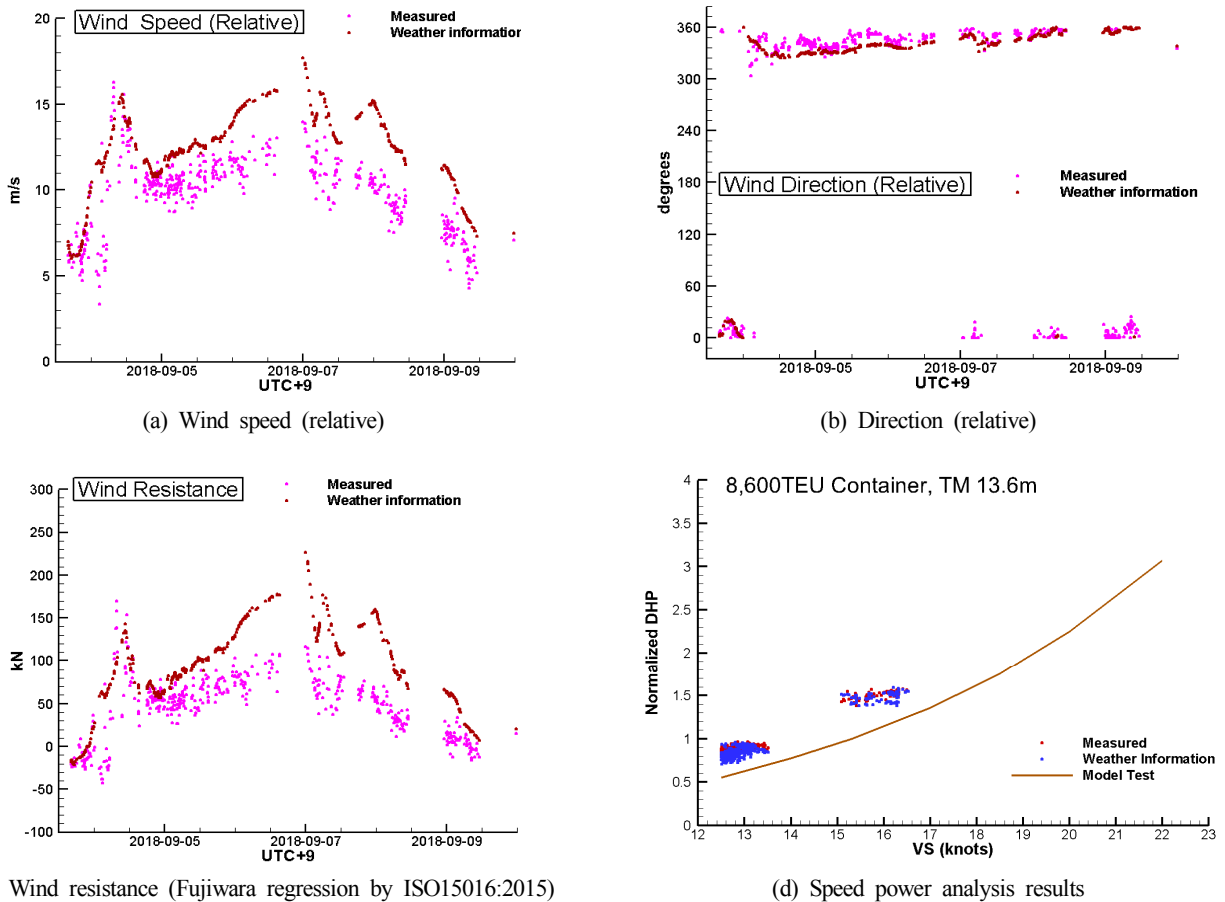


Fig. 5 Comparisons of wind speed, direction at reference height, resistance, and analysis results between onboard measured and weather information data (*TM* 13.6 m, Malaysia → India)

for the practical speed-power analysis of existing ships.

4.2 Comparison of Added Resistance Due to Waves Between Onboard Measurements by Wave Radar and Weather Information

In this section, the added resistance due to waves and speed-power analysis results obtained from the wave data measured using wave radar are compared with those obtained from weather information. The wave radar is a device that analyzes the significant wave height, wave direction, and wave period from the images obtained using the standard marine X-band radar, and it can be used for the speed trial of new ships (ISO 15016:2015). Table 3 shows the system specifications of the wave radar installed on the 8,600 TEU container ship of this study, and Fig. 6 shows its photograph. The error range for the significant wave height of 3 m or less was 0.5 m, and that for higher waves, wave direction and period was $\pm 10\%$.

Table 3 System specifications of wave radar (Shindong Digitech, 2020)

Parameter	Range	Accuracy
Significant wave height	0–3 m	± 0.5 m
	3–20 m	$\pm 10\%$
Wave period	4–20 s	$\pm 10\%$
Wave direction	0–360°	$\pm 10^\circ$

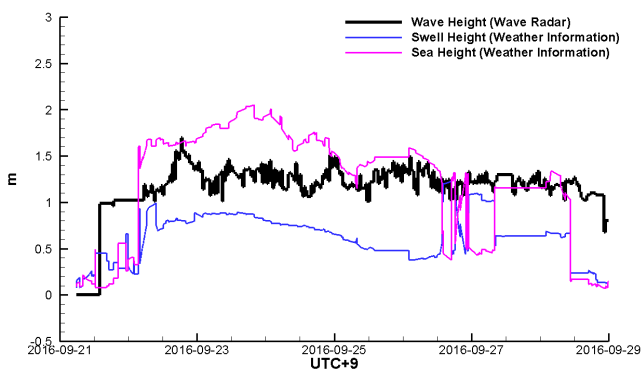


Fig. 6 Photographs of wave radar on 8,600 TEU container ship

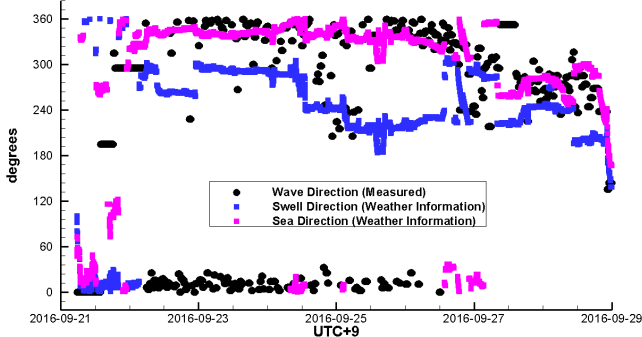
Fig. 7 shows a comparison of the wave radar measurements with the wave height, wave direction, and wave period extracted from weather information using the method presented in Section 3. The corresponding route was from Malaysia to Dubai in September 2016, and standard operating condition *TM* 13.6 m in Table 1 was applied. The x-axis is UTC+9 (Korean local time) and the y-axes are the wave height, wave direction, and wave period. For the analysis of added resistance due to waves, the relative wave direction is required. The wave direction measured by the wave radar is the relative direction, so the measured value can be applied directly to the analysis. As the wind direction extracted from the weather information is the true direction, it must be converted to the relative direction considering the heading

of the ship. The relative wave direction is the clockwise angle from the head, and the head wave is 0°. As shown in Fig. 7(a), the wave heights measured by the wave radar and the sea wave height of weather information exhibited similar tendencies. In the route, the waves were not relatively high, and the wave height around September 23rd was approximately 2 m according to the weather information. Fig. 7(b) shows that the measured wave direction agreed well with the sea wave direction of the weather information. In addition, Fig. 7(c) shows that the measured wave period was consistent with the sea wave period of the weather information.

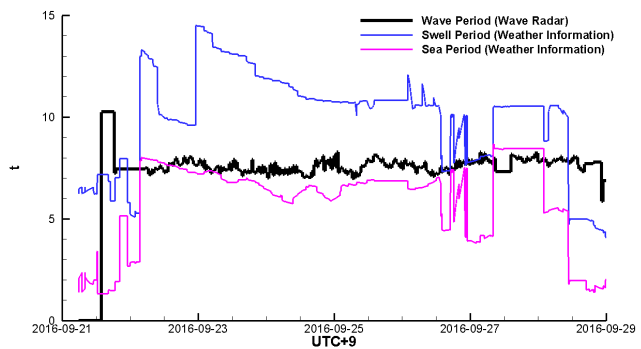
Fig. 8 shows the added resistance due to waves calculated using the STAWAVE-2 method. The x-axis is UTC+9 and the y-axis is the resistance value (kN). This STAWAVE-2 is the most frequently used



(a) Wave height

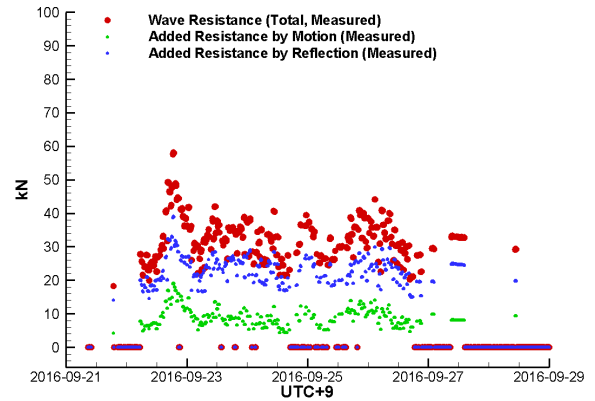


(b) Wave direction (relative)

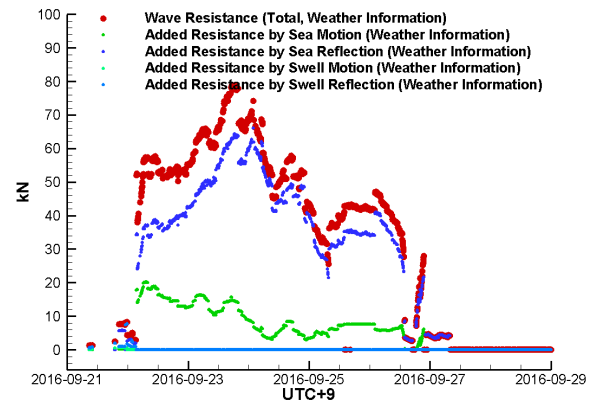


(c) Wave period

Fig. 7 Comparisons of wave height, relative direction, and period between onboard data measured by wave radar and weather information



(a) Added resistance by wave radar data



(b) Added resistance by weather information

Fig. 8 Comparisons of added resistance due to waves between data measured by wave radar and weather information (STAWAVE-2 by ISO15016:2015)

method to calculate added resistance due to waves during the speed trial of new ships. It is an empirical formula to estimate the added resistance due to bow waves, and the added resistance due to the waves out of the $\pm 45^\circ$ range from the bow is treated as zero.

The added resistance due to waves is the sum of the motion-induced resistance and the resistance increase due to wave reflection. Fig. 8(a) shows the added resistance from the wave radar measurements. A maximum value of 60 kN was observed around September 23rd, and the resistance was primarily caused by reflection. Fig. 7(b) shows that the added resistance was zero after September 27th because the wave direction was in the $240^\circ\text{--}300^\circ$ range.

The waves of the weather information were divided into swell and sea, and the added resistance was the sum of both. In addition, the added resistance due to each of the swell and sea was the sum of its motion and reflection. Fig. 8(b) shows the calculated added resistance due to waves. The resistance was primarily caused by sea reflection, and the added resistance on September 24th was calculated to be approximately 80 kN, which was higher than the wave radar value. This is because the wave height of the weather information was relatively high. For the wave radar, the added resistance due to sea was zero after September 27th because the wave direction was in the $180^\circ\text{--}300^\circ$ range. In addition, the wave direction of the swell ranged from

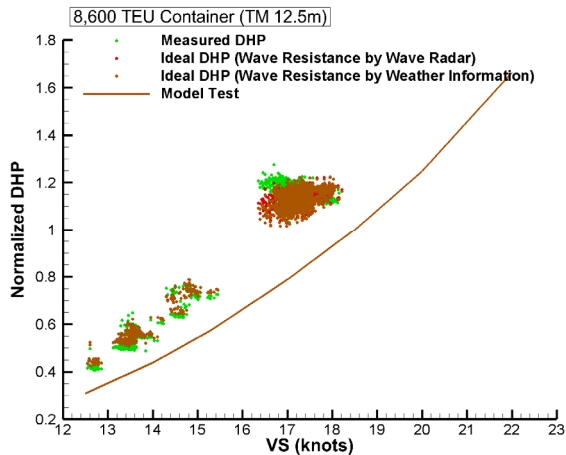


Fig. 9 Comparison of speed-power analysis results between wave measured by wave radar and weather information (*TM* 12.5 m)

180° to 300° during the entire voyage period, as shown in Fig. 7(b); hence, the added resistance due to swell was zero.

Fig. 9 shows the speed-power analysis results for the same operating data with Figs. 7 and 8. The y-axis represents the normalized DHP based on the tank test results of 18.5 kn (9.5 m/s), which is the reference speed of *TM* 12.5 m in Table 1. The wind was measured on board the ship, and the added resistance due to wind was analyzed using the Fujiwara regression formula of ISO15016:2015. The waves were analyzed using the STAWAVE-2 method of ISO15016:2015. The waves during operation were approximately 1.5 m, and the maximum difference in added resistance was approximately 20 kN; however, the speed-power analysis results in Fig. 9 exhibited no significant difference. The analysis results from the measurements of the wave radar, which was difficult to install and costly, did not differ significantly from those of the weather information.

Analyzing the speed-power performance of an existing container ship using SPA software (Park et al., 2019), both the data measured using the wave radar and the data extracted from the weather information can be used as input data for added resistance due to waves. Hence, it can be concluded that both two data sets provide reliable results.

4.3 Verification of Effects of Hull and Propeller Cleaning and Painting

Ships are docked after a certain period of operation for ship inspection and maintenance. The target ship of this study was docked in November 2017. Subsequently, cleaning and maintenance were performed for the propeller, and sand blasting and painting for the hull. Fig. 10 shows the photographs before and after docking.

Fouling is known to be the main cause of increased resistance for aged ships. Based on the hull inspection results after docking, moderate slime and seagrass were attached to 11%–30% of the vertical bottom. Slight slime was attached to 1%–10% of the flat bottom and boot top, and local damage to the coating caused by mechanical damage was found. Painting was performed using silyl-type,

self-polishing, antifouling, low-friction paint. Based on the inspection results upon the completion of painting, the hull roughness was 123 μm on average (maximum: 133 μm ; minimum: 89 μm), which satisfied the paint supplier's criterion of 150 μm or less.

Fig. 11 shows the speed-power results before and after docking for an analysis of the docking effect of the target ship. The legends in the figure indicate the port departure dates before and after docking, and the operating route included China, Taiwan, Hong Kong, Singapore, Malaysia, and the United Arab Emirates. The DHP was normalized as in Fig. 9. An analysis of before and after docking shows that the results of *TM* 12.5 m were similar. The *TM* 13.6 m analysis results improved by 10%–12% near 20–22 kn (10.3–11.3 m/s) and by approximately 5% at the reference speed of 15.3 kn (7.87 m/s). The friction resistance reduction effect by hull blasting and painting was evident in the high-speed range for *TM* 13.6 m owing to its deep draft.

The wind resistance was calculated using the Fujiwara regression formula of ISO15016:2015 based on the onboard measurements. The



(a) Before blasting & painting



(b) After blasting & painting

Fig. 10 Photographs of 8,600 TEU container during docking (dated November 2017).

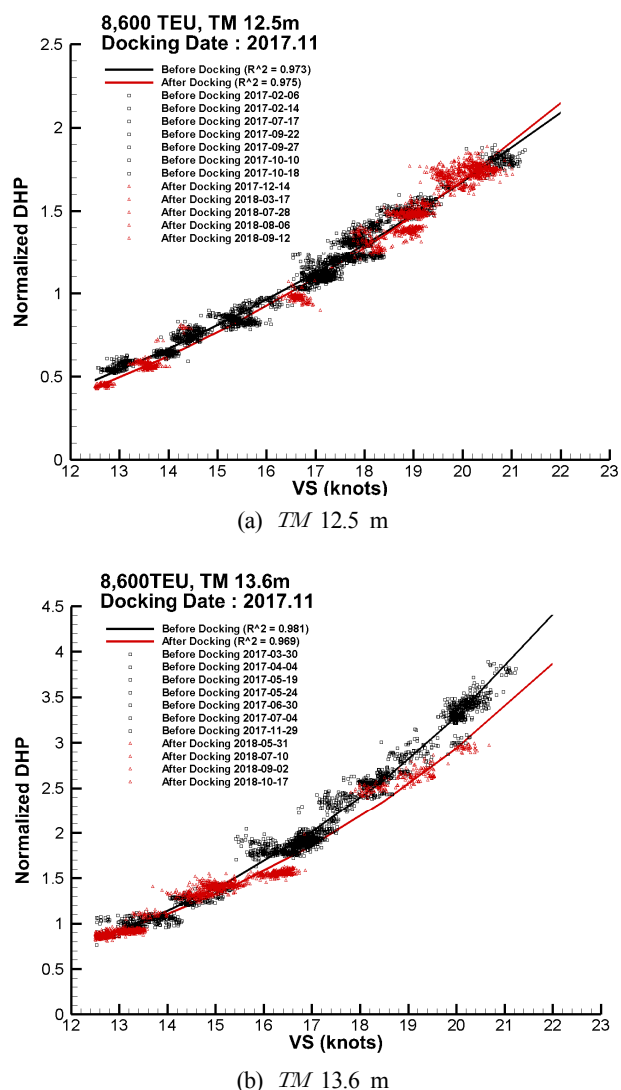


Fig. 11 Comparison of speed-power analysis result between before and after docking in November 2017.

wave resistance was calculated using STAWAVE-2 based on the wave values extracted from the weather information. The added resistance due to sea water temperature deviation was analyzed based on the onboard measurements (ISO 2015, Shin et al, 2020).

5. Conclusion

To reduce GHG emissions from existing ships operated by shipping companies, it is very important to identify accurate speed-power performance due to additional resistance from marine environment and aging effects.

In this study, onboard measurements and weather information data were compared using SPA software, and the docking effect was verified. The conclusions of this study are as follows:

(1) In estimating the added resistance due to wind for an existing ship, the onboard measurements obtained using an anemometer were

compared with the values provided by the NOAA. The wind resistance and speed-power analysis results were compared. The wind direction showed good agreement. For the wind speed, the weather information tended to be higher. The wind resistance has the same tendency, but the speed-power analysis results showed no significant difference, indicating that both methods are practically usable.

(2) The wave height, wave direction, and wave period measured using wave radar and those obtained from the NOAA were compared. In addition, the added resistance due to waves was calculated and a speed-power analysis was conducted. It can be concluded that both the data from the wave radar and those from the weather information provided reliable results for analyzing the speed-power performance of an existing ship.

(3) All of the data extracted from the weather information provided are valid and reliable results, confirming the reliability of trilinear interpolation adopted in this study.

(4) The speed-power analysis results before and after docking showed that the results of *TM* 12.5 m were similar; however, in case of the *TM* 13.6 m, analysis results improved by 10%–12% near 20–22 kn (10.3–11.3 m/s) and by approximately 5% at the reference speed of 15.3 kn (7.87 m/s). This confirmed that the effects of cleaning and painting the antifouling low-friction paint on the hull and propeller during dry-docking can be quantitatively verified.

The speed-power analysis technique and SPA software were validated in this study. To obtain highly accurate analysis results, the accuracy of the measurement data must be improved and analysis methods must be continuously verified and developed.

Acknowledgments

The authors would like to express their gratitude to Dr. Tae-II Lee of Hyundai Heavy Industries Co., Ltd. for his assistance in preparing and analyzing the data used in this study.

This research was funded by the Ministry of Trade, Industry & Energy (Korea Government), grant number PNS3650, under the project “Optimal hull cleaning and propeller polishing scheduling for minimal ship operating cost using operating performance analysis.”

References

- Ballegooijen, E., Muntean, T., & Timmer, M. (2017). Measuring the Full-Scale Performance of a Propeller and Bulbous Bow Retrofit via Propeller Thrust Measurements. 2nd Hull Performance & Insight Conference, Hamburg, Germany, 132-142. http://data.hullpic.info/hullpic2017_ulrichshusen.pdf
- IMO. (2014). 2014 Guideline on the Method of Calculation of the Attained Energy Efficiency Design Index (EEDI) for New Ships. Resolution Marine Environment Protection Committee 245(66), International Maritime Organization, London.
- IMO. (2019). Energy Efficiency Improvement Measure for Existing

- Ships. Marine Environment Protection Committee 72/7/2, International Maritime Organization, London.
- ISO. (2015). Ships and Marine Technology—Guidelines for the Assessment of Speed and Power Performance by Analysis of Speed Trial Data (ISO15016:2015). International Standardization Organization, Geneva, Switzerland.
- Lee, G.J., Shin, M.S., Park, B.J., Ki, M.S., & Jeon, K.H. (2019). Validity Analysis of Speed, Wave Height and Wind Speed for the Operational Performance of Bulk Carrier. *Journal of the Korean Society of Marine Engineering*, 43(3), 183-196. <https://doi.org/10.5916/jkosme.2019.43.3.183>
- Lysklett, K.J. (2018). Underwater Drones as Efficient Tool for Hull and Propeller Inspections. 3rd Hull Performance & Insight Conference, Redworth, UK, 244-253. http://data.hullpic.info/hullpic2018_redworth.pdf
- Noordstrand, A. (2018). Experience with Robotic Underwater Hull Cleaning in Dutch Ports. 3rd Hull Performance & Insight Conference, Redworth, UK, 4-9. http://data.hullpic.info/hullpic2018_redworth.pdf
- Paereli, S., Krapp, A., & Betram, V. (2016). Splitting Propeller Performance from Hull Performance - A Challenge. 1st Hull Performance & Insight Conference, Castello de Pavone, Italy, 62-69. <http://data.hullpic.info/HullPIC2016.pdf>
- Park, B.J., Shin, M.S., Lee, G.J., & Ki, M.S. (2019). A New Method to Analyse the Speed Power Performance of Operating Ships and its Implementation. *Journal of Advanced Marine Engineering and Technology*, 43(10), 822-829. <https://doi.org/10.5916/jkosme.2019.43.10.822>
- Shin, M.S., Ki, M.S., Park, B.J., Lee, G.J., Lee, Y.Y., Kim, Y., & Lee, S.B. (2020). Speed-Power Performance Analysis of an Existing 8,600 TEU Container Ship using SPA(Ship Performance Analysis) Program and Discussion on Wind-Resistance Coefficients. *Journal of Ocean Engineering and Technology*, 34(5), 294-303. <https://doi.org/10.26748/KSOE.2020.047>
- Shindong Digitech. (2020). Radar Wave Height Observation System. Retrieved from http://www.shindong.com/product/product_03_03.php

Author ORCIDs

Author name	ORCID
Shin, Myung-Soo	0000-0002-6017-5369
Ki, Min Suk	0000-0001-6253-0531
Lee, Gyeong Joong	0000-0001-7555-9034
Park, Beom Jin	0000-0001-9729-4313
Lee, Yeong Yeon	0000-0002-0408-6222
Kim, Yeongseon	0000-0002-0089-138X
Lee, Sang Bong	0000-0002-3300-2411

Numerical Study on the Extrapolation Method for Predicting the Full-scale Resistance of a Ship with an Air Lubrication System

Dong-Young Kim¹, Ji-Yeon Ha¹ and Kwang-Jun Paik²

¹Graduate Student, Department of Naval Architecture and Ocean Engineering, Inha University, Incheon, South Korea

²Associate Professor, Department of Naval Architecture and Ocean Engineering, Inha University, Incheon, South Korea

KEY WORDS: Air lubrication system, Full-scale resistance, Frictional resistance, Form resistance, CFD

ABSTRACT: Frictional resistance comprises more than 60% of the total resistance for most merchant ships. Active and passive devices have been used to reduce frictional resistance, but the most effective and practical device is an air lubrication system. Such systems have been applied in several ships, and their effects have been verified in sea trials. On the other hand, there are some differences between the results predicted in model tests and those measured in sea trials. In this study, numerical analyses were carried out for a model and a full-scale ship. A new extrapolation method was proposed to improve the estimation of the full-scale resistance of a ship with an air lubrication system. The volume of fluid (VOF) method was considered for the numerical models of the air layer. The numerical method was validated by comparing the experimental data on the air layer pattern and the total resistance.

Nomenclature

$SLPM$	Standard liter per minute (L/min)
t_{AL}	Air layer thickness (mm)
Q_{Air}	Volume flow rate of air (m ³ /s)
B_{Air}	Width of the air injection slit (m)
V_{Inflow}	Inflow speed of water (m/s)

1. Introduction

The International Maritime Organization (IMO) has mandated a 30% reduction in CO₂ emissions by 2025 for ships, which produce 3.3% of global CO₂ emissions. To reduce CO₂ emissions, it is essential to estimate the ship's resistance and propulsion accurately and improve performance.

Frictional resistance generally accounts for more than 60% of the total resistance of a ship. An air lubrication system injects air onto the hull surface to form a continuous air layer, reducing frictional resistance on the hull surface and fuel consumption (Bushnell and Hefner, 1990; Ceccio, 2010). The frictional resistance can be reduced in three ways: bubble drag reduction (BDR), air layer drag reduction (ALDR), and partial cavity drag reduction (PCDR). PCDR can

increase the form resistance due to remodeling of the air cavity, but it is difficult to apply to a ship. Compared to BDR, ALDR requires high pumping power, but the resistance reduction rate is very high (Ceccio et al., 2012).

Jang et al. (2014) observed air layer formation using ALDR in the lower part of a plate in the cavitation tunnel of the Samsung Ship Model Basin (SSMB). They also measured the decrease in frictional resistance. An air layer was applied to a model 66K DWT Supramax bulk carrier to estimate the power-saving effect by conducting resistance and self-propulsion tests

Mäkiharju et al. (2017) examined the gas pocket morphology with air injection at a single inlet. The formation of a V-type gas pocket and the shape of the gas pocket were observed while changing the inflow rate and air injection rate. Computational fluid dynamics (CFD) simulations and experimental results showed similar tendencies.

Kim et al. (2017) analyzed the air layer pattern and diffusion angle at the bottom of a plate numerically using CFD. The air diffusion angle pattern according to the relationship between the air inflow rate and water inflow velocity was compared with the empirical formulae. They compared the lambda, delta, and transition air-layer patterns through the velocity vectors, velocity contours, and vorticity contours. On the other hand, the practical application of ALDR required multiple

Received 11 February 2020, revised 12 October 2020, accepted 19 October 2020

Corresponding author Kwang-Jun Paik: +82-32-860-7331, kwangjun.paik@inha.ac.kr

© 2020, The Korean Society of Ocean Engineers

This is an open access article distributed under the terms of the creative commons attribution non-commercial license (<http://creativecommons.org/licenses/by-nc/4.0>) which permits unrestricted non-commercial use, distribution, and reproduction in any medium, provided the original work is properly cited.

complex injections rather than a single injection.

Mäkiharju and Ceccio (2018) observed the shape changes of airflow with complex interactions in a multi-injection experiment. In some cases, multiple injections formed a more stable air layer than a single injection because each of the air layers interacted with each other. Multiple injections generated a larger gas pocket that formed into a liquid cross-flow, but a fortuitous gas pocket formed in some cases. Therefore, additional experiments are needed. In addition, it is necessary to cover a large number of flow parameters and derive clear results through further experiments using models with greater overall lengths.

Estimating the resistance reduction effects of an air lubrication system on a full-scale ship is important before studying the influence of the position, shape, and number of injectors. A more accurate method is also needed to estimate the full-scale ship resistance from the resistance components of a model ship.

The goal of this study was to improve the estimation of the actual resistance of air lubricated ships. A numerical method was developed and verified by comparing with experimental data (Jang et al., 2014). A new extrapolation method was proposed to estimate the full-scale resistance of a ship with an air lubrication system based on the numerical simulations for a model and full-scale ship.

2. Numerical Methods and Models

Incompressible three-dimensional unsteady flow was modeled to analyze the air lubrication performance. The continuity equation and Reynolds averaged Navier-Stokes (RANS) equations were used as the governing equations.

$$\frac{d}{dt} \int_V \rho dV + \int_S \rho u_i n_i dS = 0 \quad (1)$$

$$\begin{aligned} \frac{d}{dt} \int_V \rho u_i dV + \int_S \rho u_i u_j n_j dS \\ = \int_S (\tau_{ij} n_j - p n_i) dS + \int_V \rho b_i dV \end{aligned} \quad (2)$$

where u_i is the velocity tensor, and b_i is the tensor of body forces. p and ρ are the pressure and density, respectively. τ_{ij} is the effective stress of the viscosity and turbulence:

$$\tau_{ij} = \mu_e \left[\left(\frac{\partial u_i}{\partial x_j} + \frac{\partial u_j}{\partial x_i} \right) - \frac{2}{3} \delta_{ij} \frac{\partial u_k}{\partial x_k} \right] \quad (3)$$

where μ_e is the effective dynamic viscosity.

The commercial CFD software, STAR-CCM+ 12.06, was used for numerical analysis of multiphase flow. The volume of fluid (VOF) method was used for multiphase flow replication, considering the free surface and air layer. The Reynolds stress model (RSM) was used as the turbulence model. Table 1 lists the numerical models.

Table 1 Numerical models

Tool	STAR-CCM+ ver.12.06
Turbulence model	Reynolds stress model
Time	Implicit unsteady
Multiphase	Volume of fluid (VOF)
Diffusion term	2 nd order central difference scheme
Convection term	2 nd order upwind difference scheme

3. Setup of the Numerical Simulation

A scale model of a 66K DWT Supramax bulk carrier was used in the model test by Jang et al. (2014). Table 2 lists the main specifications of the ship. The model ship was scaled at a factor of 24.0. Therefore, the same factor was applied in numerical analysis.

Table 2 Specifications of the 66K DWT Supramax bulk carrier.

Specifications	
Length overall	200.0 m
Length between perpendicular	192.0 m
Breadth	36.0 m
Draft	11.2 m
Displacement volume	65,012.3 m ³
Wetted surface area	9,909.6 m ²
C_B	0.840

3.1 Computational Domain and Boundary Conditions

Fig. 1 shows the boundary conditions and the computational domain. A Cartesian coordinate system was used. Based on the center of gravity of the hull, the x-axis was set as the direction from the stern to the bow; the y-axis was set as the portside direction, and the z-axis was set as the opposite direction of gravity. The boundary conditions of the inlet surface, top surface, and bottom surface were set as the velocity inlet, and the outlet surface was set as the pressure outlet.

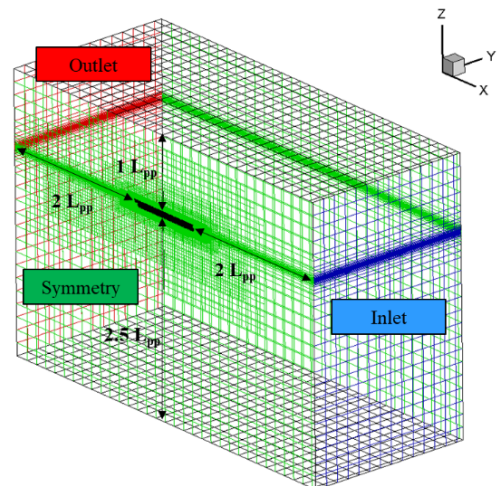


Fig. 1 Boundary conditions and grid system

Symmetric conditions were applied across the y-axis interface because the hull is perfectly symmetrical. Symmetric conditions were applied to the side to reduce the distortion of the reflected wave. The distances from the bow to the inlet, the hull to the top, the hull to the bottom, and the stern to the outlet were $2L_{pp}$, $1L_{pp}$, $2.5L_{pp}$, and $2L_{pp}$, respectively.

3.2 Injector Geometry

In the model test by Jang et al. (2014), the injector shapes were made with many holes, but they were modeled as a single slit in numerical analysis. Figs. 2 and 3 present the diagrams of the air cavity and the geometry of the air injector. The width and length of the slit were 6 mm and 260 mm, respectively. The air injection slits, C1 and C2, were located at the 17th and 15th, respectively.

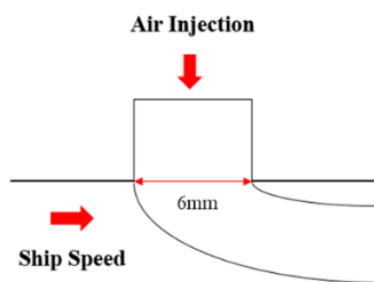


Fig. 2 Diagram of the air injector

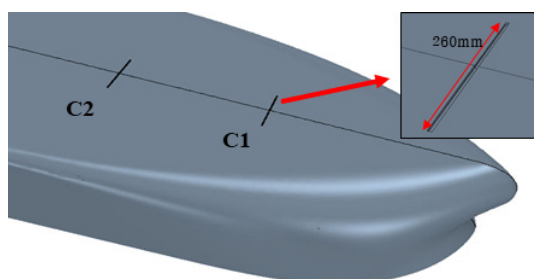


Fig. 3 Geometry of air injector

3.3 Grid Test

The grid system was verified by measuring the resistance according to the number of grid elements (approximately 1.0 million, 2.5 million, and 6.1 million). Differences of 0.118, 0.092, and 0.013% were observed compared with the model test results performed at SSMB in Fig. 4. The simulation took too much time when there were 6.1 million grid elements. When there were 1.0 million grid elements, realistic phenomena could not be observed when air was injected. Therefore, the medium grid size of 2.5 million was applied for the other simulations.

Table 3 lists the reduction ratio of the resistance due to the air layer under various combinations of the air injection flow rate and injection position. The ship speed was fixed to 1.5226 m/s, which corresponds to the design speed of 14.5 knots for a full-scale ship using Froude scaling. The total amount of air injected from C1 and C2 was set to a wide range of 0 to 400 liters per minute under standard conditions of 1 atm and 25°C (SLPM), as shown in Table 3.

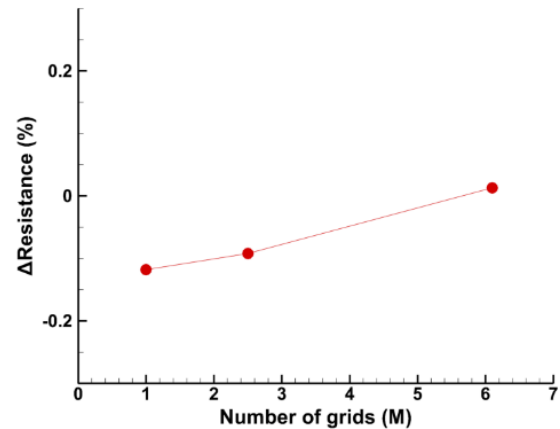


Fig. 4 Grid verification for the number of grids

Table 3 Simulation cases

Case	Injection position	SLPM	t_{AL} (mm)
Bare	-	0	0
Case 1	C1	50	2.1
Case 2	C1	100	4.2
Case 3	C1	150	6.3
Case 4	C2	100	4.2
Case 5	C2	150	6.3
Case 6	C2	250	10.5
Case 7	C1/C2	100/200	4.1/8.4
Case 8	C1/C2	100/250	4.1/10.6
Case 9	C1/C2	100/300	4.1/12.7

Eq. (4) was used to estimate the air layer thickness:

$$t_{AL} = \frac{Q_{Air}}{B_{Air} \cdot V_{Inflow}} \tag{4}$$

where Q_{Air} , B_{Air} , and V_{Inflow} are the volume flow rate of the injected air, the width of the air injection slit, and the inflow speed, respectively.

4. Results and Discussion

4.1 Reduction in Resistance

Table 4 presents the trim and sinkage of the ship that occurred when air was injected. A positive value occurs when the ship rises to the top, and the bow is trimmed. The largest change in trim ($\Delta Trim$) was 4.1% in Case 5. The ship was tilted more toward the bow by the buoyancy of air flowing from the bottom to the stern. On the other hand, the change in trim is not proportional to the amount of air. The change in sinkage ($\Delta Sinkage$) also increased continuously due to buoyancy as the amount of air injection increased.

Table 5 shows the total resistance reduction of the model ship (ΔR_{TM}), the ratio of the decrease in shear resistance to the decrease in total resistance (ΔR_{Shear}), and the ratio of the decrease in pressure resistance to the decrease in total resistance ($\Delta R_{Pressure}$). The largest

Table 4 Reduction rate of the trim and sinkage under each air injection condition

Case	ΔR_{TM} (%)	$\Delta Trim$ (%)	$\Delta Sinkage$ (%)
Bare	-	-	-
Case 1	11.2	1.0	2.7
Case 2	15.0	1.8	6.0
Case 3	17.5	0.0	8.7
Case 4	14.3	3.3	5.0
Case 5	16.8	4.1	7.3
Case 6	21.0	3.4	11.2
Case 7	23.3	2.1	13.4
Case 8	24.9	1.6	15.5
Case 9	26.1	2.5	16.5

Table 5 Resistance and reduction rate of the resistance component under each air injection condition

Case	ΔR_{TM} (N)	ΔR_{Shear} (%)	$\Delta R_{Pressure}$ (%)
Bare	-	-	-
Case 1	8.9	28.1	71.9
Case 2	11.9	36.8	63.2
Case 3	13.9	42.1	57.9
Case 4	11.4	32.7	67.3
Case 5	13.4	37.2	62.8
Case 6	16.7	44.3	55.7
Case 7	18.6	49.5	50.5
Case 8	19.8	51.2	48.8
Case 9	20.7	52.9	47.1

decrease in resistance was 20.7 N in Case 9. The amount of resistance reduction increased with increasing amount of air injected. In addition, as the amount of injected air increased, there was a greater reduction in frictional resistance. Interestingly, the rate of the decrease in the pressure resistance was as large as the rate of the decrease in shear resistance.

In Case 9, the shear resistance and pressure resistance were 52.9% and 47.1%, respectively. Previous research considered only the reduction in frictional resistance. On the other hand, both the frictional resistance and pressure resistance decreased when air lubrication was used. When air is injected, an air layer is generated on the bottom of the hull, which alters the resistance state of the ship. Thus, it is necessary to analyze the various changes due to air at these locations.

Fig. 5 shows the distribution of the volume fraction on the bottom of the hull. A larger air flow rate resulted in a larger diffusion angle and air layer thickness. The jetted air goes up on the bottom of the hull to the stern.

Fig. 6 shows the wall shear stress distribution on the hull surface, as seen from the bottom of the hull. The rate of decrease in the frictional resistance was the highest in Case 9, which has the highest air injection flow rate. The result appears similar to the shape of the volume

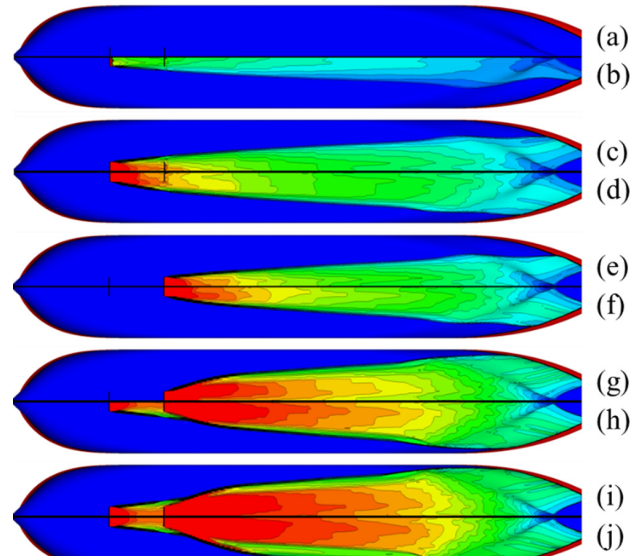


Fig. 5 Volume fraction of air on the hull surface (Bare, Cases 1-9 from top)

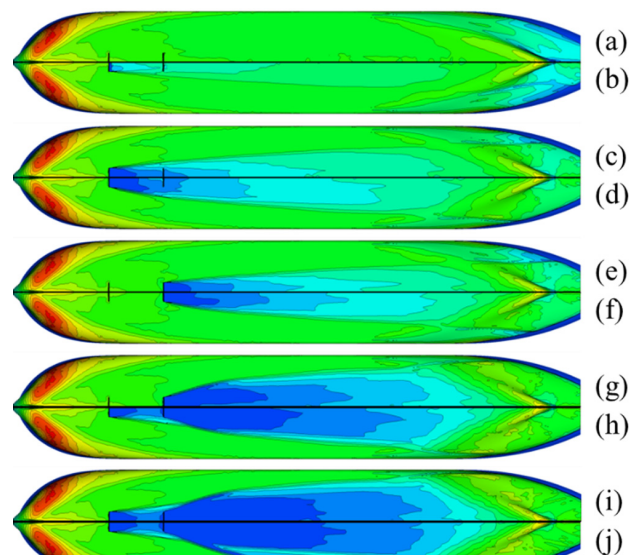


Fig. 6 Wall shear stress on the hull surface (Bare, Cases 1-9 from the top)

fraction on the hull surface.

Fig. 7 shows the distribution of the dynamic pressure on the bottom of the hull. When air is injected, the air affects the distribution of the dynamic pressure at the stern. As the quantity of air increases, a high pressure forms, and the affected area increases.

Numerical analysis of the model ship confirmed that the air layer reduces the frictional resistance through the volume fraction of air on the bottom hull surface. In addition, it changes the pressure resistance, as shown in Figs. 7 and 8. Jang et al. (2014) used a modified method based on ITTC 1957 for the estimation (Method 1). On the other hand, they did not consider the change in pressure resistance. Method 2 is proposed in this study, which considers the decrease in pressure resistance.

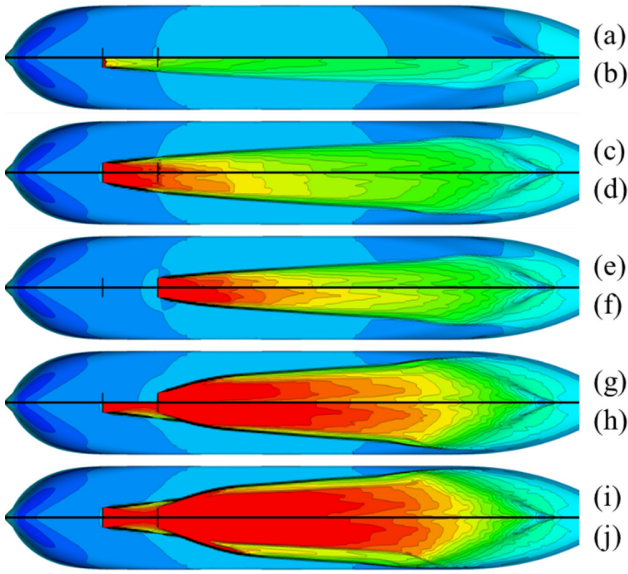


Fig. 7 Dynamic pressure on the hull surface (Bare, Cases 1-9 from the top)

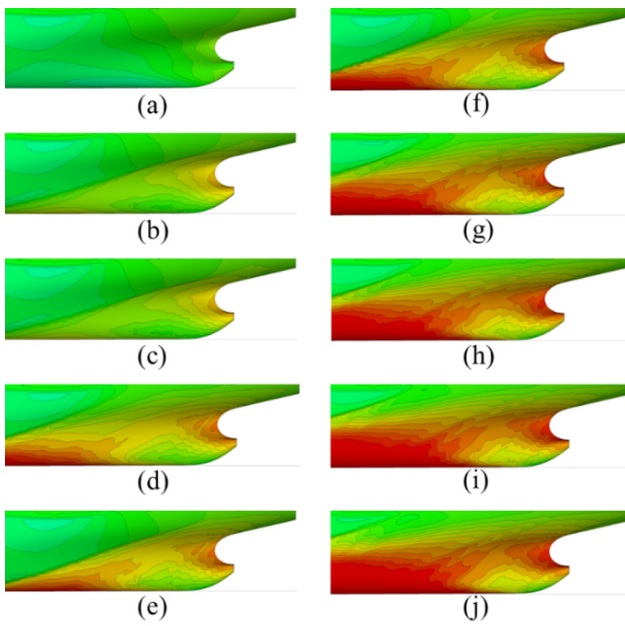


Fig. 8 Dynamic pressure on the stern (Bare, Cases 1-9 from the top and left)

Fig. 9 shows the extrapolation methods used for an air-lubricated ship. In Method 1, C_{TM} is divided into C_{FM} and C_{RM} , which are the frictional resistance and residual resistance. For C_{RM} , it is assumed that the residual resistance coefficient is the same, regardless of whether air is injected. Furthermore, $C_{RM,Air}$ and $C_{RS,Air}$ are the same. $C_{FM,Air}$ can be obtained from the relationship between $C_{TM,Air}$ and $C_{RM,Air}$. $C_{FM,Bare}$ and $C_{FS,Bare}$ are estimated using the ITTC 1957 method. In the subscript, Bare and Air refer to the case where the air is not injected and when air is injected, respectively. $C_{FS,Air}$ can be acquired from multiplying $C_{FS,Bare}$ by the ratio of C_{FM} obtained in the air and bare conditions of the model ship. As a result, $C_{TS,Air}$ can be estimated as the sum of $C_{FS,Air}$ and $C_{RS,Air}$ for a full-scale ship.

$$\begin{aligned} \text{Bare: } C_{TM,Bare} &= C_{FM,Bare} + C_{RM,Bare} \\ C_{RM,Air} &= C_{RM,Bare} \\ \text{Air: } C_{FM,Air} &= C_{TM,Air} - C_{RM,Air} \\ C_{FM,Bare}, C_{FS,Bare} &= \text{ITTC 1957} \\ C_{FS,Air} &= \frac{C_{FM,Air}}{C_{FM,Bare}} \times C_{FS,Bare} \\ C_{RS,Air} &= C_{RM,Air} \\ C_{TS,Air} &= C_{FS,Air} + C_{RS,Air} \end{aligned}$$

(a) Method 1

$$\begin{aligned} \text{Bare: } C_{TM,Bare} &= C_{VM,Bare} + C_{WM,Bare} \\ C_{VM,Bare} &= C_{TM,Bare,DB} \\ C_{WM,Air} = C_{WM,Bare} &= C_{TM,Bare} - C_{VM,Bare} \\ C_{VM,Air} &= C_{TM,Air} - C_{WM,Air} \\ C_{VS,Bare} &= (1+k)C_{FS,ITTC1957} \\ C_{VS,Air} &= \frac{C_{VM,Air}}{C_{VM,Bare}} \times C_{VS,Bare} \\ C_{WS,Air} &= C_{WM,Air} \\ C_{TS,Air} &= C_{VS,Air} + C_{WS,Air} \end{aligned}$$

(b) Method 2

Fig. 9 Extrapolation methods for an air-lubricated ship

In Method 2, C_{TM} is divided into the viscous resistance C_{VM} and wave-making resistance C_{WM} to reflect the change in the viscous pressure resistance. The residual resistance of Method 1 is defined as the wave-making resistance in Method 2. $C_{WM,Bare}$ is calculated from the relationship between $C_{TM,Bare}$ and $C_{VM,Bare}$. $C_{WM,Air}$ is assumed to be the same as $C_{WM,Bare}$. $C_{VM,Air}$ can be obtained from the relationship between $C_{TM,Air}$ and $C_{WM,Air}$ when the air is injected. $C_{VS,Bare}$ is obtained using the ITTC 1957 method. $C_{VS,Air}$ is obtained by multiplying $C_{VS,Bare}$ by the relationship with C_{VM} of the model ship when air is injected and not injected. The wave-making resistance coefficient is the same for both the full-scale ship and the model ship. This process is used to derive $C_{TS,Air}$. The largest difference between Methods 1 and 2 is the scaling of the viscous pressure resistance. In Method 2, the effects of the reduction of pressure resistance by the air lubrication are considered in the extrapolation method to predict the full-scale resistance.

To obtain the viscous resistance component, it is necessary to know the component of the wave-making resistance. Accordingly, double-body analysis was performed. The following grid conditions were used: y^+ was set to 90, and the number of grids was approximately

Table 6 Comparison of C_{VS} using full-scale analysis

Case	C_{VS}	ΔC_{VS} (based on method 2)
Method 2	0.00190	-
y^+ (300)	0.00205	8
y^+ (8000)	0.00196	3

1.8 million for the model scale.

Cases 3, 6, and 9 were investigated. A double-body analysis was also carried out for a full-scale numerical analysis. Some cases were validated to set y^+ and Method 2 was extrapolated from the result of the model analysis, as shown in Table 6. When air was not injected in y^+ (8000), the error rate was less than 3% for a full-scale ship. Yang et al. (2010) compared the wakes between the model and the full-scale ship. When the y^+ value was 8000 in numerical analysis using the RSM, the error was 1.5% compared to the full-scale ship. Therefore, y^+ was set to 8000, and the number of grid elements was approximately 5.6 million. The air flow rate was analyzed numerically by Froude scaling the quantity of injected air from the model ship.

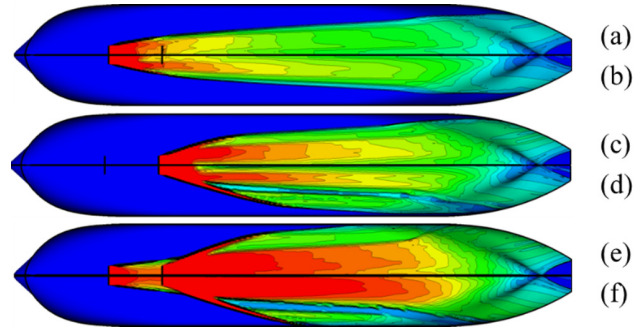
Table 7 lists the reduction rates of $\Delta Shear$, $\Delta Pressure$, and ΔC_V for the model ship and full-scale ship based on cases, in which air is not injected from the double-body analysis. There was no difference in $\Delta Shear$. The overall tendency was similar between the double-body analysis and Method 2. On the other hand, the biggest difference in $\Delta Pressure$ between the model and full-scale ship was 4.9%. Consequently, the estimation of ΔC_V by Method 2 is consistent with the numerical analysis of the model, but there was a slight difference in the full-scale ship.

The difference in $\Delta Pressure$ was attributed to the form factor, which differs between the model and the full-scale ship. The form factor was set to a constant value in Method 2. Therefore, it is believed to result in differences in ΔC_V . Fig. 10 shows the volume fraction of the hull surface when using double-body analysis. The branch was stronger at the end of the slit width for the full-scale ship than the model. The overall tendency was similar to that of the model ship.

Table 8 lists the reduction rate of ΔC_{TS} by air injection when using Methods 1 and 2. Method 1 showed a 2 - 5% difference in the numerical analysis results of the model ship; the largest gap was 5.4%

Table 7 Comparison of the full-scale ship resistance and model ship resistance, $\Delta Shear$, $\Delta Pressure$, and ΔC_V using double-body numerical analysis in Method 2

Case	Double-body analysis			Method 2
	$\Delta Shear$ (%)	$\Delta Pressure$ (%)	ΔC_V (%)	ΔC_V (%)
Model (Case 3)	8.3	11.1	19.4	19.0
Full (Case 3)	10.3	13.5	23.8	
Model (Case 6)	10.4	12.7	23.1	22.8
Full (Case 6)	10.4	14.2	24.6	
Model (Case 9)	15.9	13.0	28.9	28.4
Full (Case 9)	15.9	17.9	33.8	

**Fig. 10** Volume fraction of the hull surface using double-body analysis. (a), (c), and (e) correspond to Cases 3, 6, and 9 for the model ship, and (b), (d), and (f) are from the full-scale ship.**Table 8** Comparison of the resistance reduction rate of the full-scale ship using Methods 1 and 2

Case	ΔC_{TS} (%) (Method 1)	ΔC_{TS} (%) (Method 2)	ΔC_{TM} (%)
Bare	-	-	-
Case 1	8.9	10.4	11.2
Case 2	11.9	13.9	15.0
Case 3	13.9	16.3	17.5
Case 4	11.4	13.3	14.3
Case 5	13.4	15.7	16.8
Case 6	16.7	19.5	21.0
Case 7	18.6	21.7	23.3
Case 8	19.8	23.1	24.9
Case 9	20.7	24.2	26.1

in Case 9. Method 2, however, showed a 1 - 2% difference; the largest difference was 1.9% in Case 9. Method 2 was more accurate than Method 1 when the total resistance reduction rate was compared with that of the model ship. Overall, the variation of the pressure resistance should be considered when estimating the resistance of a ship with an air lubrication system.

5. Conclusions

A numerical study was carried out on the effect of air injection on a ship. The mesh was verified, and the reliability of the calculation was confirmed by numerical analysis. The resistance was calculated by double-body analysis, and the estimated resistances of the model and full-scale ship were compared.

Comparisons were made for a bare hull regarding the reduction rate of the total resistance (ΔR_{TM}), the ratio of the decrease in shear resistance to the decrease in total resistance ($\Delta Shear$), and the ratio of the decrease in pressure resistance to the decrease in total resistance ($\Delta Pressure$). A larger decrease in the total resistance was observed when the air injection flow rate increased. The rate of the decrease in pressure resistance was as large as the rate of the decrease in shear

resistance. Bow trim was generated due to the buoyancy by the air, and the heave increased.

Based on the results, a resistance estimation method was proposed to consider reducing the pressure resistance, and the results were compared with those of the modified ITTC 1957 method. The proposed method was more accurate than the modified method. The result of the model scaling showed less than 1% error, whereas the result of the full-scale ship shows a slight difference.

Methods 1 and 2 were compared to find the differences between ΔC_{TS} and ΔC_{TM} . Method 2 was more accurate than Method 1 in estimating the resistance of the full-scale ship from the model ship, and the error rate was less than 2%. The ultimate goal of developing an air lubrication system is to reduce the fuel consumption of a ship by 5% or more and improve the performance at sea. To achieve this goal, it is necessary to estimate the resistance of the model and full-scale ship accurately when air is injected. Future research will be needed to improve the reliability of the results on a full-scale ship.

Acknowledgments

This research was funded by a research grant for the development of an air lubrication system to reduce ship fuel consumption by approximately 5% and verify the performance at sea [10073164], which is supported by the Ministry of Trade, Industry, and Energy.

References

Bushnell, D.M., & Hefner, J.N. (1990). Viscous Drag Reduction in Boundary Layers. Proceedings of The American Institute of Aeronautics and Astronautics, Inc., Washington DC, USA.
 Ceccio, S.L., Perlin, M., & Elbing, B.R. (2010). A Cost-Benefit Analysis for Air Layer Drag Reduction. Proceedings of International Conference on Ship Drag Reduction (SMOOTH-

SHIPS), Istanbul, Turkey.
 Ceccio, S.L., & Makiharju, S.A. (2012). Air Lubrication Drag reduction on Great Lakes Ships. Great Lakes Maritime Research Institute, A University of Wisconsin – Superior and University of Minnesota Duluth Consortium.
 Jang, J.H., Choi, S.H., Ahn, S.-M., Kim, B.K., & Seo, J.S. (2014). Experimental Investigation of Frictional Resistance Reduction with Air Layer on the Hull Bottom of a Ship. International Journal of Naval Architecture and Ocean Engineering, 6(2), 363-379. <https://doi.org/10.2478/ijnaoe-2013-0185>
 Kim, H.-J., Kim, D.-Y., Shin, H.-W., Kim, S.-H., & Paik, K.-J. (2017). Numerical Study on the Bifurcation Mechanism of Air Layer on a Flat Plate. Proceedings of International Workshop on Ship and Marine Hydrodynamics, Keelung, Taiwan.
 Makiharju, S.A., & Ceccio, S.L. (2018). On Multi-point Gas Injection to form an Air Layer for Frictional Drag Reduction. Ocean Engineering, 147, 206-214. <https://doi.org/10.1016/j.oceaneng.2017.10.041>
 Makiharju, S.A., Lee, I.-H., Filip, G.-P., Maki, K.-J., & Ceccio, S.L. (2017). The Topology of Gas Jets Injected Beneath a Surface and Subject to Liquid Cross-flow. Journal of Fluid Mechanics, 818, 141-183. <https://doi.org/10.1017/jfm.2017.98>
 Yang, H.U., Kim, B.-N., Yoo, J.H., & Kim, W.-J. (2010). Wake Comparison between Model and Full Scale Ships using CFD. Journal of the Society of Naval Architects of Korea, 47(2), 150-162. <https://doi.org/10.3744/SNAK.2010.47.2.150>

Author ORCIDs

Author name	ORCID
Kim, Dong-Young	0000-0002-4353-8682
Ha, Ji-Yeon	0000-0002-3644-4450
Paik, Kwang-Jun	0000-0003-4657-5806

Development of Ice Load Generation Module to Evaluate Station-Keeping Performance for Arctic Floating Structures in Time Domain

Hyun Hwa Kang¹, Dae-Soo Lee¹, Ji-Su Lim¹, Seung Jae Lee²,
 Jinho Jang³, Kwang Hyo Jung⁴ and Jaeyong Lee⁵

¹Graduate Student, Division of Naval Architecture and Ocean Systems Engineering, Korea Maritime and Ocean University, Busan, Korea

²Professor, Division of Naval Architecture and Ocean Systems Engineering, Korea Maritime and Ocean University, Busan, Korea

³Head of Ice-covered Waters Engineering Research Center, Division of Advanced Ship Research, KRISO, Daejeon, Korea

⁴Associate Professor, Department of Naval Architecture and Ocean Engineering, Pusan National University, Busan, Korea

⁵Associate Professor, Department of Naval Architecture and Ocean Engineering, Dong-eui University, Busan, Korea

KEY WORDS: Dynamic positioning in ice, Time domain simulation, Station keeping performance evaluation, Arctic floating structures, Statistical ice load generation

ABSTRACT: To assess the station-keeping performance of floating structures in the Arctic region, the ice load should be considered along with other environmental loads induced by waves, wind, and currents. However, present methods for performance evaluation in the time domain are not effective in terms of time and cost. An ice load generation module is proposed based on the experimental data measured at the KRISO ice model basin. The developed module was applied to a time domain simulation. Using the results of a captive model test conducted in multiple directions, the statistical characteristics of ice loads were analyzed and processed so that an ice load corresponding to an arbitrary angle of the structure could be generated. The developed module is connected to commercial dynamic analysis software (OrcaFlex) as an external force input. Station-keeping simulation in the time domain was conducted for the same floating structure used in the model test. The mooring system was modeled and included to reflect the designed operation scenario. Simulation results show the effectiveness of the proposed ice generation module and its application to station-keeping performance evaluation. Considering the generated ice load, the designed structure can maintain a heading angle relative to ice up to 4°. Station-keeping performance is enhanced as the heading angle conforms to the drift direction. It is expected that the developed module will be used as a platform to verify station-keeping algorithms for Arctic floating structures with a dynamic positioning system.

1. Introduction

Despite the continued trend of low oil prices in recent times, the development of resources in the Arctic region is expected to continue, with Norway, the United States of America, and Russia at the forefront (Morgunova, 2020). In the polar regions, areas that can be developed have expanded because of global warming. Environmental conditions in the Arctic must be considered for the structures used to develop resources in these regions. Fixed structures are installed in shallow sea waters, while floating structures are considered first for deep-sea regions.

In general, the position of the floating structure is maintained using a mooring system. However, a dynamic positioning system (DPS) is sometimes used as an auxiliary system to cope with ice loads, which

are one of the characteristics of the polar regions (Lee et al., 2019).

The DPS uses various kinds of thrusters to keep the position of a vessel or an offshore structure within the acceptable range. To do so, the DPS calculates the force required to return the floater from its altered position (caused by the external environmental forces) to its original position and generates the required force using the propulsion system. In the Arctic region, DP-assisted mooring systems are used for the extreme environment. A mooring system handles station-keeping functions for normal ocean environmental loads. However, when abnormal conditions arise, the DPS alleviates the excessive tensile force acting on the mooring system. It also maintains the position of the riser on the bottom of the structure so that the riser angle is within the acceptable range.

Simulations in the time domain are needed to evaluate the

Received 27 August 2020, revised 7 October 2020, accepted 12 October 2020

Corresponding author Jaeyong Lee: +82-51-890-2596, jlee@deu.ac.kr

It is noted that this paper is revised edition based on proceedings of KAOST 2020 in Busan.

© 2020, The Korean Society of Ocean Engineers

This is an open access article distributed under the terms of the creative commons attribution non-commercial license (<http://creativecommons.org/licenses/by-nc/4.0>) which permits unrestricted non-commercial use, distribution, and reproduction in any medium, provided the original work is properly cited.

station-keeping performances of floating structures and observe how the tensile force acting on the mooring line changes over time. Modeling the environmental load acting on the structure is important. However, it is an extremely difficult task to incorporate the ice loads in the polar region into the time-domain simulations.

When it comes to evaluating the performance of a structure with DPS in seas where ice loads exist, the best method to collect data is to use the test results of a real sea experiment. In 2004, as part of the 302 Arctic coring expedition of the International Ocean Drilling Program (IODP), one drillship performed its drilling operations while being assisted by two icebreakers and collected data on how difficult it was to maintain its position (Moran et al., 2006). However, such real sea operation is extremely expensive, and the ice condition cannot be controlled; hence, it is impossible to obtain data for various situations.

Tests performed in ice tanks can also generate good data for evaluating the performance (Jenssen et al., 2009). Representative examples of such tests are the drillship-related experiments carried out as part of the Dynamic Positioning in Ice Condition (DYPIC) project, an international joint research project (Jenssen et al., 2012; Kerkeni et al., 2014), and the model tests performed by the National Research Council (NRC) of Canada (Wang et al., 2016; Islam et al., 2018). However, such ice tank tests are also costly, and there are limitations in simulating the actual conditions in these tests. For most ice tanks where the tests are performed, there is no equipment to reflect other environmental loads, such as wind, currents, and waves, in the test.

Studies are ongoing to perform simulations on the interactions between the ice and structures, considering the limitations mentioned above. Related to finding an empirical formula, Kim et al. (2018a) proposed a method for extending the application of the existing model for level ice to pack ice. Furthermore, the relationship between the size of the broken ice floes and the resistance value was proposed (Jeong et al., 2018). Methods using numerical analysis techniques to analyze the behavior of the ice where ice floes exist mostly utilize the discrete-element method. This method models and interprets each particle as a discrete object for the finite-element method that uses differential equations of dynamic variables for a continuum. The discrete-element method was first proposed by Cundall and Strack (1979) and Walton (1982), and it was later applied to the ice-related field by Løset (1994) and others. Afterward, ArcISO (Arctic Integrated Solution), a spin-off company based on the Sustainable Arctic Marine and Coastal Technology (SAMCoT) of the Norwegian University of Science and Technology (NTNU), has made simulations of ice-structure interactions, station keeping of floating structures, and navigation in icy sea waters possible through the SAMS (Simulator for Arctic Marine Structures) product (Lubbad et al., 2018a; Lubbad et al., 2018b; Raza et al., 2019).

Existing ice-structure interaction analysis methods consume too much time. To remedy this issue, Daley et al. (2012, 2014) developed graphics processing unit (GPU)-event mechanics (GEM). GEM uses a parallel structure GPU with excellent floating-point calculation performance to perform numerical computations. In general, the

direction of ice drift and the current direction are set to match for these analysis software tools. Moreover, there is a limitation of not factoring in other ocean environmental loads, such as waves. To reflect the wave conditions, methods utilizing computational fluid dynamics have been proposed; however, considering such factors as analysis duration, there are limitations in incorporating various station-keeping equipment or applying changes to the algorithm. Therefore, the analysis methods mentioned above cannot set sufficient conditions to evaluate in the time domain the station-keeping performance of floating structures where ice loads exist.

To factor in combined environmental loads, including ice loads, the use of an existing commercial software for floating body motion analysis to assess the station-keeping performance in icy sea waters could provide a solution. For this purpose, a separate module must be developed to generate ice loads and reflect the ice loads in the motion analysis. Utilizing GEM and the mean value of the ice loads obtained from a tank experiment result, Kim et al. (2018b) proposed an ice load generation method using the spectral values of the variable components. However, the ice loads were measured only at a certain angle. Hence, this method cannot reflect changes to the ice loads based on the variation of the heading angle.

In this study, the aim was to identify the basic characteristics of the motion of a floater in ice condition through statistical processing based on the experimental data of ice loads measured at various angles. A separate ice load generation module was designed and implemented to reflect partially the statistical characteristics of experimental data using OrcaFlex, a general commercial floating body motion analysis software package. This setup made it possible to assess the station-keeping performance of Arctic floating structures for combined environmental loads and was applied to the evaluation of the heading-angle-keeping performance.

2. Measurement of Ice Load in an Ice Tank Test and Post-processing of the Data

2.1 Experimental Setup and Conditions

The floating structure used in this study is an Arctic floating production storage and offloading (FPSO) unit, and its length, breadth, and draft are 244, 57, and 18.6 m, respectively. Fig. 1 shows the overall shape of the hull and the environment of the test in progress using a model with a scale ratio of 1:40. The model name assigned for the model test by Korea Research Institute of Ships and Ocean Engineering (KRISO) is KS1801. Table 1 shows a comparison between the detailed specifications of the model vessel built according to the scale ratio and the actual sizes.

For the resistance experiment for measuring the ice load, sensor values for calibration are measured at the zero section located at one end of the ice tank, as shown in Fig. 2. Afterward, the model vessel enters the ice region at a constant speed. Once the entire model vessel has entered the ice region, the vessel is in the measurement section, where data are measured stably. The data measured in this section are

used as the resistance value due to ice.

To obtain data, the load cells were installed at the center of the model vessel. Once the vessel was secured to restrict its six-degree-of-freedom movements, the vessel was towed to pass through the ice region. Values measured by the sensors were processed by the hull-mounted coordinate system. The ice tank dimension at KRISO was 32m × 35 m, and the tank was divided into sections so tests could be run multiple times. The shape of the ice floe was made irregular, and the ice concentration was set at 80%. To convert ice in a real sea, which is 1.4 m thick and has a characteristic length of 12 m, to the model scale, the actual size of the ice was divided by the scale of 40 to calculate the size of the ice used in the experiment. This result is shown in Table 2. The drift speed was 1.0 kt (= 0.5144 m/s), and it was divided by $\sqrt{40}$ to derive the towing speed (0.081 m/s) in the experiment. The heading angle in the direction of the movement ranged from -40° to 40° in intervals of 10° . Hence, the experiment was conducted for these nine intervals, and Fig. 3 shows the example of the measured values in time series, where the heading angle was set to 0° .



Fig. 1 Hull shape of the Arctic FPSO used in the experiment and simulation and overall environment of the model test in progress

Table 1 Principal particulars of the designed floater

Description	Full scale	Model scale
Length between perpendiculars (m)	244	6.1
Breath (m)	50	1.25
Draft (m)	18.6	0.465
Displacement (m ³)	163,215	2.555
Vertical center of gravity (m)	19.5	0.4875

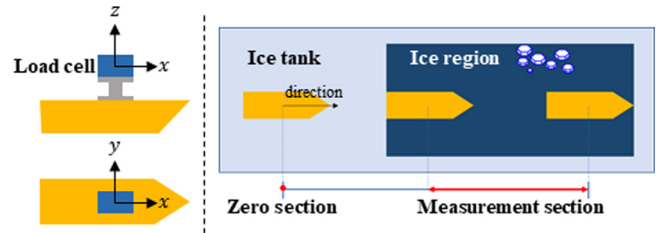


Fig. 2 Moving test vessel from the starting position (zero section) to the measurement area where ice floes are ready, and the coordinate system used in the measurement and data process

Table 2 Similitude of the ice condition

Characteristics	Full scale	Model scale
Ice thickness (m)	1.4	0.035
Characteristic length for ice floes (m)	12	0.3
Ice drift speed (m/s)	0.514	0.081
Ice concentration	8/10	
Shape of ice floes	Irregular shapes	

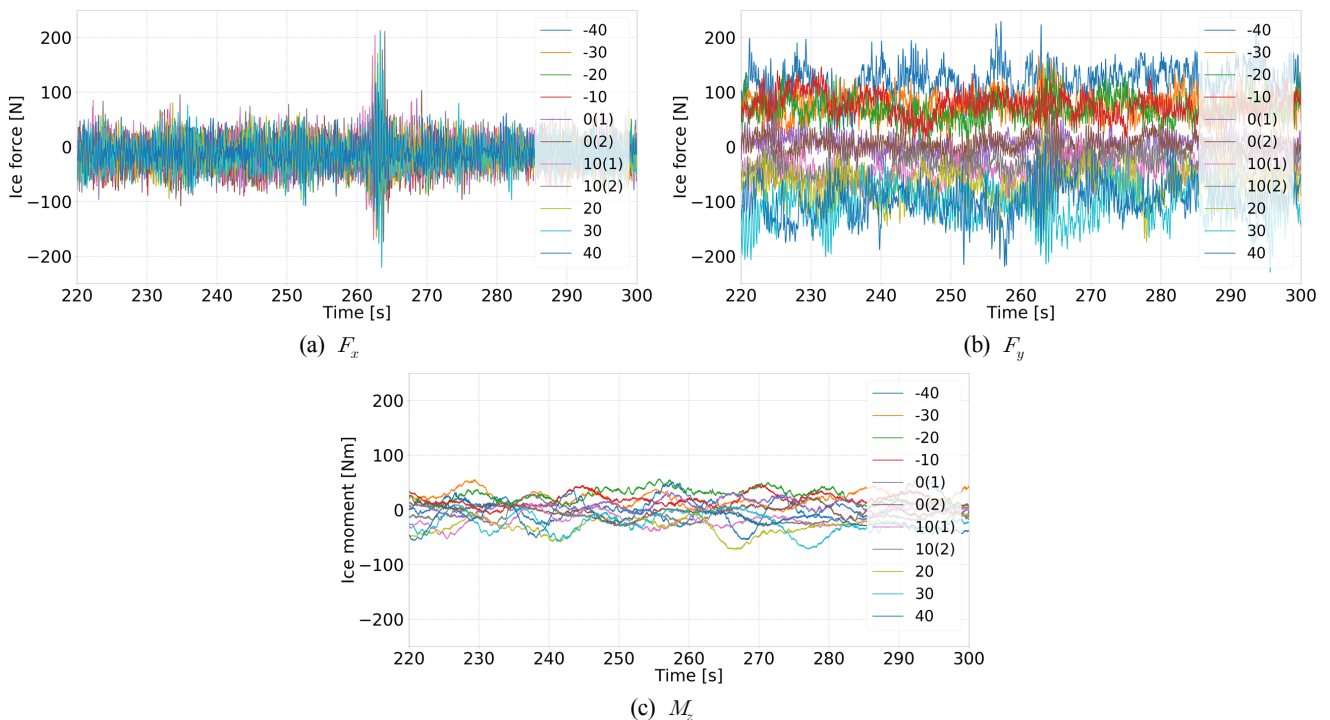


Fig. 3 Time histories of F_x , F_y , and M_z for the incident angle of 0° from the model test

(2014), the results showed that the assumed distribution was not satisfied. This result shows the difficulty of applying statistical methods to ice load generation and the differences in methods measuring the ice resistance. It was determined that F_x tends to deviate from the normal distribution at either extreme value of the QQ plot graph because of outliers measured at certain intervals (260–270 s). Here, F_y shows a tendency to form a normal distribution based on the incident angle, and M_z seems to be affected by the characteristics of the sensor, which performs calculations based on the measured values of F_x and F_y . However, there is still a need to develop an ice load generation module. This module is required for running simulations in the time domain. The statistical processing method can be developed at a later time. Furthermore, meaningful results can be achieved in determining the design parameters if the simulation is run repeatedly. Ice load generation logic that assumes a normal distribution using the mean and standard deviation of the measured values was applied in this study.

3. Ice Load Generation in Time Domain Simulation

3.1 Process to Generate Random Value to an Arbitrary Heading Angle

The mean and standard deviation values of the measured data for each angle are shown in Table 4. As shown in Fig. 6, curve fitting was performed after plotting the mean values on the graph. The formulas for mean value interpolation of F_x , F_y , and M_z for arbitrary head angles (ψ) are shown in Eq. (1).

$$\begin{aligned} F_x &= -0.0657\psi - 11.139 \\ F_y &= 0.0013\psi^3 - 0.0013\psi^2 - 4.5748\psi + 5.8412 \\ M_z &= 0.0009\psi^3 - 0.0044\psi^2 - 1.6498\psi + 1.4689 \end{aligned} \quad (1)$$

Here, F_x is expressed in a linear function, F_y and M_z and are expressed in a cubic function. When used in simulations, the Froude number is applied according to the full-scale vessel, the average value of F_x and F_y is multiplied by λ^3 , and the standard deviation function

Table 4 Mean and standard deviation values of the measured data

Angle (deg)	Mean			Standard deviation		
	F_x (N)	F_y (N)	M_z (Nm)	F_x (N)	F_y (N)	M_z (Nm)
-40	-8.802	120.469	1.265	21.167	28.615	20.557
-30	-14.236	75.561	20.466	22.028	22.557	12.486
-20	-13.537	69.616	25.512	24.545	21.779	12.426
-10	-15.336	76.145	17.586	25.819	22.304	12.03
0(1)	-17.188	2.005	7.148	26.376	17.723	10.143
0(2)	-15.112	3.102	-0.046	26.701	16.259	9.934
10(1)	-7.276	-44.398	-16.219	27.253	19.165	14.036
10(2)	-7.304	-36.329	-12.59	27.03	22.357	11.484
20	-13.455	-69.629	-30.641	26.828	28.193	14.222
30	-15.655	-106.159	-23.915	29.385	32.913	18.683
40	-11.538	-95.908	-11.428	24.576	33.22	22.276

of M_z is multiplied by.

The same method was used for the standard deviation, and curve fitting was performed to obtain the standard deviation for an arbitrary angle. Unlike the mean value, two separate trend lines were used to perform interpolation, one from -40° to 0° and another from 0° to 40° , to ensure that the trend line is as close to all the measured data points as possible. In other words, F_x , F_y , and M_z each has interpolation functions for two standard deviations, with 0° being the reference point. The results are shown in Eq. (2). The values of the interpolation function for the standard deviation were also derived based on the measured values from the model test. In the full-scale vessel simulation, the horizontal force (F_x , F_y) and moment (M_z) are multiplied by the third power and the fourth power of the scale ratio, respectively.

$$\begin{aligned} F_x &= \begin{cases} -0.0002\psi^3 - 0.0118\psi^2 - 0.0491\psi + 26.538 & \text{if } \psi \geq 0 \\ -0.0005\psi^3 - 0.0253\psi^2 - 0.2215\psi + 26.538 & \text{if } \psi < 0 \end{cases} \\ F_y &= \begin{cases} -0.0009\psi^3 - 0.0538\psi^2 - 0.9575\psi + 17 & \text{if } \psi \geq 0 \\ -0.0007\psi^3 - 0.0340\psi^2 - 0.1314\psi - 17 & \text{if } \psi < 0 \end{cases} \\ M_z &= \begin{cases} -0.0008\psi^3 - 0.0389\psi^2 - 0.5504\psi + 10.038 & \text{if } \psi \geq 0 \\ -0.0031\psi^2 - 0.1821\psi + 26.538 & \text{if } \psi < 0 \end{cases} \end{aligned} \quad (2)$$

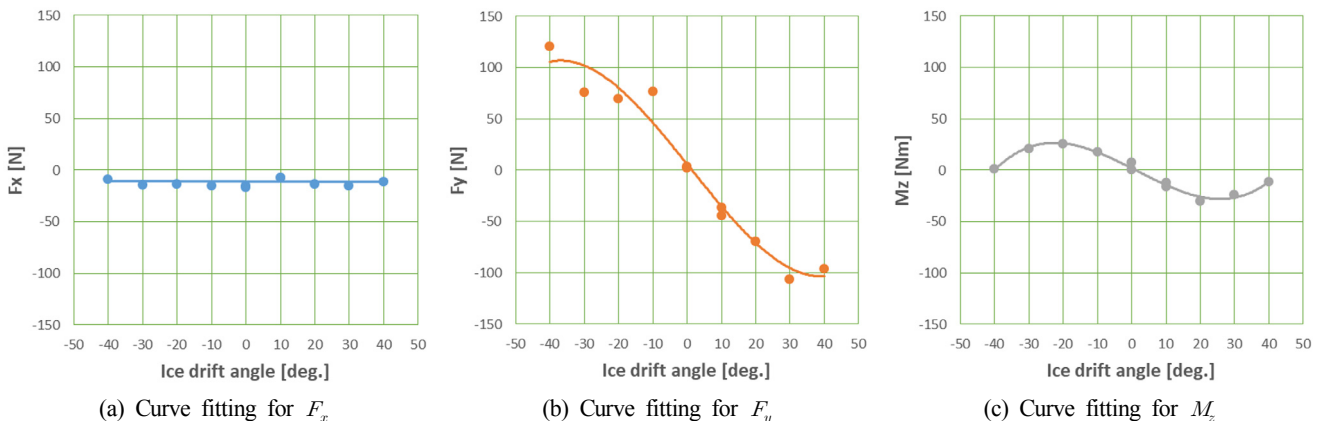


Fig. 6 Curve fittings of mean values in Table 4 for each direction

The measured values in the experiment are the resistance values obtained when the model vessel was towed in the ice tank; hence, the ice load and the current force corresponding to the speed of the vessel are included in these values. Therefore, the current force needs to be subtracted from the measured values to extract the pure ice load. This process is necessary to isolate the ice load from the direction upon which the current force is acting. Generally, ice is set to drift in the direction of the current, but the movement of the ice can be affected by the wind. Therefore, it is better to set the directions of the ice drift and current differently. However, realistically, it is difficult to conduct additional towing experiments to obtain the value of the current force. Hence, the current force was calculated after securing the structure at a fixed position in OrcaFlex and assuming the current flows in a constant direction.

The vessel was secured to restrict its six-degree-of-freedom movements, and the relative angle between the current and the structure was set from -40° to 40° in intervals of 5° . Afterward, the sea current environment was configured, and data were obtained. The data values are recorded in Table 5. Based on these data, curve fitting was performed to derive the interpolation function for calculating the current force for each angle, similar to the mean and standard deviation of the ice load.

Table 5 Current load corresponding to heading angles

Heading angle	$F_{C,x}$	$F_{C,y}$	$M_{C,z}$
-40	-31.388	-185.868	-3604.123
-30	-34.465	-141.555	-2853.264
-20	-35.696	-97.858	-2102.405
-10	-35.696	-51.083	-1201.374
0	-33.85	6.155	0
10	-35.696	51.083	1201.374
20	-35.696	97.858	2102.405
30	-34.465	141.555	2853.264
40	-31.388	185.868	3604.123

3.2 Module for Ice Load Generation

In the Arctic region, the heading angle of the floating structure keeps changing according to changes in the direction of the main environmental external force. If the heading angle is altered because of the environmental load while ice is drifting toward the structure, the ice load value acting upon it should also change. Furthermore, depending on the size and shape of the ice on the sea where the structure is operating, ice loads of varying sizes and directions are continuously applied, even if the heading angle remains constant. Therefore, to reflect how changes in the heading angle of the structure affect the ice load in the simulation, one must be able to generate the ice load applied to the vessel at the specified angle.

Fig. 7 shows a diagram of the process for how the ice load module generates ice load when performing dynamic analysis in the time domain. OrcaFlex, which is used for the dynamic analysis, is

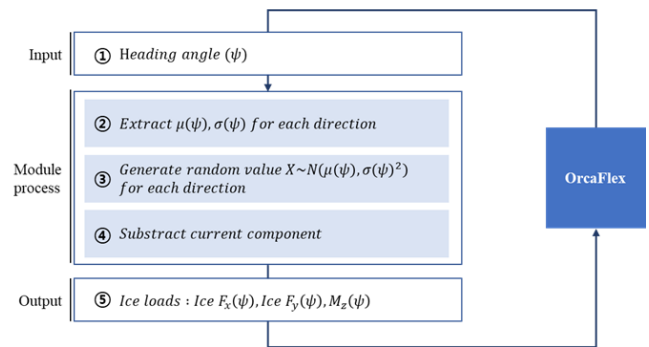


Fig. 7 Ice load generation process inside of the module

configured to perform the analysis in intervals of 0.1 s. Because the ice load generation process is repeated throughout the entire simulation duration, ice loads are generated every 0.1 s and are applied in the analysis.

① The analysis software sends the current heading angle information of the floating structure to the ice load generation module as an input.

② The mean ($\mu(\psi)$) and standard deviation ($\sigma(\psi)$) of the F_x , F_y , and M_z component measurement data are calculated for the input heading angle. The interpolation formula described in Eqs. (1) and (2) of Section 3.1 are used for this calculation.

③ The probability density function for a typical normal distribution is defined as shown in Eq. (3).

$$f(x) = \frac{1}{\sqrt{2\pi}\sigma} e^{-\frac{1}{2}\left(\frac{x-\mu}{\sigma}\right)^2} \quad (3)$$

Here, a normal distribution is assumed for the mean ($\mu(\psi)$) and standard deviation ($\sigma(\psi)$) values for the corresponding heading angle, and a random number ($X \sim \mathcal{N}(\mu(\psi), \sigma(\psi)^2)$) is generated from the probability density function as an output.

④ The current force for the input heading angle is subtracted, and a final ice load value is generated as an output.

⑤ The process is completed by applying the ice load generated by the ice load generation module to the center of gravity of the structure in the dynamic analysis software.

4. Simulation Results

4.1 Setup for Simulation

The analysis process performed by the analysis software (OrcaFlex) and two external modules is shown in Fig. 8. To perform the analysis of the floating structure, which factors in the DP in icy sea waters, the analysis software sends the information each module needs, such as the current position and speed of the floating object and the status of the mooring system. When the heading angle information is sent to the ice load module, the ice load generation process earlier explained is performed. Afterward, the ice load applied to the floating object for the corresponding heading angle is generated as output and sent to the

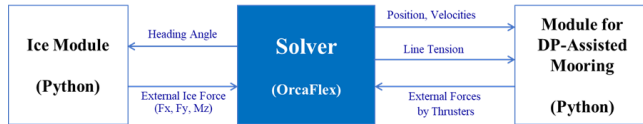


Fig. 8. Simulator configuration with external modules for ice load generation and DP force generation

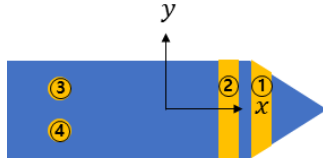


Fig. 9 Arrangement of DP thrusters

analysis software. After receiving information, such as the position and speed of the vessel and the tension on the mooring line, the DP module computes and returns the required thrust for each thruster to maintain the desired heading angle and position. The two modules were developed using Python. The ice load and thrust values returned from the modules are integrated with the environmental load, vessel motion, and mooring line information within OrcaFlex to assess the station-keeping performance.

Fig. 9 shows the arrangement of the DPS installed on the floating object subject to analysis. Two tunnel thrusters are located at the bow of the vessel, and two Azipod thrusters are located at the stern of the vessel to assist the mooring system. Considering the characteristics of the DP-assisted mooring, the arrangement was designed to focus on maintaining direction rather than station-keeping performance. Table 6 shows the thrust capacity and position of each thruster. The target position of the DPS was the initial coordinates of the vessel, and the target heading angle was set to have a constant value along the direction in which the ice load is acting.

The mooring system used for station keeping was designed using OrcaFlex, and its arrangement is shown in Fig. 10. It is an internal turret mooring system and consists of four bundles. Each bundle consists of four mooring ropes in the form of chain-wire-chain. The water depth of the sea area where the mooring system is expected to be installed is 200 m. The footprint radius was set at 5.0, which is five times the depth of the water. The minimum breaking load (MBL) of the chain was designed at 26,952 kN.

The Barents Sea in the Arctic region was selected as the area where the station-keeping simulation would be performed. Based on the maritime data measured in the selected sea area, conditions were

Table 6 Specifications and coordinates of the thrusters

Turret No.	Type of thruster	Thrust (kN)	x	y	z
1	Tunnel	330	91	0	0
2	Tunnel	330	86	0	0
3	Azipod	1600	-113	6.5	0
4	Azipod	1600	-113	-6.5	0

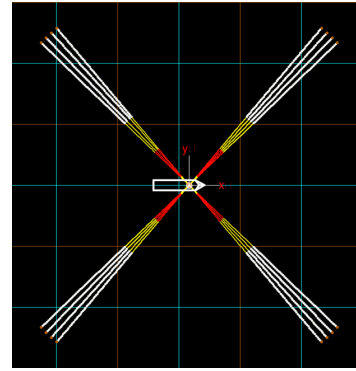


Fig. 10. Configuration of the mooring system for the floater

Table 7 Environmental conditions for the stationkeeping simulation

Case	Direction (deg)				Magnitude			
	Ice	Wave	Wind	Current	Wave		Wind	Current
					H_s (m)	T_p (s)		
1	165	165	165	165				
2	180	180	150	135	10.3	13.71	31.86	0.78
3	145	180	150	135				

determined by applying a return period of one year for the waves, 10 years for the current, and 100 years for the wind. This setting was chosen because large waves are not formed in areas covered with ice, while the wind still causes a huge impact. Applying the same ice load for the station-keeping analysis under an ice-free condition created a harsh condition. It was verified that station keeping was impossible under such a condition. Table 7 shows the magnitude of each marine environment and the direction in which it is acting. The direction in which environmental conditions of wave, wind, and current are acting was configured based on the DNVGL-OS-E301 standards. Case 1 is a collinear condition where the environmental loads act in the direction that is 15° relative to the direction towards the bow of the vessel. Cases 2 and 3 are noncollinear conditions. Here, the waves are acting in the direction toward the bow, while the wind and current are acting in the directions that are 30° and 45° relative to the direction of the waves, respectively. Meanwhile, the direction in which the ice load acts generally follows the direction of the current. However, because it is affected by the wind, there are no definitive rules for the direction of the ice load. Hence, the direction of the ice load was set to match the direction of other environmental loads for the collinear condition. In Case 2, it was configured to align with the incident angle of the waves. For Case 3, the direction of the ice load was set to be halfway between the current and the wind directions to consider the interactions between the current and the wind.

4.2 Validation Test for the Ice Load Generated by the Developed Module

The station-keeping simulation was performed using the ice load module, considering the ice load based on the changes in the heading angle. The heading angle was maintained within 10° of the target

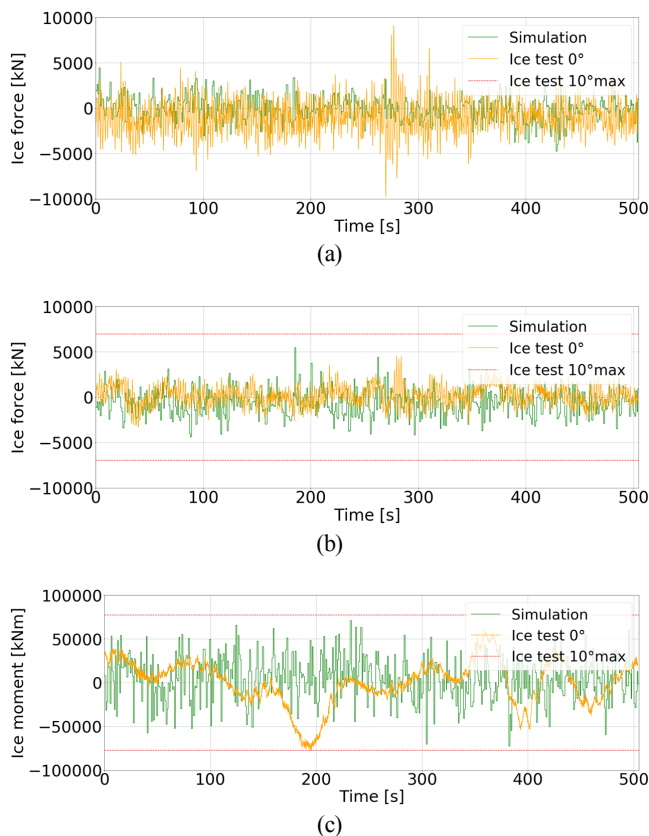


Fig. 11 Comparison between ice loads from the model test and the simulation

heading angle. Hence, the ice load data generated in time series were examined to determine whether they lie within the maximum values of the measured data in the towing experiments with incident angles of 0° and 10°. The comparison results are shown in Fig. 11. The entire set of simulation data spans over 12,000 s. However, only the simulation data from the first 500 s were represented in the graph to compare the data values directly.

The ice load data generated by the module are represented by a green line, while the measured values from the experiments are represented by a yellow line. The red lines above and below the ice load data represent the maximum measured values when the incident angle is 10°. (a) The F_x graph has the highest qualitative similarity between the values generated by the module and the experimental measurement values. (b) The F_y graph shows slight differences, but the generated values and the measured values lie within the maximum measurement values from the 10° towing experiment. (c) The M_z comparison graph has the largest difference from a normal distribution, and the generated values and the measured values are slightly different. However, the random values are still generated normally within the maximum values.

The ice load, along with other environmental loads, acts on the structure. Thus, the magnitudes of the environmental loads recorded in the simulation were compared to check the proportion of the ice load to the total load, and the comparison graphs are shown in Fig. 12. Graphs (a), (b), and (c) are plots of the entire environmental load by

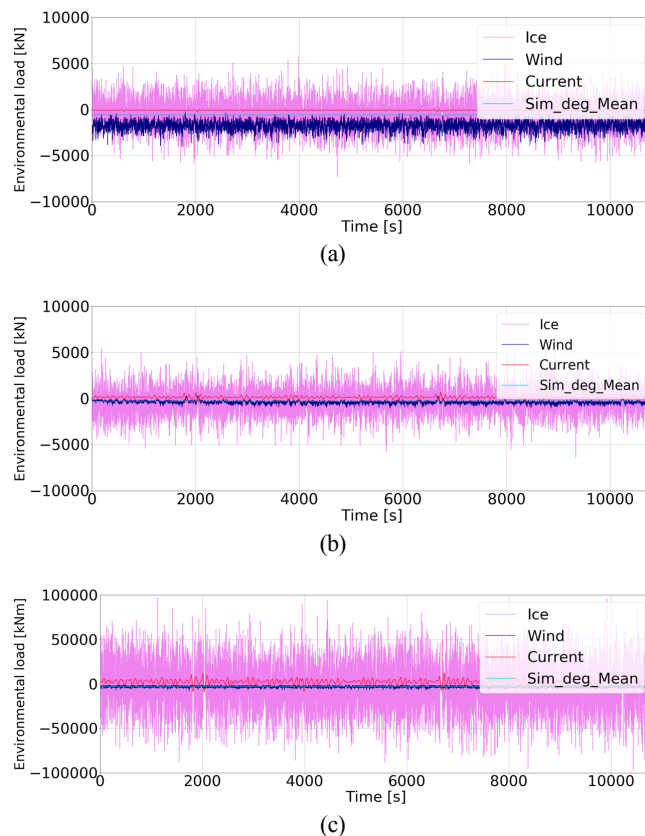


Fig. 12 Comparison of magnitude of ice load with other environmental loads

each factor for the x-axis, y-axis directional loads, and z-axis moment of the structure. The variation was approximately 10° from the target heading angle at each time point on the graph. Therefore, graph (a), which compares the loads acting on the x-axis, confirmed that the ice load is larger than other environmental loads. Furthermore, graphs (b) and (c) show that the magnitude of the wind has the greatest value. However, the variation in the heading angle is not significant; hence, the y-axis directional load and z-axis directional moment caused by waves are greater than those induced by the ice load, wind, and current.

4.3 Derivation of Limit Status of DP Heading Control

To verify that the generated ice load acts on the floating object properly and derive the limitations of the DP performance based on the direction in which the ice load acts, a position control test and heading angle control test were performed on the DPS without mooring lines

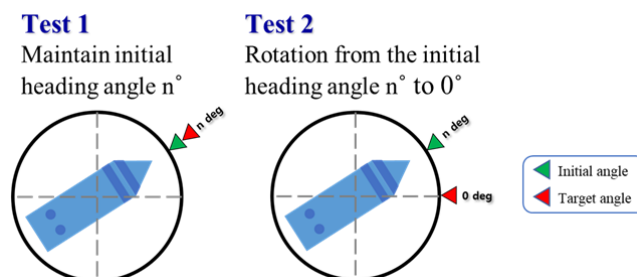
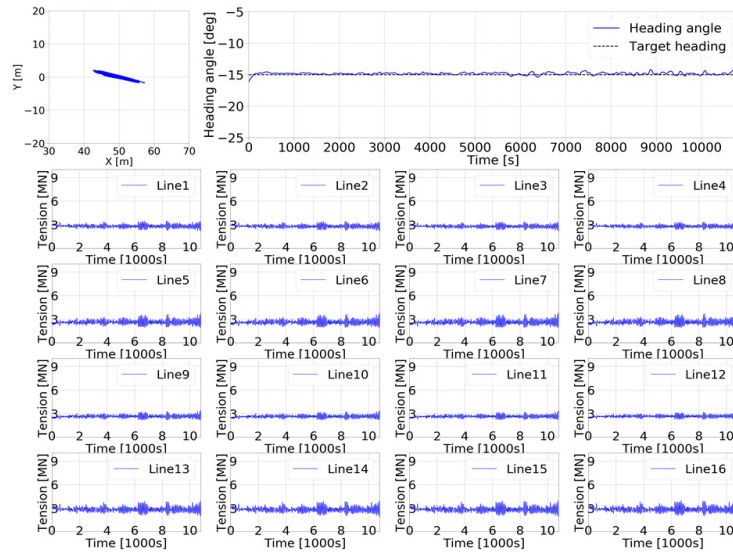
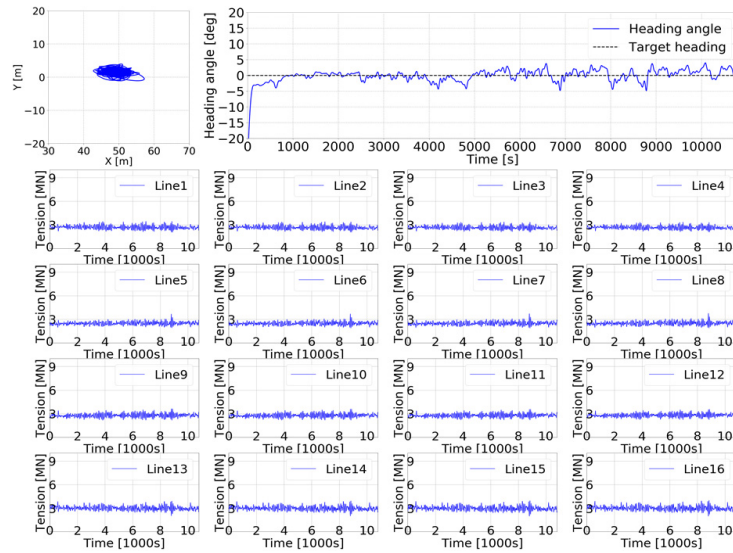


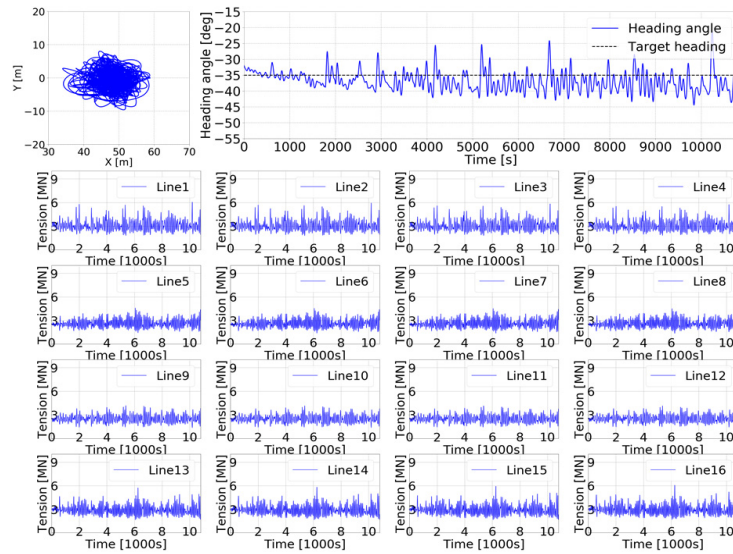
Fig. 13 Setting for the performance test of the DP heading control



(a) Case 1



(b) Case 2



(c) Case 3

Fig. 14 Simulation results of designed DP-assisted mooring system for the cases in Table 7

under the environmental conditions, considering only the ice load. Test 1, shown in Fig. 13, involved continuously maintaining the heading angle, which was initially set to an arbitrary value. In Test 2, the maximum angle that satisfies the station-keeping performance was verified when the DPS was rotated from the initial heading angle, which was set arbitrarily to the target heading angle selected based on the direction of the ice load.

In Test 1, the station-keeping and direction control performances were satisfactory from 0° to 4°. However, the DPS could not be controlled at angles greater than or equal to 5° because of the excessive environmental loads. Due to the thrust capacity of the thrusters at the stern of the vessel, based on their location, creates limitations in maintaining the position and controlling the direction simultaneously. In Test 2, station keeping and direction control were made possible by rotating in the direction in which the ice load is acting, up to 17°, to minimize the ice load. However, the control performance was lost at or above 18° because the environmental loads could not be withstood when rotating toward the target heading angle. Through this test, it was verified that the generated ice load is properly acting on the structure.

4.4 Evaluation of Stationkeeping Performance

An evaluation must be performed to determine whether the station-keeping performance of the structure is suitable for the environment of the sea area when the ice load is acting on the structure in icy sea waters. The position and heading angle information and the mooring line tension information based on the analysis results of the DP-assisted mooring system, considering the environmental loads, are shown in Fig. 14. The environmental conditions for Cases 1–3 have been explained earlier, and Figs. 14(a)–(c), respectively, are the graphs of the results for these cases. The magnitude of the environmental loads is the smallest for the collinear condition described in Case 1. When Cases 2 and 3 are compared, both having a noncollinear

condition, the overall environmental load of Case 2 is smaller than that of Case 3. In Case 2, the ice load acts in the direction toward the bow of the vessel, while the direction of the wind and the current direction have a contained angle in Case 3. All analysis results show that the position of the structure was kept within the target radius of 25 m. Moreover, it was verified that the radius tends to fluctuate in proportion to the magnitude of the environmental loads based on the target heading angle. The data for the mooring line tension graph contain values ranging from 0 to 10,000 kN. These values are small compared with 16,171.2 kN, which is equivalent to 60% of the MBL and is a tension requirement for survival conditions. In other words, the position requirements and mooring line tension requirements were met for all conditions. Thus, it can be concluded that station-keeping performance has been satisfied from the perspective of the station keeping of the structure and the tensile force of the mooring lines.

To verify the DPS auxiliary performance, the results of the DP-assisted mooring system in Case 3, which has a relatively harsher condition, were compared with the results of a stand-alone mooring system under the same environmental loads. The graphs in Fig. 15 show the comparison of the position and heading angle data and the mooring line tension data between the DP-assisted mooring system and the stand-alone mooring system.

The red line represents the stand-alone mooring system results, and the blue line represents the results of the DP-assisted mooring system. The simulation results showed that both systems satisfy the target radius for station keeping. In addition, the tension values of mooring lines fall within the acceptable range, within 60% of the MBL, and meet the criteria. However, compared with the DP-assisted mooring system, the stand-alone mooring system drifted toward the upper-left region and came close to the target radius of 25 m in the case of station keeping. Furthermore, the tension graphs in the fourth row represent the data for tension acting on the fourth bundle (mooring lines 13–16)

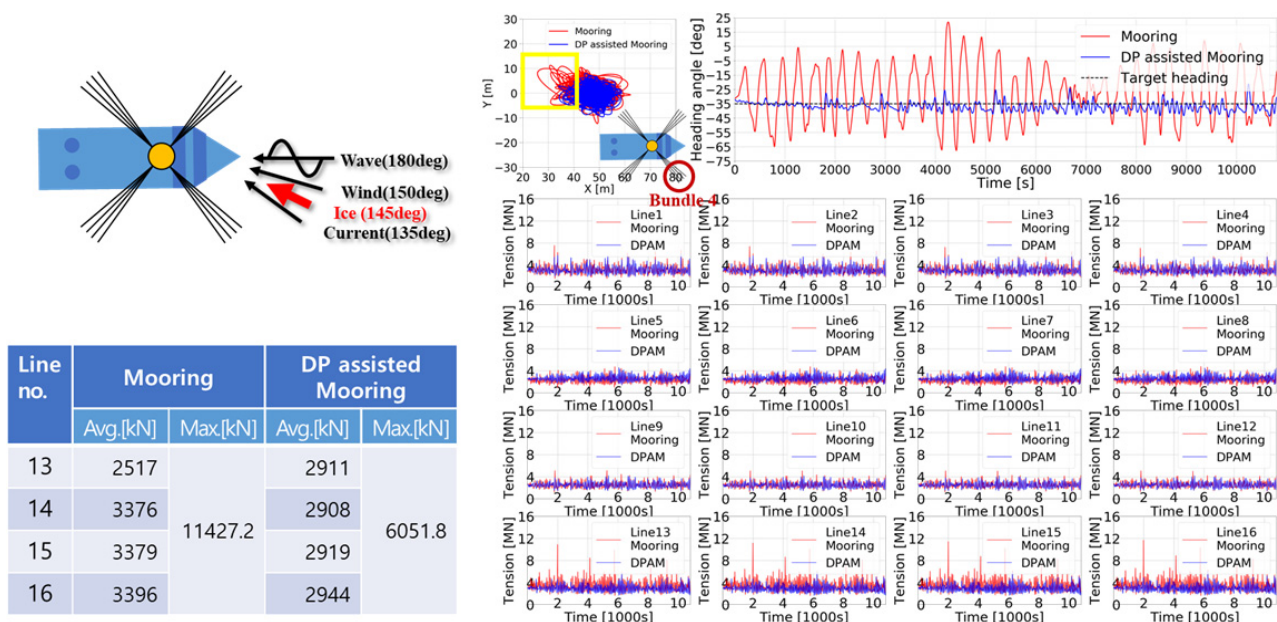


Fig. 15 Comparison of mooring line tensions between DP-assisted mooring (DPAM) and stand-alone mooring systems

as the vessel drifted toward the upper-left region. The fourth bundle is located in the lower-right part of the vessel. The graphs verified that the stand-alone mooring system tension values are greater than the tension values for the DP-assisted mooring system.

The average tension for the fourth bundle of the stand-alone mooring system is 3,167 kN, and there is a large difference in average tension between mooring line 13 and mooring lines 14–16. However, the average tension for the bundles of the DP-assisted mooring system is 2,920.5 kN, and the average tension of each mooring line is similar. The average tension reduction caused by the DPS is 200 kN, and the difference in maximum tension between the two systems is 5,375.4 kN. Hence, the tension reduction effect can be verified.

5. Conclusions

To perform a simulation of the DP-assisted mooring system in the time domain based on the results of the experiments conducted in the ice tank, an ice load generation module was developed, and its process was established. An interpolation function was generated based on the mean and standard deviation of the measured data, and the mean and standard deviation values for an arbitrary heading angle were set. An arbitrary random number was generated by assuming a normal distribution to establish a process for generating ice loads in a particular time and heading angle.

Using a module developed in Python, commercial dynamic analysis software, OrcaFlex, was configured such that the ice load can be input as an additional load. A simulation was performed to assess the station-keeping performance of the floating structure in the polar region, which was designed for combined environmental loads, including the ice load. The results of the simulation are summarized as follows.

(1) Although the simulated ice loads lacked statistical consistency with the experimental data, their validity was verified by creating ice loads that share some of the statistical characteristics and applying them to the simulation in the time domain. Although random variables were generated by assuming a normal distribution in this study, other distributions, such as a log-normal distribution, can be easily applied. Because the direction angle of the structure kept changing in the simulation, it is difficult to make a direct comparison between the simulation data and the values measured in the experiment while maintaining a particular angle. However, the analysis of the mean and maximum values, one of the main factors that characterize the ice load, is deemed acceptable.

(2) Using the relative magnitude of the ice load and the DPS, it was found that the limit for maintaining the heading angle is approximately 4°. For the floating structure applied in the simulation, there were limitations in maintaining the position and controlling the heading angle simultaneously because the difference in thrust value between the thrusters installed at the bow and stern was significant.

(3) Efforts were made to control the heading angle so it would match the ice load. As a result, the heading angle and the ice load could be

matched, even when the contained angle was at 17°. The overall load acting on the structure is reduced by rotating the heading angle in the direction where the load is exerting the greatest force. As a result, it is possible to control the station keeping. This result, along with the previous simulation results, can be used as a reference for setting the acceptable heading angle in the DP-assisted mooring system.

(4) Simulations were performed under a collinear condition, as well as under two different noncollinear conditions where the direction in which the ice load acts was different. The results showed that the station-keeping systems satisfied the performance requirements of the design phase. Because the mooring system is designed rather conservatively, the DPS did not seem to contribute to the station-keeping function. However, in a noncollinear condition, the difference in maximum tension between the stand-alone mooring system and the DP-assisted mooring system was 5,375 kN. Hence, the tension reduction effect of the DPS was shown. This result could be the basic data for redesigning a mooring system.

Based on this study, further simulations are planned to effectively operate the designed structure in harsh maritime environments. The sensor system will be replaced in the planned experiments to measure the ice load more accurately. Moreover, the ice load generation module will be enhanced so that additional factors needed to generate the ice load in the time domain can be studied and incorporated. Currently, the target position and direction of the DPS are used by setting arbitrary constant values. In the future, its logic should be reconstructed to proactively contribute to the tension reduction of the mooring system.

Acknowledgments

This research was funded by Ministry of Trade, Industry & Energy (MOTIE, Korea) under Industrial Technology Innovation Program No. 10063405, “Development of hull form of year-round floating type offshore structure based on the Arctic Ocean in ARC7 condition with dynamic positioning and mooring system,” and Dong-eui University Grant (No. 202003500001).

References

- Cundall P.A., & Strack, O.D.L. (1979). A Discrete Numerical Model for Granular Assemblies, *Géotechnique*, 29(1), 47-65. <https://doi.org/10.1680/geot.1979.29.1.47>
- Daley, C.G., Alawneh, S., Peters, D., Blades, G., & Colbourne, B. (2014). Simulation of Managed Sea Ice Loads on a Floating Offshore Platform using GPU-event Mechanics. Proceedings of the International Conference and Exhibition on Performance of Ships and Structures in Ice, Banff, Canada.
- Daley, C.G., Alawneh, S., Peters, D., Quinton, B.W.T., & Colbourne, B. (2012). GPU Modeling of Ship Operations in Pack Ice. Proceedings of the International Conference and Exhibition on Performance of Ships and Structures in Ice, Banff, Canada.

- Islam M., Wang, J., Brown, J., Lau, M., Gash, R., Millan, D., & Millan, J. (2018). Physical Model Testing for Supporting Ice Force Model Development of DP Vessels in Managed Ice. Proceedings of OTC Arctic Technology Conference, St. John's, Canada. <https://doi.org/10.4043/29157-MS>
- Jeong, S.-Y., Jang, J., Kim, C.-H., Yum, J.-G., & Kang, K.-J. (2018). A Study of Ship Resistance Characteristics for Ice-strengthened Vessel by Broken Ice Channel Width and Size of Broken Ice Pieces. *Journal of the Society of Naval Architects of Korea*, 55(1), 22-27. <https://doi.org/10.3744/SNAK.2018.55.1.22>
- Jenssen, N.A., Hals, T., Jochmann, A., Santo, X.D., Kerkeni, S., Doucy, O., ... & Løset, S. (2012). DYPIC-A Multi-National R&D Project on DP Technology in Ice. Proceedings of the Dynamic Positioning Conference, Houston, USA.
- Jenssen, N.A., Muddesitti, S., Phillips, D., & Backstrom, K. (2009). DP in Ice. Proceedings of the Dynamic Positioning Conference, Houston, USA.
- Kerkeni, S., Santo, X.D., Doucy, O., Jochmann, P., Haase, A., Metrikin, I.A., ... & Støle-Hentschel, S. (2014). DYPIC Project: Technological and Scientific Progress Opening New Perspectives. Proceedings of Arctic Technology Conference, Houston, USA.
- Kim, H.S., Han, D., Lee, J.-B., & Jeong, S.-Y. (2018a). An Estimation of Attainable Speed in Brash Ice using Empirical Formula. *Journal of the Society of Naval Architects of Korea*, 55(4), 313-320. <https://doi.org/10.3744/SNAK.2018.55.4.313>
- Kim, Y.-S., Kim, J.-H., Kang, K.-J., Han, S., & Kim, J. (2018b). Ice Load Generation in Time Domain Based on Ice Load Spectrum for Arctic Offshore Structures. *Journal of Ocean Engineering and Technology*, 32(6), 411-418. <https://doi.org/10.26748/KSOE.2018.32.6.411>
- Lee, J., Choi, S.-M., Lee, S.J., & Jung, K.H. (2019). Tension Based Heading Control Strategy of the Arctic FPSO with DP Assisted Mooring System. Proceedings of the ASME 2019 38th International Conference on Ocean, Offshore and Arctic Engineering, Glasgow, UK. <https://doi.org/10.1115/OMAE2019-96557>
- Løset, S. (1994). Discrete Element Modelling of a Broken Ice Field – Part I: Model Development. *Cold Regions Science and Technology*, 22(4), 339-347. [https://doi.org/10.1016/0165-232X\(94\)90019-1](https://doi.org/10.1016/0165-232X(94)90019-1)
- Lubbad, R., Løset, S., Lu, W., Tsarau, A., & van den Berg, M. (2018a). An Overview of the Oden Arctic Technology Research Cruise 2015 (OATRC2015) and Numerical Simulations Performed with SAMS driven by Data Collected during the Cruise. *Cold Regions Science and Technology*, 156, 1-22. <https://doi.org/10.1016/j.coldregions.2018.04.006>
- Lubbad, R., Løset, S., Lu, W., Tsarau, A., & van den Berg, M. (2018b). Simulator for Arctic Marine Structures. Proceedings of the ASME 2018 37th International Conference on Ocean, Offshore and Arctic Engineering, Madrid, Spain. <https://doi.org/10.1115/OMAE2018-78592>
- Moran, K., Backman, J., & Farrel, J.W. (2006). Deepwater Drilling in the Arctic Ocean's Permanent Sea Ice, Proceedings of the Integrated Ocean Drilling Program, 302. <https://doi.org/10.2204/iodp.proc.302.106.2006>
- Morgunova, M. (2020). Why is Exploitation of Arctic Offshore Oil and Natural Gas Resources Ongoing? A Multi-level Perspective on the Cases of Norway and Russia. *The Polar Journal*, 10, 1-18. <https://doi.org/10.1080/2154896X.2020.1757823>
- Raza, N., van der Berg, M., Lu, W., & Lubbad R. (2019). Analysis of Oden Icebreaker Performance in Level Ice Using Simulator for Arctic Marine Structures (SAMS). Proceedings of the 25th International Conference of Portand Ocean Engineering under Arctic Conditions, Delft, The Netherlands.
- Walton, O.R. (1982) Explicit Particle Dynamics Model for Granular Materials, Proceedings of 4th International Conference on Numerical Methods in Geomechanics, Edmonton, Canada.
- Wang, J., Sayeed, T., Millan, D., Gash, R., Islam M., & Millan J. (2016). Ice Model Tests for Dynamic Positioning Vessel in Managed Ice. Proceedings of OTC Arctic Technology Conference, St. John's, Canada. <https://doi.org/10.4043/27430-MS>
- Zvyagin, P., & Sazonov, K. (2014). Analysis and Probailistic Modeling of the Stationary Ice Loads Stochastic Process with Lognormal Distribution. Proceedings of the ASME 2014 33rd International Conference on Ocean, Offshore and Arctic Engineering, San Francisco, USA. <https://doi.org/10.1115/OMAE2014-24713>

Author ORCIDs

Author name	ORCID
Kang, Hyun Hwa	0000-0003-3690-4776
Lee, Dae-Soo	0000-0003-1800-2277
Im, Ji-Su	0000-0003-2154-4296
Lee, Seung Jae	0000-0001-8992-6915
Jang, Jinho	0000-0001-7979-4314
Jung, Kwang Hyo	0000-0002-8229-6655
Lee, Jaeyong	0000-0002-4469-7765

Higher-order Spectral Method for Regular and Irregular Wave Simulations

Seunghoon Oh¹, Jae-Hwan Jung¹ and Seok-Kyu Cho²

¹Senior Researcher, Korea Research Institute of Ships and Ocean Engineering, Busan, Korea

²Principal Researcher, Korea Research Institute of Ships and Ocean Engineering, Daejeon, Korea

KEY WORDS: Higher-order spectral method, Fast Fourier transform, Zero padding, Nonlinear adjustment region, Wave generation

ABSTRACT: In this study, a nonlinear wave simulation code is developed using a higher-order spectral (HOS) method. The HOS method is very efficient because it can determine the solution of the boundary value problem using fast Fourier transform (FFT) without matrix operation. Based on the HOS order, the vertical velocity of the free surface boundary was estimated and applied to the nonlinear free surface boundary condition. Time integration was carried out using the fourth order Runge-Kutta method, which is known to be stable for nonlinear free-surface problems. Numerical stability against the aliasing effect was guaranteed by using the zero-padding method. In addition to simulating the initial wave field distribution, a nonlinear adjusted region for wave generation and a damping region for wave absorption were introduced for wave generation simulation. To validate the developed simulation code, the adjusted simulation was carried out and its results were compared to the eighth order Stokes theory. Long-time simulations were carried out on the irregular wave field distribution, and nonlinear wave propagation characteristics were observed from the results of the simulations. Nonlinear adjusted and damping regions were introduced to implement a numerical wave tank that successfully generated nonlinear regular waves. According to the variation in the mean wave steepness, irregular wave simulations were carried out in the numerical wave tank. The simulation results indicated an increase in the nonlinear interaction between the wave components, which was numerically verified as the mean wave steepness. The results of this study demonstrate that the HOS method is an accurate and efficient method for predicting the nonlinear interaction between waves, which increases with wave steepness.

1. Introduction

High-precision wave prediction technology is imperative for both the design of ships and offshore structures to be operated at sea and also for their maintenance. Because ocean waves have nonlinear characteristics, a broad understanding of waves and highly precise numerical techniques are required to accurately predict their generation and propagation.

The numerical technique for predicting waves is mainly the efficiency analysis based on potential flow. There are two methods to reflect the nonlinear boundary conditions of the free surface. One is a higher-order analysis method based on the perturbation method, and another one is mixed Eulerian-Lagrangian (MEL) methods (Longuet-Higgins and Cokelet, 1976) using a completely nonlinear free surface condition.

In particular, the MEL method, which is flexible for the analysis of the strong nonlinearity of free surface and wave-body interactions, was applied using various solution methods of the Laplace equation such as

boundary element method (BEM), finite element method (FEM), and harmonic polynomial cell (HPC) (Longuet-Higgins and Cokelet, 1976; Wu et al., 1998; Shao and Faltinsen, 2014). Because the mentioned solution method of the Laplace equation inevitably requires matrix operation, the MEL method, which reconstructs the free surface grid every time step to reflect the completely nonlinear free surface, requires high computational costs for calculations of a solution of boundary value problem (Oh et al., 2018). In contrast, the higher-order spectral (HOS) method of Dommermuth and Yue (1987), based on a higher-order analysis method, can determine the solution of the boundary value problem using the fast Fourier transform (FFT) without a matrix operation. Therefore, compared to the MEL-based analysis method, this method is significantly more computationally efficient (Kim, 1993). Therefore, the HOS method is widely used for predicting the propagation and generation of nonlinear waves (Ducrozet et al., 2016). Owing to the recent developments in computing equipment, computational fluid dynamics (CFD) is being increasingly used for analyzing loads and the behaviors of offshore

Received 9 September 2020, revised 13 October 2020, accepted 14 October 2020

Corresponding author Seunghoon, Oh: +82-51-604-7825, carot541@kriso.re.kr

© 2020, The Korean Society of Ocean Engineers

This is an open access article distributed under the terms of the creative commons attribution non-commercial license (<http://creativecommons.org/licenses/by-nc/4.0>) which permits unrestricted non-commercial use, distribution, and reproduction in any medium, provided the original work is properly cited.

structures. However, the direct CFD simulation for irregular sea state requires high computational cost, and cumulative error due to long-time simulation is inevitable. Currently, studies on the potential flow method and CFD coupling are actively being conducted to address this challenge and generate efficient and highly precise irregular wave predictions. In particular, the HOS method is known to be one of the best methods for CFD coupling in terms of high accuracy and computational efficiency (Gatin et al., 2017). Therefore, it is expected that the development of a wave simulation code via the HOS method can be widely used for both the nonlinear wave prediction study and the efficient implementation of the CFD wave field.

Because boundary conditions except that of the free surface cannot be defined, it is challenging to generate waves like a wave tank using the conventional HOS method. Under the nonlinear free surface conditions, it is necessary to fine-tune the results of repetitive calculations because the transfer function can only be calculated under the linear free surface conditions although waves can be generated via the disturbance of the free surface. Therefore, to work on the boundary condition for the wave generation, Kim (1993) introduced the boundary element method to the HOS method while Bonnefoy et al. (2006) worked on the boundary condition for the wave generation using the pseudo-spectral basis of the cosine function and an additional potential technique. The aforementioned methods are cumbersome because they require the introduction of a separate additional boundary value problem. Recently, Liam et al. (2014) applied a nonlinear adjustment zone to the analytic and variational Boussinesq models to successfully transform the linear wave generated in the free surface into a nonlinear wave, which is expected to be applied to the HOS model.

In this study, a nonlinear wave simulation code using an efficient HOS method was developed. According to the expansion of Dommermuth and Yue (1987), the vertical velocity of the free surface boundary, which depends on the HOS order, was estimated and applied to the nonlinear free surface boundary condition. Time integration was performed using the fourth order Runge-Kutta method, which is known to be stable against the nonlinear free surface problem. The zero-padding method was used to secure numerical stability against the aliasing effect (Canuto et al., 1988). The nonlinear adjustment region (Liam et al., 2014) and wave damping zone were introduced for the simulations of wave generation. The adjusted simulation of Dommermuth (2000) was performed and compared with the eighth order Stokes theory to verify the developed code. The long-time simulation was performed on the irregular wave distribution to determine the characteristics of nonlinear wave propagation. Nonlinear adjustment and damping zones were introduced to implement a numerical wave tank, thus confirming that a nonlinear regular wave was successfully generated. As the mean wave steepness increased, the nonlinear interaction between wave components was numerically evaluated by simulating the generation of irregular waves based on the mean wave steepness in the numerical wave tank.

2. Mathematical Formulation and Numerical Technique

2.1 Mathematical Formulation

In this study, a rectangular fluid domain with a horizontal length L and constant depth h was considered in a Cartesian coordinate system. In this coordinate system, the mean water surface was on the x -axis while the vertical z -axis was directed upwards. Assuming that the fluid is incompressible and inviscid and the flow is irrotational, the velocity of the fluid defined as the gradient of the velocity potential ϕ and the continuity equation, which is the governing equation, is transformed into the Laplace equation as expressed in Eq. (1).

$$\nabla^2 \phi + \frac{\partial^2 \phi}{\partial z^2} = 0 \text{ in fluid domain} \quad (1)$$

where, ∇ denotes a horizontal gradient operator. According to the study conducted by Zakharov (1968), the surface potential ϕ^s at the free surface ζ can be defined by Eq. (2).

$$\phi^s(x, t) \equiv \phi(x, \zeta(x, t), t) \quad (2)$$

Using the surface potential ϕ^s , the kinematic boundary conditions and dynamic boundary conditions of the free surface can be expressed by Eqs. (3)-(4).

$$\frac{\partial \zeta}{\partial t} = (1 + |\nabla \zeta|^2) W - \nabla \phi^s \cdot \nabla \zeta \quad (3)$$

$$\frac{\partial \phi^s}{\partial t} = -g\zeta - \frac{1}{2} |\nabla \phi^s|^2 + \frac{1}{2} (1 + |\nabla \zeta|^2) W^2 \quad (4)$$

where, g and W denote the acceleration due to the gravitational acceleration and vertical velocity of the free surface expressed in Eq. (5), respectively.

$$W(x, t) = \frac{\partial \phi(x, \zeta, t)}{\partial z} \quad (5)$$

The vertical velocity W can be calculated using the HOS model presented by Dommermuth and Yue (1987) and West et al. (1987). The free surface ζ and surface potential ϕ^s based on to time progress can be obtained by integrating Eqs. (3)-(4), which substitutes the calculated vertical velocity W . It is assumed that the horizontal region is infinite in the HOS model and the periodic boundary condition is adopted as expressed in Eq. (6).

$$\begin{aligned} \zeta(0, t) &= \zeta(L, t) \\ \phi^s(0, t) &= \phi^s(L, t) \\ W(0, t) &= W(L, t) \end{aligned} \quad (6)$$

Eq. (7) was adopted in terms of the bottom boundary condition, which is the no-penetration condition.

$$\frac{\partial \phi(x, -h, t)}{\partial z} = 0 \quad (7)$$

The velocity potential, which is the solution of the Laplace equation that satisfies the aforementioned free surface boundary condition (Eqs. (3)–(4)), lateral periodic boundary condition (Eq. (6)), and bottom boundary condition (Eq. (7)), can be defined by Eq. (8) using a Fourier pseudo-spectral basis.

$$\phi(x, z, t) = \sum_m C_m(t) \frac{\cosh(k_m(z+h))}{\cosh(k_m h)} \exp(i k_m x) \quad (8)$$

where, C_m denotes the time-dependent Fourier coefficient of the velocity potential, and k_m denotes wave number defined by Eq. (9), respectively.

$$k_m = \frac{2\pi}{L} m, \quad m = 1, 2, \dots \quad (9)$$

Similar to the velocity potential, the surface potential ϕ^s and free surface ζ can be defined by a Fourier pseudo-spectral basis as expressed in Eqs. (10)–(11).

$$\phi^s(x, t) = \sum_m A_m(t) \exp(i k_m x) \quad (10)$$

$$\zeta(x, t) = \sum_m B_m(t) \exp(i k_m x) \quad (11)$$

Where, A_m and B_m respectively denote the time-dependent Fourier coefficients of the surface potential and free surface. The expansions of the surface potential and free surface in Eqs. (10)–(11) were limited to the number of points in the free surface that define the physical quantity. Moreover, the Fourier expansion in Eqs. (10)–(11) provided a horizontal differential to the time integrations of the surface potential and free surface using Eqs. (3)–(4). However, because the vertical velocity W on the free surface is unknown, the vertical velocity W of the free surface can be measured using the HOS model according to the expansion of Dommermuth and Yue (1987). In the HOS model, the surface potential ϕ^s , which is the physical quantity of the surface, and the free surface ζ were used to evaluate the vertical velocity W of the free surface. First, the velocity potential ϕ can be expressed up to the given order of M with the perturbation expansion for wave steepness as expressed in Eq. (12).

$$\phi(x, z, t) = \sum_{m=1}^M \phi^{(m)}(x, z, t), \quad m = 1, 2, \dots, M \quad (12)$$

where, the perturbation potential $\phi^{(m)}$ has a perturbation order of m

for the wave steepness. From the mean depth of $z = 0$, the perturbation potential $\phi^{(m)}$ for the free surface can be expressed by Eq. (13) using the expansion of Taylor series.

$$\begin{aligned} \phi^{(1)}(x, 0, t) &= \phi^s(x, t) \\ \phi^{(2)}(x, 0, t) &= -\zeta \frac{\partial \phi^{(1)}(x, 0, t)}{\partial z} \\ &\vdots \\ \phi^{(m)}(x, 0, t) &= -\sum_{j=1}^{m-1} \frac{\zeta^j}{j!} \frac{\partial^j \phi^{(m-j)}(x, 0, t)}{\partial z^j} \end{aligned} \quad (13)$$

The vertical velocity W can also be expressed with perturbation expansion as in Eq. (14), as presented in Eq. (12).

$$W(x, t) = \sum_{m=1}^M W^{(m)}(x, t), \quad m = 1, 2, \dots, M \quad (14)$$

where, the vertical perturbation velocity $W^{(m)}$ also has a perturbation order of m for the wave steepness and the vertical perturbation velocity $W^{(m)}$ for the free surface ζ from the mean depth of $z = 0$ can be expressed with Taylor expansion as expressed in Eq. (15).

$$W^{(m)}(x, t) = \sum_{j=0}^{m-1} \frac{\zeta^j}{j!} \frac{\partial^{j+1} \phi^{(m-j)}(x, 0, t)}{\partial z^{j+1}} \quad (15)$$

The perturbation vertical velocity $W^{(m)}$ in Eq. (15) was calculated via the perturbation velocity potential $\phi^{(m)}$, which can be used to measure the vertical velocity W at ζ using Eq. (14).

2.2 Numerical Technique

In this study, the free surface ζ and surface potential ϕ^s can be predicted depending on time integration using Eqs. (3)–(4), which define the boundary conditions of the free surface. As for time integration, the fourth order Runge–Kutta method, which ensured stability, was adopted as presented by Dommermuth and Yue (1987). The physical quantity and vertical velocity W of the spatial differential included in the boundary condition of the free surface were calculated by applying the FFT algorithm. In this study, a numerical technique was implemented using MATLAB (Matrix laboratory). Because it supports the FFT algorithm and multi-thread, MATLAB provides fast computation. Regarding the HOS method, the multiplication of the nonlinear free surface boundary conditions was performed in a physical space rather than a spectra space. Although such transformation is efficiently performed using FFT, it leads to an aliasing phenomenon. It is therefore imperative to clearly eliminate the aliasing phenomenon to ensure the stability of the analysis owing to its influence on numerical stability. In this study, the zero-padding method was used to eliminate the aliasing phenomenon. Zero padding is a method for performing multiplication operations without aliasing

in the physical space by filling in zero to expand the spectral space prior to multiplication. This is accompanied by the expansion of the spectral space, leading to an increase in computational cost as the consequence of an increase in the calculation domain. Therefore, appropriate spatial expansion was achieved via the half-rule as expressed in Eq. (16) (Canuto et al., 1988; Gatin et al., 2017).

$$N_{Extend} = \frac{p+1}{2}N \quad (16)$$

where, N_{Extend} and N represent an extended space for zero padding and the number of free modes used in HOS simulation. The parameter p is completely independent of the aliasing phenomenon when the order M is selected. An increase in computational cost owing to the expansion of the aforementioned spectral space can be expected as the order M increases, as expressed in Eq. (16). In this study, the full de-aliasing ($p = M$) was adopted because only two-dimensional calculations were performed.

The analysis of the HOS simulation is generally performed from the initial conditions of free surface ζ and surface potential ϕ^s at the free surface, in which the initialization is known to have significant influence on the numerical stability. According to the study by Dommermuth (2000), the simulation of the HOS method under the linear initial condition causes numerical instability because it does not satisfy the nonlinear free surface boundary conditions in Eqs. (3) and (4). Therefore, Dommermuth (2000) proposed an adjustment scheme to initiate the linear initial condition to the nonlinear free surface condition. This scheme enables the smooth transformation of the nonlinear solution via the relaxation of the nonlinear term of the free surface against time. Eqs. (17)–(18) express the free surface condition to which the relaxation of the nonlinear term was applied by introducing the relaxation time T_a and relaxation index n proposed by Dommermuth (2000).

$$\frac{\partial \zeta}{\partial t} = W^{(1)} + [(1 + |\nabla \zeta|^2)W - \nabla \phi^s \cdot \nabla \zeta - W^{(1)}] \left(1 - \exp\left(-\left(\frac{t}{T_a}\right)^n\right) \right) \quad (17)$$

$$\frac{\partial \phi^s}{\partial t} = -g\zeta + \left[-\frac{1}{2}|\nabla \phi^s|^2 + \frac{1}{2}(1 + |\nabla \zeta|^2)W^2 \right] \left(1 - \exp\left(-\left(\frac{t}{T_a}\right)^n\right) \right) \quad (18)$$

In this study, the linear free surface ζ_{1st} and linear potential ϕ_{1st} were adopted as the initial conditions of the regular wave under deep sea conditions, as expressed in Eqs. (19)–(20).

$$\zeta_{1st} = A_0 \cos(kx) \text{ at } z = 0 \quad (19)$$

$$\phi_{1st} = A_0 \frac{g}{\omega} \sin(kx) \text{ at } z = 0 \quad (20)$$

where, A_0 , k , and ω denote the wave amplitude, wave number, and wave frequency of the linear solution. Concerning the initial condition of the irregular wave simulation, the free surface and linear potential of

the irregular wave for the space can be defined by using the superposition of linear components. The wave amplitude for the wave frequency constituting the irregular wave from the defined wave spectrum $S(\omega)$ can be calculated using Eq. (21).

$$\frac{1}{2}A_i^2 = S(\omega_i) \Delta\omega \quad (21)$$

By substituting the calculated wave amplitude A_i into Eqs. (22)–(23), the initial conditions for the irregular wave simulation, $\zeta_{irregular}$ and $\phi_{irregular}$ can be calculated.

$$\zeta_{irregular} = \sum_{i=1}^n A_i \cos(k_i x + \epsilon_i) \quad (22)$$

$$\phi_{irregular} = \sum_{i=1}^n A_i \frac{g}{\omega_i} \sin(k_i x + \epsilon_i) \quad \text{at } z = 0 \quad (23)$$

where ϵ_i denotes a uniform random number between zero and 2π , and the wave number k_i and wave frequency ω_i are calculated via the dispersion relation. In this study, the joint North Sea wave project (JONSWAP) spectrum (DNV, 2010) was used to define the wave spectrum, as expressed in Eq. (24)

$$S(\omega_i) = \frac{5}{16} A_\gamma H_s^2 \omega_p^4 \omega^{-5} \exp\left(-\frac{5}{4} \left(\frac{\omega}{\omega_p}\right)^{-4}\right) \gamma \exp\left(-0.5 \left(\frac{\omega - \omega_p}{\sigma \omega_p}\right)^2\right) \quad (24)$$

where H_s , $T_p = 2\pi/\omega_p$, γ , and A_γ denote a significant height, peak period, peak shape parameter, and normalizing factor, respectively. Furthermore, σ is a spectral width parameter, which is determined depending on the peak wave frequency ω_p .

3. Numerical Simulation

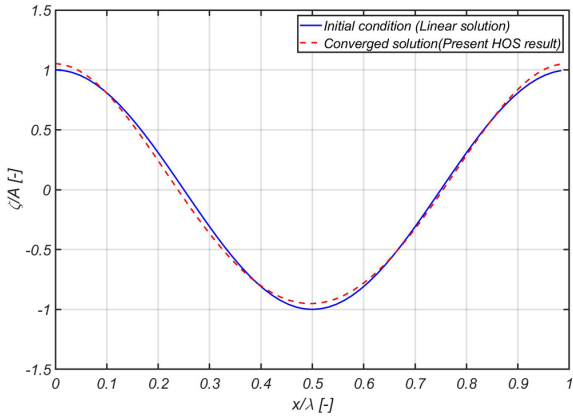
Numerical tests were performed to verify the HOS code developed in this study and to observe related characteristics. An analysis of linear single waves was performed to verify the HOS code, whereas a numerical analysis of the irregular wave field implemented was performed using the JONSWAP spectrum defined above to understand the developed HOS code characteristics.

3.1 Adjusted Simulation of Single Wave

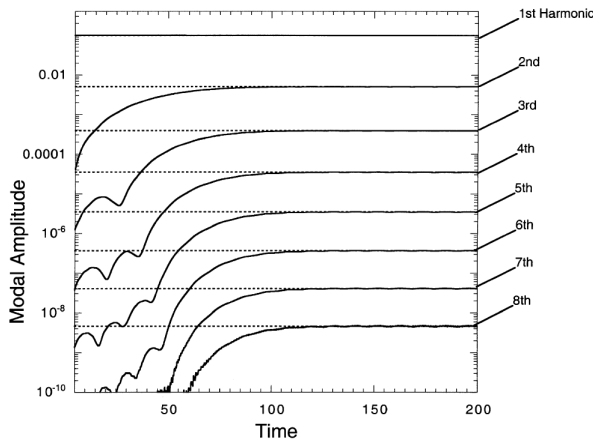
According to the study by Dommermuth (2000), when a linear solution is used as the initial condition and relaxation is applied to the HOS method for a certain period of time, it adjusts to a nonlinear solution. Dommermuth (2000) performed an adjustment simulation at a wave steepness of $kA = 0.1$ and presented the convergence result of the eighth harmonic component of the Stokes wave. In this study, the developed code was verified by performing calculation conditions, as presented in Table 1, which are the same conditions as those of Dommermuth (2000); after that, the results were compared.

Table 1 Calculation conditions for adjusted simulation

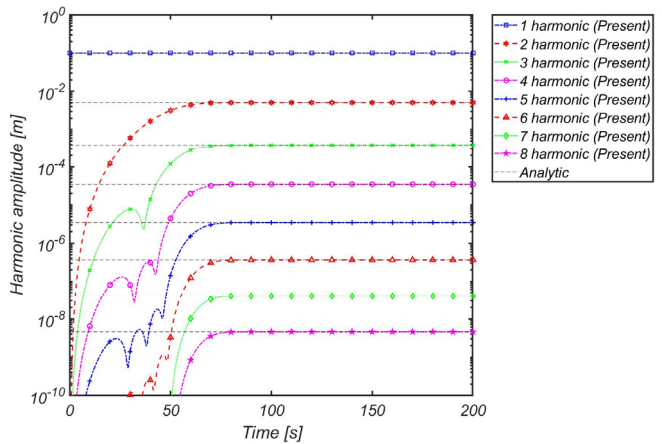
Item	Value
k	1
A (m)	0.1
T_a (s)	$8 \cdot 2\pi$
n (-)	4

**Fig. 1** HOS result of monochromatic Stokes wave

Similar to the study by Dommermuth (2000), a single wave adjustment simulation was performed using 64 modes for 200



(a) Results obtained of Dommermuth (2000)



(b) Results obtained by this study

Fig. 2 Adjusted simulation results for monochromatic Stokes wave**Table 2** Comparison of harmonic amplitudes of Stokes wave

Harmonic component	Exact	Results of Dommermuth (2000)	Present results	Relative error (%) $(A_{present} - A_{Exact})/A_{present}$
1	9.9870520E-02	9.9870521E-02	9.986907E-02	-1.451901E-03
2	5.0594125E-03	5.0594021E-03	5.059028E-03	-7.600274E-03
3	3.8584235E-04	3.8584076E-04	3.857805E-04	-1.603243E-02
4	3.4929691E-05	3.4929474E-05	3.491949E-05	-2.921291E-02
5	3.4769679E-06	3.4769122E-06	3.475166E-06	-5.185076E-02
6	3.6763951E-07	3.6762101E-07	3.673037E-07	-9.142571E-02
7	4.0531740E-08	4.0530871E-08	4.047282E-08	-1.455792E-01
8	4.6076934E-09	4.611506E-09	4.599084E-09	-1.871981E-01

seconds with a time step Δt at 0.025 intervals. In the HOS simulation, the linear solution converged to a nonlinear Stokes wave, as illustrated in Fig. 1.

It was determined that the eight harmonic components of the eighth order Stokes wave converged over time and that the convergence pattern of each harmonic component was similar to the results obtained by Dommermuth (2000), as illustrated in Fig. 2.

The converged results were compared with the analysis solution, as well as the results obtained by Dommermuth (2000), as presented in Table 2. Compared to the analysis solution, it was inferred that the relative error of the code developed in this study was insignificant at less than approximately 0.1%. The validity of the developed code was verified via this result.

3.2 Irregular Wave Simulation

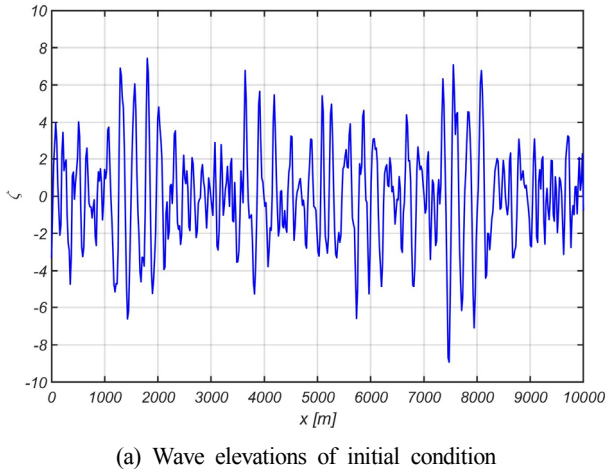
An irregular wave simulation was performed to understand the characteristics of the HOS method. Analysis conditions were defined with reference to the analysis case of Ducroz et al. (2016), as presented in Table 3. The corresponding condition was a mean steepness of $(s_{mean} = k_p H_s / (2\sqrt{2}))$ 0.1, where nonlinearity exists on the free surface

The initial conditions of the irregular wave for this case can be created using Eqs. (22)–(23), as illustrated in Fig. 3(a).

Table 3 Calculation conditions for irregular wave simulations

Item	Value
Spectrum type	JONSWAP spectrum
H_s (m)	11.0
T_p (s)	12.5
γ (-)	5
depth (m)	10,000.0
N_x (-)	512
L (m)	10,000.0
T_a (s)	$8 \cdot 2\pi$
n (-)	4
Δt (s)	0.25
Duration of simulation (s)	$600 \cdot T_p$

The spatial wave spectrum, obtained from the wave distribution generated, and the input wave spectrum were compared, as illustrated in Fig. 3(b). The two spectra exhibited satisfactory agreement, thus validating the generated wave distribution. The boundary condition at both ends was periodic and the wave from 10 000 m was re-introduced

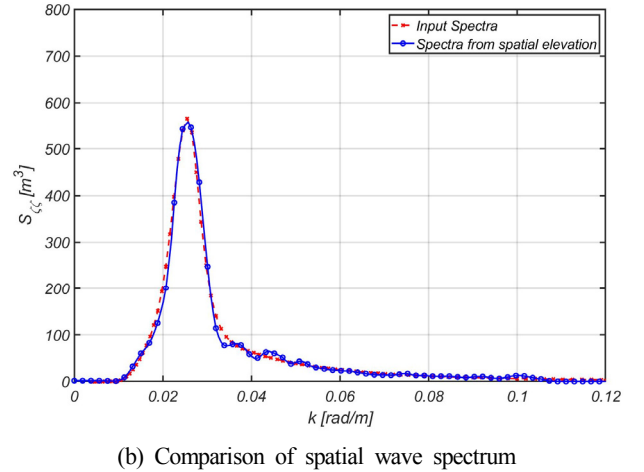
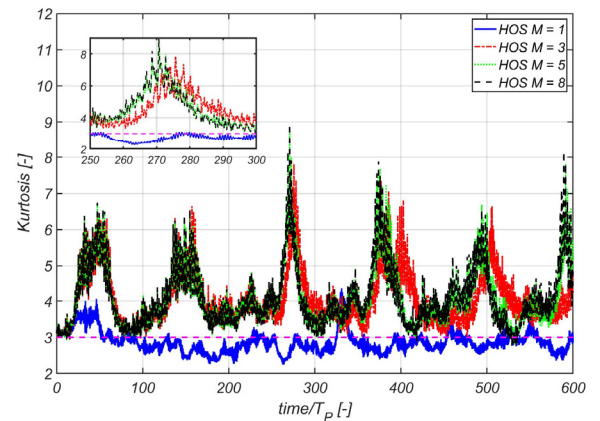
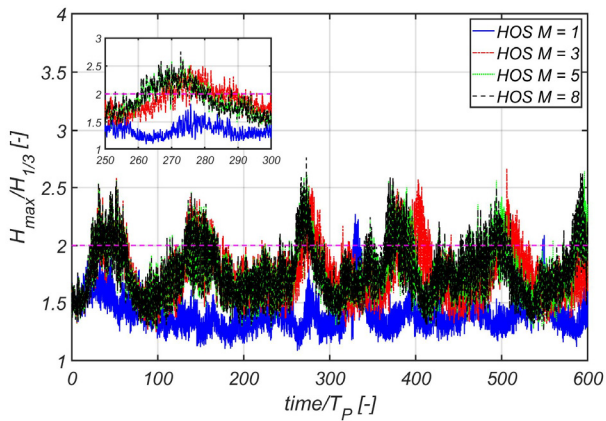


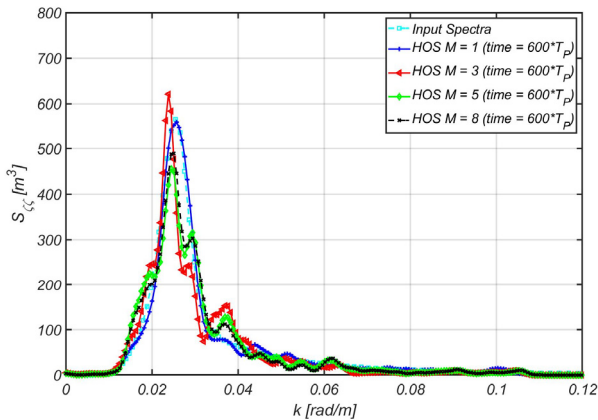
at 0 m when the simulation was performed. Therefore, the HOS method can efficiently simulate the development of irregular waves over a long period of time within a limited spatial grid.

In this study, simulation was performed by varying the order M to 1, 3, 5, and 8 for the same initial condition. Fig. 4 presents the normalized maximum wave height and kurtosis (κ) based on the change in time. When the normalized maximum wave height exceeds 2 m, it is called an abnormality index (AI). It is known that the abnormality index and kurtosis are highly correlated with the occurrence of Freak wave (Kim, 2019). The abnormality index was calculated using H_{\max} and $H_{1/3}$ was determined via the zero crossing analysis of the wave distribution at every time step. The kurtosis was a measure adopted to statistically establish the difference with the normal distribution, as defined in Eq. (25).

$$\kappa = \frac{1}{\sigma_\zeta^4} \frac{1}{N} \sum_{i=1}^N (\zeta_i - \zeta_{mean})^4 \quad (25)$$

where σ_ζ and ζ_{mean} denote the root mean square (RMS) of the spatial wave distribution of the wave height and the mean of the spatial wave

**Fig. 3** Initial condition of irregular wave simulations**Fig. 4** Evolution of normalized maximum wave height and kurtosis

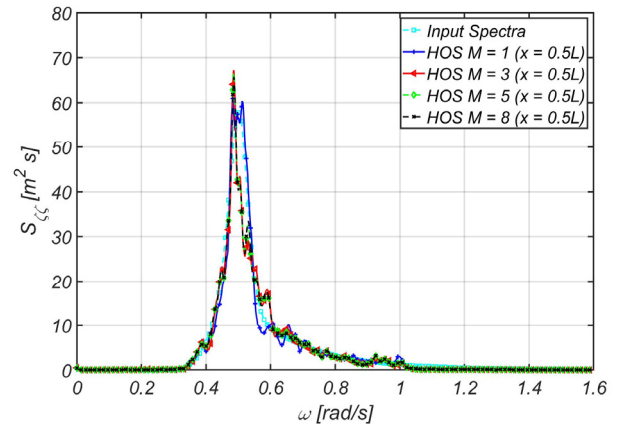


(a) Comparison of spatial wave spectrum at final time step

Fig. 5 Wave spectrums of irregular simulations

distribution, respectively. It was inferred that as time progresses, a significant difference exists between the abnormality index and kurtosis of orders 3, 5, and 8 that reflect the nonlinear effect of the free surface when the order is one, as illustrated in Fig. 4. This phenomenon occurs because of the nonlinear interaction between the wave components. Although the abnormality index and kurtosis of orders 3, 5, and 8 developed similarly up to $260 T_p$, the abnormality index and kurtosis of orders 5 and 8 exhibited different results from that of order 3 after $260 T_p$. This indirectly showed that the order needs to be 5 or above when simulating $260 T_p$ or above of the corresponding condition. Moreover, it was inferred that the normalized maximum wave height and kurtosis developed in a similar pattern, thus indicating that the two physical quantities are highly correlated.

The spatial wave spectrum was compared at the final time step, as illustrated in Fig. 5(a). The spectrum represents the distribution of energy, and the change in the spectrum indicates the change in energy distribution. Therefore, from the change in the magnitude of the spectrum of the corresponding wave number, it can be inferred that it was redistributed to the energy of other wave numbers. In the linear free surface boundary condition of order 1, it was concluded that the spatial wave spectrum is approximately similar to the initial value, thus indicating that the energy distribution between the components of the wave remains unchanged. However, the spatial wave spectra of orders 3, 5, and 8 exhibited different results from the initial values. This could be attributed to the nonlinear interaction between the wave components owing to the nonlinear free surface boundary condition, subsequently, it can be inferred that the wave energy was redistributed between the wave components. The wave displacement over time at the center point of the simulation domain was transformed into a spectrum, as illustrated in Fig. 5(b). It was similar to the initial value in the calculation condition of order 1, thus indicating the absence of interactions between wave components. However, the wave spectrum was different from the initial spectrum under the calculation conditions of orders 3, 5, and 8, which is also attributed to the nonlinear interaction between the wave components, and allows us to

(b) Comparison of wave spectrum at specific point ($x = 0.5L$)

infer that the energy between the wave components was redistributed. From these results, it was determined that the irregular wave simulation using the HOS method is a satisfactory numerical tool for observing the nonlinear interaction between wave components. As earlier mentioned, it was concluded that the conventional HOS method has the advantage of the long-time simulation for the initial conditions given as periodic boundary conditions at both ends. However, there are limitations to this simulation in that waves are generated only in a limited space and at a specific point, such as in a test tank. A separate numerical technique is required to generate and simulate waves as in a test tank. In the following chapter, a numerical technique for the simulation of wave generation is described. The technique was verified and its characteristics were identified via numerical tests.

4. Numerical Technique and Numerical Simulation for Wave Generation

4.1 Numerical Techniques for Generating Waves

Because boundary conditions are undefined except those of the free surface, the conventional HOS method has limitations in implementing the boundary conditions of the piston- or flap-type wave maker, such as a traditional wave tank. Tuning through repetitive calculations is required because wave generation owing to the forced disturbance of free surface can be represented in a transfer function under linear free surface conditions alone and cannot be represented under nonlinear free surface conditions. Therefore, Kim (1993) applied the wave generation technique based on the submerged circular cylinder by merging the HOS method and the boundary element method, whereas Bonnefoy et al. (2006) adopted the pseudo-spectral basis of the cosine function and the additional potential technique to include the boundary condition for the wave generation unlike in the conventional HOS method. In this study, the feasibility of nonlinear wave generation was investigated via the forced disturbance of free surface using the wave transfer function at specific wave generation points unlike in the studies conducted by Kim (1993) and Bonnefoy et al. (2006). As earlier mentioned, the

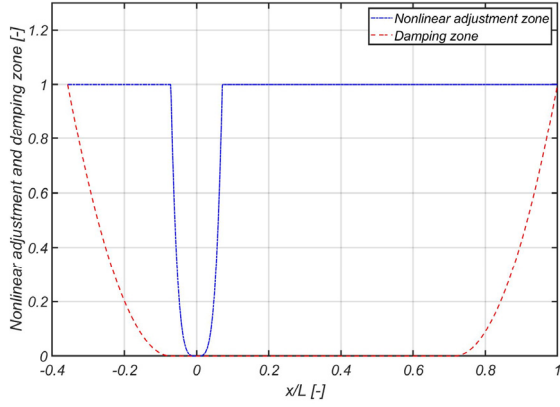


Fig. 6 Nonlinear adjustment and damping zone

wave transfer function via the forced disturbance of free surface is only feasible under linear free surface conditions. Therefore, to make the wave transfer function possible in the nonlinear free surface, the nonlinear adjustment zone applied to the analytic and variational Boussinesq models by Liam et al. (2014) was introduced to the HOS method, as illustrated in Fig. 6. To prevent the inflow of waves owing to the periodic conditions at both ends, a damping zone was also applied, as illustrated in Fig. 6.

The nonlinear adjustment zone plays a role similar to the aforementioned adjustment scheme presented by Dommermuth (2000). The nonlinear term of the free surface boundary condition degrades the simulation stability of wave generation for wave disturbances at a specific wave generation point. Therefore, similar to scheme of Dommermuth (2000), which weakens the effect of nonlinear terms against time, it is necessary to mitigate the effect of nonlinearity on spaces. The study on the nonlinear adjustment zone in Section 3.2 was conducted by Liam et al. (2014) and it was inferred that a larger adjustment interval L_{NAZ} was required as the wave steepness increased.

The nonlinear adjustment zone is defined as a function of distance, as expressed in Eq. (26). The damping zone was applied to the boundary of both ends, as illustrated in Fig. 6. This was done to prevent the inflow and outflow of waves through the boundary owing to the periodic boundary conditions at both ends. The damping zone was applied to the physical quantity of each boundary condition, as expressed in Eq. (27).

$$A(x) = \begin{cases} 1 & |x| \geq L_{NAZ} \\ 1 - \left(\frac{|x| - L_{NAZ}}{L_{NAZ}} \right)^4 & |x| < L_{NAZ} \end{cases} \quad (26)$$

$$v(x) = \begin{cases} \gamma_{damping} \omega \left(\frac{x_a - x}{\lambda_{damping}} \right)^2 & x < x_a \\ 0 & x_a \leq x \leq x_b \\ \gamma_{damping} \omega \left(\frac{x - x_b}{\lambda_{damping}} \right)^2 & x_b < x \end{cases} \quad (27)$$

where, x_a and x_b , $\gamma_{damping}$, and $\lambda_{damping}$ denote the boundary points of the damping zone, wave damping coefficient, and length of the damping zone, respectively. In this study, $\gamma_{damping}$ was set to one and $\lambda_{damping}$ was set at a wavelength longer than the generated wavelength. If the nonlinear adjustment and damping zones are applied to the free surface boundary condition of Eqs. (3)–(4), they are defined as expressed in Eqs. (28)–(29).

$$\frac{\partial \zeta}{\partial t} = W^{(1)} + [(1 + |\nabla \zeta|^2) W - \nabla \phi^s \cdot \nabla \zeta - W^{(1)}] A(x) - v(x) \zeta \quad (28)$$

$$\frac{\partial \phi^s}{\partial t} = -g \zeta + \left[-\frac{1}{2} |\nabla \phi^s|^2 + \frac{1}{2} (1 + |\nabla \zeta|^2) W^2 \right] A(x) - v(x) \phi^s \quad (29)$$

Wave disturbances for wave generation were performed at the point where x was equal to zero, and the wave transfer function was calculated using the harmonic simulation results of white noise under the boundary condition of the linear free surface, as illustrated in Fig. 6.

4.2 Wave Generation Numerical Simulation

The wave generation simulation of regular and irregular waves was performed to verify and analyze the characteristics of the numerical technique for wave generation earlier described. The analysis was performed in the same calculation domain as in Fig. 7 under the calculation conditions presented in Table 4.

Table 4 Calculation conditions for the wave generation simulation of regular and irregular waves

Item	Value
L (m)	9,500
Depth (m)	10,000.0
L_{sim} (m)	4,500.0
L_{NAZ} (m)	500.0
$\lambda_{damping}$ (-)	2,000.0
N_x (-)	1,024
Δt (s)	0.1

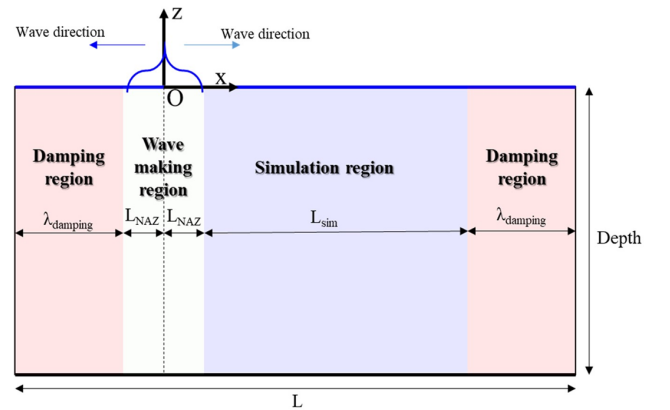


Fig. 7 Calculation domain for wave generation simulation

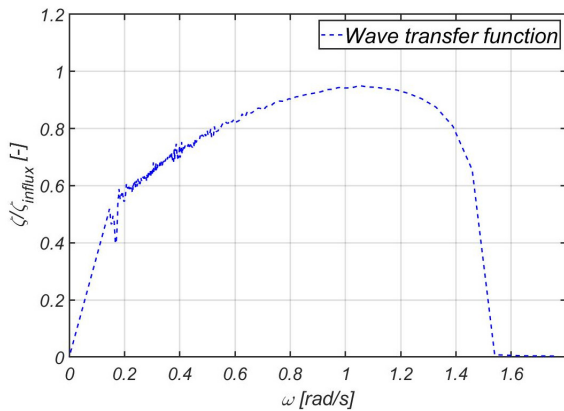
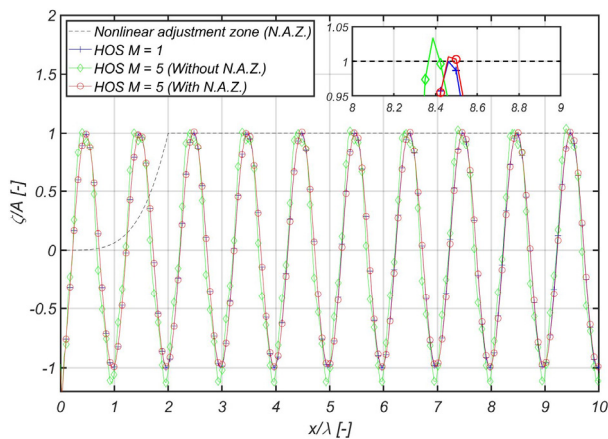


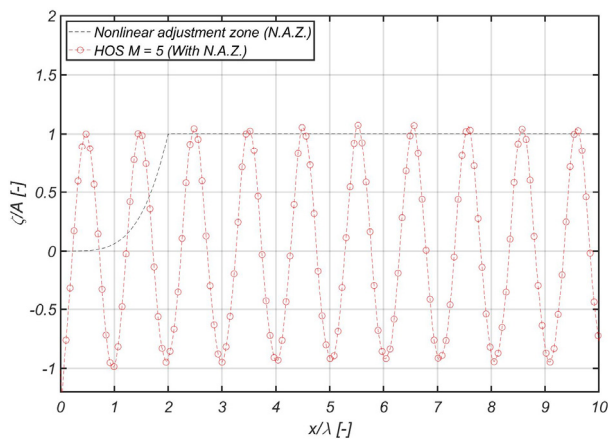
Fig. 8 Wave transfer function for specific calculation condition

A wave transfer function can be created via the harmonic simulation results of white noise for the corresponding conditions, as illustrated in Fig. 8. ζ_{influx} denotes the disturbance amplitude of the wave at the point where $x = 0$.

The wave generation simulation of regular waves was performed under the conditions of wave steepness, where kA was 0.025 and 0.126. The simulation that did not apply the nonlinear adjustment zone was additionally performed to understand the characteristics of the technique.



(a) $kA = 0.025$ ($\lambda = 250$ m, $A = 1.0$ m)



(b) $kA = 0.126$ ($\lambda = 250$ m, $A = 5.0$ m)

Fig. 9 Regular wave making simulations

It was deduced that when kA is 0.025, it indicates the condition for generating waves with weak nonlinearity, where the amplitude difference between orders 1 and 5 is insignificant, as demonstrated in Fig. 9(a). In contrast, the condition when kA is 0.126 indicates the generation of waves with strong relative nonlinearity, which shows nonlinear characteristics with a high crest and steady trough, as demonstrated in Fig. 9(b). To strictly observe these nonlinear characteristics, it was compared with the 5th order Stokes wave (Fenton, 1985), as illustrated in Fig. 10. It was inferred that the shape of the generated wave did not only agree well with the 5th order Stokes wave, but also the waves of desired periods and amplitudes can be generated via the wave transfer function determined in advance, as demonstrates in Fig. 8. Regarding the application of nonlinear free surface boundary conditions without the nonlinear adjustment zone, the amplitude and phase of the wave differed from the linear result when kA was 0.025, and the simulation of regular wave generation diverged when kA was 0.126, as illustrated in Fig. 9(a). Consequently, it was concluded that it is necessary to apply a nonlinear adjustment zone when simulating wave generation via wave disturbance. It was determined that the HOS-based numerical harmonic tank can be implemented using a numerical technique such as nonlinear adjustment and damping zones based on the above results.

In the same calculation condition as the regular wave, the simulation of the irregular wave was performed for the irregular wave condition in Table 5. To observe the nonlinear effect according to the increase in the significant wave height, the simulation was performed under the three conditions of the mean wave steepness ($s_{mean} = k_p H_s / (2\sqrt{2})$), which are 0.01, 0.05, and 0.1. The simulation of wave generation was performed by also varying orders 1, 3 and 5.

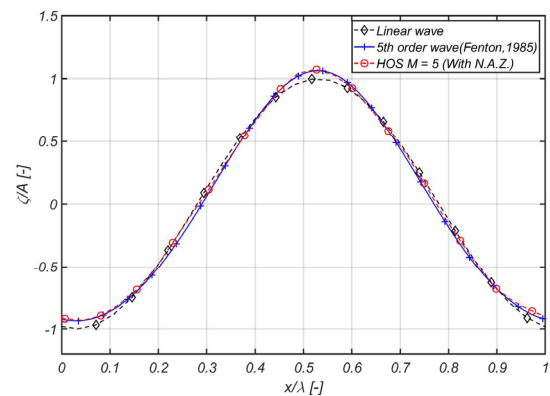


Fig. 10 Comparison of steep wave simulation ($kA = 0.126$)

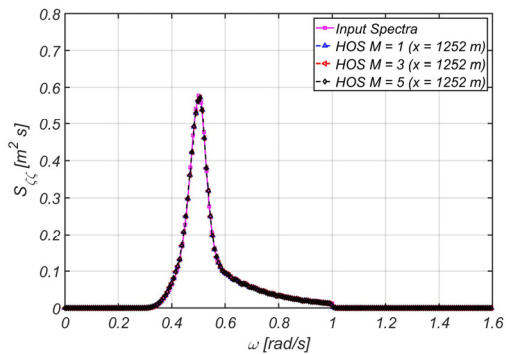
Table 5 Calculation conditions for irregular wave simulation

Item	Value
Spectrum type	JONSWAP spectrum
H_s (m)	1.1, 5.5, 11.0
T_P (s)	12.5
γ (-)	5
Duration of simulation (s)	$600 \cdot T_P$

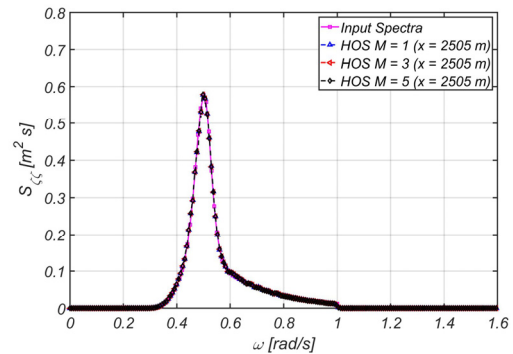
For comparison, the random phase was used identically in all simulations when generating irregular waves. After the relaxation distance of the nonlinear adjustment zone, a spectral analysis was

performed on the wave time series at 4 points ($x = 1252$ m, 2505 m, 3750 m, and 4994 m).

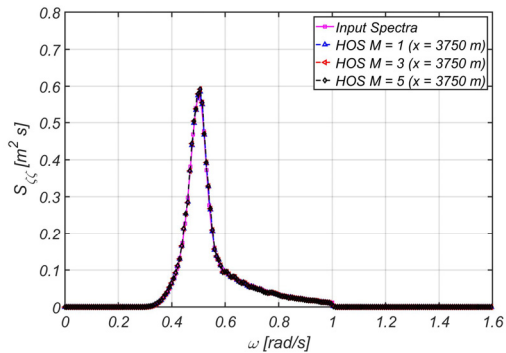
Fig. 11 illustrates the mean wave steepness of 0.01. It was



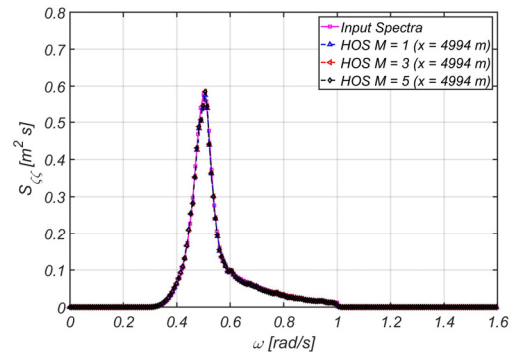
(a) Comparison of wave spectrum at $x = 1252$ m



(b) Comparison of wave spectrum at $x = 2505$ m

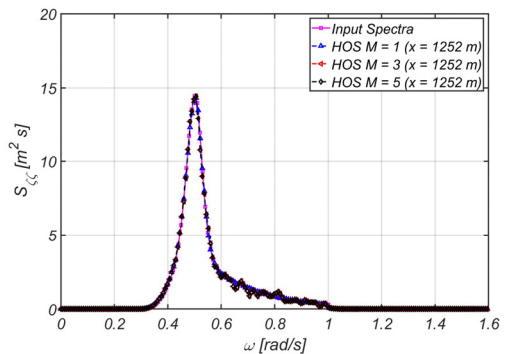


(c) Comparison of wave spectrum at $x = 3750$ m

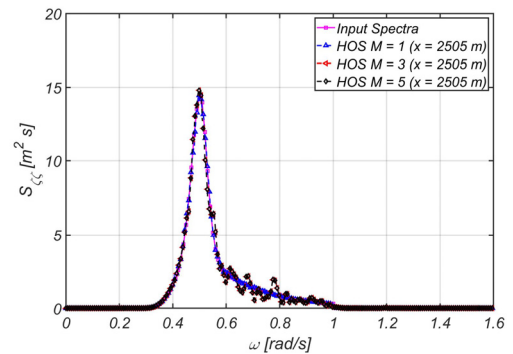


(d) Comparison of wave spectrum at $x = 4994$ m

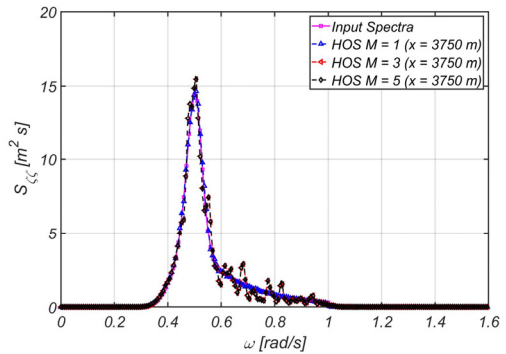
Fig. 11 Irregular wave simulations for mean steepness $s_{mean} = 0.01$ ($H_s = 1.1$ m)



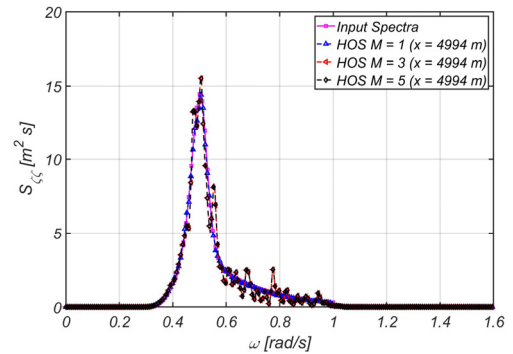
(a) Comparison of wave spectrum at $x = 1252$ m



(b) Comparison of wave spectrum at $x = 2505$ m



(c) Comparison of wave spectrum at $x = 3750$ m



(d) Comparison of wave spectrum at $x = 4994$ m

Fig. 12 Irregular wave simulations for mean steepness $s_{mean} = 0.05$ ($H_s = 5.5$ m)

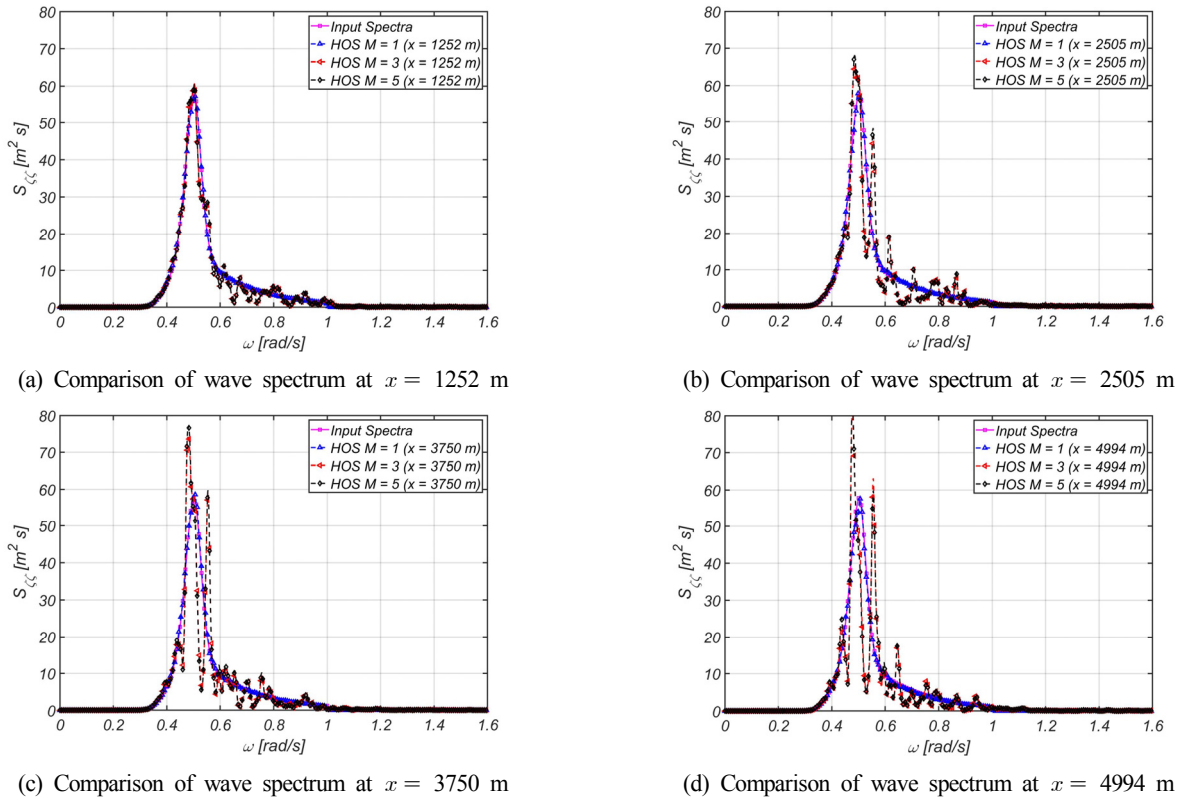


Fig. 13 Irregular wave simulations for mean steepness $s_{mean} = 0.1$ ($H_s = 11.0$ m)

determined that the spectrum of 4 points almost coincide with no difference depending on the HOS order, and also that the spectrum of 4 points almost coincide with the spectrum input when generating the wave. It can be inferred that energy was not redistributed between frequencies because there was an insignificant nonlinear interaction between wave components during the generation and propagation of irregular waves. This means that the nonlinearity that appeared was insignificant owing to the low mean wave steepness of the calculation condition. Fig. 12 illustrates the mean wave steepness of 0.05. Except for the case of order 1, it was determined that the difference in the input wave spectrum increased with an increase in the distance from the origin, which is the wave generation point. This indicates that the energy distribution between frequencies was insignificant owing to the nonlinear interaction between wave components during wave propagation as earlier mentioned. Because the results of orders 3 and 5 are almost identical, it can be inferred that nonlinear interactions can also be reflected at order 3 when the mean wave steepness is 0.05. Fig. 13 presents the results of mean wave steepness at 0.1. It's similarity to the input wave spectrum was apparent when x was equal to 1252 m, which is the closest point after the relaxation distance of the nonlinear adjustment zone during wave generation; however, the difference in the input wave spectrum increased as the wave propagated away from the origin of wave generation. Consequently, it can be inferred that the nonlinear interaction of the wave increased compared to the previously described wave steepness condition. Based on the comparison with the mean wave steepness of 0.05, it was deduced that the energy redistribution between wave components was more significant owing

to the nonlinear interaction between wave components during wave propagation. Some differences between the results of orders 3 and 5 were determined, thus indicating that for the mean wave steepness of 0.1, nonlinear interactions can be fully reflected only when the order is considered to be 5 or above similar to the results of the irregular wave simulation in Section 3.2.

5. Conclusion

In this study, a nonlinear wave simulation code was developed using an efficient HOS method. Because it can determine the solution of the boundary value problem using FFT without matrix computations, the HOS method is extremely efficient in its computation compared to other free-surface numerical techniques. The vertical velocity W was estimated based on the HOS order according to the expansion presented by Dommermuth and Yue (1987). Furthermore, the time integration for the nonlinear free surface boundary condition was stably performed using the Runge-Kutta 4th order method accordingly. The aliasing phenomenon caused by the multiplication of the nonlinear free surface boundary condition was eliminated using the zero padding method, thus securing numerical stability. The conventional HOS method is limited in its simulation of wave generation in a confined space, such as in a tank, with lateral periodic conditions. Therefore, in this study, a nonlinear adjustment and damping zones were introduced to implement a numerical tank capable of generating waves via surface disturbance. Several numerical simulations were performed using the developed code,

therefore, the following conclusions were derived based on the results of performed simulations:

(1) By performing the same nonlinear relaxation simulation as in the study by Dommermuth (2000), it was inferred that the linear solution converged to the eighth order Stoke wave solution. The HOS code developed in this study was verified by demonstrating that the convergence pattern was the same as that of Dommermuth (2000) and the convergence result was highly consistent with the analysis solution.

(2) The abnormal index and kurtosis over time were observed via the simulation of an irregular wave field with a mean wave steepness of 0.1. A high correlation between the two physical quantities was determined based on the similarity of the time series development pattern between the abnormality index and kurtosis, which are known to exhibit high correlation with the occurrence of freak waves. It was inferred that to fully reflect the nonlinear interaction between waves in this mean wave steepness 0.1, order 5 or above needs to be considered.

(3) In the simulation of an irregular wave field, it was determined that the difference between the wave spectrum given as the initial condition and that of the final time step increased as the order increased. It was therefore concluded that energy was redistributed between wave components via the change in the wave spectrum, which can be deduced to have resulted from the nonlinear interaction between wave components.

(4) It was reconfirmed that the HOS method can efficiently simulate the development of irregular waves over a long period of time within a limited grid because the wave that outflowed from the ends was re-introduced through the starting point owing to the periodic boundary conditions at both ends.

(5) Using the simulation of wave generation based on the presence of a nonlinear adjustment zone, the difference in amplitude and phase of the wave was determined, as well as its propensity to trigger numerical divergence in the absence of a nonlinear adjustment zone. Therefore, it is necessary to apply a non-linear adjustment zone when simulating wave generation via wave disturbance. In addition, it was determined that desired nonlinear regular and irregular waves can be generated by the transfer function and nonlinear adjustment zone for wave disturbance at a specific point under the boundary condition of the linear free surface.

(6) The simulation of irregular wave generation based on several changes in mean wave steepness was performed and it was determined that the difference in the input spectrum increased as the wave steepness increased. This difference indicates an increase in energy redistribution between wave components owing to nonlinear interactions between wave components. From these results, the HOS method is inferred to be an excellent numerical tool for observing nonlinear interactions between wave components.

In the future, studies on improving the proposed HOS code, as well as on the irregular wave field coupling of CFD will be continued by introducing the energy dissipation model which describes the breaking wave phenomenon, and conducting irregular wave model tests.

Acknowledgement

This study is the product of the “Development of core technology for computational fluid dynamics analysis of global performance of offshore structures (PES3500)” supported by the Korea Research Institute of Ships and Ocean Engineering.

References

- Bonnefoy, F., Le Touze, D., & Ferrant, P. (2006). A Fully-spectral Time-domain Model for Second-order Simulation of Wavetank Experiments. Part A: Formulation, Implementation and Numerical Properties. *Applied Ocean Research*, 28(1), 33-43. <https://doi.org/10.1016/j.apor.2006.05.004>
- Canuto, C., Hussaini, M., Quarteroni, A., & Zang, T. (1998). *Spectral Methods in Fluid Dynamics*. Springer Science & Business Media.
- Det Norske Veritas (DNV). (2010). *Environmental Conditions and Environmental Loads (DNV-RP-C205)*. Det Norske Veritas.
- Dommermuth, D.G., & Yue, D.K.P. (1987). A High-order Spectral Method for the Study of Nonlinear Gravity Waves. *Journal of Fluid Mechanics*, 184, 267-288.
- Dommermuth, D.G. (2000). The Initialization of Nonlinear Waves Using an Adjustment Scheme. *Wave Motion*, 32(4), 307-317. [https://doi.org/10.1016/S0165-2125\(00\)00047-0](https://doi.org/10.1016/S0165-2125(00)00047-0)
- Ducrozet, G., Bonnefoy, F., Le Touze, D., & Ferrant, P. (2016). HOS-ocean: Open-source Solver for Nonlinear Waves in Open Ocean Based on High-Order Spectral Method. *Computer Physics Communications*, 203, 245-254. <https://doi.org/10.1016/j.cpc.2016.02.017>
- Gatin, I., Vukcevic, V., & Jasak, H. (2017). A Framework for Efficient Irregular Wave Simulations Using Higher Order Spectral Method Coupled with Viscous Two Phase Model. *Journal of Ocean Engineering and Science*, 2(4), 253-267. <https://doi.org/10.1016/j.joes.2017.09.003>
- Fenton, J.D. (1985). A Fifth-order Stokes Theory for Steady Waves. *Journal of Waterway Port Coastal and Ocean Engineering*, 111, 216-234. [https://doi.org/10.1061/\(ASCE\)0733-950X\(1985\)111:2\(216\)](https://doi.org/10.1061/(ASCE)0733-950X(1985)111:2(216))
- Kim, Y.J. (1993). Study of Nonlinear Wave Diffraction Using the 2-Dimensional Numerical Wave Tank. *Journal of Ocean Engineering and Technology*, 7(2), 187-196.
- Kim, D.Y. (2019). Statistical Analysis of Draupner Wave Data. *Journal of Ocean Engineering and Technology*, 33(3), 252-258. <https://doi.org/10.26748/KSOE.2019.031>
- Longuet-Higgins, M.S., & Cokelet, E.D. (1976). The Deformation of Steep Surface Waves on Water - I. A Numerical Method of Computation. *Proceedings of the Royal Society of London. A. Mathematical and Physical Sciences*, 350(1660), 1-26. <https://doi.org/10.1098/rspa.1976.0092>
- Liam, L.S., Adytia, D., & van Groesen, E. (2014). Embedded Wave Generation for Dispersive Surface Wave Models. *Ocean Engineering*, 80, 73-83. <https://doi.org/10.1016/j.oceaneng.2014.01.008>

- Oh, S., Cho, S.K., Jung, D., & Sung, H.G. (2018). Development and Application of Two-dimensional Numerical Tank Using Desingularized Indirect Boundary Integral Equation Method. *Journal of Ocean Engineering and Technology*, 32(6), 447-457. <https://doi.org/10.26748/KSOE.2018.32.6.447>
- Shao Y.L., & Faltinsen O.M. (2014). A Harmonic Polynomial Cell (HPC) Method for 3D Laplace Equation with Application in Marine Hydrodynamics. *Journal of Computational Physics*, 274, 312-332. <https://doi.org/10.1016/j.jcp.2014.06.021>
- West, B.J., Brueckner, K.A., Janda, R.S., Milder, D.M., & Milton, R.L. (1987). A New Numerical Method for Surface Hydrodynamics. *Journal of Geophysical Research*, 92(C11), 11803-11824. <https://doi.org/10.1029/JC092iC11p11803>
- Wu, G.X., Ma, Q.W., & Taylor, R.E. (1998). Numerical Simulation of Sloshing Waves in a 3D Tank Based on a Finite Element Method. *Applied Ocean Research*, 20(6), 337-355. [https://doi.org/10.1016/S0141-1187\(98\)00030-3](https://doi.org/10.1016/S0141-1187(98)00030-3)
- Zakharov, V.E. (1968). Stability of Periodic Waves of Finite Amplitude on the Surface of a Deep Fluid. *Journal of Applied Mechanics and Technical Physics*, 9, 190-194. <https://doi.org/10.1007/BF00913182>

Author ORCIDs

Author name	ORCID
Oh, Seunghoon	0000-0002-7249-2353
Jung, Jae-Hwan	0000-0001-9384-5720
Cho, Seok-Kyu	0000-0002-7821-4848

Study on PIV-Based Pressure Estimation Method of Wave Loading under a Fixed Deck

Gang Nam Lee¹, Tien Trung Duong², Kwang Hyo Jung³, Sung Bu Suh⁴ and Jae Yong Lee⁴

¹Post-doctoral Researcher, Department of Naval Architecture and Ocean Engineering, Pusan National University, Busan, Korea

²Graduate Student, Department of Naval Architecture and Ocean Engineering, Pusan National University, Busan, Korea

³Professor, Department of Naval Architecture and Ocean Engineering, Pusan National University, Busan, Korea

⁴Professor, Department of Naval Architecture and Ocean Engineering, Dong-Eui University, Busan, Korea

KEY WORDS: PIV-based pressure estimation, Wave loading under deck, Euler equation, Focused wave, Pressure field

ABSTRACT: In this study, a particle image velocimetry (PIV)-based pressure estimation method was investigated, with application to the wave-in-deck loading phenomenon. An experimental study was performed in a two-dimensional wave tank using a fixed deck structure under a focused wave, obtaining local pressures by pressure sensors, global loads by load cells, and instantaneous velocity fields using the PIV measurement technique. The PIV-based pressure estimation method was applied using the Euler equation as the governing equation, and the proper time step for the wave impact pressure was studied using the normalized root-mean-square deviation. The pressure estimation method showed good agreement for the local impact pressure in comparison with the measured pressure by the pressure sensors. However, some differences were observed in the peak pressure due to the limitations of the Euler equation and the sampling rate of the measurement system. Using the estimation method, the pressure fields during wave-in-deck loading were determined in the study, with an analysis of the mechanism of impact and negative pressure occurrence.

1. Introduction

Ships and offshore structures operating in harsh marine environments are easily exposed to wave impact loads such as green water and slamming due to high waves, and wave-in-deck loads of offshore structures. This can cause great damage to ships and offshore structures, or even cause capsizing (Faulkner, 2001; Ersdal and Kvitrud, 2000; Faltinsen, 2005; Kaiser et al., 2009). For the structural safety design of ships and offshore structures that can overcome the impact load caused by waves, the structural design criteria must first be established with an accurate estimation on the external force along with a quantitative understanding of the flow characteristics of the wave impact load. To this end, various experimental or numerical studies are being conducted to measure the pressure applied on the occurrence of wave impact loads and to quantitatively analyze the flow characteristics that cause them. The following representative studies have been conducted, and many other studies are currently being conducted: a study on the flow characteristics of the green water phenomenon that occurs in a simplified shape, and the measurement of

the impact load by measuring the pressure applied on the deck and upper structure when a green water phenomenon occurs (Buchner and Voogt, 2000; Lim et al., 2012; Lee et al., 2020); an impact mechanism analysis using pressure measurement of the slamming phenomenon occurring at the leading edge, and a wedge-shaped model (Faltinsen et al., 2004; Shams et al., 2017; Oh and Jo, 2015; Xie et al., 2018); and an experimental pressure measurement and flow characteristics study on the wave-in-deck load (Abdussamie et al., 2014; Duong et al., 2019). Most of these studies experimentally measured and analyzed the pressure applied on the surface of the structure by using pressure sensors, and qualitative analysis was mainly performed on the flow characteristics that cause impact loads. However, it may be challenging to apply the Froude similarity when the impact pressure is measured using a pressure sensor (Rouse, 1959), which is widely used in experimental studies due to the nonlinearity and uncertainty of the phenomenon itself (Ariyaratne et al., 2012). In addition, the pressure sensors can only measure pressure locally, which can create flow disturbance due to direct contact between the fluid and the sensor. In order to solve these problems, a method of estimating the impact

Received 13 October 2020, revised 25 October 2020, accepted 27 October 2020

Corresponding author Kwang Hyo Jung; +82-51-510-2343, kjung@pusan.ac.kr

© 2020, The Korean Society of Ocean Engineers

This is an open access article distributed under the terms of the creative commons attribution non-commercial license (<http://creativecommons.org/licenses/by-nc/4.0>) which permits unrestricted non-commercial use, distribution, and reproduction in any medium, provided the original work is properly cited.

pressure using the surrounding flow velocity has been recently proposed (van Oudheusden, 2013). Thus far, the penetration method using conduction and resistance devices has mainly been used as an experimental method for measuring the flow velocity around ships and offshore structures, and a method using optical fibers has also been used (Chanson, 1997). However, these contact-type flow rate measurement methods generate disturbance of the surrounding flow due to direct contact with the fluid. Moreover, many non-contact flow rate measurement methods, which are used to measure the flow velocity through external optical image measurement, have been developed in order to overcome this shortcoming. Particle image velocimetry (PIV) is used to study the dynamics of various fluid properties, such as flow velocity and compressible fluids. PIV can be used to measure the position of particles in a fluid through optical image measurement without disturbing the flow, and to measure the velocity over the entire flow in the field of view at the same time. It is also used for high-precision verification of computational fluid dynamics (CFD) simulation, since it can provide the characteristics of the velocity field (Nila et al., 2013; Lee et al., 2016; Kim et al., 2019; Kim et al., 2020). This PIV-based velocity field measurement method can apply the Froude similarity to velocity, and can estimate the pressure field rather than the local pressure at the same time; thus, it is expanding its application range as an experimental pressure estimation method.

The pressure estimation method using the instantaneous velocity field measured through PIV was first applied in the field of aerodynamics. Van Oudheusden (2013) showed the applicability of the pressure and load estimation method through the flow field around the wing measured using PIV, and this pressure estimation method was applied to various shapes, including the wing (De Gregorio, 2006; Spedding and Hedenström, 2009). In the field of marine engineering, a study was conducted using the velocity field measured by PIV to calculate the internal pressure and acceleration of a fluid in waves (Jakobsen et al., 1997). Panciroli and Prfiri (2013) estimated the pressure during free fall of a wedge-shaped structure using the velocity field measured through PIV, and compared and verified the results with potential theory. Kim et al. (2020) investigated the damping mechanism in the roll motion of a rectangular-shaped structure in waves using the surrounding velocity field measured through PIV, and compared the estimated pressure with the CFD analysis results. These studies showed the accuracy and applicability of the pressure field estimation method using the velocity field measured using PIV.

In this study, the wave-in-deck load phenomenon was experimentally implemented, and a study was conducted on the application of the pressure estimation method using the instantaneous velocity field of the surrounding flow measured through PIV. A method of estimating pressure was proposed using the instantaneous velocity field of fluids based on the Euler equation, and measuring the local pressure for the wave impact load caused by the interference of the wave generated by the method of overlapping the regular wave with the deck structure fixed in the two-dimensional wave tank. The

pressure estimation characteristics were compared depending on the time interval between the velocity fields for the instantaneous acceleration calculation, and a time interval setting method for accurate impact pressure estimation was proposed. In addition, a hydrodynamic analysis study was conducted on the mechanism of pressure generation of wave-in-deck loads by estimating the significant pressure field around the structure when an impact load occurs.

2. Theoretical Background

In order to estimate the pressure around the structure by using the instantaneous velocity field measured through PIV, the two-dimensional inviscid Euler equation is used as the governing equation in this study. The pressure gradient of the fluid in the PIV field of view can be estimated through the Euler equation-based Eqs. (1)–(2).

$$\frac{\partial p}{\partial x}(x, z) = -\rho \frac{Du}{Dt} = -\rho \left(\frac{\partial u}{\partial t} + u \frac{\partial u}{\partial x} + w \frac{\partial u}{\partial z} \right) \quad (1)$$

$$\frac{\partial p}{\partial z}(x, z) = -\rho \frac{Dw}{Dt} - \rho g = -\rho \left(\frac{\partial w}{\partial t} + u \frac{\partial w}{\partial x} + w \frac{\partial w}{\partial z} \right) - \rho g \quad (2)$$

where p denotes pressure, ρ denotes fluid density, t denotes time, x and z denote the Cartesian coordinate systems in the horizontal and vertical directions, respectively, and u and w denote the instantaneous velocities for x and z , respectively. The spatial and temporal acceleration terms of the fluid at time t in Eqs. (1) and (2) were calculated by applying the central difference method (Eqs. (3), (4)) for the continuous velocity field measured through PIV, as shown in Fig. 1.

$$\frac{\partial u}{\partial x}(x, z, t) = \frac{u(x+h, z, t) - u(x-h, z, t)}{2h} \quad (3)$$

$$\frac{\partial u}{\partial t}(x, z, t) = \frac{u(x, z, t+n\delta t) - u(x, z, t-n\delta t)}{2n\delta t} \quad (4)$$

where δt denotes the time interval between images measured through PIV, h denotes the space interval between each vector, and n denotes the number of images between continuous velocity fields used in the acceleration calculation.

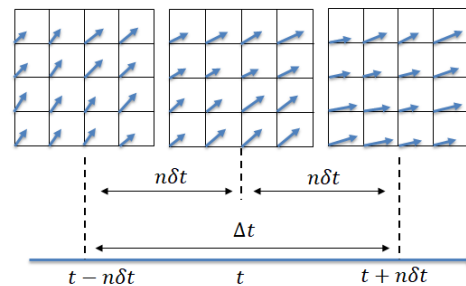


Fig. 1 Time step between each velocity field for calculation of acceleration

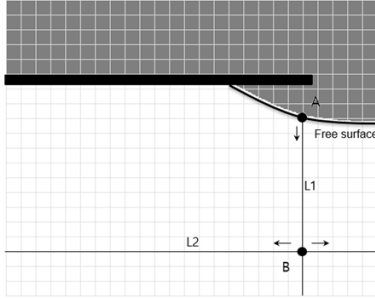


Fig. 2 Pressure integration scheme in the study

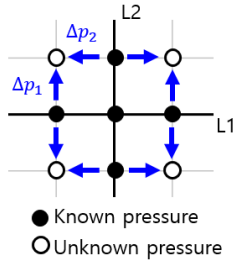


Fig. 3 Spatial forward integration method

The forward difference (Eq. (5)) and the backward difference (Eq. (6)) were used according to the location to calculate the spatial difference at the edge of the PIV field of view.

$$\frac{\partial u}{\partial x}(x, z, t) = \frac{u(x+h, z, t) - u(x, z, t)}{h} \quad (5)$$

$$\frac{\partial u}{\partial x}(x, z, t) = \frac{u(x, z, t) - u(x-h, z, t)}{h} \quad (6)$$

The pressure field of the fluid in the field of view was measured by applying spatial integration to the pressure gradient in the fluid field measured through the above process. The schematic spatial integration process is shown in Fig. 2. First, the pressure at the free surface is assumed to be atmospheric pressure, and the measured pressure gradient along the line L1 perpendicular to the x -axis direction is integrated for an arbitrary point A on the free surface. Then, the pressure for an arbitrary point B on the L1 line is measured through integration in the x direction and $-x$ direction along L2 perpendicular to L1. Based on the measured pressures on L1 and L2, the space marching integral (Eq. (7)) (Baur and Köngeter, 1999) is used to measure the pressure of the rest of the field, as shown in Fig. 3. Next, the pressure field for a location other than point A on the free surface was measured in the same way, and the average value of each location of the pressure field measured in each measurement process was used as the final pressure field.

$$p(s) = p(s_{ref}) + \int_{s_{ref}}^s \nabla p \cdot ds \quad (7)$$

where S_{ref} denotes a reference position, and s denotes a spatial position to be calculated.

3. Wave-in-Deck Load Experiment Method

3.1 Experimental Conditions

In order to examine the accuracy of the PIV-based impact pressure estimation method, the results were compared and verified by applying it to a model experiment (Duong et al., 2019) for wave-in-deck loads. The model experiment was conducted in a two-dimensional wave tank (32 m long, 0.6 m wide, 1 m deep) equipped with a piston-type wave maker and an inclined wave absorber, as shown in Fig. 4. The dimension of the deck structure was determined by referring to a jacket-type structure operating in the Gulf of Suez area with a similar ratio of 1:56 (Table 1). In addition, the breadth of the structure was set to 0.60 m, equal to the breadth of the tank, in order to exclude the three-dimensional effect of the impact load phenomenon.

In this experiment, a focused wave made with two regular waves with having different periods and wave heights was used to implement the deck impact load in extreme environments and to exclude the effects of previous waves. The focused wave has a relatively strong nonlinearity compared to the regular waves, and the main variables for the wave height and period of each regular wave used for the focused wave and the wave nonlinearity (Myrhaug and Kjeldsen, 1986) are listed in Table 2. In this experiment, the velocity field and pressure were measured when the wave-in-deck load occurred due to the focused wave. The time series of the waves used is shown in Fig. 5,

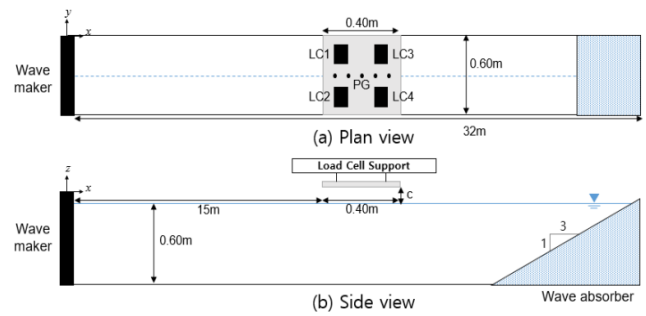


Fig. 4 Schematics of experimental setup

Table 1 Principal dimensions of prototype and model

	Prototype	Model
Length (m)	22.00	0.40
Breadth (m)	18.00	0.60
Water depth (m)	33.50	0.60
Deck clearance (m)	4.56	0.06

Table 2 Specifications of component and focused waves

Component 1		Component 2	
Period (s)	Height (m)	Period (s)	Height (m)
1.04	0.108	1.25	0.109
Focused Wave			
H_c (m)	H_t (m)	H (m)	T_r (s)
T_f (s)	T_{zd} (s)	T_{zu} (s)	
0.093	0.054	0.047	0.25
			0.22
			1.11
			1.10

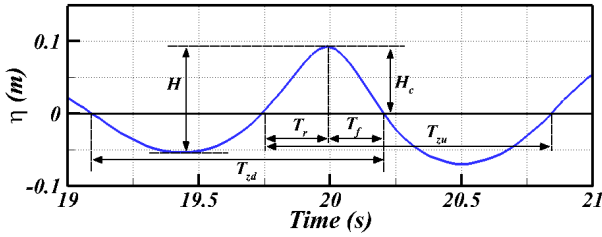


Fig. 5 Time history of focused wave

where H_c denotes the crest height, H_l denotes the trough height, H denotes the wave height, T_r and T_f denote the time taken for the wave to reach the crest from the average surface, and to reach the average surface from the crest, respectively, and T_{zu} and T_{zd} denote the zero up-crossing and zero down-crossing periods, respectively. Each variable is schematically shown in Fig. 5.

The deck structure used in the experiment was fixed at a distance of 15 m from the wave maker, all experiments were conducted at a depth of 0.60 m, and measurements were performed immediately before the reflected wave from the wave absorber returned to the experiment site. Details on the experimental conditions and the implementation of overlapping waves are shown in Duong et al. (2019) and Duong (2019).

3.2 Pressure Measurement Method

Five pressure sensors were used to measure the wave impact load applied vertically on the lower deck (Fig. 6). A piezo-resistive type pressure gauge (Kistler 4043A2) that can measure both static and dynamic pressure at the same time was used as the pressure sensor, which was installed at five points in the center of the deck, spaced at equal intervals. The sampling rate of the pressure sensor was set to 5 kHz through a pre-convergence test for the impact load. Post-processing was performed using a finite impulse response (FIR) low-pass filter to remove noise from the measured pressure signal. The cutoff frequency and filter order of the FIR filter were 150 Hz and 91st order, respectively, using the method proposed by Lee et al. (2020).

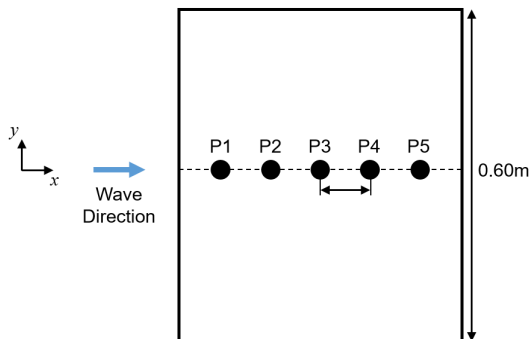


Fig. 6 Location of pressure sensor installations

3.3 PIV Measurement Setup and Method

In this study, the PIV technique was applied for the measurement of the instantaneous velocity field around the structure when the wave-in-

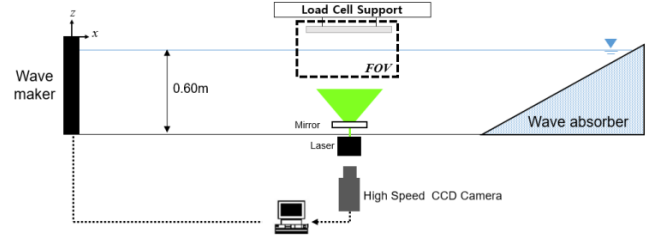


Fig. 7 Experimental setup for PIV measurement

deck load was generated, as shown in Fig. 7. The particles used for PIV measurement had a neutral buoyancy of 57 μm in diameter and a specific gravity of 1.02. A continuous laser [maximum 8 W, wavelength (λ) 532 nm] was used as a light source for the reflection of the particles.

In terms of the PIV image, a high-speed charge-coupled device (CCD) camera (Redlake Y5) with a resolution of 2352×1728 pixels and a 105-mm optical lens (Nikon, f# 2.8) were used to acquire 500 images per second ($\delta t = 500$ Hz) for a field of 0.44×0.32 m².

Adaptive cross-correlation (Theunissen et al., 2007, Eq. (8)) was used to increase the calculation accuracy by changing the size of the interrogation area to calculate the particle velocity for the measured image. The interrogation area was set to decrease from 256×256 pixels to 64×64 pixels, and the interval between the finally calculated velocity vectors was 5.95 mm by applying 50% overlap.

$$C(\Delta x, \Delta y) = \frac{1}{MN} \sum_{i=0}^{M-1} \sum_{j=0}^{N-1} f(m, n) g(m + \Delta x, n + \Delta y) \quad (8)$$

where C denotes the cross-correlation function, M and N denote the number of pixels in the x - and y -direction interrogation area, i and j denote the target image coordinates, and f and g denote the particle distribution of the continuous image.

The false vector in the velocity field was removed and post-processed through a median test (Westerweel, 1994), as expressed in Eq. (9) below.

$$|U_{2D}(\text{median}) - U_{2D}(i, j)| < \epsilon_{\text{thresh}} \quad (9)$$

where $U_{2D}(n)$ denotes the surrounding vector, $U_{2D}(i, j)$ denotes the test vector, and ϵ_{thresh} denotes the limit value used for the test, which was set to 1.1 in this study.

The measurement error of the PIV measurement method is the sum of the bias error and the random error, which is expressed as a function of d_r/d_{pix} by dividing the particle diameter (d_r) in the image by the pixel interval (d_{pix}) (Prasad et al., 1992). The term d_r can be calculated as follows:

$$d_r = \sqrt{(M d_p)^2 + d_{diff}^2} \quad (10)$$

where M denotes the ratio of the distance between the image and the

lens, and the distance between the lens and the field of view; d_p denotes the actual diameter of the particle; and d_{diff} denotes the diameter of the particle observed in the image by laser diffraction (Hecht and Zajac, 1974), which is derived from Eq. (11).

$$d_{diff} = 2.44f(M+1)\lambda \quad (11)$$

The term d_p/d_{pix} for the PIV measurement area used in this study was calculated to be approximately 0.09, and the corresponding measurement error was approximately 0.06 pixels (Raffel et al., 1998). In other words, it has a measurement error of approximately 2.55% of the local instantaneous maximum velocity (about 0.3 m/s) of the fluid measured through this PIV method.

4. Experimental Results

4.1 Comparison of Pressure Estimation Results According to Time Interval

The pressure estimation method using PIV proposed in this study may differ in accuracy and error depending on the time interval ($\Delta t = 2n\delta t$) between velocity fields used in the acceleration calculation. Therefore, the time interval selection for the pressure calculation should precede the pressure estimation for increased accuracy.

The pressure estimation results and the measurement results through the pressure sensor in P1 for the wave-in-deck load phenomenon according to the time interval change ($2\delta t$, $10\delta t$, and $20\delta t$) between the velocity fields for the acceleration calculation is shown in the time series in Fig. 8. The time (x -axis) was nondimensionalized to period of the zero down-crossing (T_{zu}) of the free surface of the wave, and the pressure (y -axis) was nondimensionalized to ρgH , as shown in Fig. 8. The red dots are the pressure estimation results based on the PIV measurement velocity field, and the black solid line is the pressure measurement results measured by the pressure sensor in the model experiment. The pressure estimation results vary greatly depending on the change in δt . When δt is relatively small (Fig. 8(a), $\Delta t = 2\delta t$), a result close to the peak value of the shock pressure can be measured that rises momentarily when the wave hits the structure, but the estimated pressure results after the peak pressure fluctuate significantly. Conversely, when δt is relatively large (Fig. 8(c), $\Delta t = 20\delta t$), the estimated pressure generally matches well with the pressure measured through the pressure sensor, but shows a significant difference in the maximum value of the pressure. In other words, it was found that the accuracy of the velocity field-based pressure estimation method measured through PIV decreased as the time interval between velocity fields for the acceleration calculation became longer or shorter. This is believed to be due to the phenomenon that the accuracy error increases when the time interval between the velocity fields is short, and the truncation error increases as the time interval increases when calculating the acceleration using the velocity field (van Oudheusden, 2013).

The normalized root-mean-square deviation (NRMSD) of the

measured pressure according to the change in time interval and the PIV-based estimated pressure were compared to determine the quantitative accuracy of the time interval between the velocity fields of the PIV-based pressure estimation method. NRMSD is calculated as follows:

$$NRMSD = \frac{\sqrt{\frac{1}{n} \sum_{i=1}^n (p_{m,i} - p_{c,i})^2}}{|p_{m,max} - p_{m,min}|} \quad (12)$$

where p_m denotes the pressure measured through the pressure sensor,

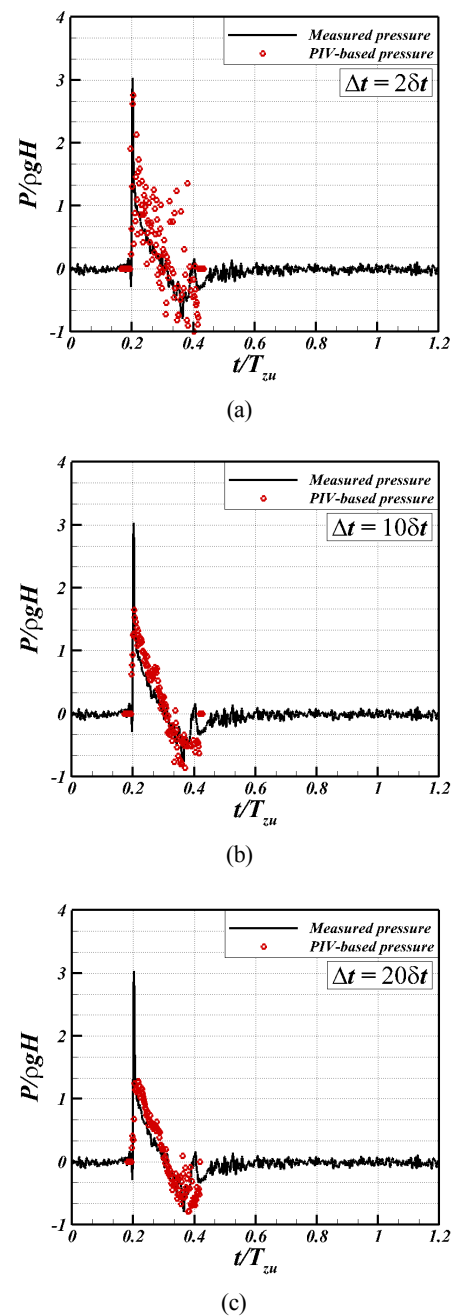


Fig. 8 Comparison of estimated pressures and measured pressures at P1 with various time steps ((a) $\Delta t = 2\delta t$, (b) $\Delta t = 10\delta t$, (c) $\Delta t = 20\delta t$)

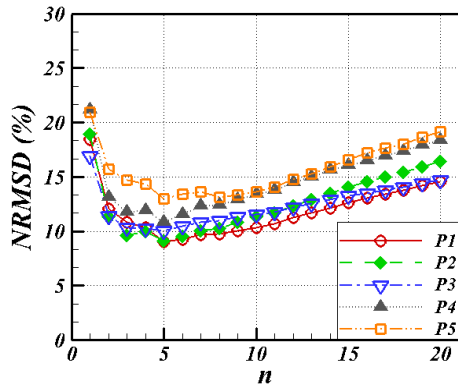


Fig. 9 NRMSD with different number of images between two velocity fields for calculation of acceleration (n)

p_e denotes the estimated pressure using the PIV measurement results, and i denotes the discretized time.

The changes in NRMSD according to the number of images (n) between the velocity fields set for the acceleration calculation at each of the five pressure sensor installation positions are compared, as shown in Fig. 9. The NRMSD had the lowest value for $n = 5$ at all pressure sensor installation positions. This means that when the time interval between the velocity fields for acceleration calculation is $10\delta t$, the result of the estimated pressure based on the PIV velocity field best matches the pressure measured by the pressure sensor. Based on this result, it was found that the time interval between the velocity fields of the PIV-based pressure estimation method for the wave-in-deck load showed the smallest difference from the pressure measurement results

for $\Delta t = 10\delta t$. The NRMSD results proposed in this study are expected to show different results depending on the flow or pressure characteristics of each phenomenon to be estimated. In addition, it is determined that an appropriate time interval needs to be selected considering the characteristics of each phenomenon.

4.2 Pressure Field Estimation Results for the Case of Wave Impact Load

Fig. 10 shows a comparison of the pressure obtained using the instantaneous velocity field based pressure estimation method measured through PIV and the measurement results through the pressure sensor for the wave-in-deck load when the time interval between the velocity fields is $10\delta t$ ($n = 5$). Overall, the instantaneous velocity field based pressure estimation method applied in this study produced results that are in good agreement with the measurement results through the sensors for the local pressure caused by the wave-in-deck load. The estimated results were close to the peak values of the impact pressure that increased for the short moment of the wave-in-deck load at each pressure measurement location. Afterward, the negative pressure generated due to the gradually decreased pressure as the wave moved away showed good agreement overall. However, the pressure was relatively low for the pressure measured by the sensors for the peak impact pressure that increased rapidly; in particular, the difference was greater for P1 and P2 located at the leading edge of the deck. This seems to be attributable to the truncation error that occurred due to the relatively large time interval between the instantaneous velocity fields measured by PIV compared to the rise

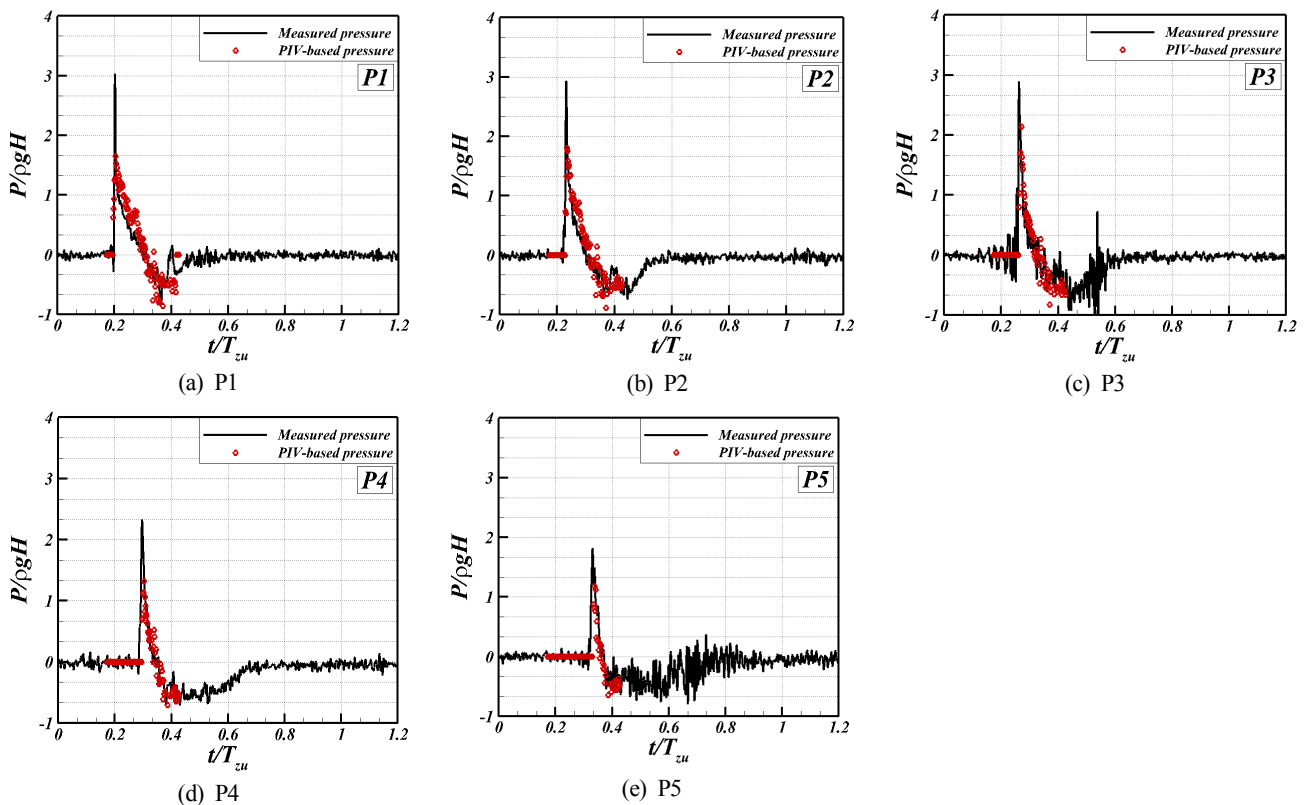


Fig. 10 Time history of measured and estimated pressure

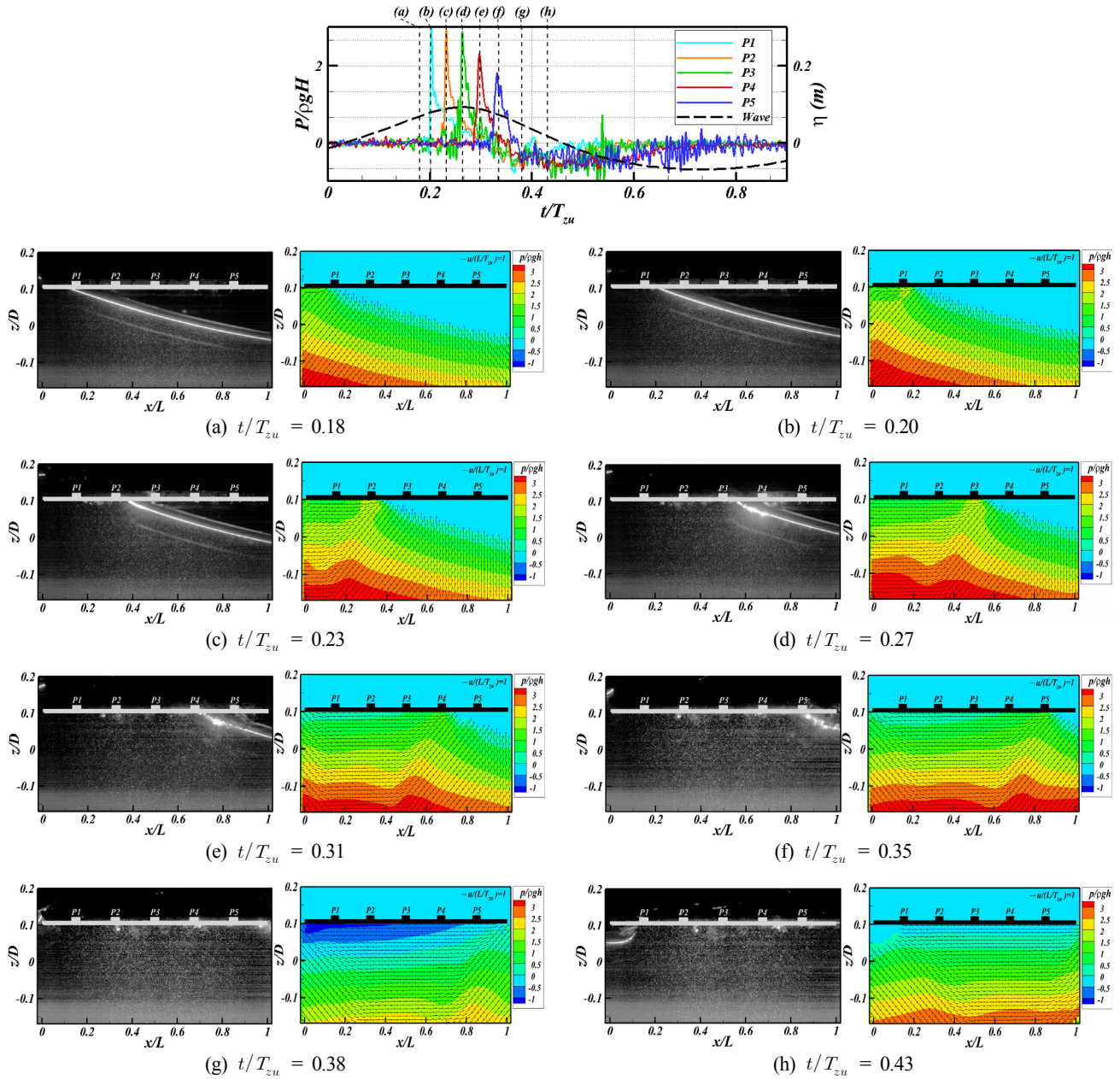


Fig. 11 Pressure and velocity fields under the deck at various wave phases

time of the pressure when the impact phenomenon occurred. In addition, it is believed to have some differences, since the impact load estimation method used in this study did not consider the viscosity of the fluid based on the Euler equation.

The pressure field under the deck estimated using the PIV measurement image and the velocity field of each occurrence of the wave-in-deck load are shown in Fig. 11. Each image of the contact at the leading edge (Fig. 11(a)), the moment the maximum pressure is measured at the pressure gauge measurement position (P1–P5) (Figs. 11(b)–11(f)), the emergence of the leading edge (Fig. 11(g)), and the moment the flow moves away from P1 according to the process of generating the wave-in-deck load are shown in Fig. 11. The x -axis is the length of the structure (L), the y -axis is the depth of water ($D = 0.60$ m), the velocity is L/T_{zu} , and the pressure is $\rho g H$

nondimensionalized, as shown in Fig. 11.

At the contact at the leading edge (Fig. 11(a)), the pressure due to the waves begins to be applied to the structure, and this pressure increases gradually as the waves cross under the deck and propagate to the trailing edge of the deck. At the moment when the local pressure at the position of each pressure sensor peaks (Figs. 11(b)–11(f)), it is observed that the pressure of the surrounding fluid increases significantly at the same time. It was also found that the flow velocity around the contact area accelerated in the horizontal direction. It is believed that the free surface was deformed by the structure, momentarily impacting the structure, and a jet phenomenon, in which fluid is accelerated, occurred at the same time. In addition, it is found that the fluid pressure is smaller at the emergence of a leading edge (Figs. 11(e)–11(f)) than the pressure at the moment the wave first

impacts the leading edge of the structure (Figs. 11(b)-11(d)) as the wave energy is transmitted to the structure as an impact when the wave crosses along the lower deck. At the emergence of the leading edge (Fig. 11(g)), it is seen that a negative pressure lower than atmospheric pressure occurs from the leading edge of the structure above the free surface. This continues until the moment P1 is exposed to the atmosphere (Fig. 11(h)), and then the pressure at the bottom of the lead becomes equal to the atmospheric pressure as the wave moves away from the structure.

5. Conclusion

In this study, the pressure measured through pressure sensors, and the velocity field-based pressure estimation results were compared and analyzed. This was accomplished by applying a method for estimating fluid pressure using the instantaneous velocity field measured through PIV based on Euler's equation to the wave impact load test under the deck conducted in a two-dimensional wave tank.

It was found that the pressure estimation results of the velocity field based pressure estimation method applied in this study were significantly different according to the time interval (Δt) between velocity fields for the acceleration calculation. When the time interval was short, the peak value of the instantaneously high impact pressure caused by the impact load was estimated well, but the overall pressure fluctuated due to an increase in the accuracy error. Moreover, the overall pressure was estimated well as the time interval increased, but the truncation error increased, resulting in a difference in the maximum value of the instantaneous impact pressure.

In order to set an appropriate time interval to improve the accuracy of the velocity field based pressure estimation method, this study utilized the NRMSD to examine the quantitative error of the pressure estimation method. As a result, it was found that the wave-in-deck load had the lowest error at 10. However, the NRMSD must vary according to the flow and pressure characteristics of each phenomenon to be estimated, and an appropriate time interval for each phenomenon must be estimated using the NRMSD.

In addition, it was found that the size of the maximum value of the impact pressure of the pressure estimation method based on the velocity field was slightly different compared to the pressure results measured by the pressure sensors. This seems to be attributable to the truncation error due to the relatively large time interval between the instantaneous velocity fields measured by PIV compared to the rise time of the impact pressure, which is believed to be the limitation of this method based on the Euler equation.

The pressure field around the structure during the wave-in-deck load was estimated and presented using the instantaneous velocity field. Through the pressure field, the hydrodynamic characteristics of the surrounding fluid were analyzed when an impact phenomenon caused by waves occurred, and the mechanism of occurrence of impact pressure and negative pressure was found through the relation with the velocity field.

The pressure field estimation method based on the instantaneous velocity field measured by using the PIV method can not only estimate the impact pressure without a pressure sensor, but it also has the advantage of being able to measure the pressure field without disturbing the flow in a wider range than conventional pressure sensors, which only measure local pressure. It is believed that this approach can be widely used not only for the fluid dynamic characteristics of complex fluid phenomena, such as impact phenomena, but also for the analysis of pressure generation mechanisms.

Acknowledgement

This work was supported by a 2-Year Research Grant of Pusan National University.

Conflict of interest

No potential conflict of interest relevant to this article was reported.

References

- Abdussamie, N., Thomas, G., Amin, W., & Ojeda, R. (2014). Wave-in-Deck Forces on Fixed Horizontal Decks of Offshore Platforms. *Proceedings of the 33rd International Conference on Ocean, Offshore and Arctic Engineering*, San Francisco, USA, 1-11. <https://doi.org/10.1115/OMAE2014-23629>
- Ariyaratne, K., Chang, K.A., & Mercier, R. (2012). Green Water Impact Pressure on a Three-dimensional Model Structure. *Experiments in Fluids*, 53(6), 1879-1894. <https://doi.org/10.1007/s00348-012-1399-9>
- Baur T., & Kongeter J. (1999). PIV with High Temporal Resolution for the Determination of Local Pressure Reductions from Coherent Turbulent Phenomena. *Proceedings of 3rd International Workshop on Particle Image Velocimetry*, Santa Barbara, USA, 101-106.
- Buchner, B., & Voogt, A. (2000). The Effect of Bow Flare Angle on FPSO Green Water Loading. *Proceedings of ETCE/OMAE2000 Joint Conference, Energy for the New Millennium*, 14-17 February 2000.
- Chanson, H. (1997). *Air Bubble Entrainment in Free-surface Turbulent Shear Flows*. Academic Press, Inc. <https://doi.org/10.1016/B978-0-12-168110-4.X5000-0>
- De Gregorio, F. (2006). Aerodynamic Performance Degradation Induced by Ice Accretion. PIV Technique Assessment in Icing wind Tunnel. *Proceedings of 13th International Symposium Applications of Laser Techniques to Fluid Mechanics*, Lisbon, Portugal.
- Duong, T.T. (2019). *Experimental Study of Wave Impact under Deck due to Focused Waves* (Thesis for Master degree). Pusan National University, Busan, Korea.
- Duong, T.T., Jung, K.H., Lee, G.N., Kim, D.S., Suh, S.B., & Kim, M.S. (2019). *Experimental Study on Wave Impact under Deck due to*

- Regular Waves. *Journal of Coastal Research*, 91(SI), 81-85. <https://doi.org/10.2112/SI91-017.1>
- Ersdal, G., & Kvitrud, A. (2000). Green Water Incidents on Norwegian Production Ships. *Proceedings of the 10th International Conference on Offshore and Polar Engineering (ISOPE 2000)*, Seattle, USA, 1, 211-218.
- Faulkner, D.J. (2001). Survival Design of Cargo Hatch Structures. *Proceedings of RINA Conference Design and Operation for Abnormal Conditions II*, London, United Kingdom.
- Faltinsen, O.M., Landrini, M., & Greco, M. (2004). Slamming in Marine Application. *Journal of Engineering Mathematics*, 48, 187-217. <https://doi.org/10.1023/B:engi.0000018188.68304.ae>
- Faltinsen, O.M. (2005). *Hydrodynamics of High-speed Marine Vehicles*. Cambridge University Press, New York.
- Hecht, E., & Zajac, A. (1974). *Optics (Addison-Wesley Series in Physics)*. Addison-Wesley Pub. Co.
- Jakobsen, M.L., Dewhurst T.P., & Greated C.A. (1997). Particle Image Velocimetry for Predictions of Acceleration Fields and Forces within Fluid Flows. *Measurement Science and Technology*, 8(12), 1502-1516.
- Kaiser, M.J., Yu, Y., & Jablonowski, C.J. (2009). Modeling Lost Production from Destroyed Platforms in the 2004-2005 Gulf of Mexico Hurricane Seasons. *Energy*, 34(9), 1156-1171. <https://doi.org/10.1016/j.energy.2009.04.032>
- Kim, M.G., Jung, K.H., Park, S.B., Suh, S.B., Park, I.R., Kim, J., & Kim, K.S. (2019). Experimental Study on Viscous Effect in Roll and Heave Motions of a Rectangular Structure. *Ocean Engineering*, 171, 250-258. <https://doi.org/10.1016/j.oceaneng.2018.11.004>
- Kim, M.G., Jung, K.H., Park, S.B., Lee, G.N., Duong, T.T., Suh, S.B., & Park, I.R. (2020). Experimental and Numerical Estimation on Roll Damping and Pressure on a 2-D Rectangular Structure in Free Roll Decay Test. *Ocean Engineering*, 196(15), 106801. <https://doi.org/10.1016/j.oceaneng.2019.106801>
- Lee, G.N., Jung, K.H., Chae, Y.J., Park, I.R., Malenica, S., & Chung, Y.S. (2016). Experimental and Numerical Study of the Behaviour and Flow Kinematics of the Formation of Green Water on a Rectangular Structure. *Brodogradnja : Teorija i praksa brodogradnje i pomorske tehnike*, 67(3), 133-145. <https://doi.org/10.21278/brod67308>
- Lee, G.N., Jung, K.H., Malenica, S., Chung, Y.S., Suh, S.B., Kim, M.S., & Choi, Y.H. (2020). Experimental Study on Flow Kinematics and Pressure Distribution of Green Water on a Rectangular Structure. *Ocean Engineering*, 195, 106649. <https://doi.org/10.1016/j.oceaneng.2019.106649>
- Lim, H.J., Park, S.H., & Rhee, S.H. (2012). Experiments and Numerical Validation for FPSO Bow Water Shipping. *Journal of the Society of Naval Architects of Korea*, 49(1), 6-13. <https://doi.org/10.3744/SNAK.2012.49.1.6>
- Myrhaug, D. & Kjeldsen, S.P. (1986). Steepness and Asymmetry of Extreme Waves and the Highest Waves in Deep Water. *Ocean Engineering*, 13(6), 549-568. [https://doi.org/10.1016/0029-8018\(86\)90039-9](https://doi.org/10.1016/0029-8018(86)90039-9)
- Nilä, A., Vanlanduit, S., Vepa, S., & Van Paepegem, W. (2013). A PIV-based Method for Estimating Slamming Loads during Water Entry of Rigid Bodies. *Measurement Science and Technology*, 23(4), 045303.
- Oh, S.J., & Jo, D.H. (2015). An Experimental Study on the Slamming Impact around Wedged type Structure in Accordance with the Weight and Height of the Change. *Journal of Navigation and Port Research*, 39(1), 77-82. <https://doi.org/10.5394/KINPR.2015.39.1.77>
- Panciroli, R., & Porfiri, M. (2013). Evaluation of the Pressure Field on a Rigid Body Entering a Quiescent Fluid Through Particle Image Velocimetry. *Experiments in Fluids*, 54, 1630. <https://doi.org/10.1007/s00348-013-1630-3>
- Prasad, A.K., Adrian, R.J., Landreth, C.C., & Offutt, P.W. (1992). Effect of Resolution on the Speed and Accuracy of Particle Image Velocimetry Interrogations. *Experiments in Fluids*, 13, 105-116. <https://doi.org/10.1007/BF00218156>
- Raffel, M., Willert, C.E., & Kompenhans, J. (1998). *Mathematical Background of Statistical PIV Evaluation*. Particle Image Velocimetry. Experimental Fluid Mechanics, Springer, Berlin, Heidelberg https://doi.org/10.1007/978-3-662-03637-2_3
- Rouse, H. (1959). *Advanced Mechanics of Fluids*. New York: John Wiley,
- Shams, A., Zhao, S., & Porfiri, M. (2017). Hydroelastic Slamming of Flexible Wedges: Modeling and Experiments from Water Entry to Exit. *Physics of Fluids*, 29(3), 037107. <https://doi.org/10.1063/1.4978631>
- Spedding, G.R., & Hedenström, A. (2009). PIV-based Investigations of Animal Flight. *Experiments in Fluids*, 46, 749-763. <https://doi.org/10.1007/s00348-008-0597-y>
- Theunissen, R., Scarano, F., & Riethmuller, M.L. (2007). An Adaptive Sapling and Windowing Interrogation Method in PIV. *Measurement Science and Technology*, 18(1), 275-287.
- Van Oudheusden, B.W. (2013). PIV-based Pressure Measurement. *Measurement Science and Technology*, 24(3), 032001.
- Westerweel, J. (1994). Efficient Detection of Spurious Vectors in Particle Image Velocimetry Data. *Experiments in Fluids*, 16, 236-247. <https://doi.org/10.1007/BF00206543>
- Xie, H., Ren, H., Deng, B., & Tang, H. (2018). Experimental Drop Test Investigation into Slamming Loads on a Truncated 3D Bow Flare Model. *Ocean Engineering*, 169, 567-585. <https://doi.org/10.1016/j.oceaneng.2018.10.003>

Author ORCIDs

Author name	ORCID
Lee, Gang Nam	0000-0002-7816-9506
Duong, Tien Trung	0000-0002-6686-6208
Jung, Kwang Hyo	0000-0002-8229-6655
Suh, Sung Bu	0000-0001-8094-4762
Lee, Jae Yong	0000-0002-4469-7765

Energetics of In-plane Motions in Coupled Plate Structures

Young-Ho Park¹ and Chang Hyun Park²

¹Professor, Department of Naval Architecture and Marine Engineering, Changwon National University, Changwon, Korea

²Hull Inspector & Repair Team Member, Submarine Force Command, R.O.K Navy, Changwon, Korea

KEY WORDS: Energy flow analysis, Kirchhoff plate, In-plane motion, High frequency, Mindlin plate, Statistical energy analysis

ABSTRACT: Energy flow analysis (EFA) has been used to predict the frequency-averaged vibrational responses of built-up structures at high frequencies. In this study, the frequency-averaged exact energetics of the in-plane motions of the plate were derived for the first time by solving coupled partial differential equations. To verify the EFA for the in-plane waves of the plate, numerical analyses were performed on various coupled plate structures. The prediction results of the EFA for coupled plate structures were shown to be accurate approximations of the frequency-averaged exact energetics, which were obtained from classical displacement solutions. The accuracy of the results predicted via the EFA increased with an increase in the modal density, regardless of various structural parameters. Therefore, EFA is an effective technique for predicting the frequency-averaged vibrational responses of built-up structures in the high frequency range.

Nomenclature

$\langle e \rangle$	Energy density (J/m ²)
c_g	Group velocity (m/s)
ω	Angular frequency (rad/s)
k	Wave number (rad/m)
q	Intensity (J/m/s)

1. Introduction

The demand for ecofriendly and lightweight systems has been gradually increasing in the transport machinery industries, e.g., shipbuilding, automobiles, aviation, and railroads, with the growing interest in environmental issues caused by global warming and the development of industrial technology. These industrial changes have increased the proportion of vibration noise in the high frequency range, exacerbating the vibration-noise issue of transportation machinery systems. Therefore, developing technology for predicting the vibration noise in the corresponding frequency range is becoming important for ensuring competitiveness in the transport machinery industries. Typically, deterministic approaches based on displacement methods, such as the conventional finite element method and boundary element method, have been utilized for vibration noise prediction method in the low frequency range. However, because these methods lack efficiency

and reliability, statistical approaches such as statistical energy analysis (SEA) and energy flow analysis (EFA) are generally applied in the high frequency range. Numerical methods such as the finite element technique can be applied in EFA because it has an energy governing equation in the form of a differential equation, in contrast to SEA. Thus, EFA has recently emerged as a new alternative to high-frequency range vibration noise analysis, because the modeling efficiency is high and a detailed design review of the design parameters can be performed. In the early days after EFA was proposed by Belov et al. (1977), an energy flow model for out-of-plane motion was developed, which was mainly based on various simple structural element theories, e.g., those of the membrane, Euler beam, and Kirchhoff plate. Recently, however, Park and Hong (2006a), Park and Hong (2006b), and Park and Hong (2008) developed an energy flow model of the Timoshenko beam and Mindlin plate that reflects the shear-deformation effect and rotatory-inertia effect to increase the accuracy of the previously developed EFA model in the high frequency range, thereby expanding the analysis area. When beams or plates are coupled at arbitrary angles in actual structures, such as ships and offshore structures, the out-of-plane motion and in-plane motion are coupled, and the modal density of the in-plane motion increases with the frequency, increasing the importance of the model for in-plane motion in EFA. Therefore, Park et al. (2001) developed an energy flow model for in-plane motion for the EFA

Received 2 November 2020, revised 22 November 2020, accepted 24 November 2020

Corresponding author Young-Ho Park: +82-55-213-3684, parkyh@changwon.ac.kr

© 2020, The Korean Society of Ocean Engineers

This is an open access article distributed under the terms of the creative commons attribution non-commercial license (<http://creativecommons.org/licenses/by-nc/4.0>) which permits unrestricted non-commercial use, distribution, and reproduction in any medium, provided the original work is properly cited.

analysis of a coupled plate structure in a high frequency range. However, a study on the effectiveness of the energy flow model according to the frequency is needed, because no systematic comparison with the exact solution for the in-plane motion of the plate was performed in the study. In the present study, an exact solution of the in-plane motion for the plate coupled at an arbitrary angle was newly derived, and the effectiveness of the energy flow model for the in-plane motion of the plate was examined through comparison with the analysis results of the energy flow model.

2. Energy Flow Model for In-plane Motion of Plate

The equation of motion for the in-plane wave of a damped plate without a load can be expressed as follows (Dym and Shames, 2013):

$$\frac{\partial^2 u}{\partial x^2} + \frac{(1-\nu)}{2} \frac{\partial^2 u}{\partial y^2} + \frac{(1+\nu)}{2} \frac{\partial^2 v}{\partial x \partial y} = \frac{(1-\nu^2)\rho}{E_c} \frac{\partial^2 u}{\partial t^2} \quad (1)$$

$$\frac{\partial^2 v}{\partial y^2} + \frac{(1-\nu)}{2} \frac{\partial^2 v}{\partial x^2} + \frac{(1+\nu)}{2} \frac{\partial^2 u}{\partial x \partial y} = \frac{(1-\nu^2)\rho}{E_c} \frac{\partial^2 v}{\partial t^2} \quad (2)$$

where u and v represent the in-plane displacements of the plate in the x and y directions, respectively, $E_c = E(1+j\eta)$ represents the complex elastic modulus, η represents the structural damping loss factor, ν represents the Poisson's ratio, and ρ represents the material density of the plate. The energy-flow model for the in-plane motion of the foregoing equation of motion can be derived by separating it into an in-plane longitudinal wave and an in-plane shear wave, as follows (Park et al., 2001):

$$-\frac{c_{g,l}^2}{\eta\omega} \left(\frac{\partial^2}{\partial x^2} + \frac{\partial^2}{\partial x^2} \right) \langle e_l \rangle + \eta\omega \langle e_l \rangle = \Pi_{in,l} \quad (3)$$

$$-\frac{c_{g,s}^2}{\eta\omega} \left(\frac{\partial^2}{\partial x^2} + \frac{\partial^2}{\partial x^2} \right) \langle e_s \rangle + \eta\omega \langle e_s \rangle = \Pi_{in,s} \quad (4)$$

where $c_{g,l}$ and $c_{g,s}$ represent the group velocities of the in-plane longitudinal wave and in-plane shear wave of a thin plate, respectively; $\langle e_l \rangle$ and $\langle e_s \rangle$ represent the energy densities of the in-plane longitudinal wave and in-plane shear wave averaged in space and time respectively; and $\Pi_{in,l}$ and $\Pi_{in,s}$ represent the vibrational input power for the in-plane longitudinal wave and in-plane shear wave, respectively.

3. Energy Flow Model for Out-of-plane Motion of Plate

The equation of motion for the out-of-plane motion of a damped Kirchhoff plate without a load can be expressed as follows (Dym and Shames, 2013):

$$D_c \left(\frac{\partial^4 w}{\partial x^4} + 2 \frac{\partial^4 w}{\partial x^2 \partial y^2} + \frac{\partial^4 w}{\partial y^4} \right) + \rho h \frac{\partial^2 w}{\partial t^2} = 0 \quad (5)$$

where $D_c = D(1+j\eta)$ represents the complex flexural rigidity. The energy flow model for the flexural wave of the Kirchhoff plate derived from the foregoing equation of motion can be expressed as follows (Bouthier and Bernhard, 1995):

$$-\frac{c_{g,f}^2}{\eta\omega} \left(\frac{\partial^2}{\partial x^2} + \frac{\partial^2}{\partial x^2} \right) \langle e_f \rangle + \eta\omega \langle e_f \rangle = \Pi_{in,f} \quad (6)$$

where $c_{g,f}$ represents the group velocity of the out-of-plane flexural wave of a thin plate, $\langle e_f \rangle$ represents the energy density of the out-of-plane flexural wave averaged in space and time and $\Pi_{in,f}$ represents the vibrational input power of the out-of-plane flexural wave.

4. Analysis of Vibration Energy of Plate Coupled at Arbitrary Angle

The plate model coupled at an arbitrary angle was considered for an analytical study of the energy flow model for the in-plane wave of the plate.

4.1 Exact Solution of Coupled Plate Structures

In the exact solution of a coupled plate for which all the outer boundaries are simply supported, the displacement can be calculated in the form of a Levy series that satisfies the y -direction boundary condition equations, i.e., Eqs. (7)–(10). The displacement in the x - and y -directions in the i^{th} region can be expressed using Eqs. (11)–(13).

$$u_1(0,y) = u_3(L_x,y) = 0 \quad (7)$$

$$\frac{\partial v_1(0,y)}{\partial x} = \frac{\partial v_3(L_x,y)}{\partial x} = 0 \quad (8)$$

$$w_1(0,y) = w_3(L_x,y) = 0 \quad (9)$$

$$\frac{\partial^2 w_1(0,y)}{\partial x^2} = \frac{\partial^2 w_3(L_x,y)}{\partial x^2} = 0 \quad (10)$$

$$u_i(x_i,y,t) = \left[\sum_{m=1}^{\infty} U_{m,i}(x_i) \sin k_m y \right] e^{j\omega t} \quad (11)$$

$$v_i(x_i,y,t) = \left[\sum_{m=1}^{\infty} V_{m,i}(x_i) \cos k_m y \right] e^{j\omega t} \quad (12)$$

$$w_i(x_i,y,t) = \left[\sum_{m=1}^{\infty} W_{m,i}(x_i) \sin k_m y \right] e^{j\omega t} \quad (13)$$

Here, $k_m = m\pi/L_y$ and $U_{m,i}(x_i)$, $V_{m,i}(x_i)$, and $W_{m,i}(x_i)$ represent the

wave solutions in the x_i direction that satisfy the equation of motion. The following equation can be obtained by substituting the out-of-plane displacement expressed by Eq. (13) into Eq.(5), i.e., the equation of motion (Park et al., 2001).

$$\frac{d^4 W_{m,i}(x_i)}{dx_i^4} - 2k_m^2 \frac{d^2 W_{m,i}(x_i)}{dx_i^2} + \frac{d^4 W_{m,i}(x_i)}{dy^4} + (k_m^4 - k_f^4) W_{m,i}(x_i) = 0 \quad (14)$$

Here, $k_{f,i} = \sqrt[4]{(\rho_i h_i \omega^2 / D_{e,i})}$ represents the flexural wavenumber of the plate in the i^{th} plate section, and ρ_i and h_i represent the density and thickness of the plate, respectively. Because Eq. (14) is a fourth-order homogeneous ordinary differential equation, the wave solution of the displacement w in the x_i direction can be obtained as follows:

$$W_{m,i}(x_i, t) = [A_{f1}^+ \exp(-\alpha_{m,i} x_i) + A_{f1}^- \exp(\alpha_{m,i} x_i) + B_{f1}^+ \exp(-\beta_{m,i} x_i) + B_{f1}^- \exp(\beta_{m,i} x_i)] \times e^{j\omega t} \quad (15)$$

where $\alpha_{m,i}^2 = k_m^2 + k_{f,i}^2$ and $\beta_{m,i}^2 = k_m^2 - k_{f,i}^2$. Although such an exact solution of the flexural wave, which is an out-of-plane displacement, was used to validate the energy flow model for the flexural wave of a plate, the exact solution of the in-plane displacement and the energy flow solution were not directly compared in previous studies (Park et al., 2001). Park and Hong (2008) derived an exact out-of-plane motion solution from the equation of motion implemented as the simultaneous differential equations for the Mindlin plate. The matrix equation can be obtained as follows by substituting Eqs. (11)–(12) into the simultaneous differential Eqs. (1)–(2) to obtain the wave solution in the x_i direction of the in-plane motion of a plate in a similar manner (Park, 2018).

$$\frac{\partial}{\partial x_i} \{M_{m,i}\} = [N_{m,i}] \{M_{m,i}\} \quad (16)$$

Here, the matrices $\{M_{m,i}\}$ and $[N_{m,i}]$ are given by Eqs. (17) and (18), respectively.

$$\{M_{m,i}\} = \left\{ U_{m,i} \quad \frac{\partial U_{m,i}}{\partial x_i} \quad V_{m,i} \quad \frac{\partial V_{m,i}}{\partial x_i} \right\}^T \quad (17)$$

$$[N_{m,i}(\omega)] = \begin{bmatrix} 0 & 1 & 0 & 0 & 0 \\ \frac{(1-\nu_i)}{2} k_m + \frac{(1-\nu_i^2)}{E_{e,i}} \rho_i \omega^2 & 0 & 0 & 0 & -\frac{(1+\nu_i)}{2} k_m \\ 0 & 0 & 0 & 0 & 1 \\ 0 & \frac{(1+\nu_i)}{2} k_m & \frac{(1-\nu_i)}{2} k_m & -\frac{(1-\nu_i^2)}{E_{e,i}} \rho_i \omega^2 & 0 \end{bmatrix} \quad (18)$$

The general solution of the above differential-equation system can be obtained as follows:

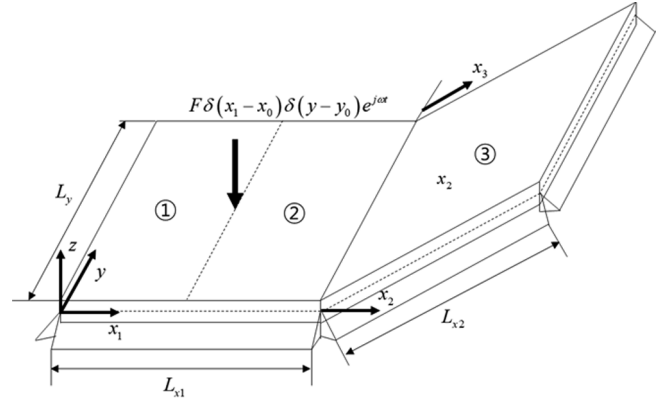


Fig. 1 Simply supported plates coupled at an arbitrary angle

$$\{M_{m,i}\} = \sum_{n=1}^4 C_{m,i,n} \vec{H}_{m,i,n} e^{\lambda_{m,i,n} x} \quad (19)$$

where $C_{m,i,n}$ is the complex coefficient of the n^{th} -order mode, and $\vec{H}_{m,i,n}$ and $\lambda_{m,i,n}$ represent the n^{th} eigenvector and eigenvalue of matrices $[N_{m,i}(\omega)]$, respectively. The number of unknowns for each plate boundary of the plate structure in Fig. 1 is 4 flexural waves and 4 in-plane waves, requiring a total of 24 boundary conditions. The boundary conditions at $x_1 = 0$ are expressed as follows.

$$u_1(0, y) = 0 \quad (20)$$

$$\frac{\partial v_1(0, y)}{\partial x_1} = 0 \quad (21)$$

$$w_1(0, y) = 0 \quad (22)$$

$$\frac{\partial^2 w_1(0, y)}{\partial x_1^2} = 0 \quad (23)$$

The boundary conditions at the excitation-point locations of $x_1 = x_0$ and $x_2 = -L_{x1} + x_0$ are expressed as follows.

$$u_1(x_0, y) = u_2(x_0 - L_{x1}, y) \quad (24)$$

$$v_1(x_0, y) = v_2(x_0 - L_{x1}, y) \quad (25)$$

$$w_1(x_0, y) = w_2(x_0 - L_{x1}, y) \quad (26)$$

$$\frac{\partial w_1(0, y)}{\partial x_1} = \frac{\partial w_2(x_0 - L_{x1}, y)}{\partial x_1} \quad (27)$$

$$N_{xx,1}(x_0, y) = N_{xx,2}(x_0 - L_{x1}, y) \quad (28)$$

$$N_{xy,1}(x_0, y) = N_{xy,2}(x_0 - L_{x1}, y) \quad (29)$$

$$V_{xz,1}(x_0, y) + F\delta(y-y_0) = V_{xz,2}(x_0 - L_{x1}, y) \quad (30)$$

$$M_{x_{x,1}}(x_0, y) = M_{x_{x,2}}(x_0 - L_{x1}, y) \quad (31)$$

Here,

$$N_{x_{x,i}} = \frac{E_{c,i} h_i}{(1-\nu_i^2)} \left(\frac{\partial u_i}{\partial x_i} + \nu_i \frac{\partial v_i}{\partial y_i} \right), N_{x_{y,i}} = \frac{E_{c,i} h_i}{(1-\nu_i)} \left(\frac{\partial u_i}{\partial y_i} + \frac{\partial v_i}{\partial x_i} \right),$$

$$V_{x_{z,i}} = -D_{c,i} \left\{ \frac{\partial^3 w_i}{\partial x_i^3} + (2-\nu_i) \frac{\partial^3 w_i}{\partial x_i \partial y_i^2} \right\} \circ | \nabla |.$$

The boundary conditions at $x_2 = x_3 = 0$, where the two plates are coupled at an arbitrary angle, are expressed as follows.

$$u_2(0, y) = -w_3(0, y) \sin \theta + u_3(0, y) \cos \theta \quad (32)$$

$$v_2(0, y) = v_3(0, y) \quad (33)$$

$$w_2(0, y) = w_3(0, y) \cos \theta + u_3(0, y) \sin \theta \quad (34)$$

$$N_{x_{x,2}}(0, y) = -V_{x_{z,3}}(0, y) \sin \theta + N_{x_{x,3}}(0, y) \cos \theta \quad (35)$$

$$N_{x_{y,2}}(0, y) = N_{x_{y,3}}(0, y) \quad (36)$$

$$V_{x_{z,2}}(0, y) = V_{x_{z,3}}(0, y) \cos \theta + N_{x_{x,3}}(0, y) \sin \theta \quad (37)$$

$$\frac{\partial w_2(0, y)}{\partial x_2} = \frac{\partial w_3(0, y)}{\partial x_3} \quad (38)$$

$$M_2^y(0, y) = M_3^y(0, y) \quad (39)$$

Lastly, the four boundary conditions at $x_3 = L_{x2}$ are expressed as follows (similar to the boundary conditions at $x_1 = 0$).

$$u_3(L_{x2}, y) = 0 \quad (40)$$

$$\frac{\partial v_3(L_{x2}, y)}{\partial x_3} = 0 \quad (41)$$

$$w_3(L_{x2}, y) = 0 \quad (42)$$

$$\frac{\partial^2 w_3(L_{x2}, y)}{\partial x_3^2} = 0 \quad (43)$$

If the displacement solution is obtained using the foregoing boundary conditions, the energy density and vibration intensity of the flexural wave and the in-plane wave of the plate can be obtained using the following equations:

$$\langle e_f \rangle_i = \frac{D_i}{4} \left\{ \left| \frac{\partial^2 w_i}{\partial x_i^2} \right|^2 + \left| \frac{\partial^2 w_i}{\partial y_i^2} \right|^2 + 2\nu_i \frac{\partial^2 w_i}{\partial x_i^2} \left(\frac{\partial^2 w_i}{\partial y_i^2} \right)^* \right. \\ \left. + 2(1-\nu_i) \frac{\partial^2 w_i}{\partial x_i \partial y_i} \left(\frac{\partial^2 w_i}{\partial x_i \partial y_i} \right)^* \right\} + \frac{\rho_i h_i}{4} \left| \frac{\partial w_i}{\partial t} \right|^2 \quad (44)$$

$$\langle q_{fx} \rangle_i = \frac{1}{2} Re \left\{ -Q_{x_{z,i}} \left(\frac{\partial w_i}{\partial t} \right)^* + M_{x,i} \left(\frac{\partial^2 w_i}{\partial x_i \partial t} \right)^* + M_{x_{y,i}} \left(\frac{\partial^2 w_i}{\partial y_i \partial t} \right)^* \right\} \quad (45)$$

$$\langle q_{fy} \rangle_i = \frac{1}{2} Re \left\{ -Q_{y_{z,i}} \left(\frac{\partial w_i}{\partial t} \right)^* + M_{y,i} \left(\frac{\partial^2 w_i}{\partial y_i \partial t} \right)^* + M_{y_{x,i}} \left(\frac{\partial^2 w_i}{\partial x_i \partial t} \right)^* \right\} \quad (46)$$

Here,

$$M_{x,i} = -D_{c,i} \left\{ \frac{\partial^2 w_i}{\partial x_i^2} + \nu_i \frac{\partial^2 w_i}{\partial y_i^2} \right\}, M_{y,i} = -D_{c,i} \left\{ \frac{\partial^2 w_i}{\partial y_i^2} + \nu_i \frac{\partial^2 w_i}{\partial x_i^2} \right\},$$

$$M_{x_{y,i}} = M_{y_{x,i}} = -D_{c,i} (1-\nu_i) \frac{\partial^2 w_i}{\partial x_i \partial y_i},$$

$$Q_{x_{z,i}} = -D_{c,i} \left\{ \frac{\partial^3 w_i}{\partial x_i^3} + \nu_i \frac{\partial^3 w_i}{\partial x_i \partial y_i^2} \right\}, Q_{y_{z,i}} = -D_{c,i} \left\{ \frac{\partial^3 w_i}{\partial y_i^3} + \nu_i \frac{\partial^3 w_i}{\partial x_i^2 \partial y_i} \right\}$$

$$\langle e_I \rangle_i = \frac{1}{4} Re \left[G_{c,i} h_i \left| \frac{\partial u_i}{\partial y} + \frac{\partial v_i}{\partial x_i} \right|^2 + K_{c,i} \left(\frac{\partial u_i}{\partial x_i} + \nu_i \frac{\partial v_i}{\partial y} \right) \left(\frac{\partial u_i}{\partial x_i} \right)^* \right. \\ \left. + K_{c,i} \left(\frac{\partial v_i}{\partial y} + \nu_i \frac{\partial u_i}{\partial x_i} \right) \left(\frac{\partial v_i}{\partial y} \right)^* + \rho_i h_i \left(\left| \frac{\partial u_i}{\partial t} \right|^2 + \left| \frac{\partial v_i}{\partial t} \right|^2 \right) \right] \quad (47)$$

$$\langle q_{Ix} \rangle_i = -\frac{1}{2} Re \left[G_{c,i} h_i \left(\frac{\partial u_i}{\partial y} + \frac{\partial v_i}{\partial x_i} \right) \left(\frac{\partial v_i}{\partial t} \right)^* + K_{c,i} \left(\frac{\partial u_i}{\partial x_i} + \nu_i \frac{\partial v_i}{\partial y} \right) \left(\frac{\partial u_i}{\partial t} \right)^* \right] \quad (48)$$

$$\langle q_{Iy} \rangle_i = -\frac{1}{2} Re \left[G_{c,i} h_i \left(\frac{\partial u_i}{\partial y} + \frac{\partial v_i}{\partial x_i} \right) \left(\frac{\partial u_i}{\partial t} \right)^* + K_{c,i} \left(\frac{\partial v_i}{\partial y} + \nu_i \frac{\partial u_i}{\partial x_i} \right) \left(\frac{\partial v_i}{\partial t} \right)^* \right] \quad (49)$$

where $G_{c,i} = E_{c,i} / \{2(1+\nu_i)\}$ and $K_{c,i} = E_{c,i} h_i / (1-\nu_i^2)$

4.2 Energy Flow Solution of Coupled-plate Structures

The energy flow solution of the coupled plate can be obtained as in previous studies (Park et al., 2001). The Levy series solution that satisfies the y -direction boundary condition of the energy governing equation in Eqs. (3), (4), and (6) was expressed, and the energy flow solution was calculated using the boundary condition of the wave solution in the x_i direction.

$$\langle e_n \rangle_i(x_i, y) = \sum_{m=0}^{\infty} E_{m,n,i}(x_i) \cos(k_n y) \quad (n = f, l, s) \quad (50)$$

Here, the wave solution of the energy density solution for each n -type wave is given by Eq. (45).

$$E_{m,n,i}(x_i) = A_{m,n,i}^+ e^{-\alpha_{m,n,i} x_i} + A_{m,n,i}^- e^{\alpha_{m,n,i} x_i} \quad (51)$$

Here, $A_{m,n,i}^{\pm}$ represents the m^{th} -order mode coefficient of the wave solution traveling in the n -type \pm direction in the i -plate region, and $A_{m,n,i}^{\pm}$.

4.3 Energy Density Comparison of Coupled-plate Structures

It was assumed that the size of the plate structure in Fig. 1 was $L_{x1} = L_{x2} = L_y = 1$ m and that the coupled angle of the plate was 30° . The material of the plate was aluminum ($E = 7.1 \times 10^{10}$ N/m² and $\rho = 2700$ kg/m³), and the structural damping loss factor of the plate was set as $\eta = 0.01$ to express the spatial damping to a certain degree. All the plate thicknesses were $h = 0.001$ m. The vertical excitation force was applied to the center of the first plate position $(L_{x1}, L_y) = (0.5$ m, 0.5 m), and the size was 10 N. The number of modes for obtaining an approximate solution was set as 200 to improve the accuracy of the analysis. The analysis results for an exact solution at an excitation frequency of 10 kHz are shown in Figs. 2-5. The energy density of the flexural wave was the highest at the excitation point because the plate was excited with a vertical load, and it tended to decrease as the distance from the excitation point increased. Additionally, the plate had the highest energy density at the boundary where the plates were coupled at an arbitrary angle, because the in-plane wave was generated at the position where the two plates were coupled at an arbitrary angle (in contrast to the flexural wave), and the energy density decreased owing to the increased structural damping toward the inside of each plate. The propagation tendency of the vibration energy can be

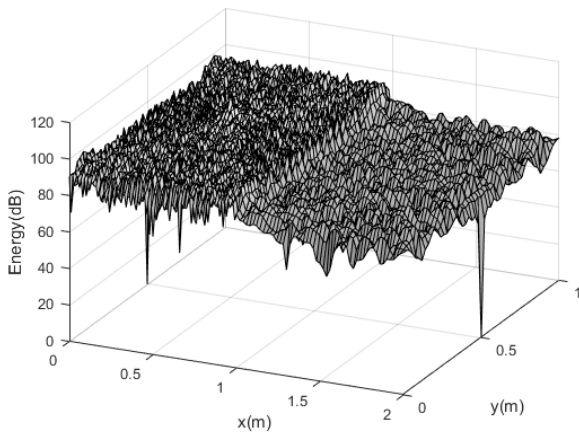


Fig. 2 Flexural energy density level (dB) distribution of exact solutions with $f = 10$ kHz and $\eta = 0.01$

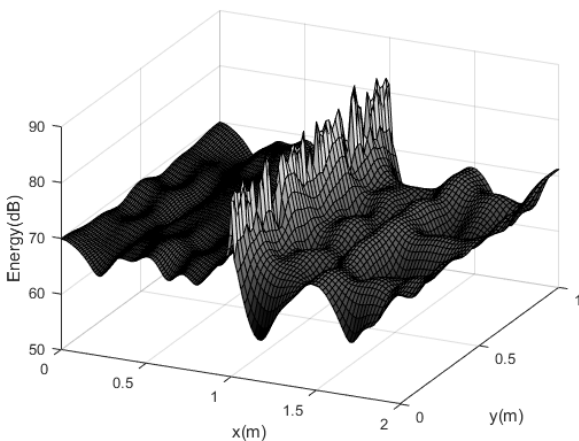


Fig. 3 In-plane energy density level (dB) distribution of exact solutions with $f = 10$ kHz and $\eta = 0.01$

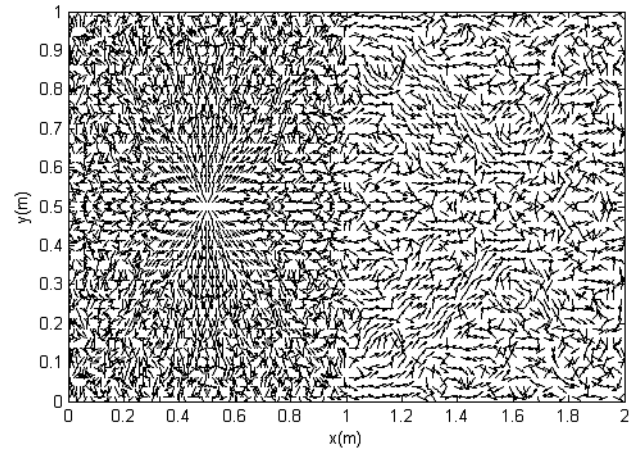


Fig. 4 Flexural intensity distribution of exact solutions with $f = 10$ kHz and $\eta = 0.01$

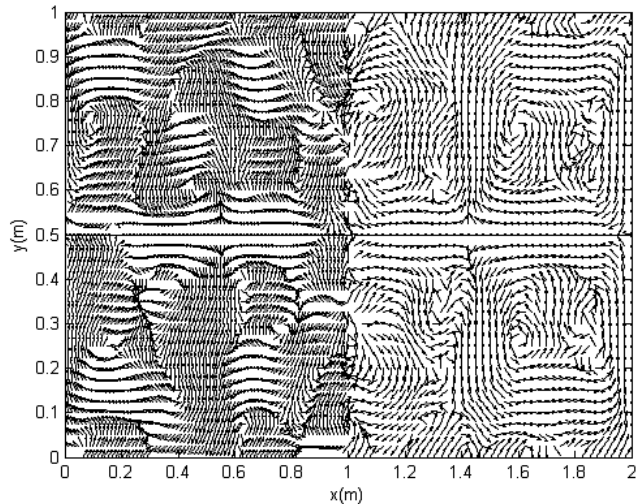


Fig. 5 In-plane intensity distribution of exact solutions with $f = 10$ kHz and $\eta = 0.01$

Table 1 Theoretical modal density of plate according to frequency change

Frequency (Hz)	Modal density (modes/Hz)		
	Flexural	Longitudinal	Shear
10,000	0.3188	0.0064	0.0021
30,000	0.3188	0.0192	0.0064
100,000	0.3188	0.0636	0.0213

observed in the excitation part of the vibrational intensity distribution, as shown in Figs. 4 and 5. The modal density of the plate vibration mode with respect to the frequency is presented in Table 1. Although the theoretical modal density of a flexural wave is constant with respect to the frequency, the in-plane wave tended to increase in proportion to the frequency.

The effectiveness of the EFA, which is a statistical approach, increased in the high frequency range with a high modal density. The energy density distributions of in-plane waves for exact solutions at

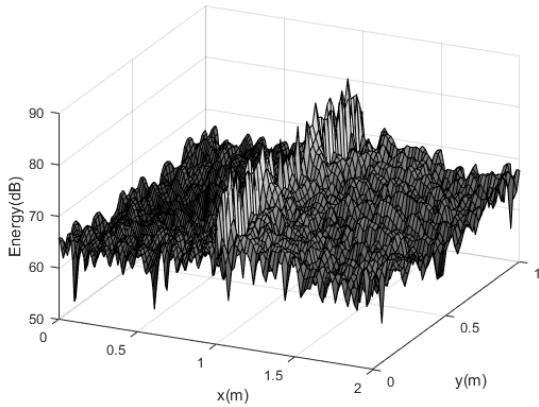


Fig. 6 In-plane energy density level (dB) distribution of exact solutions with $f = 30$ kHz and $\eta = 0.01$

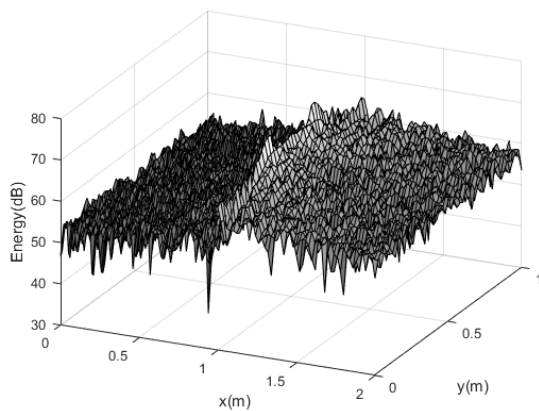


Fig. 7 In-plane energy density level (dB) distribution of exact solutions with $f = 100$ kHz and $\eta = 0.01$

excitation frequencies of 30 and 100 kHz are shown in Figs. 6 and 7, respectively. The modal density increased with the frequency, increasing the mode superposition.

The comparison results for the energy density of the exact solution and the energy flow solution at different frequencies, with $L_y = 0.5$ m, are shown in Figs. 8-10.

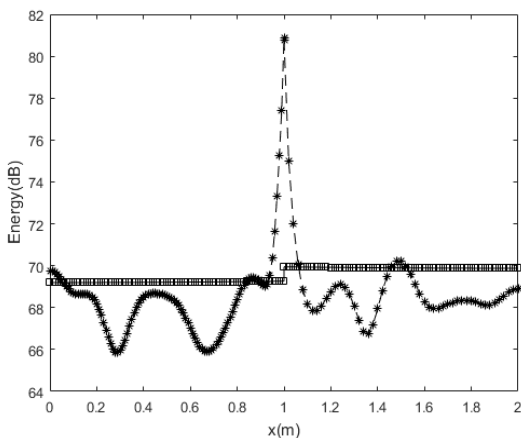


Fig. 8 Comparison between the exact solution and the energy flow solution with $f = 10$ kHz and $\eta = 0.01$: $*$, exact solution; \square , energy flow solution

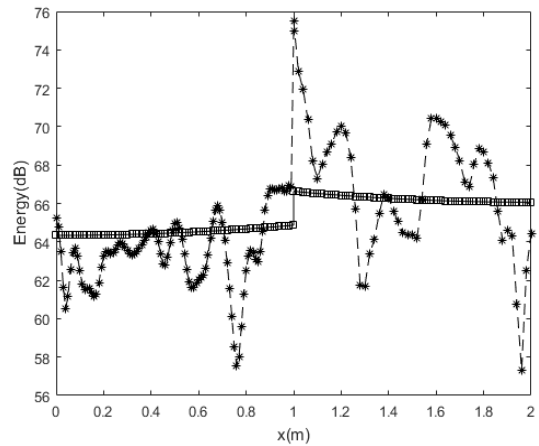


Fig. 9 Comparison between the exact and energy flow solutions with $f = 30$ kHz and $\eta = 0.01$: $*$, exact solution; \square , energy flow solution

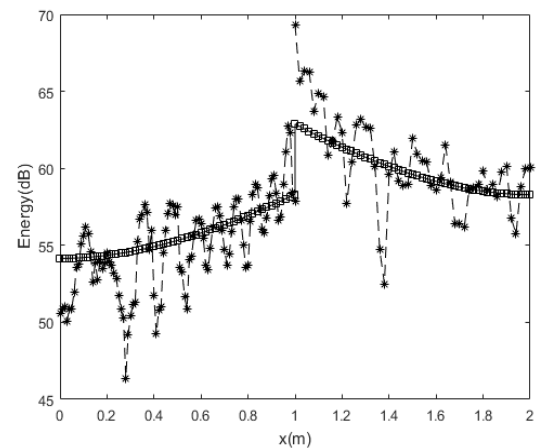


Fig. 10 Comparison between the exact and energy flow solutions with $f = 100$ kHz and $\eta = 0.01$: $*$, exact solution; \square , energy flow solution

Compared with the flexural wave, the modal density was relatively low for the in-plane wave at the same frequency, as indicated by the foregoing analysis results. Therefore, although the exact solution and energy flow solution for the flexural wave in the previous studies had similar energy density distributions owing to mode superposition even in a relatively low frequency range, the spatial distributions of the energy density of the exact solution and the energy flow solution became similar at a significantly high frequency. However, the in-plane energy flow solution successfully showed the average distribution of the exact solution even in a relatively low frequency range, indicating that the EFA is extremely effective for predicting the overall vibration energy level in the middle-high frequency broadband. The size of the plate was doubled ($L_{x1} = L_{x2} = L_y = 2$ m) to examine the effects on the plate size, plate coupled angle, and structural damping loss factor, as shown in Figs. 11-13, which present comparisons of the energy density between the exact solution and the EFA solution of the model with a plate coupled angle of 45° and a structural damping loss factor $\eta = 0.001$ for the plate material. Overall,

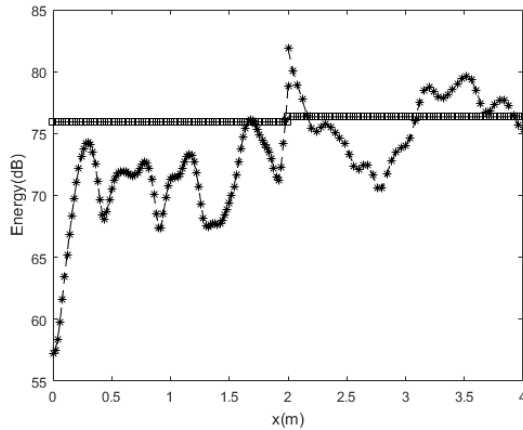


Fig. 11 Comparison between the exact and energy flow solutions with $f = 10$ kHz and $\eta = 0.001$: *, exact solution; □, energy flow solution

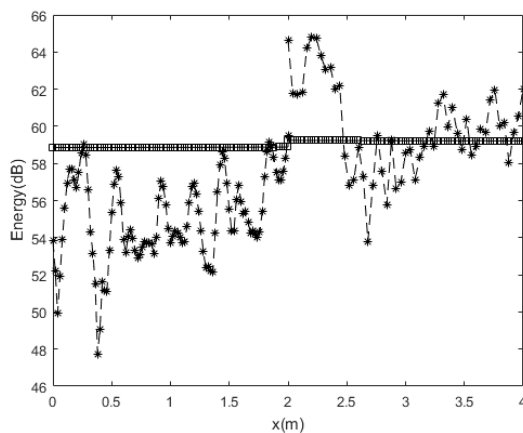


Fig. 12 Comparison between the exact and energy flow solutions with $f = 30$ kHz and $\eta = 0.001$: *, exact solution; □, energy flow solution

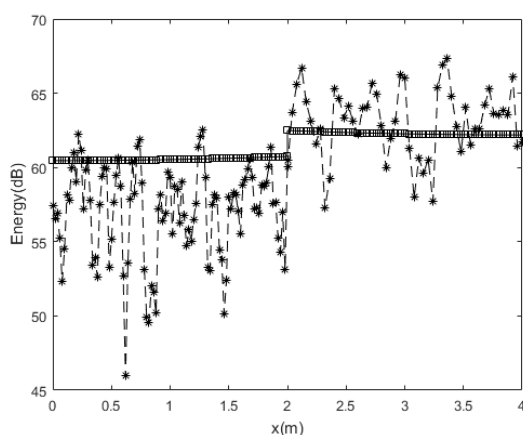


Fig. 13 Comparison between exact and energy flow solutions when $f = 100$ kHz, $\eta = 0.001$: * : exact solution; □ : energy flow solution

the results were similar to those for the first example, even when the plate size, coupled angle, and structural damping loss factor were different.

5. Conclusion

In this study, the EFA, which is attracting attention as an effective vibration noise prediction method in the middle-high frequency ranges, was used to examine in-plane motions in coupled-plate structures. In previous studies, a view of the energetic characteristics depending on the frequency was performed by comparing the energy flow solution and the exact solution for the out-of-plane motion of the plate. However, a study on the reliability of the energy flow solution for in-plane motion was required, because no comparative review of in-plane motion had been conducted. In the present study, an EFA was performed to predict the average energy density level of the exact solution successfully for both out-of-plane and in-plane motions even in relatively low frequency ranges with a high out-of-plane modal density and low in-plane modal density. The EFA method is considered to be extremely effective for vibration analysis in the middle-high frequency ranges for engineers who are interested in the spatial distribution of the overall vibration energy level inside the structure rather than the spatial mode characteristics. In the future, the in-plane wave in the coupled model of the Mindlin plate, which has improved reliability in the high frequency range, must be verified.

Acknowledgements

This research was supported by Changwon National University 2019-2020

References

- Belov, V.D., Rybak, S.A., & Tartakovskii, B.D. (1977). Propagation of Vibrational Energy in Absorbing Structures. *Journal of Soviet Physics-Acoustics*, 23, 115-119.
- Bouthier, O.M., & Bernhard, R.J. (1995). Simple Models of the Energetics of Transversely Vibrating Plates. *Journal of Sound and Vibration*, 182(1), 149-164. <https://doi.org/10.1006/jsvi.1995.0187>
- Dym, C.L., & Shames, I.H. (2013). *Solid Mechanics: A Variational Approach*, Augmented Edition. New York USA: Springer-Verlag. <https://doi.org/10.1007/978-1-4614-6034-3>
- Park, C.H. (2018). *A Study on High-Frequency Vibrational Energetics of Kirchhoff Plate Structures Coupled at Arbitrary Angles* (Master's Thesis). Changwon National University, Changwon, Korea.
- Park, D.-H., Hong, S.-Y., Kil, H.G., & Jeon, J.-J. (2001). Power Flow Models and Analysis of In-plane Waves in Finite Coupled Thin Plates. *Journal of Sound and Vibration*, 244(4), 651-668. <https://doi.org/10.1006/jsvi.2000.3517>
- Park, Y.-H., & Hong, S.-Y. (2006a). Vibrational Energy Flow Analysis of Corrected Flexural Waves in Timoshenko Beam – Part I: Theory of an Energetic Model. *Shock and Vibration*, 13, 137-165. <https://doi.org/10.1155/2006/308715>
- Park, Y.-H., & Hong, S.-Y. (2006b). Vibrational Energy Flow Analysis

of Corrected Flexural Waves in Timoshenko Beam – Part II: Application to Coupled Timoshenko Beams. *Shock and Vibration*, 13, 167-196. <https://doi.org/10.1155/2006/562762>

Park, Y.-H., & Hong, S.-Y. (2008). Vibrational Power Flow Models for Transversely Vibrating Finite Mindlin Plate. *Journal of Sound and Vibration*, 317(3-5), 800-840. <https://doi.org/10.1016/j.jsv.2008.03.049>

Author ORCIDs

Author name

Park, Young-Ho

Park, Chang Hyun

ORCID

0000-0001-8614-4897

0000-0002-4714-1367

Impact Assessment of Beach Erosion from Construction of Artificial Coastal Structures Using Parabolic Bay Shape Equation

Changbin Lim¹, Sahong Lee¹, Seung-Min Park² and Jung Lyul Lee³

¹PhD Candidate, School of Civil, Architecture and Environmental System Engineering, Sungkyunkwan University, Suwon, Korea

²Head of department, Department of Technical Research Center, Hyein E&C, Seoul, Korea

³Professor, Graduate School of Water Resource, Sungkyunkwan University, Suwon, Korea

KEY WORDS: Longshore sediment, parabolic equilibrium shoreline, shoreline deformation, impact assessment, coastal structures

ABSTRACT: Wave field changes resulting from artificial coastal structures constructed in coastal zones have emerged as a major cause of beach erosion, among other factors. The rates of erosion along the eastern coast of Korea have varied mainly owing to the construction of various ports and coastal structures; however, impact assessments of these structures on beach erosion have not been appropriately conducted. Thus, in this study, a methodology to assess the impact of erosion owing to the construction of artificial structures has been proposed, for which a parabolic bay shape equation is used in determining the shoreline angle deformation caused by the structures. Assuming that the conditions of sediment or waves have similar values in most coastal areas, a primary variable impacting coastal sediment transport is the deformation of an equilibrium shoreline relative to the existing beach. Therefore, the angle rotation deforming the equilibrium of a shoreline can be the criterion for evaluating beach erosion incurred through the construction of artificial structures. The evaluation criteria are classified into three levels: safety, caution, and danger. If the angle rotation of the equilibrium shoreline is 0.1° or less, the beach distance was considered to be safe in the present study; however, if this angle is 0.35° or higher, the beach distance is considered to be in a state of danger. Furthermore, in this study, the distance affected by beach erosion is calculated in areas of the eastern coast where artificial structures, mainly including ports and power plants, were constructed; thereafter, an impact assessment of the beach erosion around these areas was conducted. Using a proposed methodology, Gungchon Port was evaluated with caution, whereas Donghae Port, Sokcho Port, and Samcheok LNG were evaluated as being in a state of danger.

1. Introduction

Since 2000, coastal erosion has been worsening and spreading owing to disturbances of sand movement by coastal and port structures; the reduction of sediment budget by dams, weirs, and levees; and abnormal swells and storm waves. Along the eastern coast of Korea in particular, the narrowing of beach width is increasing. Furthermore, beaches are being damaged owing to the changing coastal environment and repeated beach erosion, which are emerging as serious problems in local communities. Consequently, since 2000, the government has been supporting measures against erosion through “coastal management plans” based on the Coast Management Act. However, an overdesign focusing on artificial structures is causing frequent failures owing to a lack of understanding of the phenomenon, poor reliability of predictions, and a misapplication of overseas cases. Along the eastern coast of Korea, many sand streams have developed and erosion caused by the construction of artificial structures is severe;

in addition, beach erosion on the eastern coast has reached a serious level owing to an underestimation or poor reliability of the existing shoreline and topographic change models predicting erosion.

Among the various causes of beach erosions along the eastern coast of Korea, the main cause is the change in shoreline owing to the construction of artificial structures such as breakwater and groin. Typical examples include port structures such as Sokcho Port in Sokcho-si, Gangwon-do and Gungchon Port in Samcheok-si, Gangwon-do; coastal structures on Yeongnang Beach in Sokcho-si, Gangwon-do and Bongpyeong Beach in Uljin-gu, Gyeongsangbuk-do; and the thermal power plant of Samcheok LNG in Samcheok-si, Gangwon-do. Kang et al. (2010) investigated the shoreline erosion on Yeongnang Beach that occurs from artificial structures when applying a headland construction method. Despite a large number of such types of erosion, few studies have been conducted on evaluation methods for determining how much impact coastal artificial structures have on beach erosion.

Received 18 November 2020, revised 26 November 2020, accepted 27 November 2020

Corresponding author Jung Lyul Lee: +82-31-290-7519, jllee@skku.edu

© 2020, The Korean Society of Ocean Engineers

This is an open access article distributed under the terms of the creative commons attribution non-commercial license (<http://creativecommons.org/licenses/by-nc/4.0>) which permits unrestricted non-commercial use, distribution, and reproduction in any medium, provided the original work is properly cited.

To evaluate the erosion occurring from the construction of artificial structures, it is necessary to predict the equilibrium of the shoreline owing to the transport of longshore sediment. Among the many equilibrium shoreline equations that have been proposed (Yasso, 1965; Hsu et al., 1987; Moreno and Kraus 1999), the parabolic bay shape equation of Hsu and Evans (1989) has been proven to be applicable in many coastal areas around the world. Furthermore, the Coastal Engineering Manual (USACE, 2002) adopted a parabolic bay shape equation (Hsu and Evans, 1989) as a means to preserve and manage the coasts of the U.S. In addition, Lim et al. (2019) demonstrated the validity of the parabolic bay shape equation using the wave data of the East Sea in South Korea.

In this study, the rotation angle of an existing equilibrium shoreline is calculated using the parabolic bay shape equation of Hsu and Evans (1989), and a method for evaluating the beach erosion impact proportional to this rotation angle from initial shoreline is proposed. In addition, the criteria for evaluating the beach erosion impact owing to the construction of artificial structures are established by comparing the annual average erosion width calculated using the longshore sediment formula of the Coastal Engineering Research Center (CERC; USACE, 1984) with the rotation angle of an equilibrium shoreline. Finally, the distance affected by beach erosion was calculated along the eastern coast of Korea where artificial structures including port structures and power plants are built.

2. Impact Assessment of Beach Erosion according to Rotation Angle of Equilibrium Shoreline

2.1 Parabolic Bay Shape Equation

The parabolic bay shape equation (PBSE) of Hsu and Evans (1989), which is a model that predicts the static equilibrium shoreline, is given as follows (Fig. 1):

$$R(\theta) = \frac{Y}{\sin \beta} \left[C_0 + C_1 \left(\frac{\beta}{\theta} \right) + C_2 \left(\frac{\beta}{\theta} \right)^2 \right] \quad \text{for } \theta \geq \beta \quad (1)$$

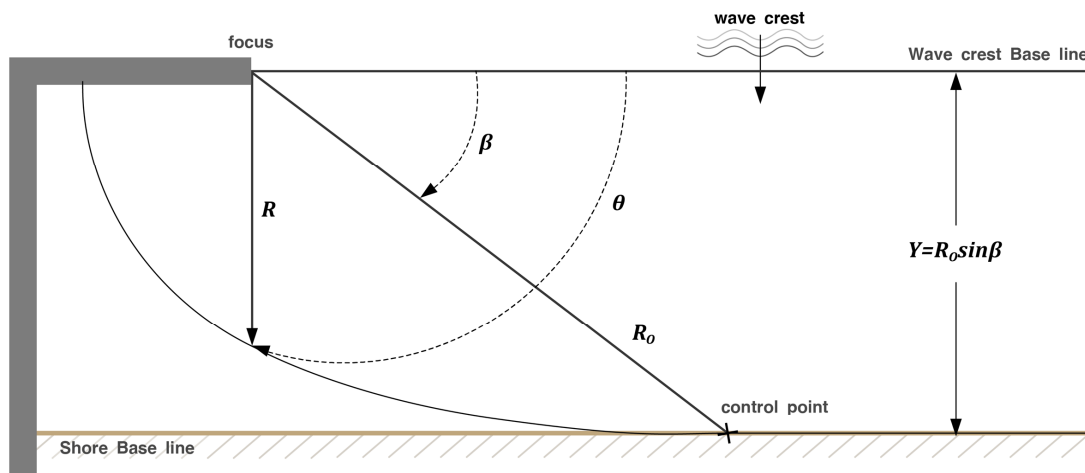


Fig. 1 Definition sketch of equilibrium shoreline gradients

$$R(\theta) = \frac{Y}{\sin \theta} \quad \text{for } \theta \leq \beta \quad (2)$$

where R is the radial distance from the focus resulting from artificial structures to the equilibrium shoreline, Y is the distance from the wave crest baseline of the shore baseline that passes through the control point, β is the angle formed by the line that passes through the control point and focuses at the wave crest baseline, and θ is the angle formed by the wave crest baseline with the radial distance R . Furthermore, C_i ($i = 1, 2, 3$) is the fitting coefficient of the parabolic bay shape equation provided by Hsu and Evans (1989).

For a long sandy beach, the control point is far from the focus, and thus a simple approximate solution such as in Eq. (3) can be obtained (Lim et al., 2019). Because β is close to zero in this case, $\sin \beta$ converges to β . Furthermore, in the case of the equilibrium shoreline coefficient, C_0 and C_2 converge at zero, and C_1 converges at 1. Therefore, the parabolic bay shape in Eq. (1) can be expressed as a simple relational expression $R(\theta)$ as follows:

$$R(\theta) \cong \frac{Y}{\theta} \quad (3)$$

The approximate solution of the parabolic bay shape equation can be used to estimate the equilibrium shoreline simply by the distance Y of the artificial structure and the angle θ formed by the radial distance of the equilibrium shoreline with the wave crest baseline.

2.2 Erosion Impact Assessment According to the Rotation Angle of Equilibrium Shoreline

According to the longshore sediment formula of CERC (USACE, 1984), the rotation angle α_b of the wave crest baseline with the shoreline is the main cause impacting the amount of longshore sediment. In other words, it can be estimated that the amount of longshore sediment increases in proportion to the rotation angle from the straight shoreline. However, it was assumed that variables such as the grain size of the sand and the wave height do not have a significant

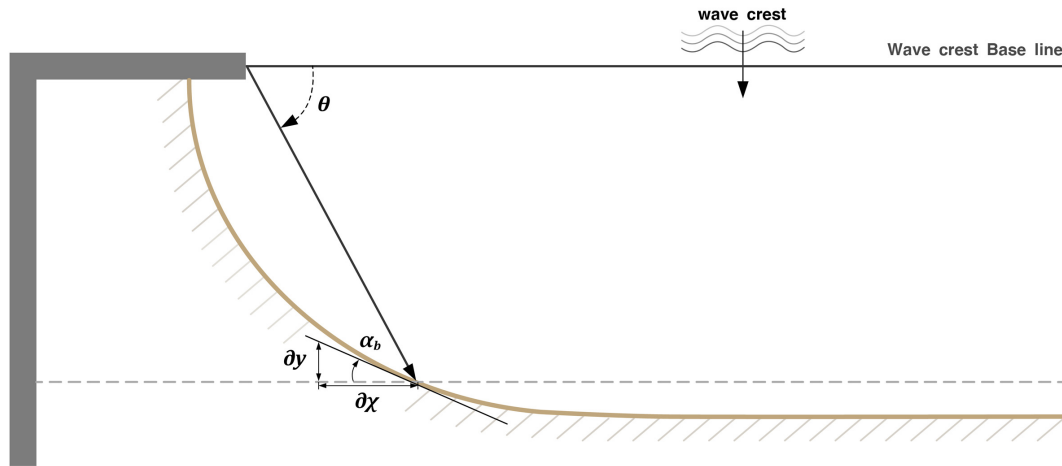


Fig. 2 Definition sketch of parabolic bay shape equation

effect because their values are similar in most coastal areas. Existing shorelines are changed to equilibrium shorelines owing to the artificial structures in harbors or ports, and the shoreline is rotated as a result. At this time, the rotational angle α_b can be calculated using the ratio of coastal to transverse shoreline changes as follows:

$$\frac{\partial y}{\partial x} = \tan \alpha_b \tag{4}$$

where α_b is the rotation angle of the equilibrium shoreline from the original shoreline, x is the equilibrium shoreline length from the existing shoreline toward the coast, and y is the shoreline length in the transverse direction from the existing shoreline. From the approximate solution of the equilibrium shoreline of Hsu and Evans (1989), the shore rotation angle is derived from Eq. (4) as follows (Fig. 2):

$$\alpha_b(\theta) = \tan^{-1} \left[\frac{\sin \theta - \theta \cos \theta}{\cos \theta + \theta \sin \theta} \right] \tag{5}$$

Using Eq. (5), the rotation angle of the equilibrium shoreline owing to the construction of artificial structures can be calculated simply using the angle θ formed by the radial distance of the equilibrium shoreline with the wave crest baseline.

Therefore, from Eq. (5), the erosion impact distance L according to the distance Y of the artificial structures can be derived as follows:

$$L = \left(\frac{1 - \theta \times \tan \alpha_b}{\tan \alpha_b + \theta} \right) Y \tag{6}$$

where θ is a variable that changes according to the distance Y of the structure and erosion impact distance L , and can be expressed as follows:

$$\theta = \tan^{-1} \left(\frac{Y}{L} \right) \tag{7}$$

The erosion impact distance L according to the distance of the

structure that satisfies the above two equations can be determined. The risk level from the erosion is proportional to the rotation angle of the equilibrium shoreline α_b from the existing shoreline. In other words, the erosion impact can be evaluated based on the amount of longshore sediments. In addition, L_{safe} and L_{danger} can be calculated as follows according to the distance Y of the artificial structure:

$$L_{safe} = Y \left[\frac{1 - \theta \times \tan \alpha_{safe}}{\tan \alpha_{safe} + \theta} \right] \tag{8}$$

$$L_{danger} = Y \left[\frac{1 - \theta \times \tan \alpha_{danger}}{\tan \alpha_{danger} + \theta} \right] \tag{9}$$

where L_{safe} is the critical distance at which the impact is considered insignificant if the target beach is farther than L_{safe} according to distance Y of the artificial structure. If $L_{safe}/L < 1$, the beach is at a safe level. By contrast, L_{danger} is the critical distance at which the impact is considered serious if the target beach is closer than L_{danger} according to the distance Y of the artificial structure. If $L_{danger}/L > 1$, the beach is at a dangerous level. Furthermore, if the distance of the target beach is between L_{danger} and L_{safe} , the beach is at a level of caution.

3. Coastal Erosion Impact Analysis Using Longshore Sediment Formula

3.1 Longshore Sediment Formula

The construction of artificial structures causes a diffraction of waves, and the diffracted waves flow at an oblique angle between the incident wave and the coast and cause the transport of the longshore sediments. Komar and Inman (1970) conducted a field experiment on the coastal energy flux P_l and longshore sediment amount Q_l , and proposed the following equation:

$$Q_l = \frac{I_l}{(\rho_s - \rho)(1 - p)g} = \frac{KP_l}{(\rho_s - \rho)(1 - p)g} \tag{10}$$

where I_l is the magnitude of the wave power, ρ_s is the sediment density, ρ is the seawater density, p is the sediment porosity, which has a value of 0.3–0.4, and α_b is an angle between the shoreline and breaking wave crest line. Furthermore, K is the longshore sediment coefficient and can have wide ranging values of between 0.04 and 1.1 depending on the amount of sediment, but 0.77, the value suggested by Komar and Inman (1970), is mainly used. The coastal energy flux component P_l is defined as follows:

$$P_l = EC_g \cos \alpha_b \sin \alpha_b \quad (11)$$

where E is the wave energy and C_g is the group velocity. The CERC (USACE, 1984) formula based on Eq. (10) to express the wave energy and group velocity is as follows:

$$Q_l = C' H_b^{5/2} \sin 2\alpha_b \quad (12)$$

where H_b is the breaking wave height, and $C' = [K\sqrt{g/\kappa}]/[16(s-1)(1-p)]$, which is a related coefficient such as the unit weight of the sediment and porosity, which are not related to the wave conditions. Furthermore, $K = 0.77$ and $g = 9.81 \text{ m/s}^2$, and $s = 2.57$ and $p = 0.35$, are applied for general maritime cases. Thus, the coefficient has a value of approximately 0.167 for most sands. Furthermore, the rotation angle α_b of an equilibrium shoreline from the shore baseline can be calculated using Eq. (5).

3.2 Calculation of Erosion Width Per Unit Time According to the Rotation Angle of Equilibrium Shoreline

In this section, the erosion width per unit time according to the rotation angle of an equilibrium shoreline is calculated using the longshore sediment formula. In addition, the appropriate rotation angle for the beach erosion impact assessment equation derived from the bay shape equation of Hsu and Evans (1989) is calculated. The beach erosion occurring from longshore sediment is caused by the difference in amount of sediment transport, as shown in Fig. 3, and the erosion width per unit time is expressed as follows:

$$\frac{\partial W}{\partial t} = \frac{1}{h_B + h_c} \frac{\partial Q_l}{\partial L} \quad (13)$$

where h_B is the berm height, h_c is the sand movement limit depth, and W is the erosion width. Furthermore, the erosion width per unit time can be calculated by applying the longshore sediment formula of CERC (USACE, 1984) in Eq. (12) to Eq. (13).

Fig. 4 shows graphically the annual erosion width $\partial W/\partial t$ and the rotation angle of equilibrium shoreline α_b according to distance Y of an artificial structure and the shore length L . If the annual erosion width is less than 0.1 m, the beach is considered safe from erosion; if the annual erosion width is 2.5 m or larger, the beach is considered at a dangerous level. As shown in Fig. 4, if the rotation angle α_{safe} of an

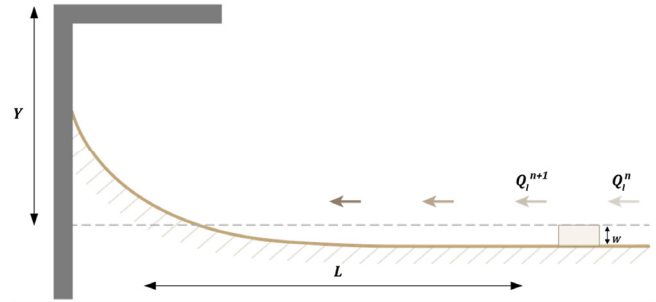


Fig. 3 Definition sketch of beach erosion owing to longshore sediment transport

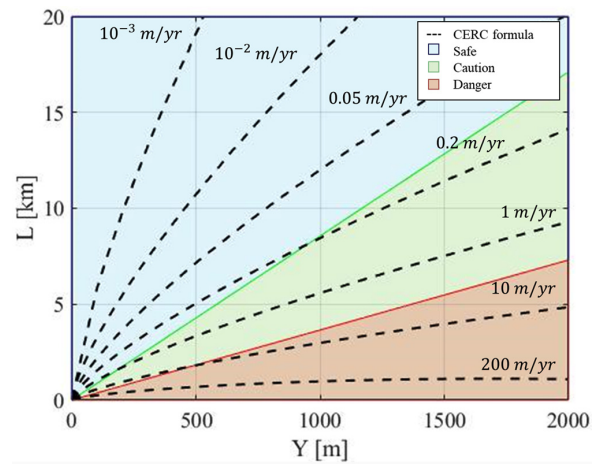


Fig. 4 Comparison of beach erosion according to CERC formula and shore rotation angle

equilibrium shoreline at a safe level is smaller than 0.1° , it is estimated that there is almost no impact from the artificial structures. By contrast, if the rotation angle α_{danger} of an equilibrium shoreline at a danger level is larger than 0.35° , there is a high risk of erosion owing to artificial structures. For the coefficient C of the longshore sediment amount, 0.167 was applied as mentioned above, and the breaking wave height was assumed as 1 m. The erosion impact of artificial structures can be assessed more easily using the rotation angle α_b of an equilibrium shoreline. However, according to Fig. 4, the erosion width is slightly underestimated when the distance Y is small and overestimated when it is large.

4. Assessment of Impact of Beach Erosion by Artificial Structures in Eastern Coast of Korea

The impact of beach erosion increases if the coastal and port structures are constructed too far from the coast. In this study, the erosion impact from artificial structures on the eastern coast of Korea is assessed using Eqs. (6) and (7). The impacts of the construction of port structures along the eastern coast including Donghae Port, Sokcho Port, and Gungchon Port, as well as the Samcheok LNG thermal power plant, on beach erosion are assessed. Fig. 5 shows the distances and shore lengths of the port structures and thermal power

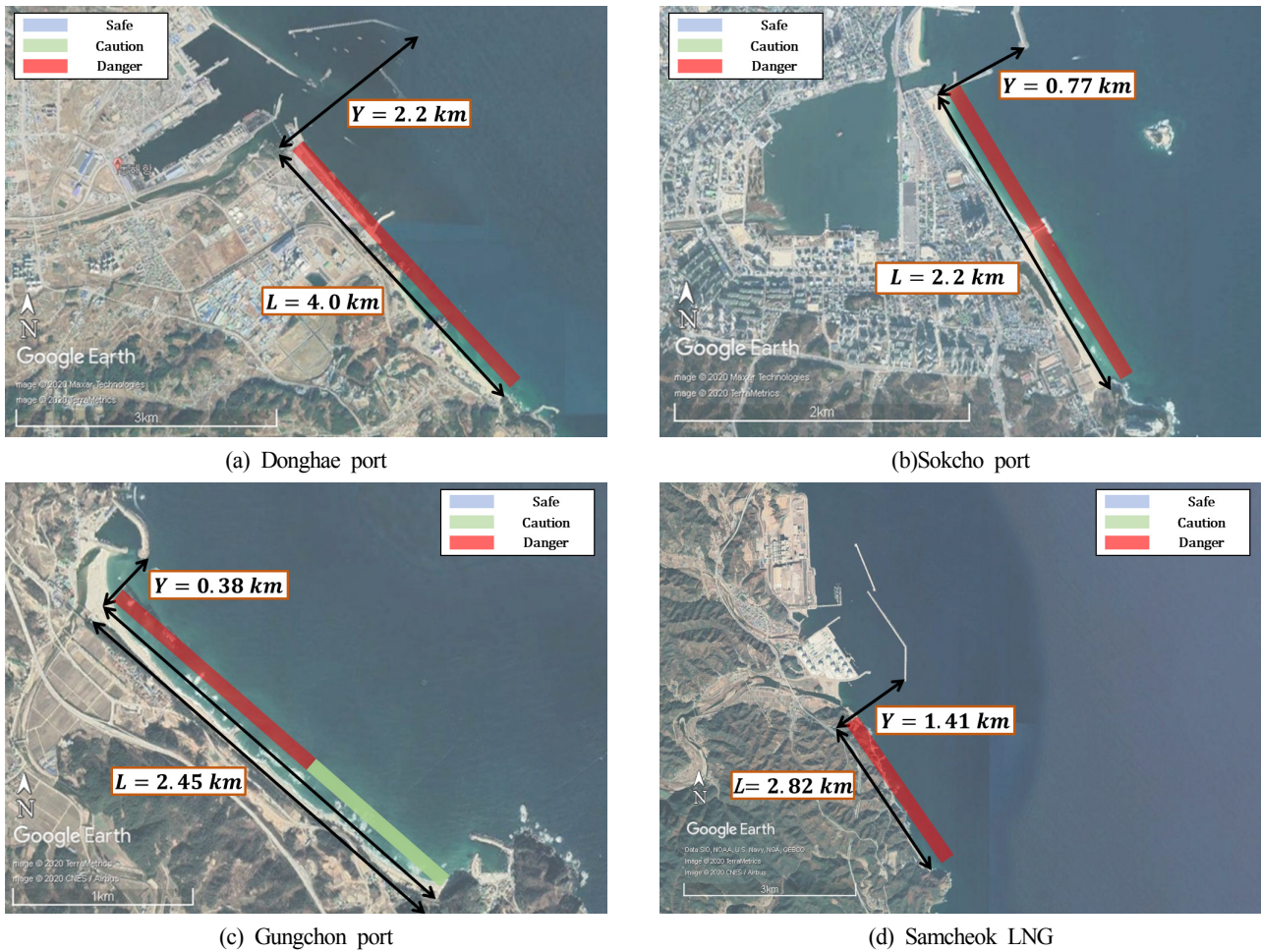


Fig. 5 Construction information of coastal structures in East Sea of Korea (Google Earth Image)

Table 1 Evaluation of beach erosion from coastal structures in East Sea of Korea

Structure	Beach	Y (km)	D (km)	D_{safe} (km)	D_{danger} (km)	$\frac{D_{safe}}{D}$	$\frac{D_{danger}}{D}$	Impact
Donghae port	Samcheok Beach	2.20	4.00	18.82	8.03	4.7055	2.01	danger
Sokcho port	Sokcho Beach	0.77	2.20	6.59	2.81	2.9944	1.28	danger
Gungchon port	Chogok Beach	0.38	2.45	3.25	1.39	1.3270	0.57	caution
Samcheok LNG	Gopo Beach	1.41	2.82	12.06	5.15	4.2777	1.83	danger

plant and impact levels in each coastal area.

The distances of beaches at safe levels in terms of beach erosion from the artificial structures built in Donghae Port, Sokcho Port, Gungchon Port, and Samcheok LNG are 18.82, 6.59, 3.25, and 12.06 km, respectively, according to distance Y . Furthermore, the distances of beaches at a level of danger from erosion are 8.03, 2.81, 1.39, and 5.15 km, respectively (Table 1). Therefore, the Chogok Beach located of Gungchon Port in the southern part is assessed as a level of caution, whereas the Donghae Port, Sokcho Port, and Samcheok LNG are assessed as at levels of danger.

5. Discussion

The assessment method for erosion impact from artificial structures

using the rotation angle of the equilibrium shoreline proposed above has the disadvantage in that Eqs. (6) and (7) need to be repeatedly calculated. Therefore, an approximate solution for the equation of the erosion impact from artificial structures is proposed in this section. The distance Y of artificial structures and the shore length L receiving the erosion impact derived from Eqs. (6) and (7) have the following proportional relationship:

$$L = \beta Y \quad (14)$$

where β is the erosion impact coefficient and has a different value depending on the rotation angle of an equilibrium shoreline. For the values of α_{safe} and α_{danger} calculated using Eq. (14), the erosion impact coefficients β have values of 8.5554 and 3.6514, respectively

Table 2 Variables according to beach erosion impact

Impact	$\partial W/\partial t$	α_b	β
Safe	0.1 m/yr	0.1°	8.5554
Danger	2.5 m/yr	0.35°	3.6514

(Table 2). When the result of Eq. (6) is compared with the approximate solution of Eq. (14), they have almost identical trends in a straight line.

6. Conclusions

Among the 96 coastal areas on the eastern coast of South Korea, 75 are at a danger level of erosion (Gangwon Province, 2017). It is therefore necessary to establish a method of assessing the impact of artificial structures built on the coast on beach erosion. In this study, an assessment method for the impact of artificial structures is proposed based on the rotation angle of an equilibrium shoreline obtained from the parabolic bay shape equation of Hsu and Evans (1989). It can be considered that beach erosion from artificial structures is at a more dangerous level in proportion to the rotation angle of an equilibrium shoreline from the shore baseline. For a quantitative assessment, the results were compared with the annual average erosion width calculated using the longshore sediment formula of CERC (USACE, 1984). The qualitative assessment criteria were established as being at a safe level if the rotation angle of the equilibrium shoreline is less than 0.1° and at a level of danger if it is 0.35° or greater.

Using the method proposed in this study, the impacts on beach erosion owing to the construction of large artificial structures in Donghae Port, Sokcho Port, Gungchon Port, and the Samcheok LNG Plant were evaluated. The values of D_{danger}/D , which is the assessment criterion of the danger level, were 2.01, 1.28, 0.57, and 1.83 in these four coastal areas, respectively. In other words, Gungchon Port was evaluated as at a level of caution, whereas the others were evaluated as at a dangerous level. However, caution should be practiced because these results are slightly different from the values calculated using the longshore sediment formula

Acknowledgement

This research was a part of the project titled 'Practical Technologies for Coastal Erosion Control and Countermeasure', funded by the Ministry of Oceans and Fisheries, Korea.(20180404)

References

- Hsu, J.R.C., Silvester, R., & Xia, Y.M. (1987). New Characteristics of Equilibrium Shaped Bays. Proceedings of 8th Australasian Conference on Coastal and Ocean Engineering, ASCE, 140-144.
- Hsu, J.R.C., & Evans, C. (1989). Parabolic Bay Shapes and Applications. Proceedings of Institution of Civil Engineers, London, Part 2, 87, 557-570.
- Kang, Y.K., Park, H.B., & Yoon, H.S. (2010). Shoreline Changes Caused by the Construction of Coastal Erosion Control Structure at the Youngrang Coast in Sockcho, East Korea. Journal of the Korean Society for Marine Environmental Engineering, 13(4), 296-304.
- Komar, P.D., & Inman, L.D. (1970). Longshore Sand Transport on Beaches. Journal of Geophysical Research, 75(30), 5914-5927. <https://doi.org/10.1029/JC075i030p05914>
- Lim, C.B., Lee, J.L., & Kim, I.H. (2019). Performance Test of Parabolic Equilibrium Shoreline Formula by Using Wave Data Observed in East Sea of Korea. Journal of Coastal Research, S.I. 91, 101-105.
- Moreno, L.J., & Kraus, N.C. (1999). Equilibrium Shape of Headland-Bay Beaches for Engineering Design. Proceedings of Coastal Sediments, ASCE, 860-875.
- The Province of Gangwon. (2017). An Analysis of Coastal Erosion Survey Report, 2015~2016, 953-57.
- USACE (1984). Shore Protection Manual (4th Ed.). U.S. Army Engineers Waterways Experiment Station, Coastal Engineering Research Center, U.S. Government Printing Office, Washington, D.C
- USACE. (2002). Coastal Engineering Manual(Online). US Army Corps of Engineers, Washington, DC. Retrieved from http://chl.erdc.usace.army.mil/chl.aspx?p_s&a_articles;104.
- Yasso, W.E. (1965). Plan Geometry of Headland-Bay Beaches. The Journal of Geology, 73(5), 702-714.

Author ORCIDs

Author name	ORCID
Lim, Changbin	0000-0002-7684-2453
Lee, Sahong	0000-0002-3862-8405
Park, Seung-Min	0000-0003-0138-976X
Lee, Jung Lyul	0000-0001-9410-9725

Single Image-based Enhancement Techniques for Underwater Optical Imaging

Do Gyun Kim¹ and Soo Mee Kim²

¹Graduate Student, Department of control and instrument engineering, Korea Maritime and Ocean University, Busan, Korea

²Senior Researcher, Maritime ICT R&D Center, Korea Institute of Ocean Science and Technology, Busan, Korea

KEY WORDS: Dark channel prior, Generative adversarial network, Gradient transform enhancement, Image fusion enhancement, Underwater color image, Single image enhancement

ABSTRACT: Underwater color images suffer from low visibility and color cast effects caused by light attenuation by water and floating particles. This study applied single image enhancement techniques to enhance the quality of underwater images and compared their performance with real underwater images taken in Korean waters. Dark channel prior (DCP), gradient transform, image fusion, and generative adversarial networks (GAN), such as cycleGAN and underwater GAN (UGAN), were considered for single image enhancement. Their performance was evaluated in terms of underwater image quality measure, underwater color image quality evaluation, gray-world assumption, and blur metric. The DCP saturated the underwater images to a specific greenish or bluish color tone and reduced the brightness of the background signal. The gradient transform method with two transmission maps were sensitive to the light source and highlighted the region exposed to light. Although image fusion enabled reasonable color correction, the object details were lost due to the last fusion step. CycleGAN corrected overall color tone relatively well but generated artifacts in the background. UGAN showed good visual quality and obtained the highest scores against all figures of merit (FOMs) by compensating for the colors and visibility compared to the other single enhancement methods.

1. Introduction

Optical images generated by the reflected light from an object are useful and intuitive for visual monitoring in unknown underwater environments. On the other hand, reflected light is typically scattered and absorbed by water and floating particles. This light attenuation causes low visibility with haziness and color cast in the resulting optical image (Mobley, 1994). The color cast effect produces a greenish or bluish hue in underwater optical images due to different attenuations depending on the light wavelength. Red light is attenuated more than green and blue light because of its longer wavelength. Depending on the transmission distance, water attenuation can cause limited visibility due to the loss of light intensity and contrast.

Considerable efforts have been made to compensate for the limited visibility and color cast effect of underwater optical images. The focus of most studies is on estimating a distance map because light attenuation of a specific wavelength is dependent on the distance from the camera. Stereo imaging has been used in some studies to obtain a distance map or enhance image quality directly (Roser et al., 2014;

Zhang et al., 2014). Stereo imaging has been used to recover underwater images through a physical image formation model and an estimated distance map. One other approach has enhanced the underwater image by utilizing multi-directional light sources and fusing these different light images (Treibitz and Schechner, 2012). This study focused solely on single image enhancement as opposed to multi-images. This is because the utilization of multi-image enhancements requires additional hardware devices that are not available as a general imaging platform in the context of an underwater environment.

Single image enhancement improves image quality using the information extracted from a given underwater image. A single image enhancement technique is to adopt prior physical knowledge of light. Dark channel prior (DCP) is popular and was proposed to improve the haze of outdoor images using a light transmission map estimated from the darkest color channel (He et al., 2011). DCP has been applied widely to remove the turbidity of underwater images. On the other hand, it is imperfect for estimating a light transmission map due to nearly zero red channel values in the underwater environment.

Received 5 June 2020, revised 25 November 2020, accepted 27 November 2020

Corresponding author Soo Mee Kim: +82-51-664-3041, smeekim@kiost.ac.kr

© 2020, The Korean Society of Ocean Engineers

This is an open access article distributed under the terms of the creative commons attribution non-commercial license (<http://creativecommons.org/licenses/by-nc/4.0>) which permits unrestricted non-commercial use, distribution, and reproduction in any medium, provided the original work is properly cited.

Underwater DCP estimates light transmission, excluding the red channel (Drews et al., 2013). For single image enhancement, the maximum intensity prior calculates the difference between the maximum values of red, green, and blue channels to estimate the light transmission map (Carlevaris-Bianco et al., 2010).

Domain transform methods were applied to single image enhancement. A homomorphic filter was used to help suppress noise and amplify details in the image frequency domain (Luo et al., 2019). The wavelet transform has been used for denoising (Jian and Wen, 2017) or fusing images (Khan et al., 2016; Wang et al., 2017a). The gradient-domain transform method has been found to recover the original gradient instead of the image intensity itself based on the image formation model (Li et al., 2012; Mi et al., 2016; Park and Sim, 2017; Zetian et al., 2018). Typical image processing techniques have been applied for contrast and turbidity enhancements. Multiple image processing steps have been established to improve the contrast, noise, and color successively (Arnold-Bos et al., 2005; Bazeille et al., 2006; Ghani and Isa, 2014; Ghani and Isa, 2015). The image fusion method was also proposed to combine the characteristics enhanced in multiple image processing steps (Ancuti et al., 2017). The combined technique of domain transform and fusion was proposed to dehaze general color images in air (Cho et al., 2018).

Recent research has found that deep neural networks for underwater optical imaging can enhance underwater images directly (Anwar et al., 2018; Fabbri et al., 2018; Guo et al., 2019; Hou et al., 2018; Li et al., 2019a; Li et al., 2019b; Sun et al., 2018; Uplavikar et al., 2019; Wang et al., 2017b) or estimate inherent information, such as background light intensity and transmission maps (Cao et al., 2018; Li et al., 2018a; Li et al., 2018b). Training convolutional neural networks require huge pairs of underwater images and clean images, but clean images are difficult to obtain in an underwater environment. Therefore, some researchers have used indoor datasets of color images and the corresponding depth information (Anwar et al., 2018; Cao et al., 2018; Hou et al., 2018; Uplavikar et al., 2019) or applied unsupervised networks, such as a generative adversarial network (GAN), to produce the image pairs (Fabbri et al., 2018; Guo et al., 2019; Li et al., 2019b). A detailed review of underwater image enhancement techniques can be found elsewhere (Anwar and Li, 2019; Wang et al., 2019; Yang et al., 2019).

In this study, six single image enhancement methods were considered: original DCP, gradient transform method with Tarel's and Peng's transmission maps, image fusion of successive three image processing steps, and two GANs. Although original DCP and Tarel's methods were designed to enhance the haze outdoor environments, they were applied to underwater images because underwater images suffer from haziness. The gradient-domain transform was selected from the domain transform methods available because it simplifies the image formation model, and two different methods proposed by Tarel and Hautière (2009) and Peng and Cosman (2017) were applied to estimate a transmission map. Peng and Cosman (2017) proposed specific ways to estimate a depth map and background lights

considering the underwater environments. The image fusion method should be an effective way to improve by combining appropriate image processing techniques. Two GANs, CycleGAN and underwater GAN, which are designed for underwater image enhancement, were applied because GAN is a new remarkable deep learning algorithm for various applications of image processing. The enhancement performance was assessed quantitatively in terms of underwater image quality measure (UIQM) considering the colorfulness, sharpness, and contrast, underwater color image quality evaluation (UCIQE) considering color saturation, chroma, and contrast and gray world (GW) assumption as color correction metrics, and blur metric. The comparison results would help other researchers better understand the advantages and disadvantages of single image enhancement methods for their studies.

This paper is organized as follows. Section 2 describes the single image enhancement methods considered in this study. Qualitative and quantitative comparisons are reported in Section 3. Sections 4 and 5 discuss the results and outline the conclusions of this study.

2. Single Image Enhancement

The light transmitted through water can be defined by the simple image formation model as follows (Fattal, 2008):

$$I(x) = \mathcal{J}(x)t(x) + A(1-t(x)) \quad (1)$$

where I is the measured light intensity; \mathcal{J} is the recovered original light intensity; t is the light transmission map, and A is the uniform background light. The intensity is conventionally expressed with three representative color channels: red (R), green (G), and blue (B). The single image enhancement method was considered for the recovery of the original light intensity. The information is derived solely from a single underwater image using this method. This includes methods that derive the transmission map and the background light to solve Eq. (1) with observation-based assumptions and those that combine conventional image processing techniques to enhance the deteriorated underwater color image quality. Recently, deep learning has been the center of research attention with regard to image enhancement. This section describes the DCP, gradient transform, image fusion, and two GAN methods for single image enhancement.

2.1 Dark Channel Prior Enhancement

He et al. (2011) reported that at least one of the R, G, B-color channels in a pixel tends to approach zero in a colorful image. They proposed DCP to estimate the transmission from the darkest color channel in a local patch of given observed light, I . The dark channel image, J_{dark} , of a clean original image can be defined by the minimum operator ($\min[\]$) over a local patch and three color channels. This will approach zero according to DCP as follows:

$$J_{dark}(x) = \min_{y \in \Omega(x)} \left[\min_{c \in \{r,g,b\}} [J_c(y)] \right] \approx 0 \quad (2)$$

where c indicates each color channel in an image, and $\Omega(x)$ is a local patch centered at x . The patch size is a key parameter determining the performance of DCP enhancement. The transmission can be estimated by substituting the dark channel image in Eq. (2) into Eq. (1), as follows:

$$\tilde{t}(x) = \text{softmat} \left[1 - \min_{y \in \Omega(x)} \left[\min_{c \in \{r, g, b\}} \left[\frac{I_c(y)}{A} \right] \right] \right] \quad (3)$$

The intensity of background light was first determined from the dark channel (I_{dark}) of the underwater image, I , reflecting the amount of haziness in an underwater image. The pixel with the highest intensity in I was chosen as the background light among candidates in the top 10 percent of the brightest pixels in I_{dark} . The initial transmission was estimated using the background light and I_{dark} . It was then refined using a soft matting operator to reduce the halo effect around the edges. Finally, the enhanced image was recovered with the refined transmission, $\tilde{t}(x)$, as follows:

$$\tilde{J}(x) = \frac{I(x) - A}{\max(\tilde{t}(x), \varepsilon)} + A \quad (4)$$

where ε is the lowest transmission value and was set to 0.1 to avoid the zero denominator. The smaller patch size was used to estimate the initial transmission where the higher color saturation appeared in the final image (\tilde{J}). The large patch size produced a halo effect around the edges. In this paper, the same patch size of 15×15 was used for all underwater images.

2.2 Gradient Transform Enhancement

The gradient transform method was derived by adopting a gradient of Eq. (1) (Li et al., 2012). Assuming that the transmission is constant in a local patch, the gradient of I may be represented simply as follows:

$$\|\nabla I(x)\| \approx t \|\nabla J(x)\| \quad (5)$$

The gradient transform method estimates the transmission for obtaining the original image gradient, ∇J , from a given ∇I . The enhanced original image, \tilde{J} , was then reconstructed from its gradient, ∇J , via the Poisson equation solver assuming *Dirichlet* boundary conditions. Based on the calculus of variations, the cost function can be defined using Eq. (6) to recover the image intensity from its gradient:

$$\arg \min_{\tilde{J}} \iint F(\nabla \tilde{J}, \nabla J) dx dy = \arg \min_{\tilde{J}} \iint \|\nabla \tilde{J} - \nabla J\|^2 dx dy \quad (6)$$

where \tilde{J} is an estimate of J and can be determined by minimizing the integral of the difference between the derivatives of J and \tilde{J} , as follows:

Table 1 Image reconstruction from a given gradient

Workflow of image recovery from a given gradient	
(1) Compute $\text{div} \nabla J$ and $\nabla^2 B$	$\text{div} \nabla J \approx \nabla J_x(x, y) - \nabla J_x(x-1, y) + \nabla J_y(x, y) - \nabla J_y(x, y-1)$ $\nabla^2 B \approx B(x+1, y) + B(x-1, y) + B(x, y+1) + B(x, y-1) - 4B(x, y)$
(2) $Y = \text{div} \nabla J - \nabla^2 B$	
(3) Discrete sine transformation of Y : $\Psi_{uv}(Y)$	
(4) $\tilde{\Psi}_{uv}(T) = \frac{\Psi_{uv}(Y)}{2\cos(\pi u/M) + 2\cos(\pi v/N) - 4}$	
(5) Compute inverse the discrete sine transform of $\tilde{\Psi}_{uv}(T)$	
(6) Reconstruction: $\tilde{J} = T + B$	

$$\frac{\partial F}{\partial \tilde{J}} - \frac{d}{dx} \frac{\partial F}{\partial \tilde{J}_x} - \frac{d}{dy} \frac{\partial F}{\partial \tilde{J}_y} = 0 \quad (7)$$

The Euler-Lagrange equation was adopted to minimize the integral of $F(\cdot)$ in (6) and the Poisson equation in Eq. (8) was then derived from Eq. (7):

$$\nabla^2 \tilde{J} = \text{div} \nabla J \quad (8)$$

Here, ∇^2 is Laplacian operator, and div is the divergence operator. Using the *Dirichlet* boundary condition, a boundary image, B of \tilde{J} was defined as containing all zero pixel values, except for the boundary pixels of \tilde{J} . Table 1 lists the estimated final recovered image, \tilde{J} , from the Poisson equation (Simchony et al., 1990).

This paper considered two transmission estimation methods. Tarel and Hautière (2009) proposed patch-based processing, such as DCP, and adopted the Median operator Along Lines (MAL). This preserves the edges without the halo effect as well as the corners, unlike the classical median operator, as shown in Eq. (9):

$$m(x) = \text{MAL}_{y \in \Omega(x)} \left[\min_c [I(x)] \right]$$

$$n(x) = m(x) - \text{MAL}_{y \in \Omega(x)} \left[\left| \min_c [I(y)] - m(y) \right| \right]$$

$$t(x) = 1 - \max \left[\min \left[n(x), \min_c [I(x)] \right], 0 \right] \quad (9)$$

$\Omega(x)$ was defined as the line segments over a square patch centered at x . Each line segment must pass through the center of the square patch. The MAL performs a classical median filter along each line segment and then calculates the median of the median values of each line segment. The number of line segments and the patch size are key parameters determining the enhancement performance. This study set five line segments and a 61×61 patch size.

Peng and Cosman (2017) estimated the transmission from a depth map based on image blurriness and light absorption by water and floating particles and the attenuation coefficients (μ_c) corresponding to RGB colors, as follows:

$$t_c(x) = e^{-\mu_c d(x)}, c \in \{r, g, b\} \quad (10)$$

The depth map, $d(x)$ can be calculated with two relative depth estimates, d_0 and d_{mix} . This is based on different light absorption phenomena of RGB colors and the mixed additional distance information relative to the closest distance as follows:

$$d(x) = d_{act}(d_0 + d_{mix}(x)) \quad (11)$$

where d_{act} is a scaling constant to convert the sum of two depth estimates to the actual distance in meters and was set to 8 m. d_0 represents the normalized closest distance from the underwater camera to the scene, as follows:

$$d_0 = 1 - \max_{x,c} \left[\frac{|A_c - I_c(x)|}{\max[A_c, 1 - A_k]} \right] \quad (12)$$

k indicates the color channel with a maximum absolute difference between the background light and the input intensities.

d_{mix} was determined using three depth-related values accommodating the different attenuations of RGB color signals and blurriness of the underwater image, as follows:

$$d_{mix}(x) = \beta \{ \alpha d_{diff}(x) + (1 - \alpha) d_{red}(x) \} + (1 - \beta) d_{blur}(x) \quad (13)$$

The mixing weights, α and β were determined from the average intensities of background light and the red channel in the input image as follows:

$$\alpha = \frac{1}{1 + e^{-32(\frac{\text{mean}[A_c] - 0.5}{\text{mean}[I_r(x)] - 0.1})}}, \beta = \frac{1}{1 + e^{-32(\frac{\text{mean}[A_c] - 0.5}{\text{mean}[I_r(x)] - 0.1})}} \quad (14)$$

d_{diff} and d_{red} , expressed by Eqs. (15) and (16), respectively, were estimated assuming that the intensity of the red channel (I_r) measured increased as the scene point to the camera became closer.

$$d_{diff} = 1 - f_N \left[\max_{y \in \Omega(x)} I_r(y) - \max_{y \in \Omega(x)} [I_y(y), I_b(y)] \right] \quad (15)$$

$$d_{red}(x) = 1 - f_N \left[\max_{y \in \Omega(x)} I_r(y) \right] \quad (16)$$

The local patch size was set to 5×5 in $\max[\]$ operator. $f_N[\]$ normalizes the input value in the range of 0 to 1. d_{blur} is estimated by the blurriness in the underwater image as follows:

$$d_{blur}(x) = 1 - f_N[\text{Fill}[I_{blur}(x)]] \quad (17)$$

Blurriness was defined by the mean of edge information extracted at various Gaussian kernel sizes, as follows:

$$I_{blur}(x) = \max_{\Omega(x)} \left[\frac{1}{L} \sum_{l=1}^L |I_{gray}(x) - \text{Gauss}_{\sigma} [I_{gray}(x)]| \right] \quad (18)$$

I_{gray} is a gray-scaled image of the underwater color image. Gauss is a Gaussian filter with a kernel size, σ of $2^l L + 1$ at different kernel levels, $\{l = 1, \dots, L\}$. L was set to 4. $\text{Fill}[\]$ operator performs a morphological opening to compensate for the sparse regions and holes in I_{blur} to become denser (Vincent, 1993). Calculation of background light intensity is required to determine the closest distance and the mixing weights. The background light intensity was determined by combining the maximum and minimum of the three background light components, A_c^{high} , A_c^{mean} , and A_c^{var} , as expressed in Eq. (19):

$$A_c = \gamma_c \cdot \max[A_c^{high}, A_c^{mean}, A_c^{var}] + (1 - \gamma_c) \min[A_c^{high}, A_c^{mean}, A_c^{var}] \quad (19)$$

A_c^{high} is the mean value of the input image pixels, which correspond to the same locations of the top 0.1% pixels of an image blurriness map, P_{blur} ($= \text{softmat}[\text{Fill}[I_{blur}]]$). A_c^{mean} and A_c^{var} are mean values of the input image pixels belonging to sub-regions that have the largest mean in P_{blur} and the lowest variance in the input image, respectively. The sub-regions were selected through an iterative process where an image was divided into four quadrants, and the region with the largest mean and the lowest variance among the quadrants were selected. This iteration continues until the quadrant size is 1,024 times smaller than the initial image. γ_c is the weight calculated by the exponential of the rate of pixels greater than 0.5, as shown in Eq. (20):

$$\gamma_c = \frac{1}{1 + e^{-32(\text{rate}[I_c > 0.5] - 0.2)}} \quad (20)$$

First, the transmission of the red channel, t_r , was determined using the estimated distance map in Eq. (11), background light in Eq. (19), and the attenuation coefficient, μ_r , was set to 1/7 for Ocean Type-I water (Zhao et al., 2015). The attenuation coefficient ratios between the red and other colors were used for transmission conversion from red to blue and green colors as follows:

$$t_k(x) = t_r(x)^{\frac{\mu_k}{\mu_r}} = t_r(x)^{\frac{A_r(-0.00113\lambda_k + 1.62517)}{A_k(-0.00113\lambda_r + 1.62517)}}, k \in \{g, b\} \quad (21)$$

The wavelengths, λ_c of the red, green and blue colors are 620, 540, and 450 nm, respectively.

2.3 Image Fusion Enhancement

Image fusion enhances features in an image and fuses the enhanced images (Ancuti et al., 2017). This consists of three processing steps: white balancing, feature enhancing, and image fusing. In the image fusion method, white balancing compensates the red and blue signals giving them flatter distributions compared to the green signal, which tends to maintain its intensity through water somewhat.

$$I_k^{wb} = I_k + (I_g^{mean} - I_k^{mean})(1 - I_k)I_g, k \in \{r, b\} \quad (22)$$

where I^{wb} is a white-balanced image for the red and blue channels. I_c^{mean} is an average value across all image pixels for each color channel.

After white balancing to correct for color casting by water, two feature enhancing techniques were applied independently. First, contrast-limited adaptive histogram equalization (CLAHE) was adopted instead of gamma correction in the original method to enhance image contrast ($I^{contrast}$). CLAHE performs an ordinary histogram equalization over the predefined patch with a limited clip level. The parameters of CLAHE are the patch size, Ω , and a histogram clip level, h_l . Furthermore, unsharp masking was applied to sharpen features, such as an edge in an image, as follows:

$$I^{edge} = I^{wb} + (I^{wb} - \text{Gauss}_\sigma[I^{wb}]) \quad (23)$$

Three weight maps of Laplacian contrast, saturation, and saliency were determined to fuse two images enhanced from the previous step. The Laplacian contrast weight map, ω_{Lap} , depends on global contrast in an image and was calculated as the absolute value of the Laplacian filtered luminance signal of each enhanced image, as follows:

$$\omega_{Lap}^E = |\text{Laplacian}_\sigma[I_Y^E]|, E \in \{\text{contrast}, \text{edge}\} \quad (24)$$

where I_Y is the luminance channel of an image. The kernel size, σ , of the Laplacian filter was set to 3×3 . The saturation weight map, ω_{Sat} , reflects chromatic information in an image and was defined by the average difference between the luminance and three-color signal, as follows:

$$\omega_{Sat}^E = \sqrt{\frac{1}{3} \sum_{c \in \{r, g, b\}} (I_c^E - I_Y^E)^2} \quad (25)$$

The saliency weight map, ω_{Sal} , represents the prominent features of an image in CIELAB color space (Achantay et al. 2009), and can be expressed using Eq. (26):

$$\omega_{Sal}^E = \sqrt{\sum_{c \in \{L^*, a^*, b^*\}} (\text{mean}_x[I_c^E] - \text{Gauss}_\sigma[I_c^E])^2} \quad (26)$$

The Gaussian kernel size was set to 3×3 . The final weight map for each enhanced image from the previous step, combined three weight maps with normalization, as follows:

$$\omega^E = \frac{\omega_{sum}^E}{\omega_{sum}^{contrast} + \omega_{sum}^{edge}} \quad (27)$$

$\omega_{sum}^E = \omega_{Lap}^E + \omega_{Sat}^E + \omega_{Sal}^E + 0.1$. To fuse two enhanced images, $I^{contrast}$ and I^{edge} , with the corresponding weights, $\omega^{contrast}$ and ω^{edge} , multiscale fusion was applied to avoid artifacts in the low-frequency components of the fused image. Multiscale fusion performs Laplacian

(L_l) and Gaussian (G_l) pyramids repetitively on the enhanced images and the weight maps, as shown in Eq. (28):

$$\tilde{J}(x) = \sum_{p_l} \sum_E L_l[I^E(x)] G_l[\omega^E(x)] \quad (28)$$

The Laplacian pyramid at each l^{th} level quantifies the difference between an input image and its Gaussian filtered image after sampling-down the operation by a factor of 2. The size of the Gaussian kernel in the pyramid computation was set to 5×5 . The number of pyramid levels, p_l , was set to 3.

2.4 Generative Adversarial Network Enhancement

A convolutional neural network is a widely used deep learning network for many image processing applications. Robust training in a deep learning network requires huge datasets and a reliable ground truth. On the other hand, it is difficult to construct ground truth for underwater color images. Fabbri et al. (2018) proposed underwater GAN (UGAN) to increase the reliability of synthetic training data and enhance underwater color imagery using synthetic data. GAN typically consists of the generator and discriminator networks, and the training process is performed by optimizing the loss function in Eq. (29):

$$\min_G \max_D \mathbb{E}_J[\log(D(\mathcal{J}))] + \mathbb{E}_J[\log((1 - D(G(\mathcal{J}))))] \quad (29)$$

The generator network (G) competes against discriminator (D) during training to generate exquisite fake images and deceive the discriminator. The discriminator is trained to distinguish a fake image from a generator. The loss function of UGAN was defined with the Wasserstein GAN loss function and gradient penalties.

$$\mathcal{L}_{UGAN} = \min_G \max_D \mathcal{L}_{WGAN}(G, D) + \eta_1 \mathcal{L}_{L1}(G) + \eta_2 \mathcal{L}_{GDL} \quad (30)$$

Wasserstein loss function, \mathcal{L}_{WGAN} , was proposed to solve the training issue induced by the general GAN loss function, which measures a difference between real and generated data distributions in Eq. (29) (Arjovsky et al., 2017). \mathcal{L}_{WGAN} is expressed as follows:

$$\mathcal{L}_{WGAN} = \mathbb{E}[D(\mathcal{J})] - \mathbb{E}[D(G(\mathcal{J}))] + \eta_0 \mathbb{E}[(\|\nabla_z D(\hat{z})\|_2 - 1)^2] \quad (31)$$

The weight, η_0 was set to 10. \mathcal{L}_{L1} is defined by the L1-norm of the difference between the ground truth and the image predicted, J^P , by the generator, as follows:

$$\mathcal{L}_{L1} = \mathbb{E}[\|J - G(\mathcal{J})\|_1] = \mathbb{E}[\|J - J^P\|_1] \quad (32)$$

\mathcal{L}_{GDL} is a function with respect to the gradient difference between the ground truth and the predicted image (Mathieu et al. 2015), as follows:

$$\mathcal{L}_{GDL} = \sum_{x,y} \left| \left| \frac{\partial J}{\partial x} \right| - \left| \frac{\partial J^P}{\partial x} \right| \right| + \left| \left| \frac{\partial J}{\partial y} \right| - \left| \frac{\partial J^P}{\partial y} \right| \right| \quad (33)$$

The hyper-parameters, η_1 and η_2 were set to 100 and 1, respectively.

Fig. 1 summarizes the architecture of the discriminator and generator networks of UGAN. The discriminator network adopted the PatchGAN model (Isola et al., 2017) that was comprised of five convolutional layers, and the resulting output feature map was 32×32 . Each convolutional layer of the PatchGAN model performs the convolution operation, followed by ReLU activation. The generator has a U-Net model consisting of encoder and decoder sections in a U-shape (Ronneberger et al., 2015). The encoder and decoder sections in U-Net have eight convolutional and seven deconvolutional layers, respectively. Each convolutional layer of the U-Net model performs successive convolutions with a 4×4 kernel and stride of 2, batch normalization, and leaky ReLU activation. The deconvolution layer also includes a 4×4 convolution kernel with a stride of 2 and ReLU activation, without batch normalization. The outputs from the second to seventh convolutional layers were connected to the outputs of deconvolutional layers in U-Net. UGAN was trained with the paired synthetic datasets of underwater and clean ground truth images. To construct the paired datasets, an unsupervised network, cycleGAN, was applied to a mapping function of clean to underwater images: $F: J \rightarrow I$ (Zhu et al., 2018). CycleGAN consists of a Resnet-9 block generator and a PatchGAN discriminator outputting a 70×70 feature map. CycleGAN was trained with two batches and 100 epochs using 6,050 clean images and 5,202 underwater images. This included 1,813 images from ImageNet (Deng et al., 2009) and 3,389 real images taken in Korean waters. The trained cycleGAN generated pairs of clean and underwater images where 5,202 underwater images were used for training. From the paired training images, UGAN was trained with 32 batches and 20 epochs.

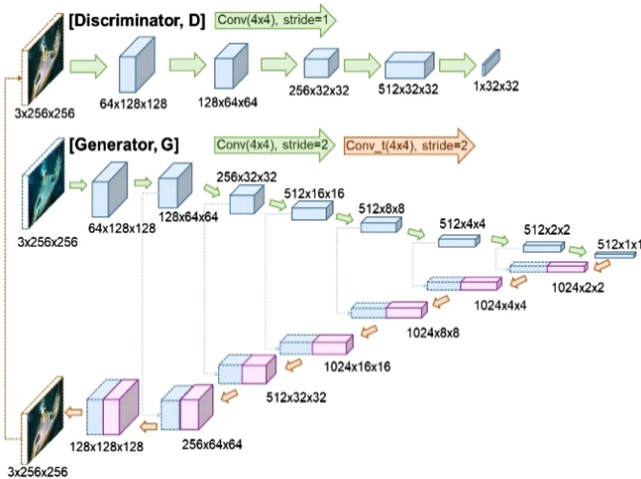


Fig. 1 UGAN network architecture: The generator transforms an underwater image into a fake clean image through a u-shape network consisting of an encoder and decoder. The discriminator takes the generated image as input and produces a 32×32 patch image to distinguish between the real clean image and the fake clean image.

3. Results

The performances of the DCP, two gradient transform methods, image fusion, cycleGAN, and UGAN were compared by evaluating the image quality of real underwater images taken in Korean waters. The enhancement was evaluated quantitatively based on UIQM, UCIQE, GW assumption, and blur metric.

UIQM was calculated using the weighted sum of colorfulness (UICM), sharpness (UISM), and contrast (UIConM) measures (Panetta et al., 2016). This study used the same weighting as Panetta et al. (2016); $a_1 = 0.0282$, $a_2 = 0.2983$, and $a_3 = 0.0339$. The computation of UIQM is expressed in Eq. (34):

$$\text{UIQM} = a_1 \text{UICM} + a_2 \text{UISM} + a_3 \text{UIConM} \quad (34)$$

UICM was measured by the mean and standard deviation in two combined color domains of the image to be evaluated; red-green and yellow-blue colors, as follows:

$$\text{UICM} = -0.0268 \sqrt{\mu_{\rho,rg}^2 + \mu_{\rho,yb}^2} + 0.1586 \sqrt{\sigma_{\rho,rg}^2 + \sigma_{\rho,yb}^2} \quad (35)$$

In the combined color domains, $I_{rg} = I_r - I_g$ and $I_{yb} = (I_r - I_g)/2 - I_b$. μ_α and σ_α are the mean and standard deviation of I_{rg} and I_{yb} . ρ is a ratio to trim the upper and lower intensity pixels. The UISM sharpness was evaluated based on the weighted sum of the difference between the maximum and minimum values in the edge map for each color channel, as shown in Eq. (36). The edge map was determined by the Sobel operator as follows:

$$\text{UISM} = \sum_c \delta_c \text{EME} [\text{Sobel}[I_c]] \quad (36)$$

$$\text{EME}[Edge_n] = \frac{2}{N} \sum_{n=1}^N \log \left[\frac{\max[Edge_n]}{\min[Edge_n]} \right] \quad (37)$$

where δ_c is a weight for each color channel. $\delta_r = 0.299$; $\delta_g = 0.587$; $\delta_b = 0.114$. $\text{EME}[\]$ divides the edge image, $\text{Sobel}[I_c]$, into N sub-blocks and calculates the logarithmic difference between the maximum and minimum values for each sub-block. It then outputs the mean of the difference in values over the sub-blocks. UIConM divided a gray-scaled image, I_{gray} into N sub-blocks and then calculates the parameterized logarithmic image processing operators, Θ , \oplus , and \otimes (Panetta et al., 2011), as follows:

$$\begin{aligned} \text{UIConM} &= \frac{1}{N} \otimes \sum_{n=1}^N \frac{\max[I_{gray,n}] \Theta \min[I_{gray,n}]}{\max[I_{gray,n}] \oplus \min[I_{gray,n}]} \\ &\times \log \frac{\max[I_{gray,n}] \Theta \min[I_{gray,n}]}{\max[I_{gray,n}] \oplus \min[I_{gray,n}]} \end{aligned} \quad (38)$$

UCIQE is calculated by a weighted sum of three measures in terms

of the chroma (σ_{chr}) and luminance (con_{Lum}) in CIELAB color space and saturation (μ_{sat}) (Yang and Sowmya 2015), as expressed in Eq. (39):

$$UCIQE = b_1 \sigma_{chr} + b_2 con_{Lum} + b_3 \mu_{sat} \quad (39)$$

In CIELAB color space, $[L, a, b]$ of an image, the standard deviation of chroma (σ_{chr}) was calculated by $\sqrt{a^2 + b^2}$. The contrast in the luminance channel (con_{Lum}) was determined by the mean value difference in the top 1% and bottom 1% of pixels in the luminance channel, $I_{L,top_1\%} - I_{L,bottom_1\%}$, respectively. The saturation measure (μ_{sat}) was calculated by $\sqrt{a^2 + b^2} / L$. The weighting for chroma, luminance, and saturation in UCIQE was set to $b_1=0.4680$, $b_2=0.2745$, and $b_3=0.2576$, respectively. Larger UIQM and UCIQE values indicate better enhancement performance.

The GW assumption is that an equal mixture of RGB color channels should be neutral gray under a color-balanced situation. An underwater GW assumption was used to measure the degree of color correction (Berman et al., 2018). Here, the calculation process for the GW value was modified with a standard deviation over three mean color values. The color balance improves as the GW becomes lower, as follows:

$$GW = \sqrt{\frac{1}{2} \sum_{c \in \{r, g, b\}} (\text{mean}[I_c] - \text{mean}[I_r, I_g, I_b])^2} \quad (40)$$

The blur metric is derived based on observing that humans find it difficult to perceive differences between a blurred and re-blurred image (Crété-Roffet et al., 2007). The blur measure compares the horizontal and vertical derivatives of an input and its blurred images by the max operator. Blur metric was normalized from 0 to 1; a larger blur metric value indicated more blurring.

$$B_{metric} = \max \left[\frac{I_{hor} - D_{hor}}{I_{hor}}, \frac{I_{ver} - D_{ver}}{I_{ver}} \right] \quad (41)$$

Directional sum, difference, and derivative operators were applied to input (I) and its blurred images ($I_b = \text{blur}[I_Y]$) in the luminance channel according to Eqs. (42) and (43). The $\text{blur}[\]$ operator averaged nine elements horizontally and vertically.

$$I_{dir} = \text{sum}_{dir} [|\nabla_{dir}[I_Y]|], \quad dir \in \{hor, ver\} \quad (42)$$

$$D_{dir} = \text{sum}_{dir} [\max[0, |\nabla_{dir}[I_Y]| - |\nabla_{dir}[I_b]|]] \quad (43)$$

If the input image already has high blurriness, the difference between the directional derivatives of the input and blurred image would be small, resulting in a larger blur metric value.

Figs. 2 to 4 present images enhanced using single enhancement methods from real underwater images. Three underwater images were

captured with a dominant greenish color tone and exposure to a strong light source from standard definition (SD) videos recorded in the late afternoon. Figs. 2 and 3 were taken in May 2015 at Jangmok Port, Geoje-si, Gyeongsangnam-do using a camera equipped with a Pro 4 ROV (VideoRay, USA). Fig. 4 was recorded in November 2017 at Yokjido, Tongyeong-si, Gyeongsangnam-do, using an SD camera equipped with a BlueROV (BlueRobotics, USA). All scenes were illuminated by LED lighting equipped in the ROVs. DCP, (b) in Figs. 2 to 4, tends to emphasize a green color in the overall scene and darkens the background signal. DCP was ineffective in correcting the greenish color cast effect, which is the main artifact of underwater imagery. Gradient transform with Tarel and Peng transmissions were sensitive to the brightness change in an underwater image, as shown in (c) and (d) of Figs. 2-3. This was also found to be ineffective in enhancing the object details, as illustrated in Figs. 4(c) and (d). Two gradient-Tarel and Peng inadequately corrected for the overall greenish color tone in all underwater images. Image fusion moderately compensated for the overall color tones in (e) of Figs. 2 to 4. On the other hand, it did not enhance the image contrast of objects or reduce the haziness in the background. CycleGAN provided good correction of the overall colors

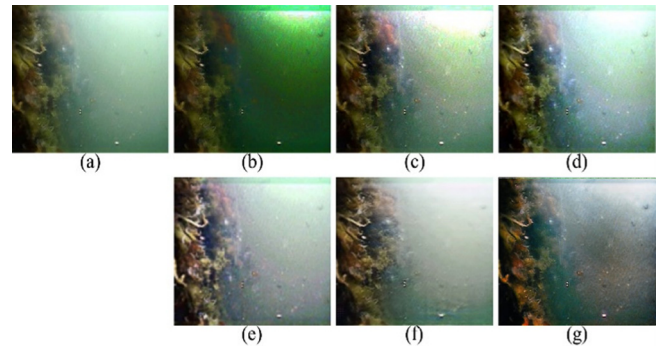


Fig. 2 (a) Real original underwater image of 481×416, showing a dominant greenish color tone and exposure to strong light at the top, and the enhanced images by (b) DCP, (c) gradient-Tarel, (d) gradient-Peng, (e) image fusion, (f) cycleGAN, and (g) UGAN.

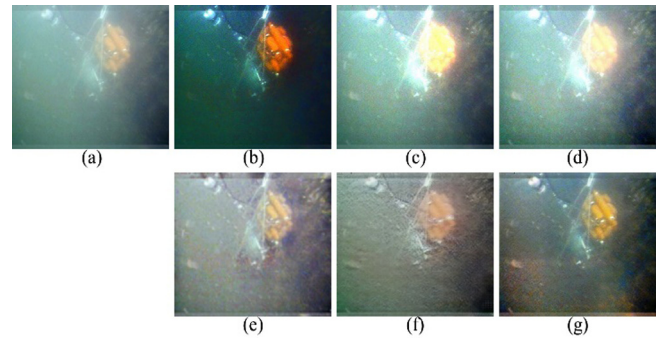


Fig. 3 (a) Real original underwater image of 481×416, showing a dominant greenish color tone and expose to strong light in the middle, and the enhanced images by (b) DCP, (c) gradient-Tarel, (d) gradient-Peng, (e) image fusion, (f) cycleGAN, and (g) UGAN.

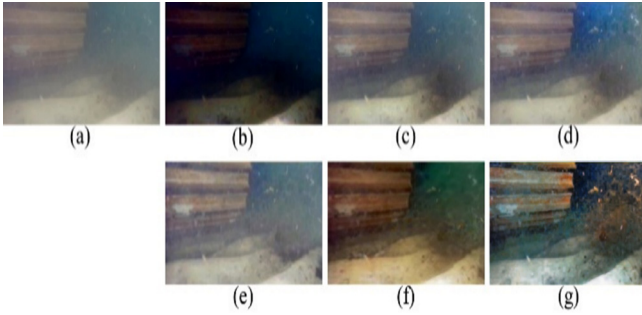


Fig. 4 (a) Real original underwater image of 711×406 , showing low contrast and visibility, and the enhanced images by (b) DCP, (c) Gradient-Tarel, (d) Gradient-Peng, (e) Image fusion, (f) CycleGAN, and (g) UGAN.

and enhanced the object details, but it generated artifacts in the background, as shown around objects in Fig. 3(f). UGAN provided good visual quality in terms of compensating for the greenish color tone, enhancing the object details, and reducing haziness comparing to the other enhancement methods in (g) of Figs. 2 to 4.

Tables 2 to 4 compare the figures of merit (FOM), i.e., UIQM, UCIQE, GW, blur metric, and computational time, evaluated from the original and the enhanced underwater images in Figs. 2 to 4. UIQM and UCIQE were difficult to interpret because they focus on different aspects depending on the example image. Unlike a visual comparison, two gradient transform methods and DCP obtained a high UIQM and UCIQE for Figs. 2 and 3. For all underwater images, DCP obtained the highest UCIQEs for Figs. 2 and 3 because of high color scores with respect to σ_{chr} and μ_{sat} . This might be due to DCP's tendency to increase the saturation of underwater images for a specific color. Gradient transform methods tended to emphasize the bright region exposed to light, which increases the sharpness and contrast score. Thus, two gradient transform methods had the highest UIQM and UCIQE because of the high sharpness ($UISM$) and contrast (con_{lum}) measures, respectively. Image fusion had the best and the worst scores in terms of the GW color quality and blur metrics, respectively. This shows that image fusion is effective in balancing underwater colors, but makes the images blurry. CycleGAN and UGAN showed high UIQM and UCIQE in all figures. Furthermore, the two GANs had better GW scores than the original underwater images and the same blur scores as the original image for Figs. 2 and 3. Marginal differences were observed between the two GANs in terms of all FOMs for Figs. 2 and 3. In terms of Fig. 4, UGAN had higher UIQM and GW scores than cycleGAN. The computational time associated with each enhancement method was compared on an Intel Core i7-7700HQ CPU. The training time of cycleGAN and UGAN are approximately 46 hours and 12 hours on a Nvidia Quadro P4000 GPU, respectively. The two GANs ran on Python with the Tensorflow framework. The other methods ran on MATLAB. Image fusion and two GANs had the best and moderate computational time performance, respectively, compared to the other single enhancement methods.

4. Discussion

This study applied single image enhancement approaches, DCP, gradient transform method with Tarel and Peng transmission maps, image fusion, and two GANs of cycleGAN and UGAN, to compensate for the color cast effect and low visibility due to the light attenuation underwater. The enhanced performance was evaluated in terms of UIQM, UCIQE, GW, and blur metrics with real underwater images taken in Korean waters.

The original DCP was proposed to improve the hazy outdoor images by saturating the inherent color in a haze-free image. Saturation with a specific color produced strong greenish or bluish hues on the underwater image; both are already dominant color tones in underwater images. In DCP, the user needs to adjust the patch size of the min operator in Eq. (3). The DCP result was evaluated with different patch sizes of 11×11 to 21×21 with intervals of 2; however, there were no different effects on color correction depending on patch sizes.

The gradient transform method recovers the underwater image from its gradient enhanced with an estimated transmission map and the gradient of the given input image. The gradient transform method with

Table 2 Figure of merits and computational time of original underwater image in Fig. 2 and single enhancements

	UIQM	UCIQE	GW	Blur metric	Computational time (s)
Original	2.20	29.20	0.052	0.36	-
DCP	2.62	33.40	0.094	0.36	13.3
Gradient-Tarel	4.29	31.06	0.043	0.31	12.3
Gradient-Peng	4.41	31.27	0.040	0.30	11.4
Image fusion	2.42	28.72	0.013	0.55	1.1
CycleGAN	2.25	29.06	0.024	0.35	1.5
UGAN	3.13	29.11	0.019	0.35	3.5

Table 3 Figure of merits and computational time of original underwater image in Fig. 3 and single enhancements

	UIQM	UCIQE	GW	Blur metric	Computational time (s)
Original	1.69	22.34	0.059	0.30	-
DCP	2.50	27.40	0.076	0.31	12.7
Gradient-Tarel	4.64	26.44	0.054	0.25	14.3
Gradient-Peng	4.87	27.96	0.054	0.24	12.3
Image fusion	2.03	22.11	0.008	0.50	0.7
CycleGAN	3.34	24.40	0.019	0.29	1.4
UGAN	4.09	27.92	0.029	0.32	3.5

Table 4 Figure of merits and computational time of original underwater image in Fig. 4 and single enhancements

	UIQM	UCIQE	GW	Blur metric	Computational time (s)
Original	0.48	12.12	0.008	0.44	-
DCP	1.13	22.38	0.033	0.44	18.6
Gradient-Tarel	1.27	16.61	0.005	0.43	20.0
Gradient-Peng	1.48	18.22	0.016	0.43	17.8
Image fusion	1.15	15.00	0.001	0.60	0.9
CycleGAN	1.62	26.06	0.071	0.44	1.4
UGAN	2.97	26.93	0.013	0.49	3.6

Tarel and Peng transmissions produced bright regions that appear as though they are exposed to strong light in Figs. 2 and 3. This method was also ineffective in reducing the color-cast effect and low visibility of underwater images. The adjustable parameters in the Tarel transmission estimation are the number of line segments and a patch size in Eq. (9). Successive numbers of line segments from 3 to 8 and different patch sizes from 41×41 to 101×101 in intervals of 20 were applied. On the other hand, there were no significant differences between the final enhanced images with different adjustable parameters. An estimation of Peng transmission can depend on the patch size for depth-related values in Eqs. (15) and (16) and the number of Gaussian kernel levels in Eq. (18). This study examined the dependency on different patch sizes from 5 to 17 in intervals of 3 and found little dependency on the patch size.

Image fusion had the worst blur scores in Figs. 2 to 4 and resulted in a loss of object detail. It contained a contrast enhancement step, which was replaced with CLAHE instead of gamma correction. The blurry results were attributed to the last fusion step, with multiple levels of Laplacian and Gaussian pyramids. When more than three levels of pyramids were set, the final result increased the blurriness. In contrast, small pyramid level numbers resulted in noisier images.

$$\tilde{J}(x) = \sum_E I^E(x) \omega^E(x), E \in \{\text{contrast}, \text{edge}\} \quad (44)$$

If naïve fusion is performed, as per Eq. (44), there is an increase in the sharpness of underwater images compared to multiscale fusion, but it produces random pattern artifacts in the background.

GAN might be affected by the generality of the training data to express underwater color images. Training data were constructed with ImageNet and real underwater images taken in Korean waters to identify the turbidity and color cast. The inclusion of real underwater imagery in Korean waters improved the color tone and visibility compared to the training data in the ImageNet database. The pre-trained cycleGAN was applied to improve underwater image quality and generate underwater and clean image pairs for training UGAN. CycleGAN and UGAN were compared to confirm the

performances of unsupervised and supervised learning for single image enhancement because they do not require additional data, such as a depth map for training. CycleGAN had incomplete enhancement performance producing artifacts in the background. UGAN acted moderately to enhance the color balance and visibility of underwater images compared to the other enhancement methods, but it was not effective in dehazing the underwater images. To enhance visibility, a new network architecture needs to be constructed and trained with the paired underwater images and additional information like depth maps (Li et al., 2018b).

UIQM and UCIQE are popular FOMs used in studies of underwater enhancement. The method to combine three quality measures in UIQM and UCIQE is dependent on the weights in Eqs. (34) and (39). On the other hand, there were no proposed ways to determine the weights properly. In this study, it was difficult to interpret the general tendencies of UIQM and UCIQE because these FOMs fluctuated in each case by case, and the quantitative interpretations based on the scores were different from the visual comparisons. It is necessary to normalize the individual image quality measure of UIQM and UCIQE and to set reasonable weights to evaluate the overall image quality adequately. The GW assumption and blur metric were adopted to evaluate color balancing and blurriness in the enhanced underwater image. Individual FOMs, such as GW and blur metrics, reflected the consistent quantitative image quality measures compared to the combined FOMs of UIQM and UCIQE for underwater images.

5. Conclusions

In this study, six single underwater image enhancement approaches were compared: DCP, two gradient transforms, image fusion, and two GANs. The enhancement performances were evaluated qualitatively and quantitatively. DCP caused saturation of the underwater images to either a greenish or bluish color tone and reduced the brightness of the background signal. The gradient transform methods with two transmission maps were sensitive to the light source and highlighted the region exposed to light. Image fusion provided reasonable color correction, but the object details were lost due to the last fusion step. CycleGAN corrected the overall color tone well, but generated artifacts in the background. Although UGAN was not rated with the best scores for three sample images, it showed fairly good visual quality and quantitative scores for all FOMs.

Acknowledgments

This study was supported in part by research grants from Basic Science Research Program through the National Research Foundation of Korea (NRF) funded by the Ministry of Education (NRF-2018R1D1A1B07049296), and by the project titled 'Development of the support vessel and systems for the offshore field test and evaluation of offshore equipment', funded by the Ministry of Oceans and Fisheries (MOF), Korea.

References

- Achantay, R., Hemamiz, S., Estraday, F., & Susstrunk, S. (2009). Frequency Tuned Salient Region Detection. *Proceeding of IEEE Conference on Computer Vision and Pattern Recognition*, Miami, FL, USA, 1597-1604. <https://doi.org/10.1109/CVPR.2009.5206596>
- Ancuti, C.O., Ancuti, C., Vleeschouwer, C.D., & Bekaert, P. (2017). Color Balance and Fusion for Underwater Image Enhancement. *IEEE Transactions on Image Processing*, 27(1), 379-393. <https://doi.org/10.1109/TIP.2017.2759252>
- Anwar, S., Li, C., & Porikli, F. (2018). Deep Underwater Image enhancement. arXiv:1807.03528. Retrieved from <https://arxiv.org/abs/1807.03528>
- Anwar S. & Li, C. (2019). Diving Deeper into Underwater Image Enhancement: A Survey. arXiv:1907.07863. Retrieved 2019 from <https://arxiv.org/abs/1907.07863>
- Arjovsky, M., Chintala, S., & Bottou, L. (2017). Wasserstein GAN. arXiv:1701.07875. Retrieved from <https://arxiv.org/abs/1701.07875>
- Arnold-Bos, A., Malkasse, J.-P., & Kervern, G. (2005). A Preprocessing Framework for Automatic Underwater Images Denoising. *Proceeding of European Conference on Propagation and Systems*, Brest, France, 1-8. Retrieved from <https://hal.archives-ouvertes.fr/hal-00494314>
- Bazeille, S., Quidu, I., Jaulin, L., & Malkasse, J.-P. (2006). Automatic Underwater Image Pre-processing. *Proceeding of Characterisation Du Milieu Marin*, 16-19. Retrieved from <https://hal.archives-ouvertes.fr/hal-00504893/>
- Berman, D., Levy, D., Avidan, S., & Treibitz, T. (2018). Underwater single Image Color Restoration Using Haze-lines and a New Quantitative Dataset. arXiv:1811.01343. Retrieved from <https://arxiv.org/abs/1811.01343>
- Cao, K., Peng, Y., & Cosman, P. (2018). Underwater Image Restoration Using Deep Networks to Estimate Background Light and Scene Depth. *Proceeding of IEEE Southwest Symposium on Image Analysis and Interpretation*, Las Vegas, NV, USA, 1-4. <https://doi.org/10.1109/SSIAL.2018.8470347>
- Carlevaris-Bianco, N., Mohan, A., & Eustice, R.M. (2010). Initial Results in Underwater Single Image Dehazing. *Proceeding of Oceans 2010 MTS/IEEE Seattle*, WA, USA, 1-8. <https://doi.org/10.1109/OCEANS.2010.5664428>
- Cho, Y., Jeong, J., Kim A. (2018). Model-assisted Multiband Fusion for Single Image Enhancement and Applications to Robot Vision. *IEEE Robotics and Automation Letters*, 3(4), 2822-2829. <https://doi.org/10.1109/LRA.2018.2843127>
- Crété-Roffet, F., Dolmière, T., Ladret, P., & Nicolas, M. (2007). The Blur Effect: Perception and Estimation with a New No-Reference Perceptual Blur Metric. *Proceeding SPIE Electronic Imaging Symposium Conf Human Vision and Electronic Imaging*, San Jose, USA, EI6492-16. Retrieved from <https://hal.archives-ouvertes.fr/hal-00232709>
- Deng, J., Dong, W., Socher, R., Li, L.-J., Li, K., & Fei-Fei, L. (2009). Imagenet: A Large-scale Hierarchical Image Database. *Proceeding of IEEE Conference on Computer Vision and Pattern Recognition*, Miami, FL, USA, 248-255. <https://doi.org/10.1109/CVPR.2009.5206848>
- Dreus, P., Nascimento, E., Moraes, F., Botelho, S., & Campos, M. (2013). Transmission Estimation in Underwater Single Images. *Proceeding of IEEE International Conference on Computer Vision Workshops*, Sydney, NSW, Australia, 825-830. <https://doi.org/10.1109/ICCVW.2013.113>
- Fabbri, C., Islam, M.J., & Sattar, J. (2018). Enhancing Underwater Imagery Using Generative Adversarial Networks. *Proceeding of IEEE International Conference on Robotics and Automation*, Brisbane, QLD, Australia, 7159-7165. <https://doi.org/10.1109/ICRA.2018.8460552>
- Fattal, R. (2008). Single Image Dehazing. *ACM Transactions on Graphics*, 27(3), 1-9. <https://doi.org/10.1145/1360612.1360671>
- Ghani, A.S.A., & Isa, N.A.M. (2014). Underwater Image Quality Enhancement Trough Composition of Dual-intensity Images and Rayleigh-stretching. *SpringerPlus*, 3, 757. <https://doi.org/10.1186/2193-1801-3-757>
- Ghani, A.S.A., & Isa, N.A.M. (2015). Underwater Image Quality Enhancement Through Integrated Color Model with Rayleigh Distribution. *Applied Soft Computing*, 27, 219-230. <https://doi.org/10.1016/j.asoc.2014.11.020>
- Guo, Y., Li, H., & Zhuang, P. (2019). Underwater Image Enhancement Using a Multiscale Dense Generative Adversarial Network. *IEEE Journal of Oceanic Engineering*, 45(3), 862-870. <https://doi.org/10.1109/JOE.2019.2911447>
- He, K., Sun, J., & Tang, X. (2011). Single Image Haze Removal Using Dark Channel Prior. *IEEE Transactions on Pattern Analysis and Machine Intelligence*, 33(12), 2341-2353. <https://doi.org/10.1109/TPAMI.2010.168>
- Hou, M., Liu, R., Fan, X., & Luo, Z. (2018). Joint Residual Learning for Underwater Image Enhancement. *Proceeding of IEEE International Conference on Image Processing*, Athens, Greece, 4043-4047. <https://doi.org/10.1109/ICIP.2018.8451209>
- Isola, P., Zhu, J., Zhou, T., & Efros, A.A. (2017). Image-to-Image Translation with Conditional Adversarial Networks. arXiv:1611.07004. Retrieved from <https://arxiv.org/abs/1611.07004>
- Jian S., & Wen, W. (2017). Study on Underwater Image Denoising Algorithm Based on Wavelet Transform. *Journal of Physics: Conference Series*, 806, 012006. Retrieved from <https://iopscience.iop.org/article/10.1088/1742-6596/806/1/012006>
- Khan, A., Ali, S.S.A., Malik, A., Anwer, A., & Meriaudeau, F. (2016). Underwater Image Enhancement by Wavelet Based Fusion. *Proceeding of IEEE International Conference on Underwater System Technology: Theory and Applications*, Penang, Malaysia, 83-88. <https://doi.org/10.1109/USYS.2016.7893927>
- Li, W.J., Gu, B., Huang, J.T., Wang, S.Y., & Wang, M.H. (2012). Single Image Visibility Enhancement in Gradient Domain. *IET Image Processing*, 6(5), 589-595. <https://doi.org/10.1049/iet-ipr.2010>

0574

- Li, C., Guo, C., & Guo, J. (2018a). Emerging from Water: Underwater Image Color Correction Based on Weakly Supervised Color Transfer. *IEEE Signal Processing Letters*, 25(3), 232-327. <https://doi.org/10.1109/LSP.2018.2792050>
- Li, J., Skinner, K., Eustice, R., & Johnson-Roberson, M. (2018b). Watergan: Unsupervised Generative Network to Enable Real-time Color Correction of Monocular Underwater Images. *IEEE Robotics and Automation Letters*, 3(1), 387-394. <https://doi.org/10.1109/LRA.2017.2730363>.
- Li, C., Guo, C., Ren, W., Cong, R., Hou, J., & Kwong, S. (2019a). An Underwater Image Enhancement Dataset and Beyond. arXiv:1901.05495. Retrieved from <https://arxiv.org/abs/1901.05495>
- Li, H., Li, J., & Wang, W. (2019b). A Fusion Adversarial Underwater Image Enhancement Network with a Public Test Dataset. arXiv:1906.06819. Retrieved from <https://arxiv.org/abs/1906.06819>
- Luo, M., Fang, Y., & Ge, Y. (2019). An Effective Underwater Image Enhancement Method Based on CLAHE-HF. *Journal of Physics: Conference Series*, 1237(3), 032009. Retrieved from <https://iopscience.iop.org/article/10.1088/1742-6596/1237/3/032009>
- Mathieu, M., Couprie, C., & LeCun, Y. (2015). Deep Multi-Scale Video Prediction Beyond Mean Square Error. arXiv:1511.05440. Retrieved from <https://arxiv.org/abs/1511.05440>
- Mi, Z., Zhou, H., Zheng, Y., & Wang, M. (2016). Single Image Dehazing via Multiscale Gradient Domain Contrast Enhancement. *IET Image Processing*, 10(3), 206-214. <https://doi.org/10.1049/iet-ipr.2015.0112>
- Mobley, C. (1994). *Light and Water: Radiative Transfer in Natural Waters*. San Diego: Academic Press.
- Panetta, K., Aghaian, S., Zhou, Y., & Wharton, E.J. (2011). Parameterized Logarithmic Framework for Image Enhancement. *IEEE Transactions on Systems, Man, and Cybernetics, Part B*, 41(2), 460-473. <https://doi.org/10.1109/TSMCB.2010.2058847>
- Panetta, K., Gao, C., & Aghaian, S. (2016). Human-Visual-System-Inspired Underwater Image Quality Measures. *IEEE Journal of Oceanic Engineering*, 41(3), 541-551. <https://doi.org/10.1109/JOE.2015.2469915>
- Park, E.P., & Sim, J. (2017). Gradient-based Contrast Enhancement and Color Correction for Underwater Images. *Proceeding of Asia-Pacific Signal and Information Processing Association Annual Summit and Conference*, Kuala Lumpur, Malaysia, 1444-1447. <https://doi.org/10.1109/APSIPA.2017.8282259>
- Peng, Y., & Cosman, P.C. (2017). Underwater Image Restoration Based on Image Blurriness and Light Absorption. *IEEE Transactions on Image Processing*, 26(4), 1579-1594. <https://doi.org/10.1109/TIP.2017.2663846>
- Ronneberger, O., Fischer, P., & Brox, T. (2015). U-net: Convolutional Networks for Biomedical Image Segmentation. arXiv:1505.04597. Retrieved from <https://arxiv.org/abs/1505.04597>
- Roser, M., Dunbabin, M., & Geiger, A. (2014). Simultaneous Underwater Visibility Assessment, Enhancement and Improved Stereo. *Proceeding of IEEE International Conference on Robotics and Automation*, Hong Kong, China, 3840-3847. <https://doi.org/10.1109/ICRA.2014.6907416>
- Simchony, T., Chellappa R., & Shao, M. (1990). Direct Analytical Methods for Solving Poisson Equations in Computer Vision Problems. *IEEE Transactions on Pattern Analysis and Machine Intelligence*, 12(5), 435-446. <https://doi.org/10.1109/34.55103>
- Sun, X., Liu, L., Li, Q., Dong, J., Lima, E., & Yin, R. (2018). Deep Pixel to Pixel Network for Underwater Image Enhancement and Restoration. *IET Image Processing*, 13(3), 469-474. <https://doi.org/10.1049/iet-ipr.2018.5237>
- Tarel, J., & Hautière, N. (2009). Fast Visibility Restoration from a Single Color or Gray Level Image. *Proceeding of IEEE International Conference on Computer Vision*, Kyoto, Japan, 2201-2208. <https://doi.org/10.1109/ICCV.2009.5459251>
- Treibitz, T., & Schechner, Y.Y. (2012). Turbid Scene Enhancement Using Multi-Directional Illumination Fusion. *IEEE Transactions on Image Processing*, 21(11), 4662-4667. <https://doi.org/10.1109/TIP.2012.2208978>
- Uplavikar, P., Wu, Z., & Wang, Z. (2019). All-in-One Underwater Image Enhancement Using Domain-Adversarial Learning. arXiv:1905.13342. Retrieved from <https://arxiv.org/abs/1905.13342>
- Vincent, L. (1993). Morphological Grayscale Reconstruction in Image Analysis: Applications and Efficient Algorithms. *IEEE Transactions on Image Processing*, 2(2), 176-201. <https://doi.org/10.1109/83.217222>
- Wang, Y., Ding, X., Wang, R., Zhang, J., & Fu, X. (2017a). Fusion-Based Underwater Image Enhancement by Wavelet Decomposition. *Proceeding of IEEE International Conference on Industrial Technology*, Toronto, ON, Canada, 1013-1018. <https://doi.org/10.1109/ICIT.2017.7915500>
- Wang, Y., Zhang, J., Cao, Y., & Wang, Z. (2017b). A Deep CNN Method for Underwater Image Enhancement. *Proceeding of IEEE International Conference on Image Processing*, Beijing, China, 1382-1386. <https://doi.org/10.1109/ICIP.2017.8296508>
- Wang, Y., Song, W., Fortino, G., Qi, L.-Z., Zhang, W., & Liotta, A. (2019). An Experimental-Based Review of Image Enhancement and Image Restoration Methods for Underwater Imaging. *IEEE Access*, 7, 140233-140251. <https://doi.org/10.1109/ACCESS.2019.2932130>
- Yang, M., & Sowmya, A. (2015). An Underwater Color Image Quality Evaluation Metric. *IEEE Transactions on Image Processing*, 24(12), 6062-6071. <https://doi.org/10.1109/TIP.2015.2491020>
- Yang, M., Hu, J., Li, C., Rohde, G., Du, Y., & Hu, K. (2019). An In-Depth Survey of Underwater Image Enhancement and Restoration. *IEEE Access*, 7, 123638-123657. <https://doi.org/10.1109/ACCESS.2019.2932611>
- Zetian, M., Zheng, L., Yafei, W., Xianping, F., & Zhengyu, C. (2018). Multiscale Gradient Domain Underwater Image Enhancement. *Proceeding of 2018 Oceans - MTS/IEEE Kobe Techno-Oceans*, Kobe, Japan, 1-5. <https://doi.org/10.1109/OCEANSKOB.2018>

8559180

Zhao, X., Tao, J., & Song, Q. (2015). Deriving Inherent Optical Properties from Background Color and Underwater Image Enhancement. *Ocean Engineering*, 94, 163-172. <https://doi.org/10.1016/j.oceaneng.2014.11.036>

Zhang, S., Zhang, J., Fang, S., & Cao, Y. (2014). Underwater Stereo Image Enhancement Using a New Physical Model. *Proceeding of IEEE International Conference on Image Processing, Paris, France*, 5422-5426. <https://doi.org/10.1109/ICIP.2014.7026097>

Zhu, J., Park, T., Isola, P., & Efros, A.A. (2018). Unpaired

Image-to-Image Translation Using Cycle-Consistent Adversarial Networks. arXiv:1703.10593. Retrieved from <https://arxiv.org/abs/1703.10593>

Author ORCIDs

Author name	ORCID
Kim, Do Gyun	0000-0002-2574-962X
Kim, Soo Mee	0000-0001-8414-1297

Response Analysis of MW-Class Floating Offshore Wind Power System using International Standard IEC61400-3-2

Youngjae Yu¹ and Hyunkyung Shin²

¹Graduate Student, Department of Floating Offshore Wind Power Generation Systems, University of Ulsan, Ulsan, Korea

²Professor, Department of Floating Offshore Wind Power Generation Systems, University of Ulsan, Ulsan, Korea

KEY WORDS: Floating offshore wind power system, Response analysis, Extreme sea state, IEC61400-3-2, Fault condition

ABSTRACT: In 2019, the Korean government announced the 3rd Basic Plan for Energy, which included expanding the rate of renewable energy generation by 30-40% by 2040. Hence, offshore wind power generation, which is relatively easy to construct in large areas, should be considered. The East Sea coast of Korea is a sea area where the depth reaches 50 m, which is deeper than the west coast, even though it is only 2.5 km away from the coastline. Therefore, for offshore wind power projects on the East Sea coast, a floating offshore wind power should be considered instead of a fixed one. In this study, a response analysis was performed by applying the analytical conditions of IEC61400-3-2 for the design of floating offshore wind power generation systems. In the newly revised IEC61400-3-2 international standard, design load cases to be considered in floating offshore wind power systems are specified. The upper structure applied to the numerical analysis was a 5-MW-class wind generator developed by the National Renewable Energy Laboratory (NREL), and the marine environment conditions required for the analysis were based on the Ulsan Meteorological Buoy data from the Korea Meteorological Administration. The FAST v8 developed by NREL was used in the coupled analysis. From the simulation, the maximum response of the six degrees-of-freedom motion and the maximum load response of the joint part were compared. Additionally, redundancy was verified under abnormal conditions. The results indicate that the platform has a maximum displacement radius of approximately 40 m under an extreme sea state, and when one mooring line is broken, this distance increased to approximately 565 m. In conclusion, redundancy should be verified to determine the design of floating offshore wind farms or the arrangement of mooring systems.

Nomenclature

α	Power exponent alpha
ECM	Extreme current model
ESS	Extreme sea state
EWM	Extreme wind speed model
EWLR	Extreme water level range
MBL	Minimum breaking load (kN)
MSL	Mean sea level
NCM	Normal current model
NSS	Normal sea state
NTM	Normal turbulence model
NWLR	Normal water level range
SSS	Severe sea state
SWL	Sea water level
z_h	Hub height above sea water level (m)
z_r	Reference height above sea water level (m)

1. Introduction

In 2017, the South Korean government established a plan to increase the rate of renewable energy development to 20% by 2030 through the Renewable Energy 3020 Policy. To achieve this, the security of additional renewable energy installation of 48.7 GW is required by 2030, among which 16.5 GW will be replaced by wind power generation. According to a detailed plan published by the Ministry of Trade, Industry, and Energy, approximately 13 GW will be provided by offshore wind power generation. The resource technical saving potential of the domestic offshore wind power is approximately 33.2 GW, whereas the geological saving potential including the offshore with a water level exceeding 50 m is approximately 215.9 GW (Korea New & Renewable Energy Center, 2016). Based on these values, to achieve the policy objectives seamlessly, offshore wind power generation must be considered because of the high wind resource-saving potential and relatively easy construction of large-scale

Received 5 September 2020, revised 22 November 2020, accepted 30 November 2020

Corresponding author Hyunkyung Shin: +82-52-259-2692, hkshin@ulsan.ac.kr

© 2020, The Korean Society of Ocean Engineers

This is an open access article distributed under the terms of the creative commons attribution non-commercial license (<http://creativecommons.org/licenses/by-nc/4.0>) which permits unrestricted non-commercial use, distribution, and reproduction in any medium, provided the original work is properly cited.

complexes. Moreover, the depth of the East Sea coast of Korea reaches 50 m even though it is only 2.5 km away from the coastline, and the depth of water becomes deeper rapidly compared with those of the west and south coasts. Therefore, it is more suitable to consider the floating system instead of the fixed system for offshore wind power generation on the east coast. In this study, the response analysis of a 5-MW-Class floating offshore wind power generation system was performed while applying the marine environmental conditions of the east coast, and the spar-type platform of the Offshore code comparison collaboration (OC3) project was applied as a substructure. The target sea area for the installation was determined to be the sea with a 150-m-deep water level near the east sea gas field that is 58 km away from the Ulsan port. For a marine environment, the extreme marine design external force was estimated using the data of the Ulsan automatic ocean observation buoy managed by the meteorological office (KMA, 2020). The numerical analysis was performed under an extreme marine environmental condition and the failure condition considered in the floating offshore wind power generation system specified in the IEC61400-3-2 standard revised in April 2019. Based on the numerical analysis results, the six degree-of-freedom motion response and maximum load response were proposed, and the drift response of the floating structure in the one mooring chain fracture condition was identified.

2. Numerical Analysis Input

2.1 Floating Offshore Wind Power Systems

The 5-MW-Class wind power generator of the National Renewable Energy Laboratory (NREL) was utilized for the upper structure of the floating offshore wind power generation system in the numerical analysis. The NREL 5-MW-Class wind power generator is a model widely used in numerous studies worldwide (Jonkman et al, 2009). The properties of the upper turbine are summarized in Table 1. For the lower floating platform, the cylindrical floating platform used in the OC3 (offshore code comparison collaboration) project manufactured by IEA Wind Task 23 was utilized, the shape of which is shown in Fig. 1 (Jonkman, 2010). The OC3-Spar floating platform is shaped as a symmetrical cylinder, and its six degrees-of-freedom motion response is less sensitive to the different operating directions of hydraulic force compared with floating platforms of different shapes.

Table 1 NREL 5-MW baseline wind turbine properties

Rating	5 MW
Rotor, hub diameter	126 m, 3 m
Hub height	90 m
Cut-In/Out wind speed	3 m/s / 25 m/s
Rated wind speed	11.4 m/s
Rotor mass	111,000 kg
Nacelle mass	240,000 kg
Tower mass	347,460 kg
Overall center of mass	(-0.2 m, 0.0 m, 64.0 m)

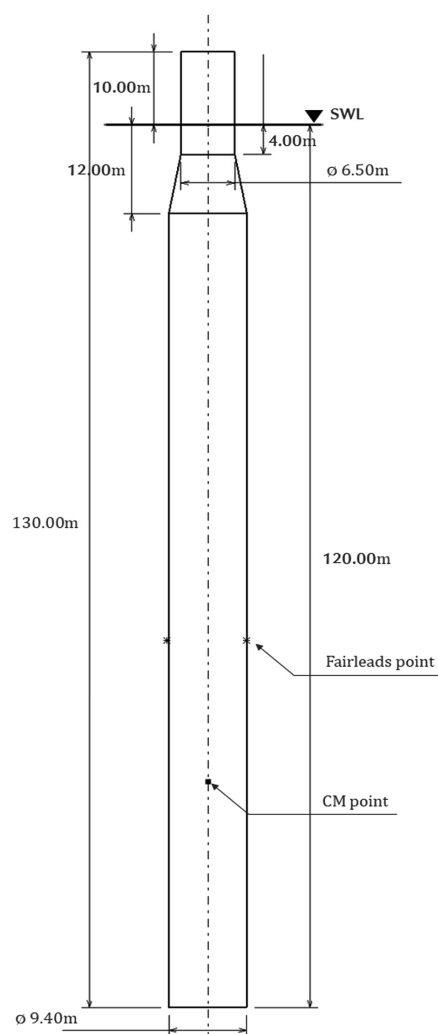


Fig. 1 OC3 Spar platform general arrangement

The specifications of the floating platform are summarized in Table 2, and because the mooring system designed in the OC3 project reflects the water depth of 320 m, a mooring system was redesigned based on the 150-m water depth of the sea near the east sea gas field in this study. During this process, the angle of the mooring chain connected at the fairlead and the pretension was maintained identical, and the touchdown length at the sea bottom was designed to be longer to prevent lift up at the anchor. Information regarding the mooring system of the OC3-spar floating platform and the redesigned mooring system is summarized in Table 3.

Table 2 OC3 spar floating platform properties

Depth to platform base below SWL	120 m
Elevation to platform top above SWL	10 m
Platform mass, Including ballast	7,466,330 kg
Center of mass (CM) location below SWL	89.9155 m
Platform roll inertia about CM	4,229,230,000 kg·m ²
Platform pitch inertia about CM	4,229,230,000 kg·m ²
Platform yaw Inertia about platform centerline	164,230,000 kg·m ²

Table 3 OC3 spar mooring system arrangement

Parameters	Original	Redesigned
Number of mooring lines	3	3
Angle between adjacent lines	120°	120°
Depth to anchors below SWL	320 m	150 m
Depth to fairlead below SWL	70 m	70 m
Radius to anchors from platform center line	853.87 m	485.4 m
Radius to fairlead from platform center line	5.2 m	5.2 m
Unstretched mooring line length	902.2 m	500 m
Mooring line diameter	0.09 m	0.117 m
Equivalent mooring line mass density	77.707 kg/m	300 kg/m
Equivalent mooring line weight in water	698.09 N/m	2567 N/m
Equivalent mooring line extensional stiffness	384,243,000 N	1.30E+09 N
Additional yaw spring stiffness	98,340,000 N·m/rad	98,340,000 N·m/rad

2.2 Environmental Conditions

In this study, the environmental conditions of the sea near the east sea gas field that is 58 km away from the Ulsan offshore were utilized as input data to design the external force. The gas production in the east sea gas field platform is scheduled to be halted in June 2021, and it is planned to be used to develop a floating offshore wind power generation complex thereafter. The depth of water in this sea is approximately 150 m, and because actual measurement data of the east sea gas field are currently unavailable, the analysis was conducted using the measurement data of the Ulsan automatic ocean observation buoy managed by the meteorological office. The Ulsan automatic ocean observation buoy is located approximately 17 km away from the east sea gas field platform, and it has been measuring marine physics from October 2015 until the present day. To estimate the offshore design external force, the measurement data from 3 years (from 2016 to 2018) were used, and the meta information of the analyzed data are provided in Table 4. The wind speed at a height of 4.3 m measured at the buoy was converted to the wind speed at 100 m height by applying the power law wind shear expressed in Eq. (1) based on the IEC61400-3-1 standard. For the extreme statistical analysis for estimating the extreme marine design external force, the Gumbel method presented in Eq. (2) was utilized, and 36 standard datasets were used by extracting 12 peak values from one year.

$$V(z_h) = V(z_r) \left(\frac{z_h}{z_r} \right)^\alpha \quad (1)$$

$$\text{Gumbel CDF, } F(x) = \exp \left\{ - \exp \left[\frac{-(x-\mu)}{\beta} \right] \right\} \quad (2)$$

Table 4 Meta information of Ulsan meteorological buoy data

Data set	Ulsan buoy (22189)
Data acquisition date	2016-01-01 00:00 to 2019-01-01 00:00
Location coordinate	N35.345 E129.841
Measure interval	1 h
Measure height	4.3 m
Power law exponent alpha (α)	Average = 0.14 / Ultimate = 0.11
Extreme statistic method	Gumbel method

Table 5 Marine environmental condition of East Sea gas field

Wind speed	Wave height	Wave period	Current velocity	Highest water level
11.4 m/s	2.50 m	7.53 s	101.3 cm/s	0.0 m
25 m/s	8.88 m	12.44 s	101.3 cm/s	0.33 m
39.83 m/s	11.12 m	14.17 s	163.0 cm/s	0.7 m

Based on the extreme statistical analysis results, the extreme wind speed for the 50-year cycle was estimated to be 39.83 m/s, and for the regression analysis coefficient of the Gumbel function, a scale parameter (β) of 1.802 and a mode parameter (μ) of 19.798 were applied. The 50-year cycle extreme significant wave height value was calculated to be 11.117 m, and a β of 1.206 and μ of 6.411 were applied. Moreover, the correlation between the wave period and wind speed of the target sea along with the selection of extreme current were determined based on a paper published by the coauthor of this study (Shin et al, 2019). Table 5 presents the waves, current velocity, and tide level at different wind speeds used as input data for the numerical analysis. The main directions of the measured wind were Northeast, Southwest, and South-Southwest, whereas the main directions of the wave were North, Northeast, and South.

2.3 Design Load Cases

In the IEC61400-3-2 newly revised in April 2019, the analysis conditions that must be considered in the floating system are specified, i.e., DLC9.x is a fault condition at the normal operation status, and DLC10.x is a fault condition under extreme marine environment. The fault condition of the floating offshore wind power generation system defines the fracture of the one mooring chain and a leakage condition due to the damage to the floating platform. In this study, to investigate the response characteristics of the floating platform in an extreme marine condition, DLC1.6 and DLC6.1 were selected by referring to the IEC61400-3-1 standard. Furthermore, to analyze the drifting response of a floating platform due to the fracture of a mooring chain specified in the IEC61400-3-2 standard, the DLC9.2 and DLC10.2 conditions were selected (IEC, 2019a; IEC, 2019b). The design load cases for which the numerical analysis was performed are tabulated in Table 6. DLC1.6 is a normal operation status, where the wind power generator produces electricity and the severe sea state was applied for the marine condition. The most severe marine state in the power

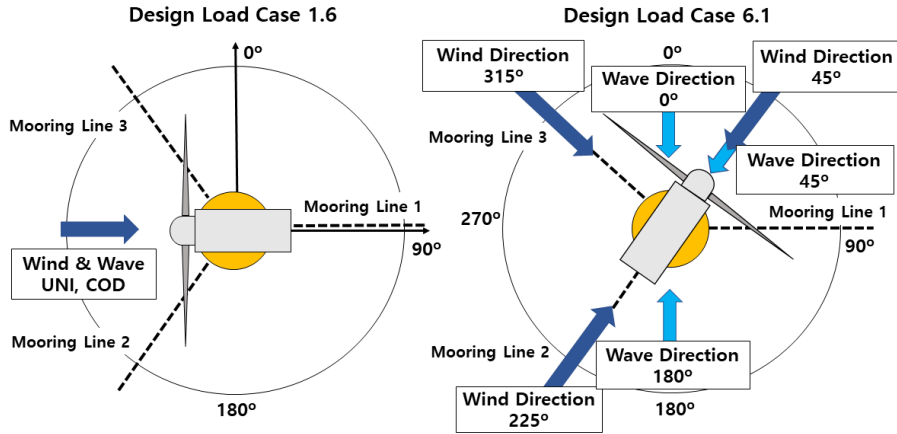


Fig. 2 Configurations of DLC1.6 and DLC6.1

Table 6 Design load cases for numerical simulation

DLC	Condition	Wind	Wave	Current	Water level
1.6	Power production	NTM	SSS	NCM	NWLR
6.1	Parked	EWM	ESS	ECM	EWLR
9.2	Power production	NTM	NSS	NCM	MSL
10.2	Parked	EWM	ESS	ECM	EWLR

production condition is a cut-out wind speed of 25 m/s, and the corresponding significant wave height is 8.88 m. DLC6.1 is a condition that considers the extreme marine condition with a 50-year duration of the design life, and it is a parked state where the wind power generator does not produce electricity. The extreme design wind speed for the 50-year duration for the east sea gas field is 39.83 m/s, and the corresponding significant wave height is 11.12 m. DLC9.2 is a normal sea state condition at a power production condition and the external force at a rated wind speed of 11.4 m/s, where the maximum thrust of the upper turbine is produced, is applied. To investigate the maximum response characteristics based on the direction of the environmental load, the environmental external force of nine directions was applied in DLC6.1 by combining the main directions of wind and wave, as shown in Fig. 2. The multidirection and misalignment conditions of the environmental load must be considered in DLC9.2 and DLC10.2. However, in this study, the numerical analysis was performed using only the design external force of the single direction to investigate the maximum response characteristics. The load response results at each analytical condition were suggested using the safety factor tabulated in Table 7.

Table 7 IEC61400-3-2 safety factor recommendation

Design load case	Notes
Ultimate (1.1, 1.3-1.6, 2.1, 3.2, 3.3, 4.2, 5.1, 6.1, 6.3, 8.1a)	IEC safety factor is 1.35. IEC return period is 50 years.
Abnormal (6.2, 7.1, 8.2, 9.2, 9.3, 10.2, 10.3)	Safety factor for abnormal load cases is 1.1 in general.

2.4 Numerical Analysis Tool

For the numerical analysis, Fast v8, a complex coupled analysis tool developed at the NREL (USA), was used (Jonkman and Buhl, 2005). The hydrodynamic force applied at the OC3 Spar floating platform was calculated using the University of Ulsan in-house code and was inserted in the Hydrodyn as an input value. The wind turbulence, which comprised three random seeds, was generated using TurbSim. The wave comprised two random seeds with Jonswap spectrum irregular waves applied for 1 h. Therefore, each analysis condition comprised six simulations with a duration of 1 h. For the numerical analysis results, the maximum value of the time series was extracted using Mextremes, a post-processing program, and the first 200 s of the analysis initial stage, which was a transient response region, was disregarded. Fig. 3 shows the flow diagram of the numerical analysis simulation.

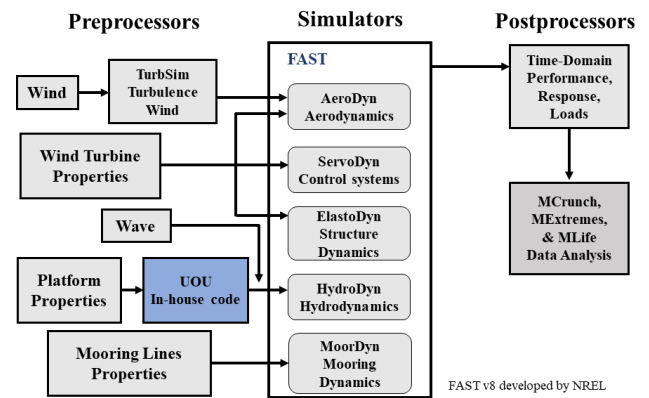


Fig. 3 FAST simulation flow chart

3. Numerical Analysis Result

3.1 Ultimate Response Verification

Table 8 presents the maximum six degree-of-freedom motion response that occurred in DLC1.6 and DLC6.1. The straight-line motion of the floating platform in the sea was governed by the hydraulic force; hence, the surge and heave responses were greater at

Table 8 Platform displacement of DLC1.6 and DLC6.1

	Platform displacement			
	DLC1.6		DLC6.1	
	Maximum	Mean	Maximum	Mean
Surge (m)	26.16	21.76	37.94	31.75
Sway (m)	1.41	0.50	3.84	0.24
Heave (m)	2.96	0.92	6.67	3.57
Roll (°)	1.50	0.56	3.61	0.23
Pitch (°)	4.63	2.00	5.49	3.64
Yaw (°)	4.06	0.29	9.51	0.37

Table 9 Maximum bending moment of DLC1.6 and DLC6.1

	Maximum bending moment			
	Blade root (kN·m)		Tower base (kN·m)	
	DLC1.6	DLC6.1	DLC1.6	DLC6.1
	13903.39	21779.25	196360.20	177432.42

Table 10 Maximum fairlead tension of DLC1.6 and DLC6.1

	Maximum fairlead tension		
	Line1 [kN]	Line2 [kN]	Line3 [kN]
	DLC1.6	632.48	2331.45
DLC6.1	516.11	5518.80	5625.45

DLC6.1 with a larger significant wave height applied. Yaw motions of 4° and 9.5° occurred in DLC1.6 and DLC6.1, respectively. The yaw motion in DLC6.1 was higher due to the environmental external force was in misalignment and the multi-directions. Table 9 lists the maximum bending moment occurring at the connected part of the blade and tower. The moment that occurred at the blade connected part was approximately 1.6 times larger in the stationary DLC6.1, whereas the moment that occurred at the tower base was approximately 1.1 times larger than that in DLC1.6. Table 10 presents the maximum tension response applied to the mooring chain in the fairlead. Line 1 of the mooring chain was placed in the (+) surge direction of the floating platform, whereas lines 2 and 3 were installed diagonally to the (-)

surge direction. Because lines 2 and 3 are applied to restore tension when surge motion occurs in the floating platform, the maximum tension of these lines was larger than that of line 1. To identify the fracture of the mooring chain in the extreme marine environmental condition, the breaking load of the mooring chain was calculated using Eq. (3) (DNV GL, 2015). For the mooring chain of studless chain class R3 the MBL was calculated to be 10574 kN when the diameter was set at 117 mm. Because the maximum tension that occurred in DLC6.1 was 5625 kN, the mooring chain did not fracture.

$$MBL = 0.0223d^2(44.0 - 0.08d) \text{ [kN]} \tag{3}$$

d = mooring chain nominal diameter [mm]

3.2 Redundancy Verification

Table 11 lists the maximum six degree-of-freedom motion response observed in DLC9.2 and DLC10.2. DLC9.2 assumes the mooring chain fracture condition at a normal operating condition. To identify the response when the maximum thrust occurs at a rotating rotor, a wind speed of 11.4 m/s, i.e., the rated wind speed, was applied and the corresponding significant wave height was 2.5 m. In this study, for redundancy verification, two mooring chain fracture scenarios were assumed (Fig. 4). Case 1 is a fracture scenario involving a mooring chain placed parallel to the operating direction of the environmental load, and case 2 is one involving a mooring chain placed diagonally to the applied load. DLC10.2 considers the mooring chain fracture in the

Table 11 Platform displacement of DLC9.2 and DLC10.2

	Platform displacement			
	DLC9.2		DLC10.2	
	Case 1	Case 2	Case 1	Case 2
Surge (m)	558.60	281.70	565.80	284.10
Sway (m)	1.10	427.80	13.72	435.10
Heave (m)	2.91	1.71	5.56	3.22
Roll (°)	0.65	1.43	3.87	2.98
Pitch (°)	13.06	10.50	4.79	5.49
Yaw (°)	0.19	0.56	11.28	19.38

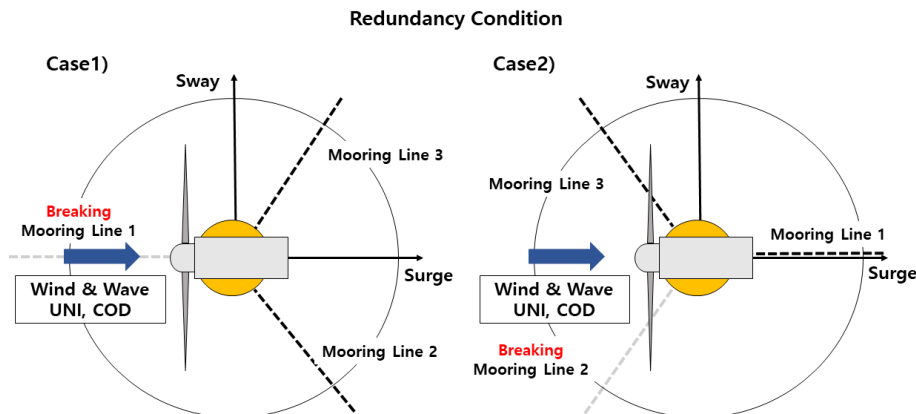


Fig. 4 Mooring line breaking configuration

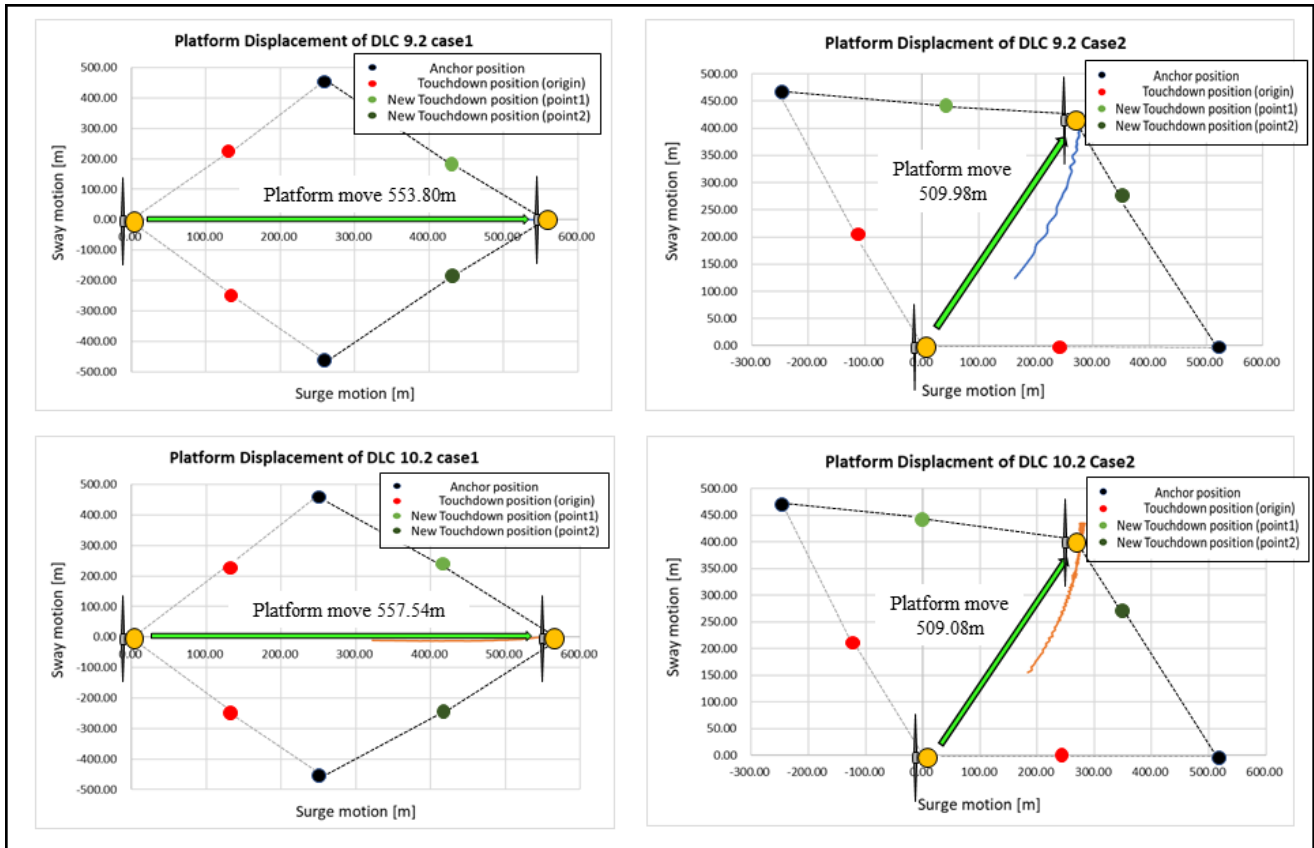


Fig. 5 Platform new mean position of DLC9.2 and DLC10.2

extreme marine environment condition and the fracture condition is the same as that of DLC9.2. Fig. 5 shows the new mean position of the floating platform, the drift motion of which was stopped after the mooring chain fractured. First, in DLC9.2 case 1, a maximum surge motion of 565.8 m occurred and for the case of mooring chain fracture, the floating platform drifted 554 m in a straight displacement and then stopped. A similar surge motion was observed in DLC10.2 case 1, where the floating platform drifted 558 m in a straight displacement and then stopped. In DLC9.2 case 2, a maximum surge motion of 281.7 m and a sway motion of 427.8 m occurred simultaneously. For case 2 of both DLC9.2 and DLC10.2, it was discovered that the floating platform drifted 510 m in a straight displacement in the diagonal direction then stopped. Because the movement displacement difference of the floating platform was not significantly affected by the environmental external force condition, it was confirmed that the new average location of the floating platform was governed primarily by the mooring tension than by the environmental load. In terms of the rotating movement, yaw motion almost did not occur in DLC9.2 because the control system operated normally and corrected the yaw error. On the contrary, a maximum pitch angle of approximately 13° was achieved because the maximum thrust occurred at the rotor at the rated wind speed and the mooring chain fractured; hence, the angular motion of the floating platform could not be maintained.

Table 12 lists the maximum load response results of DLC9.2 and

DLC10.2, which were abnormal scenarios; hence, a low safety factor of 1.1 was applied, whereas the maximum bending moment that occurred at the tower base of DLC9.2 was approximately 205 MN·m, which was the highest among all the conditions analyzed. Therefore, this abnormal condition must be partially considered during structural analysis, along with redundancy verification. It was discovered that the bending moment at the blade root part of case 1 in DLC10.2 differed significantly from that of case 2 in DLC10.2. Based on the time history results of the analysis, a transient response was observed at the out-of-plane and in-plane of the blade tip up to 800 s after 200 s; consequently, the bending moment appeared to be high. The results showed that under the same analysis condition, the load response occurred differently depending on the mooring chain fracture characteristics.

Table 13 lists the tension of the mooring chain. As the maximum tension that occurred was lower than that of the three-point mooring, no additional mooring chain fracture was anticipated.

Table 12 Maximum bending moments of DLC9.2 and DLC10.2

	Maximum bending moment			
	Blade root (kN·m)		Tower base (kN·m)	
	DLC9.2	DLC10.2	DLC9.2	DLC10.2
Case 1	15694.93	16690.84	204611.22	146670.79
Case 2	16259.23	6441.67	201656.81	147308.34

Table 13 Maximum fairlead tension of DLC9.2 and DLC10.2

		Maximum fairlead tension		
		Line 1 (kN)	Line 2 (kN)	Line 3 (kN)
DLC9.2	Case 1	-	2245.10	2258.30
	Case 2	439.67	-	2178.00
DLC10.2	Case 1	-	4386.80	4381.30
	Case 2	474.32	-	5349.30

4. Conclusions

In this study, the numerical analysis of a megawatt-level floating offshore wind power generation system was performed by applying the internal standard of the International Electrotechnical Commission. The 5-MW-level wind power turbine of the NREL and the OC3-Spar-type floating platform were used for the numerical analysis. Subsequently, the response analysis was performed in an extreme marine environmental condition and a failure condition. Based on the results of the extreme marine environment, the maximum movement radius of the floating platform was 39 m for three-point mooring, whereas it was 565 m for two-point mooring owing to the fracture of the mooring chain. Based on these results, the redundancy verification condition specified in IEC61400-3-2 must be requisitely reviewed to secure a safe separation distance of the wind power generator when constructing a large-scale floating offshore wind power complex. Moreover, the moving displacement difference of the floating platform in DLC9.2 and DLC10.2 was less than 1%, suggesting that the movement radius for the two-point mooring was governed by the mooring tension instead of the environmental external force. The maximum bending moment at the connected part of the blade appeared in DLC 6.1 where the output was halted, whereas the maximum bending moment of the tower and the connected part of the platform occurred in DLC9.2 during the normal operation. Although DLC9.2 is an abnormal status wherein the mooring chain is fractured, the maximum load response was observed; hence, it is an analysis condition that must be considered during structure analysis. The maximum tension applied at the mooring chain did not result in fracture when a diameter of 117 mm was employed for the mooring chain redesigned in this study. However, the redundancy verification indicated that the touchdown point of the mooring chain moved with a drift in the floating platform; hence, it must be analyzed to prevent fracture due to interference among mooring chains for the wind farm design. In future studies, a comparative investigation pertaining to cylindrical and semisubmersible floating platforms as well as an analysis of leakage, i.e., a failure condition specified in IEC61400-3-2, will be performed to investigate the movement performance and load response of each floating platform.

Acknowledgments

This research was supported by the Korea Institute of Energy Technology Evaluation and Planning (KETEP) grant funded by the Korean government (MOTIE) (20184030202280) and the Korea Electric Power Corporation (R18XA03).

References

- DNV GL. (2015). Offshore Standard – Offshore Mooring Chain (DNVGL-OS-E302).
- International Electrotechnical Commission (IEC). (2019a). Wind Energy Generation Systems – Part3-1: Design Requirements for Fixed Offshore Wind Turbines (IEC61400-3-1). Geneva, Switzerland: International Electrotechnical Commission.
- International Electrotechnical Commission (IEC). (2019b). Wind Energy Generation Systems – Part3-2: Design Requirements for Floating Offshore Wind Turbines (IEC61400-3-2). Geneva, Switzerland: International Electrotechnical Commission.
- Jonkman, J.M., & Buhl, M.L. (2005). FAST User's Guide (NREL/TP-500-38230). Colorado, USA: National Renewable Energy Laboratory.
- Jonkman, J.M., Butterfield, S., Musial, W., & Scott, G. (2009). Definition of a 5-MW Reference Wind Turbine for Offshore System Development (NREL/TP-500-38060). Colorado, USA: National Renewable Energy Laboratory.
- Jonkman, J.M. (2010). Definition of the Floating System for Phase IV of OC3 (NREL/TP-500-47535). Colorado, USA: National Renewable Energy Laboratory.
- Korea New & Renewable Energy Center. (2016). 2016 New & Renewable Energy White Paper (Knrec/11-1410000-001321-11). 110-116.
- Korea Meteorological Administration (KMA). (2020). Weather Data Opening Portal. Retrieved from <https://data.kma.go.kr/cmmn/main.do>
- Shin, H.K., Yu, Y.J., Pham, T.D., Ahn, H.J., Seo, B.C., & Kim, J.B. (2019). Analysis of Environmental Conditions for the Conceptual Design of a 200 MW Floating Offshore Wind Farm in the East Sea, Korea. Proceedings of ASME 2019 2nd International Offshore Wind Technical Conference, Julian's, Malta. <https://doi.org/10.1115/IOWTC2019-7605>

Author ORCIDs

Author name	ORCID
Yu, Youngjae	0000-0002-8877-8196
Shin, Hyunkyung	0000-0002-3093-1784

Trend Analysis on Korea's National R&D in Logistics

Jae Yun Jeong¹, Gysung Cho² and Jieon Yoon³

¹Senior Researcher, Policy Research Division, BISTEP, Busan, Korea

²Professor, Department of Port Logistics System Tongmyong University, Busan, Korea

³Senior Researcher, Evaluation & Coordination of Regional Innovation Program Division, BISTEP, Busan, Korea

KEY WORDS: Logistics, National R&D, Network analysis, Keyword network, Cluster map, Centrality

ABSTRACT: This study examined how national research and development (R&D) in the domain of logistics has changed recently in the Republic of Korea. We conducted basic statistical analysis and social network analysis on 5,327 logistics-related R&D projects undertaken during 2005–2019. Data for performing these analyses were collected from the R&D database of the National Science and Technology Information Service (NTIS). By constructing a co-occurrence matrix with keywords, we conducted degree and betweenness centrality analysis and visualized the network matrix to display a cluster map. This study presents our observations related to the following findings: (1) the chronological trends of logistics R&D, (2) focused fields of logistics R&D, (3) the relations among keywords, and (4) the characteristics of logistics R&D. Finally, we suggest policy implications to boost and diversify logistics R&D.

1. Introduction

Recently, the scale and importance of the logistics industry has been increasing as e-commerce has become active worldwide and with the proliferation of cross-border logistics. In particular, Industry 4.0 is modifying all industries. Moreover, the logistics paradigm is rapidly changing to Logistics 4.0, in which fourth industrial revolution technologies such as IoT (Internet of things), AI (Artificial intelligence), big data, and cloud computing are integrated into logistics systems, thus leading to hyper-intelligence and hyper-connection. Additionally, unmanned logistics has been realized using robots and drones, and currently, no boundary exists between distribution and logistics businesses (BISTEP, 2019; Lee, 2018; Wang, 2016). Amid these changes, domestic logistics-related research has been conducted using several approaches, and techniques based on logistics technologies such as block chain and radio frequency identification (RFID) have been developed and applied most extensively (Seon and Kim, 2019; Lee et al., 2013; Lee, 2011; Sheen et al., 2010). In relation to the logistics industry, several studies have focused on efficiency analysis and economic analysis (Kim and Lee, 2018; Lee and Lee, 2016; Park and Kim, 2014). Numerous studies on the advancement of the logistics industry or logistics policies have also been conducted. However, research on investments in logistics

research and development (R&D) and the possible directions for logistics R&D at the national level is insufficient. Therefore, the purpose of this study is to examine the changes in national R&D trends related to logistics in the Republic of Korea. Accordingly, we conducted keyword network analysis using national R&D information provided by the National Science and Technology Information Service (NTIS). It was found that government expenditure in logistics R&D, which had been inactive for nearly 10 years since 2005, has rapidly increased since 2015. Moreover, technologies related to Logistics 4.0 are also being researched actively.

2. Research Design

2.1 Analysis Target and Data Collection

In this study, national R&D projects related to logistics were analyzed, and raw data for a total of 15 years, from 2005 to 2019, were obtained from the NTIS. Logistics-related keywords such as “distribution” and “logistics” were used. To identify relevant projects, unrelated projects were discarded from the original raw data based on the title, content, and keywords. The number of relevant projects extracted for each of three five-year periods considered in this study are presented in Table 1.

Received 11 October 2020, revised 12 November 2020, accepted 12 November 2020

Corresponding author Jieon Yoon: +82-51-795-5073, jyoon@bistep.re.kr

© 2020, The Korean Society of Ocean Engineers

This is an open access article distributed under the terms of the creative commons attribution non-commercial license (<http://creativecommons.org/licenses/by-nc/4.0>) which permits unrestricted non-commercial use, distribution, and reproduction in any medium, provided the original work is properly cited.

Table 1 The number of projects and keyword used for analysis

Period	No. of projects	No. of keywords
2005–2009	1,341	3,218
2010–2014	1,546	3,889
2015–2019	2,440	5,073

2.2 Analysis Method

To explore the changes in national R&D trends in the logistics field, first, a basic statistical analysis was performed to extract the fundamental information of R&D projects. Thereafter, network analysis methods were used with English keywords for R&D projects. Synonyms related to abbreviations or resulting from typing errors were integrated into one representative word, and all keywords were converted to lowercase letters to improve the accuracy of the network analysis results. Furthermore, using the co-occurrence analysis method, network and cluster analyses were performed on the keywords extracted for each period. Specifically, in cluster analysis, only the keywords recorded at least 7 times were selected to highlight issue keywords and to use high frequency keywords (Fig. 1). Furthermore, centrality, which is an important parameter in network analysis, was measured based on frequency and distance, which represent the linkage between nodes. In this study, the analysis was focused on degree centrality and betweenness centrality. In particular, a high degree centrality for a keyword indicates that many other keywords are linked to it, which indicates that research is being actively conducted in a specific field related to that keyword. Since betweenness centrality represents the shortest path between two unconnected keywords, a high betweenness centrality implies that the keyword is acting as a bridge between different research fields (Jeong et al., 2018; Lee, 2012; Borgatti et al., 2009). We used Knowledge MatrixPlus 0.80, developed by Korea Institute of Science and Technology Information, to generate the keyword matrix, Gephi 0.80 for centrality measurement through network analysis, and VOSviewer 1.6.10 for keyword cluster analysis and visualization.

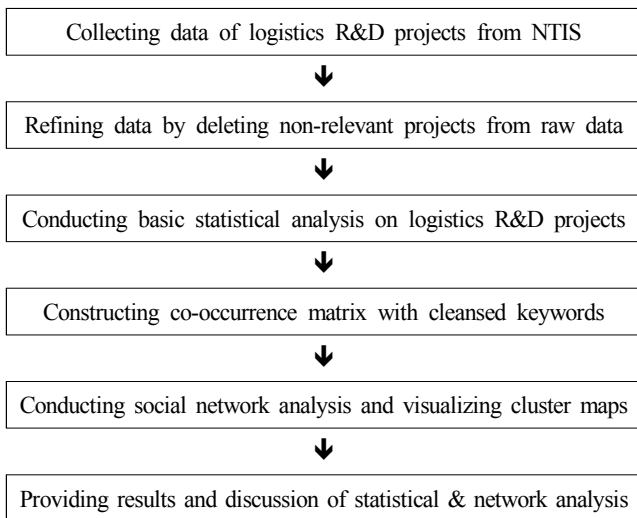


Fig. 1 Research framework

3. Analysis

3.1 Analysis of the State of National Logistics R&D Projects

We observed that the number of national R&D projects in the logistics sector had increased steadily from 280 in 2005 to 327 in 2013 after repeated fluctuations. This number then increased significantly to 618 in 2019 (Fig. 2). The government expenditure in logistics R&D increased from 82 billion won in 2005 to 163 billion won in 2009, after which it significantly decreased to 98 billion won in 2011. However, it has increased steadily since then to 231 billion won in 2019 (Fig. 3). The increase in national R&D expenditure in the logistics sector since 2012 is the result of the increased need in R&D for digitalization, hyper-intelligence, and advancement of logistics systems with the expansion of the e-commerce market, parallely with the transition in the logistics paradigm toward Logistics 4.0.

Statistics regarding the regional distribution of national R&D projects in the logistics sector from 2005 to 2019 show that 1,178 projects were undertaken in the Gyeonggi region, which was the largest number. This was followed by 1,163 in Seoul, 550 in Daejeon, and 492 in Busan (Fig. 4). These four regions accounted for 63% of the total number of logistics R&D projects. For the same period, the largest amount of government expenditure in logistics R&D was 558 billion won in Daejeon, followed by 537 billion won in Gyeonggi Province, 319 billion won in Seoul, 7.5 billion won in Busan, and 48.3

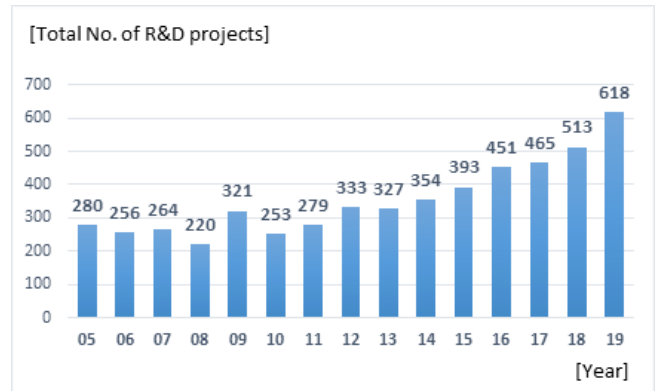


Fig. 2 Number of national logistics R&D projects

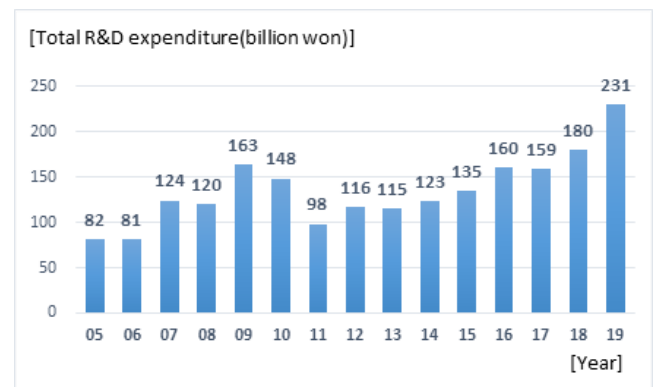


Fig. 3 Total governmental expenditure on national logistics R&D projects (unit: billion won)

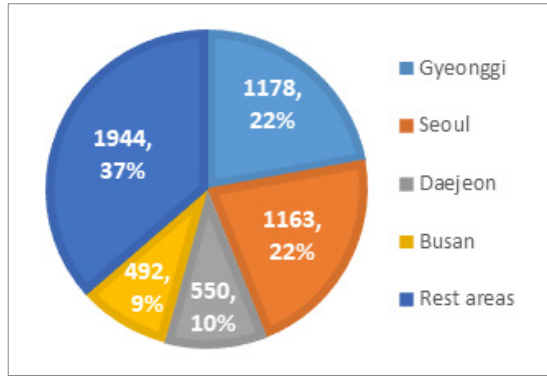


Fig. 4 Regional proportion of national logistics R&D projects

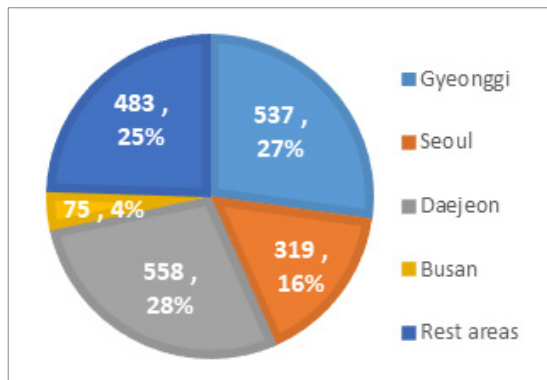


Fig. 5 Regional proportion of total governmental expenditure on national logistics R&D (unit: billion won)

billion won in all other regions combined. In terms of government expenditure, 75% of the total research investment was in the top four regions; this indicated that the investment was highly concentrated in certain regions. Furthermore, in terms of the level of research expenditure per project (Fig. 5), several large-scale R&D projects have been conducted in Daejeon, which is home to several government-funded research institutes. It is believed that in the metropolitan area, a variety of large, small, and medium-scale R&D projects are being conducted by various entities, such as universities and companies. Moreover, it was found that apart from the metropolitan area and Daejeon, logistics research is being conducted most actively in Busan. This is likely because Busan has the world's sixth largest port, the Port of Busan, in addition to numerous logistics companies and the largest number of logistics-related departments among all the community colleges in the Republic of Korea (BISTEP, 2019). Therefore, logistics R&D should evolve in a direction that would allow companies, research institutes, and universities from various regions to participate in order to improve the technologies being utilized by domestic logistics companies and enhance the current overall level of the logistics industry.

3.2 Keyword Network Analysis Results

3.2.1 Centrality analysis result

The top 10 keyword centrality results for national R&D in the logistics sector from 2005 to 2009 are presented in Table 2. A high

Table 2 Top 10 keywords with highest centrality (2005–2009)

Rank	Keyword	Degree centrality	Keyword	Betweenness centrality
1	Analysis	2.000	RFID	0.201
2	RFID	1.000	Logistics	0.052
3	Security manager	0.238	SCM	0.048
4	Ubiquitous	0.233	Ubiquitous	0.035
5	Logistics	0.200	Automation	0.025
6	SCM	0.185	ERP	0.018
7	USN	0.168	GPS	0.017
8	Middleware	0.155	Inventory	0.016
9	WMS	0.134	Optimization	0.016
10	GPS	0.132	Transportation	0.015

Table 3 Top 10 keywords with highest centrality(2010–2014)

Rank	Keyword	Degree centrality	Keyword	Betweenness centrality
1	RFID	1.000	RFID	0.002
2	Logistics	0.759	Logistics	0.002
3	SCM	0.652	SCM	0.001
4	Mobile	0.267	NFC	0.001
5	Simulation	0.228	Localization	0.001
6	NFC	0.215	Cloud	0.001
7	Smart	0.194	Mobile	0.001
8	Optimization	0.191	Anti-collision	0.001
9	Port	0.184	GPS	0.001
10	Cloud	0.183	Big data	0.001

degree centrality was observed for the following keywords: RFID, Security, Ubiquitous, Supply Chain Management (SCM), Warehouse Management System (WMS), and GPS. This means that national R&D in the logistics sector was active in logistics supply, management, storage, and logistics communications such as RFID and GPS during the considered period. On the other hand, keywords with a high betweenness centrality were Ubiquitous, Automation, and Enterprise resources planning (ERP), along with RFID, SCM, Logistics, and GPS, which exhibited a high degree centrality as well. This indicates in that the logistics sector, technologies related to system management and communication have become a major topic of convergence research in various fields. Based on the keyword-centrality analysis for 2010–2014 (Table 3), RFID, SCM, and Logistics were the most active areas of research. In addition, digital integration fields such as Mobile, Simulation, Smart, and Cloud had emerged as major research fields. This shows that hyper-connectivity had gradually started being introduced into the logistics system from the ICT (Information & communication technology) technology-based systemization of logistics management systems in the Republic of Korea. While the rankings for betweenness centrality and degree centrality were almost

the same in this period, localization and big data had newly emerged. Although convergence research has been performed in the fields of logistics management systems and in telecommunication fields such as RFID, SCM, Cloud, Mobile, and Big data, it is believed that such research was not active during 2010–2014 compared with other periods, as the betweenness centrality of the related keywords was relatively low.

According to Table 4, all keywords related to fourth industrial revolution technologies, such as IoT, Smart factory, Big data, Machine

learning, AI, and Deep learning, exhibited a high degree centrality and betweenness centrality during 2015–2019. In the aforementioned period, these keywords showed a completely different trend from the logistics R&D trend for the previous 10 years. In particular, research on logistics automation, unmanned logistics, logistics sharing, etc. through Robot, Automation, Autonomous vehicle, Cloud, and Platform technologies is being extensively conducted. It is important to incorporate fourth industrial revolution technologies such as AI, IoT, and Cloud into existing logistics systems and facilities to promote innovation. Presently, the characteristics of Logistics 4.0 are being reflected in domestic logistics R&D.

Table 4 Top 10 keywords with highest centrality(2015–2019)

Rank	Keyword	Degree centrality	Keyword	Betweenness centrality
1	IoT	1.000	IoT	0.179
2	Smart factory	0.525	Logistics	0.092
3	Big data	0.458	Smart factory	0.066
4	Logistics	0.404	Big data	0.055
5	Machine learning	0.374	AI	0.048
6	AI	0.360	Drone	0.046
7	Deep learning	0.271	Machine learning	0.038
8	Drone	0.216	Autonomous driving	0.030
9	Platform	0.214	Simulation	0.027
10	Robot	0.209	Platform	0.027

3.2.2 Cluster analysis result

In this study, a network was mapped using the VOSviewer program for cluster analysis using the keyword network matrix for each period considered in the centrality analysis. To maintain the same analysis conditions for each period (2005–2009, 2010–2014, and 2015–2019), the resolution was set to 0.8, the minimum cluster size was set to 5 as a clustering analysis option, and the average number of keywords used for mapping was limited to approximately 200.

As shown in Fig 6, the network map of the first period (2005–2009) revealed seven clusters. RFID, which exhibited high centrality, was located at the center of the network map and formed a cluster with Green logistics, Port logistics, Mobile, Simulation, and Monitoring. Communication-related technology fields such as Ubiquitous, Sensor network, Wibro (Wireless broadband) and Logistics were the next

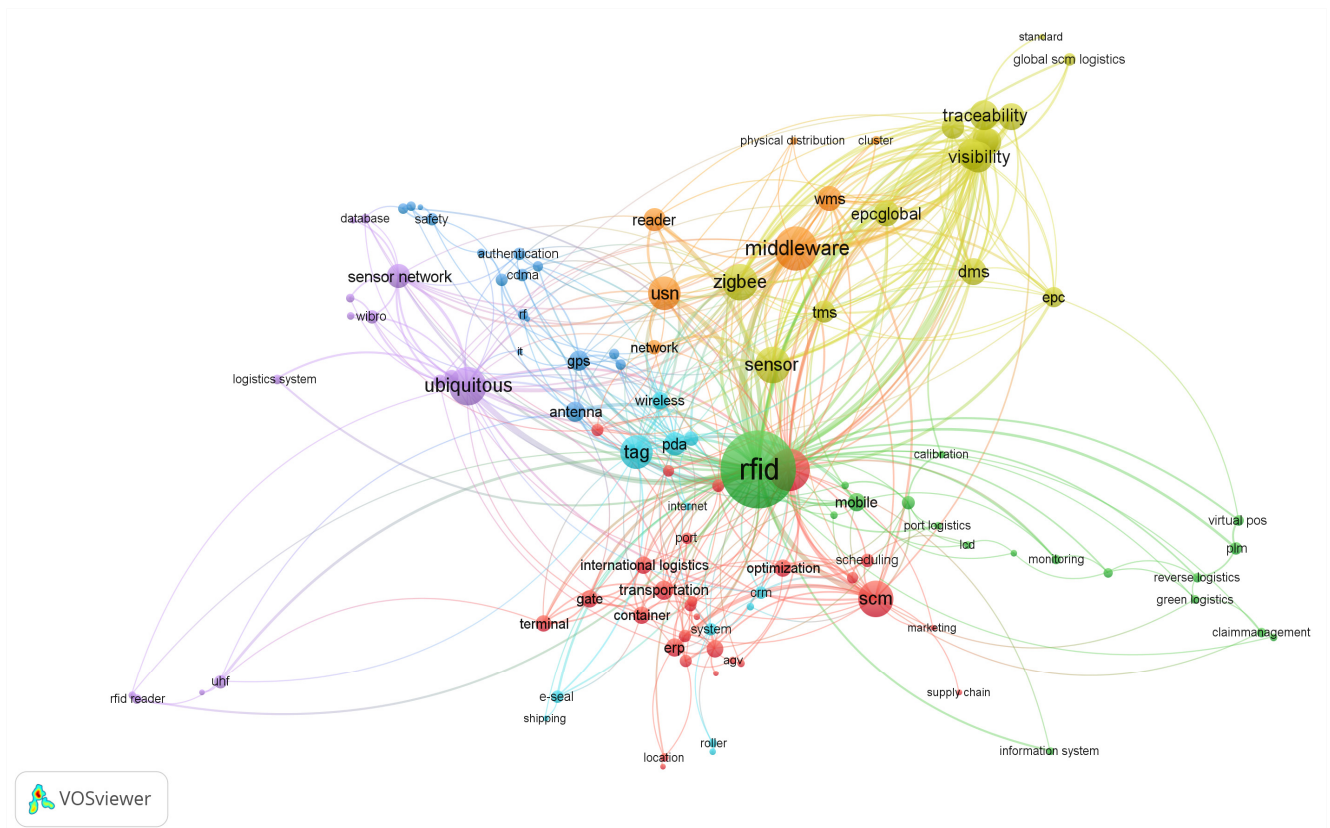


Fig. 6 Network map of logistics R&D presenting technology clusters (2005–2009)

major clusters. In the aforementioned period, the government strongly emphasized fostering the ICT field. In particular, government expenditure in Ubiquitous and Wibro-related technologies increased, and this trend is believed to have significantly affected logistics R&D. In addition, other focus areas were a cluster representing the field of international and maritime logistics, including Container, Transportation, Terminal, ERP, and International logistics, and another cluster related to transport management systems such as Standard, Traceability, and Visibility. As depicted in the network map (Fig. 7) of logistics R&D conducted between 2010 and 2014, seven clusters were obtained. Logistics and RFID, both of which exhibit high degree centrality and betweenness centrality, were located at the center of the network map, and each was clustered as an important research field. Specifically, Logistics formed an eco-friendly logistics-related cluster with keywords such as Green SCM, Risk management, and Eco-friendly, whereas RFID formed a logistics and communication cluster with Antenna, Computing, Mobile, and Network. In addition, cold-chain clusters, such as Cold chain, Substitution system, and Package, and smart logistics clusters, such as IoT, Big data, Cloud, and Data gathering, had newly emerged. This indicates that domestic logistics R&D was evolving from the existing conventional logistics field to a more advanced type of logistics. Furthermore, the network map for 2015–2019 revealed eight clusters, as shown in Fig. 8. This network map is significantly different from that obtained for the logistics R&D conducted in the previous 10 years. Specifically, intelligent and digitizing technologies such as IoT, Big data, Platform, and AI emerged as key research areas in this period. First, clusters related to unmanned logistics, such as Robot, Unmanned aerial vehicle (UAV), and Autonomous, indicated the major research fields, while those related to logistics digitalization, such as Big Data, Simulation, and Process mining, were also present. In addition, clusters related to logistics intelligence such as AI and Cloud were located on one side. Moreover, logistics safety-related clusters, such as Security and Safety, and logistics standard-related clusters for systematization of logistics systems, such as International standard, Technical management, and System integration, had emerged. In particular, technology-related clusters, such as Platform and Export, were also being proposed to promote logistics sharing.

3.3 Implications

Since 2015, major changes have occurred in logistics-related national R&D in terms of the number of projects, government expenditure, and research fields. Since 2005, government expenditure in logistics R&D had not changed significantly, exhibiting a box pattern at a certain level; however, since 2015, it has shown a steady rise. In particular, since 2007, national R&D projects have been planned and conducted actively in the fields of transportation logistics, logistics system improvement, technology development, intelligent port logistics, and advanced logistics technology development (KOTI, 2015). However, the effect of increasing investment in logistics R&D

became apparent only after several years. Meanwhile, the global e-commerce market had grown rapidly since mid-2010 and was expected to grow from USD 233 billion in 2014 to USD 994 billion in 2020 (CJ Logistics, 2017). As a result, cross-border logistics also proliferated (BISTEP, 2019), and it is believed that the rapid change in the logistics environment led to the increased investment in domestic logistics R&D. In other words, national R&D in the logistics sector seems to have been considerably influenced not only by government policies but also by the changing logistics paradigm and the growth potential of the logistics market. Furthermore, we analyzed the status of logistics R&D by region. We found that the regional concentration was high in the metropolitan area of Seoul and Gyeonggi, in Daejeon and in Busan. This means that research on logistics-related technology development is being actively conducted, mainly by large and medium-sized logistics-related companies, universities, research institutes, and government-funded research institutes located in these regions. Therefore, based on corporate demand, logistics R&D must be undertaken by several logistics companies that do not possess their own technology, to respond to the latest changes in the logistics paradigm. In future, the logistics industry will continue to undergo major changes in response to rapidly changing environments, which will involve diversification of customer demand (dawn delivery, last mile, product diversification, etc.), development of IT technology, and globalization of corporate management. In this era of Logistics 4.0, unmanned logistics, shared logistics, personalized logistics, logistics security, and logistics safety will be strengthened. In particular, the importance of cold-chain logistics is growing with the increasing global demand for pharmaceuticals and fresh foods. Therefore, in terms of domestic logistics R&D, greater investments should be made for the development of technologies such as robots, unmanned vehicles, and drones and for that of logistics systems using intelligent information technologies, such as AI and AR, to respond to the advancement of unmanned logistics and automation. In addition, the need for logistics security and safety also increases with the increasing use of shared logistics and automation. Therefore, investment in R&D is also required for systems that can systematically and stably manage logistics information using IoT and big data, based on ICT. To respond to diversification and personalization of logistics items, national R&D expenditure also needs to be increased in areas related to logistics forecasting using advanced cold-chain systems and in AI and big data analysis. The results of keyword network analysis show that national logistics R&D has responded swiftly to the changing logistics paradigm. In particular, R&D capabilities were concentrated on conventional logistics communication and logistics management systems such as RFID, SCM, and WMS until the early 2010s. However, the studies that have been conducted recently are focused on convergence with fourth industrial revolution technologies such as IoT, AI, and Cloud, and smart logistics. Therefore, the technology convergence of the fourth industrial revolution needs to be strengthened, on-site demand needs to be reflected, and investment in

Logistics 4.0 technology development needs to be increased gradually while sustaining this trend in future logistics R&D. As a result, logistics R&D must transcend research and contribute to the development of the domestic logistics industry.

4. Conclusion

In this study, we examined the current state of expenditure and the major trends in national R&D in the logistics sector in the Republic of Korea from 2005 to 2019. The scale of government expenditure in the logistics sector has been increasing rapidly since 2015, parallely with the rapidly growing global logistics market. Logistics R&D trends assessed through social network analysis were found to be different for each of three five-year periods (2005–2009, 2010–2014, and 2015–2019). In the first period (2005–2009), several areas related to the conventional logistics industry, such as communication and management systems, which include RFID, SCM, and GPS, emerged. In the second period (2010–2014), ICT-related technologies such as mobile and cloud began to emerge as the key fields for investment, along with conventional logistics fields such as RFID and SCM. However, in the most recent period (2015–2019), technologies related to Logistics 4.0 such as IoT, Big data, and AI were observed to be major research areas, and the national logistics research capabilities were focused on the latest technology trends. This study showed that the logistics R&D expenditure of the Korean government, which was stagnant in the early 2000s, has grown in response to the rapid growth of the logistics market and to the changes in the logistics paradigm occurring since the mid-2010s. In the future, logistics technologies and industrial fields are expected to undergo rapid advancements. Therefore, the need to concentrate and expand R&D in the advanced fields of Logistics 4.0 (such as logistics automation, sharing, personalization, and cold chain) and in logistics security and safety was emphasized in this study, along with the continuous increase in government expenditure in logistics R&D. However, the level of logistics technology data and descriptions of applied industries were insufficient in this study because the trend analysis was performed by focusing only on the keywords of R&D projects. Therefore, in our future research, a systematic analysis will be conducted using various types of information regarding R&D projects, focusing on the logistics technology tree and the logistics industry.

Acknowledgments

This work was supported by Busan Regional Agency for Science, Technology & Innovation grant funded by the Korea government (MSIT) (No. 1711102671, The Plan for Supporting Research and Development Department in Busan).

Conflict of Interest

No potential conflict of interest relevant to this article was reported.

References

- BISTEP (Busan Innovation Institute of Industry, Science & Technology Planning). (2019). A Study on Condition and Development Direction of Logistics Industry in Busan. Busan, Korea: BISTEP. Retrieved from <https://www.bistep.re.kr/web/trebook/download.do?mld43&treIdx80&itldpdfFile>
- Borgatti, S., Mehra, A., Brass, D., & Labianca, G. (2009). Network Analysis in the Social Sciences. *Science*, 323(5916), 892-895. <https://doi.org/10.1126/science.1165821>
- CJ Logistics. (2017). Borderless e-commerce End-to-End Logistics Platform Construction (Report 2017-11-26). Korea: CJ Logistics. Retrieved from https://www.cjlogistics.com/ko/tes/insights/IT_00000011
- Jeong, J.Y., Kang, I., Choi, K.S., & Lee, B.H. (2018). Network Analysis on Green Technology in National Research and Development Projects in Korea. *Sustainability*, 10(4), 1043. <https://doi.org/10.3390/su10041043>
- Kim, J.H., & Lee, C.B. (2018). A Study on the Competitiveness of Korean Logistics Industry. *Korea Logistics Review*, 28(3), 41-55. Retrieved from <http://kiss.kstudy.com/thesis/thesis-view.asp?key3627608>
- orea Transport Institute (KOTI). (2015). Research on the Establishment of Comprehensive Logistics Innovation Plan. Sejong, Korea
- Lee, C.U. (2018). New Technology of Logistics Security. LoTIS. Retrieved November 2019 from https://www.lotis.or.kr/tia03v.do?cn_id2018110200003&cn_type_cdTIA&MENU_IDTIA00&searchKindCN_TITLE&searchWord&currPage&detailKind
- Lee, J.H. (2011). An Empirical Study on the Adoption of Technology Acceptance Model in The Port Logistics Service. *Journal of Korea Port Economic Association*, 27(4), 13-35. Retrieved from <https://www.koreascience.or.kr/article/JAKO201121537470075.pdf>
- Lee, J.M., Lee, K.H., & Kim, D.S. (2013). Image Analysis Module for AR-based Navigation Information Display. *Journal of Ocean Engineering and Technology*, 27(3), 22-28. <https://doi.org/10.5574/KSOE.2013.27.3.022>
- Lee, M.K., & Lee, K.Y. (2016). The Regional Economic Impacts of the Port Logistics Industry-Focused on Busan, Incheon, and Ulsan. *Journal of Shipping and Logistics*, 32(2), 299-320. <https://doi.org/10.37059/tjosal.2016.32.2.299>
- Lee, S. (2012). *Network Analysis Methodology*. Seoul: Nonhyung.
- Park, C.M., Kim, T.S. (2014). A Study on the Efficiency of Logistics Industry in Korea using DEA-SBM. *Korean Journal of Logistics*, 22(4), 27-46. <https://doi.org/10.15735/klj.2014.22.4.003>
- Seon, H., Kim, H.D. (2019). A Study on the Impacts of Block Chain Technology on the Logistics Industry. *Journal of Global e-Business Association*, 20(3), 137-148. <https://doi.org/10.20462/TeBS.2019.6.20.3.137>
- Sheen D.M., Choi, S.H., Lee, G.S. (2010). RFID Applications from 2005 to 2010. *Journal of Ocean Engineering and Technology*, 24(4),

86-93. Retrieved from <https://www.joet.org/journal/view.php?number2242>

Wang, K. (2016), Logistics 4.0 Solution-New Challenges and Opportunities. In 6th International Workshop of Advanced Manufacturing and Automation, Atlantis Press. <https://doi.org/10.2991/iwama-16.2016.13>

Author ORCIDs

Author name

Jeong, Jae Yun
Cho, Gyusung
Yoon, Jieon

ORCID

0000-0003-0689-3535
0000-0002-1289-4908
0000-0003-0077-8878

Study on Modularization of Components for Cost Reduction of Sail Yacht Steering System

Young-Hun Kim¹

¹Professor, Department of Naval Architecture and Ocean System Engineering, Kyungnam University, Changwon, Korea

KEY WORDS: Sail yacht, Steering system, Modularization, Cost reduction, Productivity improvement

ABSTRACT: This study aims to improve the price competitiveness of a steering system with a relatively high cost portion among sail yacht components. Hence, the components of the steering system were analyzed, and steering system modularization was proposed. The fabrication processes before and after the application of modularization was presented. For modularization, primary components such as the pedestals and quadrants of the steering system were developed, and the structural safety of the components was reviewed. It was confirmed that the manufacturing cost of the developed steering system decreased by approximately 33% compared with the existing system. The new steering system presented herein is expected to contribute to the localization of components and price competitiveness of sail yachts.

1. Introduction

An increase in national income generally increases the level of interest in marine leisure activities and the demand for vessels used for such activities. As sale yachts approximately 30 ft in length have recently gained global popularity, many of these vessels have been manufactured in many countries, including South Korea. International competitiveness in sale yacht manufacturing can be achieved only through the satisfaction of conditions related to exterior design and price competitiveness based on the performance and price of fittings and production process efficiency. A steering system is an essential vessel device for marine navigation; it is connected to a rudder to enable an operator to control the direction of the vessel. Both the steering system and sails are main vessel equipment that require the operator to control them appropriately with less power applied (Song et al., 2017). Although the steering system serves as the core facility for sail yachts, South Korean manufacturers have primarily imported most components of these systems, such as the pedestals, sheaves, chain gears, and quadrants have been imported. The steering system requires a considerable amount of time and labor for its installation in the body of a sail yacht owing to connections to various components, such as those mentioned above. Hence, its price competitiveness is affected significantly. In this study, methods for improving the structural stability and functionality of existing steering systems and

reducing the cost of these systems based on their characteristics were investigated. Accordingly, a steering system modularization method based on the development of components that can replace imported components for reducing manufacturing cost and increasing productivity during production is proposed. In addition, it is confirmed that the proposed method increased the price competitiveness of the developed steering system and its technological competitiveness through performance enhancement.

2. Structure and Modularization of Steering Systems

2.1 Overview of Steering Systems

Steering systems in sail yachts are devices connected to rudders and are used to change the direction of the vessels. They are classified into tiller- and wheel-based steering systems based on steering methods. Furthermore, they can be categorized into single- and twin-wheel steering systems according to wheel operation methods (Miyata et al., 1998/2006). Fig. 1 shows the process of operating a steering wheel system. When the steering wheel is rotated to change the direction of the sail yacht, the torque from the wheel is transmitted to a rudder and used to change the direction of the sail yacht. The components involved in transmitting the wheel torque to the rudder include a steering wheel, cable sheave, bulkhead, quadrant, and a rudder on a steering stand.

Received 4 November 2020, revised 29 November 2020, accepted 3 December 2020

Corresponding author Young-Hun Kim: +82-55-249-2686, younghun@kyungnam.ac.kr

© 2020, The Korean Society of Ocean Engineers

This is an open access article distributed under the terms of the creative commons attribution non-commercial license (<http://creativecommons.org/licenses/by-nc/4.0>) which permits unrestricted non-commercial use, distribution, and reproduction in any medium, provided the original work is properly cited.

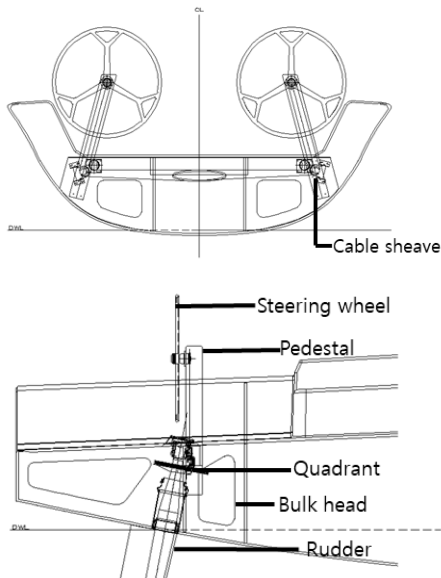


Fig. 1 Component of steering system of sail yacht

However, existing steering systems are technically inefficient in terms of torque transmission and manufacturing. Specifically, indirect steering methods based on cables reduce the torque transmission efficiency. Most components of existing steering systems are imported from other countries and are additionally processed and assembled. However, it is difficult to install a steering system based on these components owing to the complex system structure. Moreover, all the components require additional assembly processes and space for the process. In addition, the import of the components of the steering system used in a sail yacht of approximately 30 ft (9.14 m) in length incurs approximately 11,000,000 KRW including tariffs. Such an amount of import expense accounts for 5% to 6% of the entire sail yacht production cost.

2.2 Steering System Modularization

The bulkheads, pedestals, and sheaves of existing steering systems are separate from each other and hence must be connected for installation. In other words, a certain amount of time and labor are required for the sequential assembly of these components. However, the modularization of these components facilitates the assembly of components based on a bulkhead in advance and renders installation for connecting these components unnecessary. Fig. 2 shows the conceptual diagrams of an existing steering system assembled based on imported components and a steering system assembled through modularization.

When the components of a steering system are modularized, pedestals are bolted and fixed to bulkheads. Consequently, processes for fixing pedestals and decks at their correct locations are not required in this method, unlike the existing method. Moreover, plates used for the fixture of sheaves need not be manufactured additionally because these components are directly installed on the bulkheads. Hence, processes for producing and installing plates for the fixture of sheaves

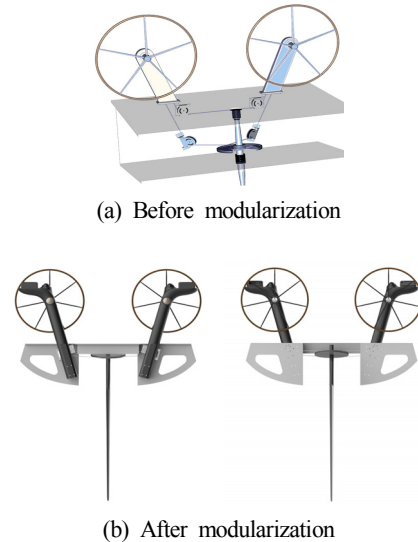


Fig. 2 Comparison of the before and after modularization of steering system

can be eliminated. Accordingly, such process change can reduce the number of installation tasks in confined spaces, increase productivity, and decrease factors that might cause quality issues. However, as the form of existing pedestals imported from other countries is inappropriate for the component modularization, it should be redesigned accordingly.

2.3 Comparison of Processes Before and After Steering System Modularization

Table 1 lists the assembly and production processes of the steering system before and after modularization. During yacht manufacturing, steering system installation begins with bulkhead installation, followed by deck mounting, and installation of main components of the steering system, such as the pedestal, sheave, quadrant, rudder, wheel, and cable.

The steering system modularization replaces the existing process of pedestal bonding with direct pedestal bolting, thereby eliminating the processes of fixing pedestals for bonding and producing plates for these components as well as the processes of producing and bonding plates for connecting blocks. Consequently, six to twelve stages of the existing steering wheel installation process before modularization become unnecessary, and the number of stages required for steering wheel installation is reduced from 16 to 9 after modularization. The modularization method reduces the amount of installation time by approximately 5 d and that of man hours by 20 MH based on a decrease in work time and loss caused by the waiting time for CNC (Computerized numerical control) processing and resin curing. Furthermore, it increases the productivity of steering system installation and curtails the number of main and subsidiary materials. Additionally, it is expected to ultimately improve the performance and quality of the steering system through increased installation precision and joint quality via the adjusted pedestal joint method.

Table 1 Comparison of before and after steering system modularization

	Production order of steering system
When modularization is not applied	1. Bulkhead installation
	2. Deck mounting
	3. Pedestal body processing
	4. Deck hole processing
	5. Panels production to fix pedestal deck
	6. Fixing plates to pedestal angle
	7. Pedestal deck bonding
	8. Making plates for installation of connecting block of housing including sheave
	9. Plates bonding (left)
	10. Plates bonding (right)
	11. Laminated reinforcement with glass fiber above and below the plate joint (left)
	12. Laminated reinforcement with glass fiber above and below the plate joint (right)
	13. Block connection and sheave assembly
	14. Rudder and quadrant assembly
	15. Wheel assembly
	16. Cable connecting
When applying modularization	1. Bulkhead modular installation
	2. Deck mounting
	3. Pedestal body processing
	4. Deck hole processing
	5. Pedestal and bulkhead bolting through the deck
	6. Block connection and sheave assembly
	7. Rudder and quadrant assembly
	8. Wheel assembly
	9. Cable connecting

2.4 Development of Components and Replacement of Imported Components

Existing pedestals imported from other countries cannot be connected with the bulkheads through bolting in the proposed steering system modularization method. Hence, a pedestal was redesigned and manufactured. Additionally, other components such as the quadrant, steerer, and cable sheave were developed for cost reduction.

2.4.1 Pedestal

The exterior of the pedestal was designed by a professional design company based on the result of a survey conducted based on yacht users to increase practicality and esthetic satisfaction. It was manufactured with carbon to ensure durability. As shown in Fig. 3(a), its length was extended with a bulkhead for bolting. An interference section was removed to prevent interference by sheaves, and an resin infusion process was applied.

2.4.2 Quadrant

A quadrant was manufactured via resin transfer molding, and 11 molds were used for its complex form, as shown in Fig. 3(b). The molds were cast with aluminum because this material is unlikely to be

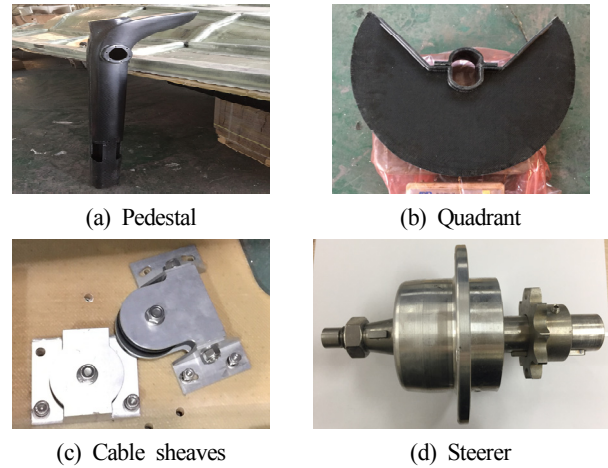


Fig. 3 Components of steering system developed for substituting imported components

transformed by heat during heat curing, and it facilitates fine and detailed processing. The quadrant was produced using highly durable carbon.

2.4.3 Cable sheave

A sheave for rotating a cable and its housing for bolting using a bulkhead were designed and manufactured, as shown in Fig. 3(c). They were produced using AL6061 owing to its favorable structural strength.

2.4.4 Steerer

A steerer used as a rotation gear for a steering wheel can halt the rotation of a steering wheel, and a chain gear that can be connected with a chain. This component was manufactured using SUS316 to ensure corrosion resistance and strength against seawater, and its housing was produced using AL6061. In addition, a retainer was inserted to prevent the inflow of seawater.

3. Structural Evaluation of Steering System Applying Modularization Method

3.1 Review of Mechanism of Developed Steering System

The mechanical mechanism for force transmission in the developed steering system is based on the order of the steering wheel, chain, cable sheave, cable, quadrant, and rudder. Specifically, components such as the steering wheel, chain, cable, and rudder are used to transfer force directly. Components such as the cable sheave and quadrant serve as media for facilitating more flexible direction adjustments during force transmission. The ultimate force refers to pressure loads represented as a head applied to the rudder in the sea (ISO, 2009). The rudder is constantly affected by dynamic loads during the navigation of sail yachts, including static loads from the surface of water on which the rudder is placed, dynamic loads under the wave loads applied, loads that might occur because of the sailing velocity of the sail yacht,

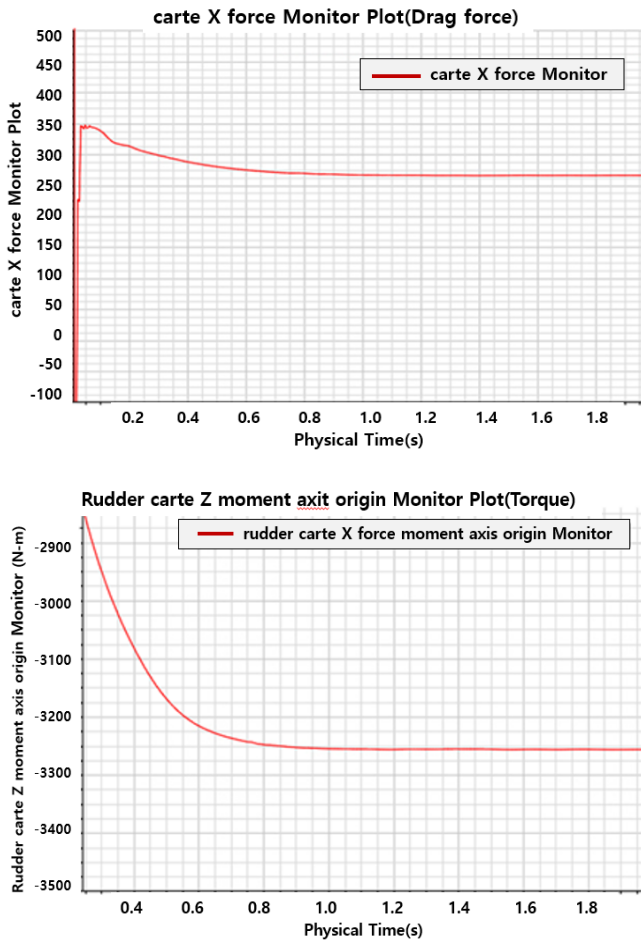


Fig. 4 Result of drag force and torsional load

Table 2 Materials of steering system components

Components	Carbon (Uni-D)	Multiaxial fiberglass (E-Glass)	PVC foam
Bulkhead module		•	•
Pedestal	•	•	
Quadrant	•	•	•
Sheave		Aluminum (AL6061)	

and loads caused by tidal currents (Marchaj, 1996). However, loads caused by tidal currents were assumed to be insignificant and hence disregarded in this study. Considering the constant and complex effects of the aforementioned loads, the structural safety of the developed steering system was analyzed under a sail yacht speed of 7.8 kn (14.4km/h) and a rudder angle of 13°, in which the most significant effects of loads were applied. At this time, the surface area and depth of the rudder were set at 1,153,388.2 mm² and 1,775 mm, respectively.

The drag force and torque were calculated to be 266 N and 3,256 N·m, respectively, under the conditions as shown in Fig. 4. Moreover, it was analyzed that the bulkhead module connected to the pedestal supporting the steering system and the body of the sail yacht were safe

in terms of its structure and material. Table 2 shows the types of materials used for the components of the developed steering system.

3.2 Structural Safety Evaluation of Quadrants

The structural stability of the quadrant was evaluated based on loads transferred to the quadrant connected to the rudder when the maximum load was applied to the rudder. The material properties of the quadrant were identified through a specimen test, in which the yield strength and density were calculated to be 381 N/mm² and 1.538 g/cm³, respectively. Moreover, a structural analysis was performed based on a commercial analysis program, Abaqus. As for the modeling conditions, the number of nodes was established as 42,709, number of elements as 26,400, and rotation torque in the Z-direction considering external loads as 3,256 N·m.

Boundary conditions for the structural analysis were established as follows. First, a reference point (RP) was set in the center of the model, and kinematic coupling was applied to the inner wall. The displacement and rotation in all directions, except rotation in the Z-direction, based on the RP were restricted as constraints for setting the loads and boundary conditions. To restrict the displacement caused by inertial force in the tangential direction to the circumference, only the Y-direction was restricted through the establishment of a local coordinate system for the tangential direction (refer to Fig. 5.)

The analytical result indicated that the stress applied to the quadrant occurred at the part connecting the quadrant and rudder. The maximum tensile strength of the quadrant was calculated to be 278.6 N/mm², which was lower than its yield strength of 381 N/mm². Therefore, this component was evaluated to be structurally safe (refer to Fig. 6.)

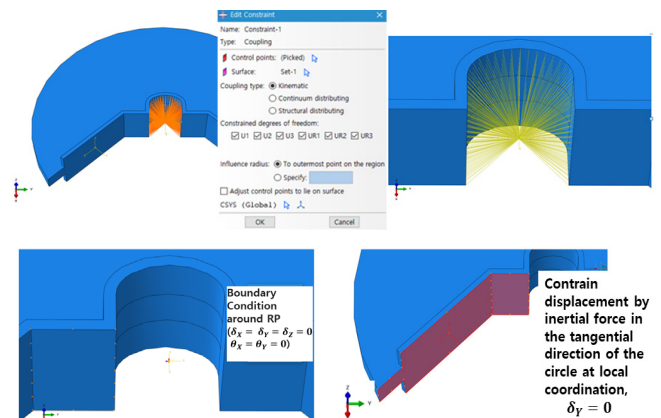


Fig. 5 Boundary conditions of modeling

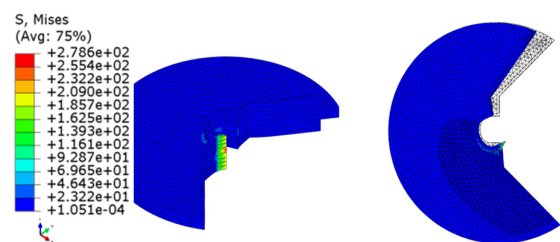


Fig. 6 Stress distribution of quadrant

4. Review of Manufacturing Cost of Steering System Before and After Modularization

The difference in manufacturing cost of the steering system before and after the development of its components and modularization is as follows. Before steering system modularization, only the purchasing cost for imported components was incurred. After steering system modularization, the mold casting cost, which is considered an initial investment cost for component manufacturing, material cost for component manufacturing, and labor cost were incurred owing to the manufacturing and installment of components developed in this study. However, the entire cost for steering system manufacturing after steering modularization was calculated to be lower than that based on imported components, as will be explained in detail below. The mold casting cost can be offset from the second cycle of manufacturing, in that additional cost reduction can be achieved through mass manufacturing. Moreover, steering system modularization resulted in a decrease in the number of processes for steering system installment, cost for materials (such as plates for fixing the pedestal, and fiber and resin for fixing sheaves, which are required in the existing method), work time, and waiting time for CNC processing and resin curing.

Table 3 shows the cost calculated for the reduced production process and material cost. When the existing purchasing cost for imported components was converted to 100, the total amount of material cost and labor cost for manufacturing the components developed in this study was calculated to be 76.7. The labor cost was calculated based on the man hours required for the assembly of components. Moreover, the work time reduced by approximately 5 d owing to the reduced production processes. Subsequently, the amount of reduced cost such as the labor cost was calculated to be 9.8. When the reduced amount

Table 3 Cost comparison of before and after modularization

Case	Production cost ratio (%)
When installing existing imported products and not applying modularization	Pedestal: 57.9
	Quadrant: 9.1
	Cable sheaves: 10.7
	Steerer: 12.1
	Transportation: 10.9
	Total: 100
When installing products developed and modularization application	Pedestal: 17.1
	Quadrant: 4.0
	Cable sheaves: 7.1
	Steerer: 17.1
	AI mold: 1.4
	FRP mold: 4.7
Labor costs	Pedestal: 17.0
	Quadrant: 7.7
	Cable sheaves: 0.3
	Steerer: 0.3
	Total: 76.7

1 man-hour = 16,700 KRW (assumed)

1 Euro = 1,302 KRW application

Import prices were confirmed by domestic companies

was applied to 76.7, the ultimate cost required for the steering system manufactured using the proposed method was calculated to be 66.9. Therefore, the entire cost for sail yacht manufacturing after steering system modularization was reduced by approximately 33% compared with that based on the imported components. In addition, the steering system manufacturing cost is expected to reduce even further by applying steering system modularization based on the components developed in this study, considering the increased structural strength of the developed quadrant compared with that of imported quadrants based on materials, tariffs for imported components, and other expenses.

5. Conclusions

The difference in the steering system of a sail yacht before and after the modularization of its steering system components was analyzed in this study. The findings of this study are as follows:

(1) In the steering system manufacturing process, the number of stages for the installation process was reduced from 16 to 9 after modularization considering steering system operation. Seven stages of CNC processing, plate and fixture manufacturing, and bonding were eliminated, and the required amount of man hours and work time decreased through such a process. The performance of the steering system improved after replacing the existing bonding-based pedestal fixture method to the developed mechanical pedestal fixture method.

(2) As the imported pedestals were not suitable to be used in the developed steering system modularization method, a new pedestal was developed in this study and resulted in cost reduction. Furthermore, a steering wheel, steerer, and cable sheave were developed in this study and resulted in cost reduction. A structural analysis based on the developed components was performed, and structural safety of these components was confirmed through the analysis.

(3) The cost for steering system manufacturing after modularization reduced by approximately 33% compared with that based on imported components in single steering system manufacturing although an initial mold casting cost for component development was incurred. Furthermore, because the amount of time required for sail yacht manufacturing decreased by approximately 5 d, the steering system modularization method was confirmed to be effective in terms of production cost and productivity. In addition, it was superior to the existing methods using imported components, as its mold casting cost can be offset from the second cycle of steering system manufacturing through mass production.

References

- Miyata, H., Yokoyama, E., Dakahashi, D., & Nagai, J. (2006). Science of Yacht (Hong, S.W., Kim, S.S., Kim, H.C., Lee, S.H., Lee, Y.G., Kim, Y.J., Kim, & S.H., Trans.). Seoul, Korea : Jisungsa. (Original Work Published in 1998, Japan: Senkyo Company).
- ISO. (2009). Hull Construction and Scantlings-Rudders (ISO 12215-8).

Song, Y.H., Kim, D.J., Chang, S.R., Lee, Y., & Min, K.C. (2017). Research on Arrangement Design for Sailing Yacht Winch using 3D Human Simulation. *Journal of Ocean Engineering and Technology*, 31(6), 419-424. <https://doi.org/10.26748/KSOE.2017.12.31.6.419>

Marchaj, C.A. (1996). *Sail Performance: Techniques to Maximize Sail Power*. London : UK Adlard Coles Nautical.

Author ORCID

Author name

Kim, Young Hun

ORCID

0000-0002-3072-6852

Study on Unmanned Hybrid Unmanned Surface Vehicle and Unmanned Underwater Vehicle System

Han-Sol Jin¹, Hyunjoon Cho¹, Ji-Hyeong Lee¹, Huang Jiafeng¹,
 Myung-Jun Kim¹, Ji-Youn Oh² and Hyeung-Sik Choi³

¹Graduate Student, Department of Mechanical Engineering, Korea Maritime and Ocean University, Busan, Korea

²Post Doctor, Maritime ICT R&D Center, Korea Institute of Ocean Science & Technology, Busan, Korea

³Professor, Department of Mechanical Engineering, Korea Maritime and Ocean University, Busan, Korea

KEY WORDS: Unmanned surface vehicle, Unmanned underwater vehicle, Autonomy, Autonomous control, Integrated system, Field test

ABSTRACT: Underwater operating platforms face difficulties regarding power supply and communications. To overcome these difficulties, this study proposes a hybrid surface and underwater vehicle (HSUV) and presents the development of the platform, control algorithms, and results of field tests. The HSUV is capable of supplying reliable power to the unmanned underwater vehicle (UUV) and obtaining data in real time by using a tether cable between the UUV and the unmanned surface vehicle (USV). The HSUV uses global positioning system (GPS) and ultra-short base line sensors to determine the relative location of the UUV. Way point (WP) and dynamic positioning (DP) algorithms were developed to enable the HSUV to perform unmanned exploration. After reaching the target point using the WP algorithm, the DP algorithm enables USV to maintain position while withstanding environmental disturbances. To ensure the navigation performance at sea, performance tests of GPS, attitude/heading reference system, and side scan sonar were conducted. Based on these results, manual operation, WP, and DP tests were conducted at sea. WP and DP test results and side scan sonar images during the sea trials are presented.

1. Introduction

The importance of unmanned surface vehicles (USVs) and unmanned underwater vehicles (UUVs) has recently increased as various marine resources, such as petroleum and gas, are gaining importance (Bentley, 2002; Nicholson and Healey, 2008). Although massive amounts of resources are present in the oceans, marine exploration is difficult to perform due to ocean currents and weather conditions (Hou, 2013). Particularly, the operation of a UUV in water poses difficulties that are not encountered on land, such as difficulties in supplying power, communication issues, low visibility, and water pressure. Recently, studies on platforms that combine USVs and UUVs have been performed to resolve such difficulties. Sarda and Dhanak proposed a hybrid surface and underwater vehicle (HSUV) that assists in launching and recovering vessels using tether cables (Sarda and Dhanak, 2017). However, this platform is limited in terms of power supply and real-time transmission of large amounts of data. Zwolak et al. proposed a similar platform that can additionally acquire

large amounts of data (Zwolak et al., 2017); however, this platform faces difficulties in real-time data transmission and power supply for long-term operation. In addition, it is difficult to obtain the real-time location of a UUV.

To resolve the aforementioned limitations, an HSUV that combines a USV and a UUV, retaining their advantages, is proposed in this study. The USV used is a stable catamaran designed to easily accelerate (Molland et al., 1994). The UUV used is also a catamaran that receives power from the USV, liberating space that would be occupied by batteries and increasing the payload capacity. Sensor data of the UUV can be verified in real time on land through a tether cable, and control commands can be transmitted. The power supplied from the USV enables UUV to be operated for a long period of time using its function for real-time communication with land. In addition, images from the UUV can be acquired in real time on land. The real-time relative locations of the USV and UUV can be identified by utilizing ultra-short base line (USBL) sensors.

The system components, kinetics, and control algorithm of the

Received 30 June 2020, revised 12 October 2020, accepted 19 October 2020

Corresponding author Hyeung-Sik Choi: +82-51-410-4297, hchoi@kmou.ac.kr

It is a recommended paper from the proceedings of 2019 Fall Conference of the Korea Marine Robot Technology (KMRTS).

© 2020, The Korean Society of Ocean Engineers

This is an open access article distributed under the terms of the creative commons attribution non-commercial license (<http://creativecommons.org/licenses/by-nc/4.0>) which permits unrestricted non-commercial use, distribution, and reproduction in any medium, provided the original work is properly cited.

developed HSUV are described in Sections 2, 3, and 4, respectively. Kinematic performance and control test results from offshore tests are described in Section 5.

2. System Structure of Hybrid Surface & Underwater Vehicle

Fig. 1 shows the structure of the HSUV constructed for this study. Operation console commands are transferred to the USV and UUV via a hub through wireless bridges, and USV and UUV are connected through a tether cable. The total weight of the HSUV, excluding the operation console, is 350 kg.

2.1 System Components of the Hybrid Surface and Underwater Vehicle

The system of the HSUV was constructed as in Fig. 2, and the console was constructed to control it. A personal computer (PC) in a land station has a program written in C# to identify the real-time condition of the surface and underwater vehicles via a graphical user interface (GUI). The main controller of the USV uses CYBCKIT-059 PSoC to operate the propellers, and the code was written to autonomously sail based on global positioning system (GPS) and attitude and heading reference system values. The surface vehicle is equipped with two cameras, a battery management system (BMS), a USBL, and light detection and ranging (Lidar), which can be verified

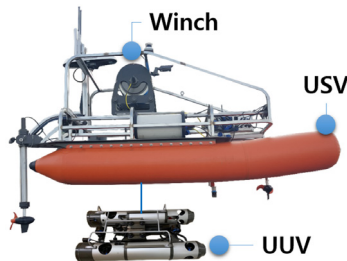


Fig. 1 HSUV components

on the operation console. The main controller of the underwater vehicle uses Pixhawk, and the cameras and side scan sonar data can be verified in real time on the operation console.

2.2 System Components of Unmanned Surface Vehicle

The components of the USV are shown in Fig. 3. The USV is a stable catamaran that has a buoyancy gain and can quickly accelerate. It transports the UUV to an exploration point by realizing GPS location information-based autonomous sailing. Voltage decreases and efficiency are considered to install batteries of 48 V and 24 V in the USV. The winch system of the USV consists of a brushless direct-current motor, a slip ring, and a level shaft. This system stably winds the tether cable, supplies electric current to the UUV, and controls exploration depths. The lidar and camera sensors were attached to recognize obstacles. The Lidar is capable of 360° omnidirectional identification. Front and docking verification cameras provide visual assistance in operation. The specifications of the USV are listed in Table 1.

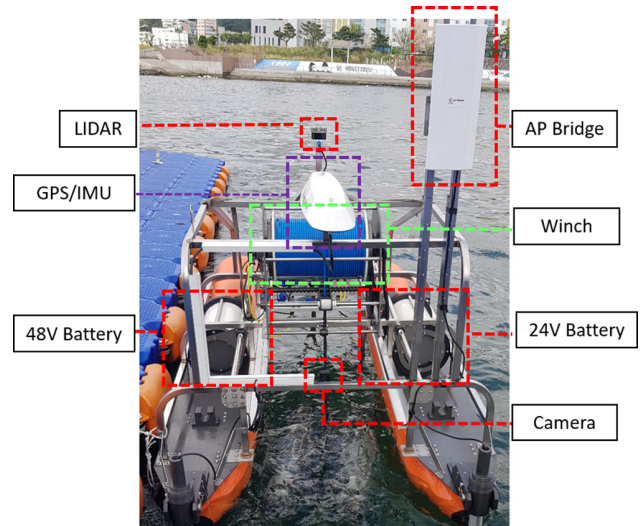


Fig. 3 USV components

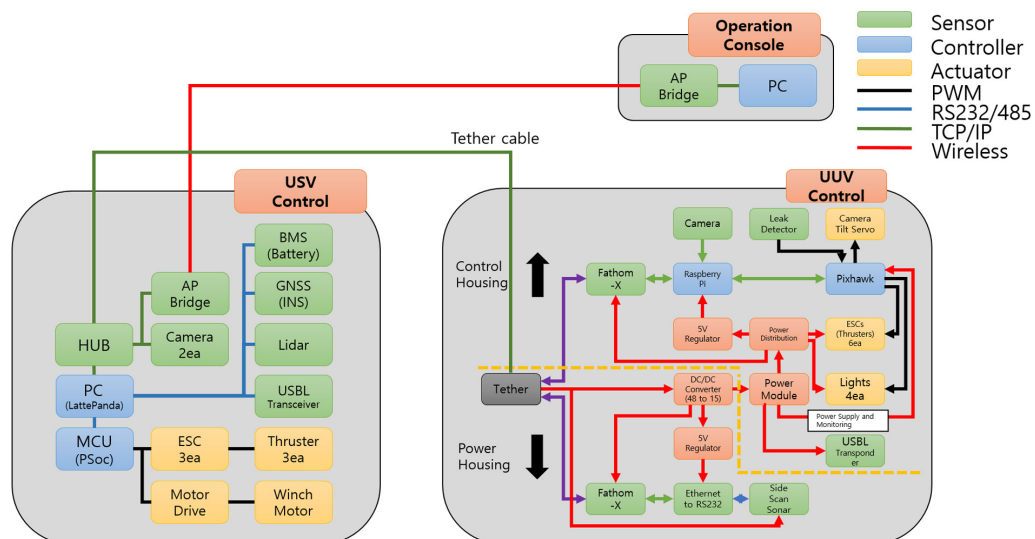


Fig. 2 HSUV system configuration

Table 1 USV and UUV specifications

Item	Specification
USV size (m)	3.3 × 2.5 × 1.6
USV weight (kg)	310
UUV size (m)	1.15 × 0.55 × 0.3
UUV weight (kg)	49.5

2.3 System Components of Unmanned Underwater Vehicle

Fig. 4 shows the UUV components. The UUV has an underwater tilt camera and a side scan sonar as sensors for exploring seabed terrain and underwater structures. The UUV weighs 49.5 kg on land and has a negative buoyancy of 14 kg. It is constructed in the form of a catamaran with relatively stable rolling to acquire high precision data from the side scan sonar. Depths are controlled using the depth sensor-based winch system and six propellers are used in the hull to allow six-axis control. The kinematic performance and USBL data are used to accurately identify the location of the underwater vehicle and perform various tasks. Ethernet is used for data transmission, and the data transmission rate to/from the land station is approximately 86 Mb/s. This value is verified using the iperf program, as shown in Fig. 5, and the data of each sensor can be verified in real time at the land station. The underwater camera is mounted in the dome-shaped space on the front of the underwater vehicle and its direction can be adjusted up to 90° using a tilt servo motor. It is a low-light camera for exploration in dark water and has horizontal and vertical visual fields

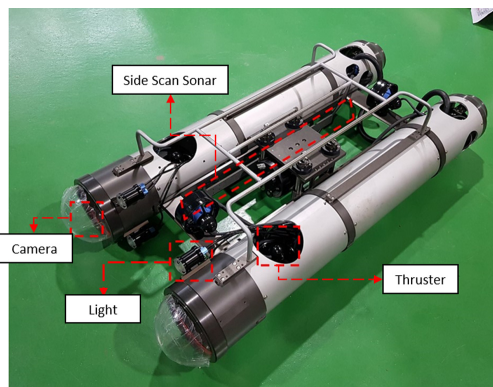


Fig. 4 UUV components

```

Microsoft Windows [Version 10.0.17134.677]
(c) 2018 Microsoft Corporation. All rights reserved.

C:\Users\WTEST>cd C:\Users\WTEST\Desktop\iperf-3.1.3-win64
C:\Users\WTEST\Desktop\iperf-3.1.3-win64>iperf3.exe -c 192.168.2.7
Connecting to host 192.168.2.7, port 5201
[ 4] local 192.168.2.1 port 49677 connected to 192.168.2.7 port 5201
[ ID] Interval      Transfer    Bandwidth
[ 4] 0.00-1.00  sec  10.0 MBytes  83.6 Mbits/sec
[ 4] 1.00-2.00  sec  10.8 MBytes  90.2 Mbits/sec
[ 4] 2.00-3.00  sec  8.75 MBytes  73.4 Mbits/sec
[ 4] 3.00-4.00  sec  11.0 MBytes  92.2 Mbits/sec
[ 4] 4.00-5.00  sec  11.0 MBytes  92.3 Mbits/sec
[ 4] 5.00-6.00  sec  11.1 MBytes  93.3 Mbits/sec
[ 4] 6.00-7.00  sec  11.0 MBytes  92.4 Mbits/sec
[ 4] 7.00-8.00  sec  9.82 MBytes  80.7 Mbits/sec
[ 4] 8.00-9.00  sec  11.0 MBytes  92.3 Mbits/sec
[ 4] 9.00-10.00 sec  9.38 MBytes  78.7 Mbits/sec

[ ID] Interval      Transfer    Bandwidth
[ 4] 0.00-10.00 sec  104 MBytes  86.9 Mbits/sec
[ 4] 0.00-10.00 sec  103 MBytes  86.7 Mbits/sec

iperf Done.
C:\Users\WTEST\Desktop\iperf-3.1.3-win64>
    
```

Fig. 5 Ethernet speed measurement result using ‘iperf’ program

of 80° and 68°, respectively.

Considering voltage decreases through the tether cable, the underwater vehicle received 48 V direct-current power. Data are transmitted between the surface and underwater vehicles through the tether cable via power over Ethernet. A light whose brightness can be adjusted up to 1,500 lm was attached for dark underwater exploration.

2.4 Operation Console and GUI Program

Fig. 6 shows the operation console of the HSUV. The operation console was built to verify side scan sonar data, cameras, and the current states and control commands of the USV and UUV in real time. A commercial PC, a joystick, and Wi-Fi equipment are loaded in a case, and an inverter is mounted inside the console to supply power to access point (AP) bridges. The console has sufficient space to efficiently store the power cable, mouse, and joystick required for operation. A cooling fan was also attached, considering the strong direct sunlight on the sea.

Fig. 7 shows a part of the operation program used in this study. This program was written to verify numerical data of surface and underwater vehicles and GPS and intuitively view the data via GUI. Google Map is provided to verify real-time locations and paths. Joystick, way point (WP) and dynamic positioning (DP) modes, and winch control are implemented as functions of the program. The four cameras of the HSUV are connected to the operation console via dual monitors to conveniently monitor their output.

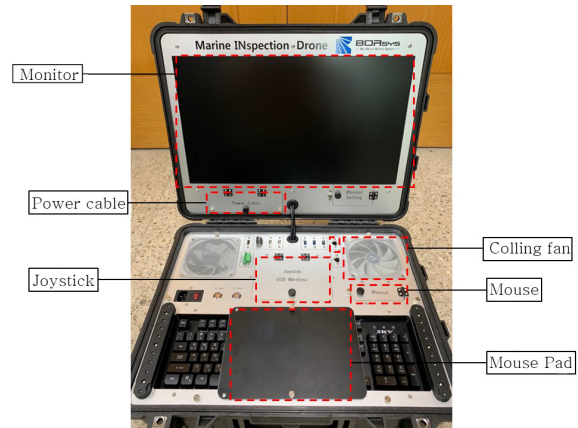


Fig. 6 Operation console components

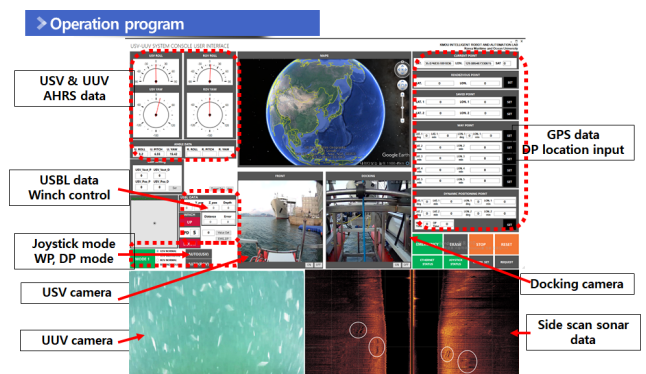


Fig. 7 Operation console program

3. Kinetics of Hybrid Surface and Underwater Vehicle

The dynamics of the HSUV is based on the Newton–Euler equations and vectors. The USV moves along the x-axis and y-axis; hence, its motion can be expressed as surge, sway, and yaw. The notation associated with each axis is presented in Table 2. Considering the Coriolis centripetal force and attenuation acting on the USV, the dynamic equations can be expressed as Eqs. (1)–(3). The detailed definitions for the parameters and states are described in Fossen (2011) and Cho et al. (2020).

Table 2 Notation of Society of Naval Architects and Marine Engineers for USV and UUV

Translational motion	Force	Position	Linear velocity
Surge	X	x	u
Sway	Y	y	v
Heave	Z	z	w
Rotational motion	Moment	Euler angle	Angular velocity
Roll	K	ϕ	p
Pitch	M	θ	q
Yaw	N	ψ	r

$$(m - X_u)\dot{u} - mur + (Y_v v_r r + Y_r r - m X_G r) - (X_u + X_{u|u}|u|)u = \tau_X \quad (1)$$

$$(m - Y_v)\dot{v} + (m x_G - Y_r)\dot{r} - mur - X_u u_r r - (Y_v + Y_{v|v}|v|)v - (Y_r + Y_{r|r}|r|)r = \tau_Y \quad (2)$$

$$(m x_G - N_v)\dot{v} + (J_z - N_r)\dot{r} - (Y_v v_r r - Y_r r + m x_G r)u + X_u u_r v - (N_v + N_{v|v}|v|)v - (N_r + N_{r|r}|r|)r = \tau_N \quad (3)$$

Here, m is the mass, I is the mass moment of inertia, and τ is the thrust of two rear thrusters attached to the USV.

Eqs. (4)–(6) represent the motion of the UUV. The UUV follows the considerations for USV, but surge, sway, and yaw are considered as relative locations and relative direction angles. The subscript R in Eqs. (4)–(6) was used to avoid confusion with the equations of the USV. The symbol on the right side of sigma represents the sum of environmental disturbance and thrust.

$$m_R [\dot{u}_R - v_R r_R + w_R q_R - x_{G_R} (q_R^2 + r_R^2) + y_{G_R} (p_R q_R - r_R \dot{r}_R) + z_{G_R} (p_R r_R + \dot{q}_R)] = \sum X_R \quad (4)$$

$$m_R [\dot{v}_R - w_R p_R + u_R r_R - y_{G_R} (r_R^2 + p_R^2) + z_{G_R} (q_R r_R - p_R \dot{p}_R) + x_{G_R} (p_R q_R + r_R \dot{r}_R)] = \sum Y_R \quad (5)$$

$$I_{Z_R} \dot{r}_R + (I_{y_R} - I_{x_R}) p_R q_R + m_R [x_{G_R} (v_R \dot{r}_R - w_R p_R + u_R r_R) - y_{G_R} (\dot{u}_R - v_R r_R + w_R p_R)] = \sum N_R \quad (6)$$

4. Control Algorithm of Hybrid Surface and Underwater Vehicle

4.1 Dynamic Positioning Algorithm

The DP algorithm of the USV is illustrated in Fig. 8. The DP process is performed as follows: when the USV moves out of a target radius due to the effect of tidal current or wind, it obtains its rotational direction angle toward a DP point and adjusts its heading. The platform moves when the heading of the platform coincides with the target direction angle, and stops when it reaches the target point.

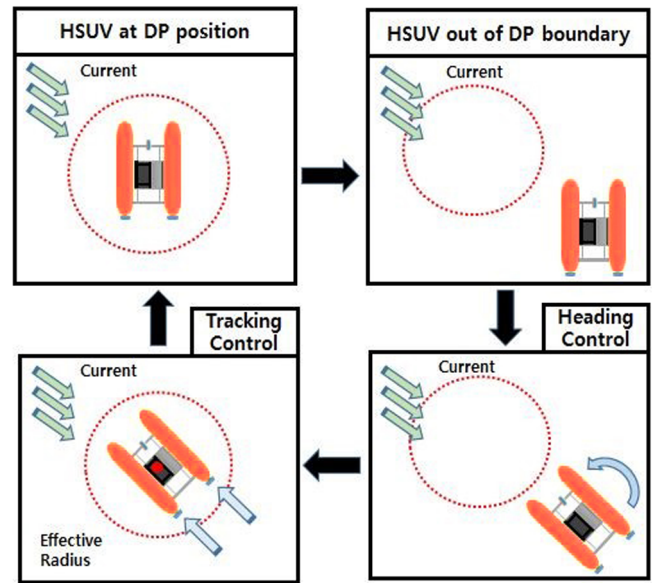


Fig. 8 DP algorithm

$$[X_k - X(t)]^2 + [Y_k - Y(t)]^2 < \rho_c^2 \quad (7)$$

Eq. (7) represents the distance error. $[X(t), Y(t)]$ represents the location of the HSUV, represents the target point location, and ρ_c is the target radius.

4.2 Way Point Algorithm

The WP algorithm is illustrated in Fig. 9. When the latitude and longitude of a target point are given, the USV obtains its target direction angle using the line of sight and adjusts its heading. The platform moves when the heading of the platform corresponds to the target direction angle, and stops when it reaches the target point. This process is completed and repeated toward the next WP.

$$\phi_U = \tan^{-1} \left[\frac{Y_k - Y(t)}{X_k - X(t)} \right] \quad (8)$$

Eq. (8) represents the direction angle error. $[X(t), Y(t)]$ represents the location of the HSUV, and $[X_k, Y_k]$ represents the target point location.

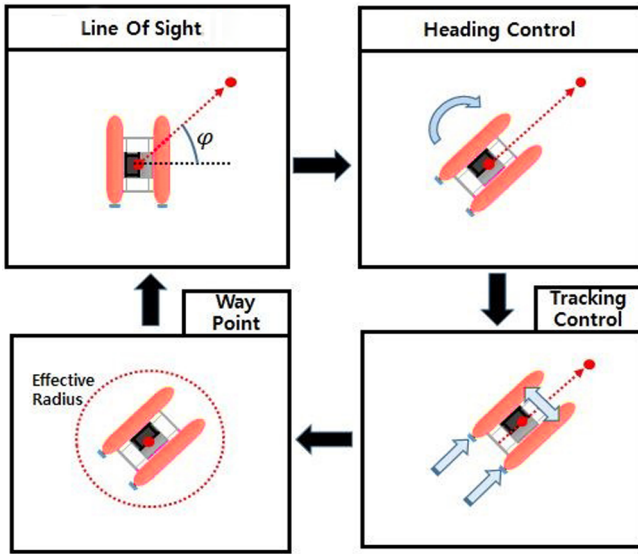


Fig. 9 WP algorithm

5. Offshore Tests

Offshore tests were performed on the relatively calm coast of the Korea Maritime and Ocean University to evaluate the performance of the proposed HSUV and its control system. The offshore tests include accuracy tests of the GPS, which is the key sensor on land, and communication tests. Based on these tests, route tracking tests of the USV, DP, and performance tests of the side scan sonar were performed.

Tests for the communication distance of the platform were performed prior to the main tests. The communication equipment used in the unmanned vessel has a high effective transmission rate of 360 Mb/s and additionally uses an omnidirectional antenna.

The test results indicated that data are effectively received and transmitted up to 890 m in the absence of obstacles between the wireless communication devices. Fig. 10 shows a picture of the offshore tests performed.



Fig. 10 Sea experiment

5.1 GPS Sensor Tests

The GPS sensor used in the proposed hybrid system provides true north data, magnetic north data, and altitude values. Tests for moving

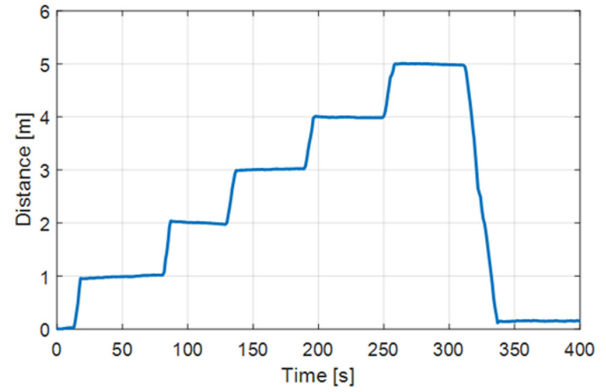


Fig. 11 GPS performance test

the system 5 m and then returning to the initial point were performed to verify the reliability of sensor values. The test results are shown in Fig. 11.

5.2 WP Tests

Route control tests were conducted on the USV to individually evaluate the accuracy of the sensors.

The WP algorithm of Section 4.2 was used for the USV to reach four WPs on the sea in these tests. Fig. 12 shows the corresponding results, and Table 3 lists the WPs designated in the operation console. The latitude and longitude of the four WPs were input into the operation console and WPs 1-4 were reached from the start point. The maximum error obtained for the WPs was 2.6 m.

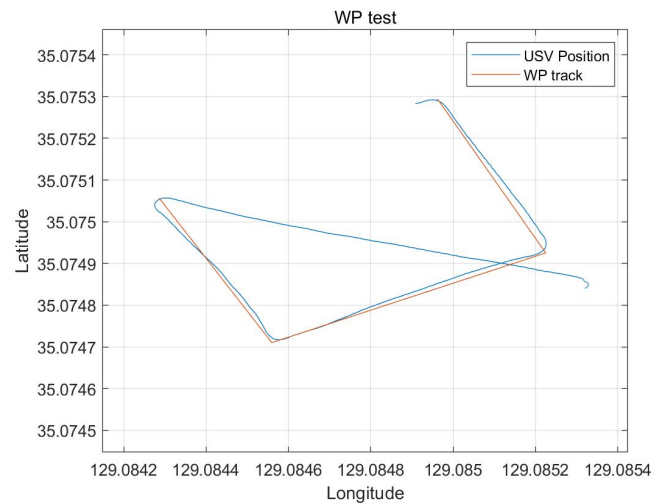


Fig. 12 WP results of USV

Table 3 USV way points

Way point	Latitude	Longitude
Start point	35.0748403	129.0853198
Way point 1	35.0749253	129.0852248
Way point 2	35.0752943	129.0849620
Way point 3	35.0750570	129.0842860
Way point 4	35.0747102	129.0845596

5.3 Side Scan Sonar Performance Tests

A side scan sonar was mounted on an underwater drone to measure the state of the bottom of a river. The tests were performed on the estuary bank of the brackish water zone of Nakdong River. As the river is not deep, the UUV was lowered 0.5 m, towed by the USV, and moved straight-line distances. Fig. 13 shows pictures of captured bridge posts and fishes.

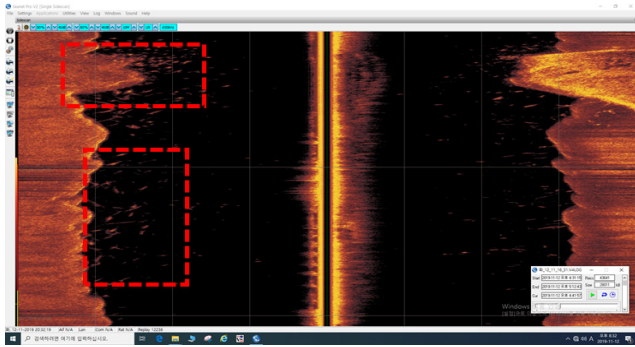


Fig. 13 Search result of the river bottom using side scan sonar

5.4 Dynamic Positioning Tests

The DP algorithm of Section 4.1 developed for this study was used to perform the DP of the USV on the sea. The DP algorithm was constructed to operate the controller when the USV moves out of a target radius of 3.0 m to extend the operation time of the USV. With the algorithm, the 3.3 m USV was controlled to remain within a certain radius. Fig. 14 shows the results of ten minutes of DP in measurement units of 500 ms. The test results generally satisfied the target error radius of 3.0 m, and the average DP error was 2.03 m, which shows that DP was adequately performed in comparison to the full length of the vehicle.

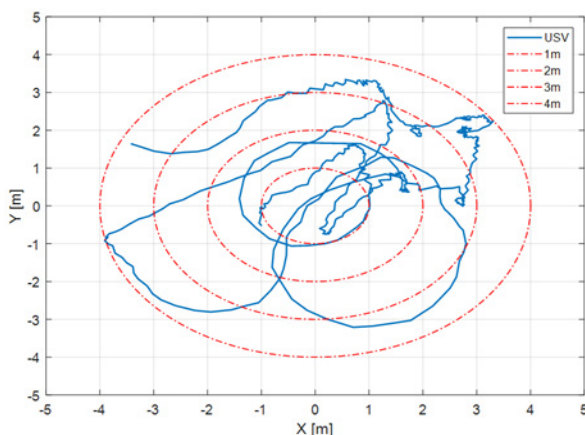


Fig. 14 DP results for the USV

6. Conclusions

In this study, the structure and control system of the HSUV were designed and constructed and basic performance tests were performed. The sensor data of the USV and UUV can be verified in real time through the tether cable, and the UUV can be used for a long period of time. The individual sensor performance tests were performed,

followed by offshore tests using the controller algorithms constructed in Section 4 to verify the performance. The maximum error of the WPs of the USV was 2.60 m, and the average DP error was 2.03 m, which indicates the excellence of the control system. In addition, the side scan sonar of the UUV was used in the same sea area to explore the bottom of a river. The river, surrounding terrain, and fish search information could be monitored in real time at the land station by utilizing the real-time communication system.

References

- Bentley, R.W. (2002). Global Oil & Gas Depletion: an Overview. *Energy Policy*, 30(3), 189-205. [https://doi.org/10.1016/S0301-4215\(01\)00144-6](https://doi.org/10.1016/S0301-4215(01)00144-6)
- Cho, H., Jeong, S.-K., Ji, D.-H., Tran, N.-H., Vu, M.T., & Choi, H.-S., (2020). Study on Control System of Integrated Unmanned Surface Vehicle and Underwater Vehicle. *Sensors*, 20(9), 2633. <https://doi.org/10.3390/s20092633>
- Fossen, T.I. (2011). *Handbook of Marine Craft Hydrodynamics and Motion Control* (1st ed.). New Jersey, USA: Jhon Wiley & Sons.
- Hou, W. (2013). *Ocean Sensing and Monitoring: Optics and Other Methods* (1st ed.). Washington, USA: SPIE. <https://doi.org/10.1117/3.1002079>
- Nicholson, J.W., & Healey, A.J. (2008). The Present State of Autonomous Underwater Vegicle (AUV) Applications and Technologies. *Marine Technology Society Journal*, 42(1), 44-51. <https://doi.org/10.4031/002533208786861272>
- Molland, A.F., Wellicome, J.F., & Couser, P.R. (1994). *Resistance Experiments on a Systematic Series of High Speed Displacement Catamaran Forms: Variation of Length-displacement Ratio and Breadth-draught Ratio* (Ship Science Reports, 71). Southampton, UK: University of Southampton.
- Sarda, E.I., & Dhanak, M.R. (2017). A USV-Based Automated Launch and Recovery System for AUVs. *IEEE Journal of Oceanic Engineering*, 42(1), 37-55. <https://doi.org/10.1109/JOE.2016.2554679>
- Zwolak, K., Simpson, B., Anderon, R., Bazhenowa, E., Falconer, R., Kearns, T., ... & Tinmouth, N. (2017). An Unmanned Seafloor Mapping System: The Concept of an AUV Integrated with the Newly Designed USV SEA-KIT. *Proceedings of the OCEANS, Aberdeen, UK*. <https://doi.org/10.1109/OCEANSE.2017.8084899>

Author ORCIDs

Author name	ORCID
Jin, Han-Sol	0000-0002-3400-3272
Cho, Hyunjoon	0000-0003-1084-8542
Lee, Ji-Hyeong	0000-0002-3226-6036
Huang, Jiafeng	0000-0002-2866-0778
Kim, Myung-Jun	0000-0002-9018-3837
Oh, Ji-Youn	0000-0003-3588-5892
Choi, Hyeung-Sik	0000-0002-4060-8163

Material Property-Estimate Technique Based on Natural Frequency for Updating Finite Element Model of Orthotropic Beams

Kookhyun Kim¹, Sungju Park², Sangjoong Lee³,
Seongjun Hwang³, Sumin Kim³ and Yonghee Lee³

¹Professor, School of Naval Architecture & Ocean Engineering, Tongmyong University, Busan, Korea

²Assistant Professor, School of Naval Architecture & Ocean Engineering, Tongmyong University, Busan, Korea

³Undergraduate Student, School of Naval Architecture & Ocean Engineering, Tongmyong University, Busan, Korea

KEY WORDS: Composite material, Carbon-fiber reinforced plastic, Orthotropic beam, Material property, Natural frequency, Discrete genetic algorithm, Cost function

ABSTRACT: Composite materials such as glass-fiber reinforced plastic and carbon-fiber reinforced plastic (CFRP) shows anisotropic property and have been widely used for structural members and outfitings of ships. The structural safety of composite structures has been generally evaluated via finite element analysis. This paper presents a technique for updating the finite element model of anisotropic beams or plates via natural frequencies. The finite element model updates involved a compensation process of anisotropic material properties, such as the elastic and shear moduli of orthotropic structural members. The technique adopted was based on a discrete genetic algorithm, which is an optimization technique. The cost function was adopted to assess the optimization problem, which consisted of the calculated and referenced low-order natural frequencies for the target structure. The optimization process was implemented with MATLAB, which includes the finite element updates and the corresponding natural frequency calculations with MSC/NASTRAN. Material properties of a virtual cantilevered orthotropic beam were estimated to verify the presented method and the results obtained were compared with the reference values. Furthermore, the technique was applied to a cantilevered CFRP beam to successfully estimate the unknown material properties.

1. Introduction

Composite materials such as GFRP (glass-fiber reinforced plastic) and CFRP (carbon-fiber reinforced plastic) provide superior material properties compared to structural steels in terms of specific strength, fatigue resistance, and anti-corrosion. Consequently, composite materials are widely used for structural materials in various fields, such as the aviation, automotive, shipbuilding, and marine industries (Weitzenböck et al., 2010). Particularly, CFRP is steadily garnering attention both as the hull construction material of small ships and high-speed crafts that require weight reduction, and also as a high-load auxiliary material for engine parts, such as propellers (Chen et al., 2003; Oh et al., 2013; Lee et al., 2014).

In this study, the structural safety of CFRP structures was generally evaluated via finite element analysis. Regarding this process, the mechanical properties of the material approximate to the actual values, as well as the shape of the target structure, should be introduced to the

finite element analysis. Although methods for manufacturing CFRP materials in the design shape (during ship building) have been implemented with recent advancements in technology, the mechanical properties of these materials remain unclear owing to the significantly different mechanical properties of CFRP structures depending on the stacking sequence and direction, manufacturing environment (temperature and humidity), and expertise of workers, as well as the differences in the physical properties of the base materials, such as carbon fiber and resin.

Meanwhile, the importance of digital twin technology is growing in the field of ship structural mechanics. The core technology here involves the use of a virtual ship with similar structural properties to an actual ship (JASTRA Channel, 2020). A structural digital twin platform with both static and dynamic structural responses should be implemented according to the external force generated during the virtual ship's operation similar to that of an actual ship. The structural digital twin implementation requires the development of a finite

Received 30 November 2020, revised 3 December 2020, accepted 3 December 2020

Corresponding author Kookhyun Kim: +82-51-629-1658, kimk@tu.ac.kr

This paper is updated from the proceedings of 2020 fall meeting of the Korea Society of Ocean Engineers(KSOE)

© 2020, The Korean Society of Ocean Engineers

This is an open access article distributed under the terms of the creative commons attribution non-commercial license (<http://creativecommons.org/licenses/by-nc/4.0>) which permits unrestricted non-commercial use, distribution, and reproduction in any medium, provided the original work is properly cited.

element model that reflects the static and digital characteristics of an actual ship.

The properties of the composite material, such as Poisson’s ratio, elastic, and shear moduli are generally calculated via static tests, such as tensile, compression, and bending tests, on beams or sheet specimens made of the corresponding material. However, equivalent finite element model update techniques have been proposed in recent years to implement the dynamic properties of a target structure by adopting modal characteristics, such as natural frequency, mode shape, and mode damping. Zahari et al. (2016) proposed a method and procedure for identifying the parameters that influence the dynamic properties of a joint structure via sensitivity analysis, as well as calculating the equivalent material properties, such that a natural frequency identical to that of the actual structure is obtained. Hofmeister et al. (2019) proposed an optimization-based equivalent finite element model update to address wind turbine blade damages. Giagopoulos et al. (2009) introduced the finite element model update of an experimental vehicle using measured modal characteristic data.

This study presents a finite element model update technique, which calculates the equivalent material properties of a target structure using the natural frequencies of CFRP ships or structures. The technique involves the processes of optimization parameter selection, finite element model development and update. Additionally, in this study, the validity of the proposed technique is evaluated by conducting numerical analysis on a cantilevered orthotropic beam. Furthermore, the feasibility of the proposed technique is verified by estimating the equivalent material properties of the target structure using the natural frequency information obtained from a random CFRP cantilever beam.

2. Finite Element Model Update

The finite element model update for composite structures is a process that involves performing the inverse method on the equivalent material properties of finite element model by applying the optimization technique to obtain the same natural frequencies as the target structure. Fig. 1 illustrates the finite element model update procedures with processes of optimization parameter selection, finite

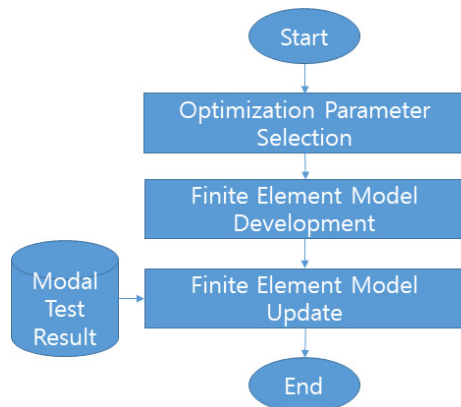


Fig. 1 Finite element model update process applying an optimization algorithm

element model development and update. The finite element model update process for composite structures was implemented in MATLAB while MSC/NASTRAN was adopted to carry out the low-order natural frequency analysis required in the optimization process.

2.1 Optimization Parameter Selection

To accurately identify the mechanical properties of composite structures, material properties need to be derived via standardized material tests, such as tensile, compression, and bending tests. Mechanical properties can vary significantly depending on the stacking environment and expertise of workers, even if the same base material is used and stacked with the exact same specifications. As an alternative to address this challenge, an inverse method can be applied to calculate the material’s properties using the dynamic properties of target structure, such as modal test results. This study updates the finite element model based on an optimization process that involves minimizing the difference between the natural frequencies obtained via the finite element model and modal test results, respectively. In the optimization process, density, thickness, number of layers, elastic and shear moduli, as well as Poisson’s ratio can be employed as the targets of optimization parameters. In this study, the elastic moduli, E_{11} and E_{22} , and shear moduli, G_{12} , G_{13} , and G_{23} , which are considered to significantly influence the mechanical properties of orthotropic plate materials, were selected as optimization parameters.

2.2 Finite Element Model Development

The finite element model is saved in the bulk data file format (*.bdf), which is an MSC/NASTRAN input file. Fig. 2 illustrates an

```

UD.bdf
SOL 103
CEND
TITLE = Uni-directional Composite Beam
ECHO = NONE
RESVEC = NO
SUBCASE 1
  TITLE= Modal Analysis
  METHOD = 1
  SEC = 2
  VECTOR(SORT1, REAL)=ALL
  SPCFORCES(SORT1, REAL)=ALL
BEGIN BULK
PARAM      POST      0
PARAM      PRINTMAX  YES
ETGRL      1          30      0
PCOMP      1
          1          .010    0.    YES
INCLUDE 'MAT.INC'
CQUAD4     1          1          1          2          63      62      0.
CQUAD4     2          1          2          3          64      63      0.
.
.
.
GRID       1          0.        0.        0.
GRID       2          .01       0.        0.
.
.
.
GRID       305        .6        .04       0.
SPCADD     2          1
SPC1       1          123       1          2          3          4          5          62
          63          64          65          66          123       124       125       126
          127       184       185       186          187       188       245       246
          247       248       249
ENDDATA
mat.inc
MAT8       1          1.380+111.040+102.900-016.900+096.900+096.900+091.590+03
  
```

Fig. 2 Example of finite element model of an orthotropic beam: an MSC/NASTRAN input file (bdf-file) and external file for defining the material properties

example of a bdf-file of the finite element model for an orthotropic beam used in this study. The modal analysis adopts the SEMODES (SOL 103) module of MSC/NASTRAN. The finite element is formulated using CQUAD4, a quadrilateral shell element. The material properties of the composite structure were defined using PCOMP. Although the orthotropic material properties were defined by MAT8, they were saved as separate MAT.INC files for defining the elastic and shear moduli to enable the easy control of optimization parameters. The file was designed to be retrieved by the “include” command from the bulk data file of MSC/NASTRAN during the optimization process.

2.3 Finite Element Model Update

The finite element model update for the composite structure is conducted such that the natural frequency of the target structure is induced to approach the actual value. The optimization process for the finite element model update adopted the discrete genetic algorithm, which is a typical global optimization algorithm.

The discrete genetic algorithm is accompanied by the following procedure:

- (1) The optimization parameters are discretized and coded as bits to construct the first generation.
- (2) The modal analysis is conducted for each object that belongs to the first generation and the fitness assessment is conducted via derived natural frequencies.
- (3) The construction of the next generation is conducted until the required fitness is fulfilled or the maximum number of iterations is reached, via elitist model, selection phase, crossover phase, and mutation phase processes, as well as the fitness assessment process on the constructed next generation.

More details on the finite element model update using the discrete algorithm are presented in Chapter 3.

3. Discrete Genetic Algorithm

Fig. 3 illustrates a flow chart of the discrete genetic algorithm adopted in this study for the finite element model update process. As shown in the figure, the process proceeds in the following order: first generation construction, fitness assessment for first generation and convergence check, application of elitist model, selection phase, crossover phase, mutation phase, and fitness assessment for next generation and convergence check. Fitness assessment is conducted based on the cost function that reflects the modal test results of the target structure, as well as the modal analysis results of each object. In the convergence check step, if the required cost or maximum number of iterations is not fulfilled, the elitist model step and later steps are repeated until convergence is achieved.

3.1 Optimization Parameter Discretization and Coding

The optimization parameters are discretized and coded in the discrete genetic algorithm. The elastic and shear moduli, which are

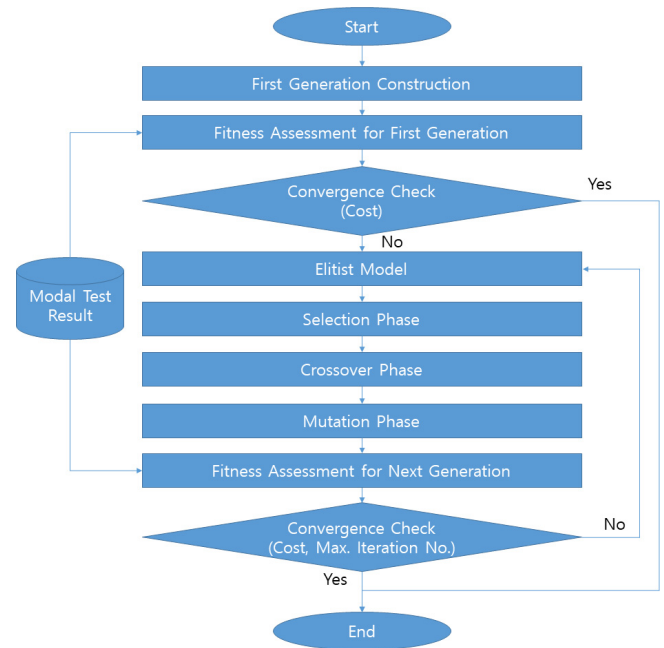


Fig. 3 Process of finite element model update via discrete genetic algorithm

optimization parameters, are discretized in equal intervals for the desired range and stored as databases with unique numbers.

In the discrete genetic algorithm, the unique number of the database is coded as a chromosome in the form of an array composed of bits.

Given the number of databases discretized for each optimization parameter as N_{ij} , the selected database is expressed as an array L_{ij} composed of $N_{i,j,b}$ ($=\log_2 N_{ij}$) number of bits ($N_{i,j,b}$ -bit), as expressed in Eq. (1).

$$L_{ij} = [l_{ij}^1, l_{ij}^2, \dots, l_{ij}^{N_{i,j,b}}] \quad (1)$$

where l_{ij}^k denotes the k -th bit value in the coded array of the optimization parameter. For example, when the optimization parameters, l_{11}^k , l_{22}^k , l_{12}^k , l_{13}^k , and l_{23}^k , are discretized and coded, each of E_{11} , E_{22} , G_{12} , G_{13} , and G_{23} becomes the k -th bit value of the $N_{i,j,b}$ -bit array, respectively.

The chromosome array G , consisting of all database information of the optimization parameters, can be expressed in Eq. (2), which links the chromosome array to each of the optimization parameters. The total number of bits, N , of the chromosome array is expressed in Eq. (3).

$$G = [L_{11}, L_{22}, L_{12}, L_{13}, L_{23}] \quad (2)$$

$$N = N_{11b} + N_{22b} + N_{12b} + N_{13b} + N_{23b} \quad (3)$$

3.2 Fitness Assessment

Fitness is a quantitative index that indicates the proximity of the calculated natural frequency to the actual natural frequency when the material properties corresponding to individuals of each generation are

reflected in the finite element model. A cost function was employed in this study to assess fitness, with lower costs representing higher fitness. The cost function J is expressed by Eq. (4) and was defined by considering the weight of the relative squared error for each natural frequency of the modal test and finite element analysis results (Zahari et al. 2016).

$$J = \sum_{i=1}^n W_i \left(\frac{f_i^{fem} - f_i^{exp}}{f_i^{exp}} \right)^2 \quad (4)$$

where f_i^{fem} and f_i^{exp} , W_i , and n represent the i -th natural frequency derived from finite element analysis and modal test, weight for the i -th natural frequency ("1" was applied as the weight in this study), and number of natural frequencies used in the optimization process, respectively. The natural frequency f_i^{exp} of the target beam model utilized the modal test results.

3.3 Discrete Genetic Algorithm Development

3.3.1 First generation construction

As illustrated in Fig. 4, the N_{pop} populations that formulate the initial generation are generated as chromosome groups ($G_1, G_2, \dots, G_{N_{pop}}$) with bit arrays. Each chromosome is randomly allocated with a bit value of "0" or "1."

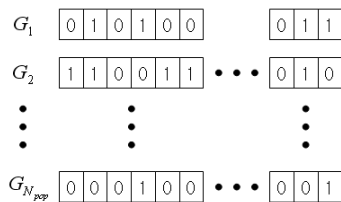


Fig. 4 Chromosome group for first generation

3.3.2 Elitist model

In the elitist model, the elitist chromosome group, which exhibits the best fitness in the present population is considered an individual of the next generation (Fig. 5). This approach is used to achieve quicker convergence by maintaining the properties of the individual that exhibits outstanding fitness in the previous generation.

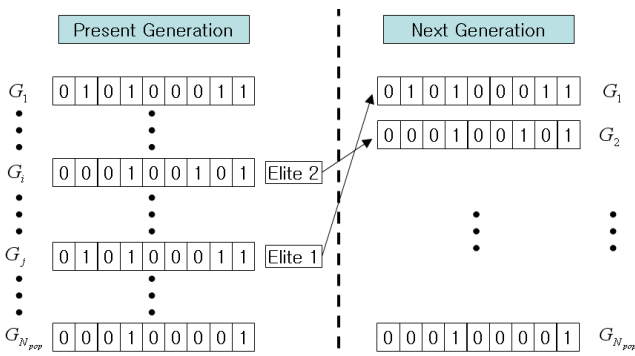


Fig. 5 Elitist model

In this study, two individuals, exhibiting the best fitness in the present generation, are adopted as the first and second individuals in the next generation.

3.3.3 Selection phase

In the selection phase, chromosomes are selected from the present generation to generate chromosomes for the next generation population. Two of the most widely used selection methods are the roulette and tournament selections. The roulette selection increases selection probability based on the fitness proportion of each chromosome of the present population, whereas the tournament selection selects an individual with optimal fitness from a population of two randomly selected chromosomes in the present generation. This study adopted the tournament selection method, which is more straightforward than the roulette selection method.

3.3.4 Crossover phase

After selecting two chromosomes from the present population, chromosomal crossover was conducted to generate new genes for the next generation by exchanging the genetic materials of the selected specific chromosomes. The crossover process is carried out by exchanging preceding genes with following genes based on the random array reference point of chromosomes. Depending on the number of reference points, the crossover can be classified into one-point and multi-point crossovers. However, to avoid bias toward a certain solution and increase convergence, a probability of crossover was set, and a real value between "0" and "1" was randomly extracted before the crossover. Subsequently, if the extracted value is less than the specified probability of crossover, crossover is carried out, otherwise the selected chromosomes are transferred to the next generation population. In this study, one-point cross over was adopted, as shown in Fig. 6.

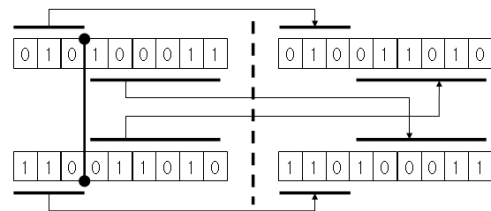


Fig. 6 One-point crossover

3.3.5 Mutation phase

The chromosomes that passed through selection and crossover phases were designed to induce mutation by intentionally altering the information of one or more genes. Mutations typically demonstrate the tendency of reducing the average fitness of the entire population, thus providing the effect that enables access to more diverse optimal solutions by implanting new information inside the chromosomes during the algorithm's execution. However, if the probability of mutation for the chromosomes is set too high, there is a limitation of moving away from the optimal solution as the process is repeatedly

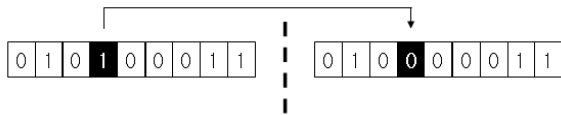


Fig. 7 Mutation

iterated. Therefore, an appropriate mutation probability should be configured.

In this study, mutation was permitted for one gene of the chromosome alone, as shown in Fig. 7.

3.3.6 Convergence check

In the convergence check, the fitness of the new population with genes modified via crossover and mutation phases, was calculated. The algorithm was terminated if the calculated fitness was less than that of the previous generation or a maximum number of algorithm iterations was achieved. Otherwise, the process returned to the elitist model step and the entire process was repeated again.

4. Numerical Examples

4.1 Verification of the Finite Element Model Update Method

The feasibility of the inverse method on the material properties of the composite structure was evaluated by performing inverse operation on the material properties of an orthotropic beam. In general, cantilevered beam type specimens are widely used to determine the dynamic properties of structures. Therefore, a cantilevered orthotropic beam was selected as the target structure for verification. Natural frequencies corresponding to the exact solution were calculated after conducting modal analysis on the target structure. Table 1 summarizes the material properties of the target cantilevered orthotropic beam. The material direction was assumed to be longitudinal. The finite element model for the target structure was designed with 240 rectangular shell elements and 305 nodes (Fig. 8). The length, width, and thickness of

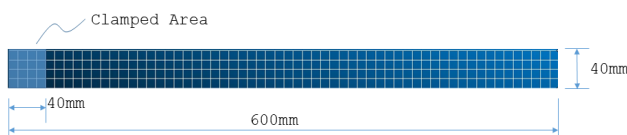


Fig. 8 Finite element model of the cantilevered orthotropic beam

Table 1 Material properties of cantilevered orthotropic beam

Material property		Value
Elastic modulus (N/m ²)	E_{11}	138.0E+09
	E_{22}	10.40E+09
Poisson's ratio	ν_{12}	0.29
	G_{12}	6.900E+09
Shear modulus (N/m ²)	G_{13}	6.900E+09
	G_{23}	6.900E+09
Density (kg/m ³)	ρ	1,590

Table 2 Modal frequencies of cantilevered orthotropic beam

Order	Natural frequency (Hz)	Mode shape
1	45.62	vertical bending (1st)
2	187.61	lateral bending (1st)
3	284.69	vertical bending (2nd)
4	422.27	twisting (1st)
5	789.60	vertical bending (3rd)
6	1044.78	lateral bending (2nd)

the finite element model were 600, 40, and 10 mm, respectively while the clamp fixture boundary condition was applied to the 0–40 mm area in the longitudinal direction. The natural frequencies of the target structure were extracted for a total of six generations, from first to sixth, and the values obtained are summarized in Table 2 together with the mode shape information.

The inverse operation was performed to calculate the material properties of the target structure in reverse solely via the natural frequency information presented in Table 2. In this process, elastic moduli, E_{11} and E_{22} , and shear modulus, G_{12} , were selected as optimization parameters. Table 3 summarizes the ranges of material properties, as well as those of the discrete genetic algorithm parameters. The ranges were configured to include the material properties from Table 1. As a reference, 16 (4-bit) optimization parameter databases were configured for each parameter, and the moduli, G_{23} and G_{13} were fixed at 6.900E+09 N/m². However, the number of individuals for each generation was set as 50, and the probabilities of crossover and mutation were set as 0.9 and 0.1, respectively. The convergence criteria were established by setting 1E-10 and 100 as the required cost and maximum number of iterations, respectively.

Fig. 9 presents a convergence plot graph illustrating the minimum cost function value for each generation. The sixth generation's

Table 3 Material property ranges and indiscrete genetic algorithm parameters of cantilevered orthotropic beam

Parameter name	Value
Elastic modulus (N/m ²)	E_{11} 1.300E+11~1.450E+11 (4-bit)
	E_{22} 1.000E+10~1.280E+10 (4-bit)
Poisson's ratio	ν_{12} 0.29
Shear modulus (N/m ²)	G_{12} 6.000E+09~7.500E+09 (4-bit)
	G_{13} 6.900E+09
	G_{23} 6.900E+09
Density (kg/m ³)	ρ 1,590
Number of population, N_{pop}	50
Probability of crossover	0.9
Probability of mutation	0.1
Convergence criteria	1E-6
Maximum number of iteration	100

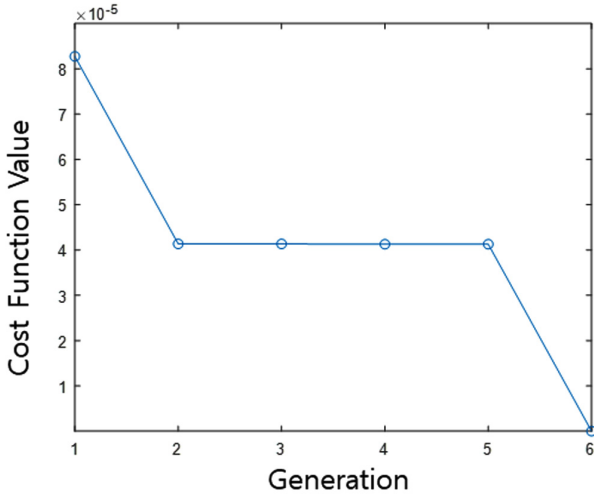


Fig. 9 Convergence plot: generation vs. cost function value

minimum cost function J converged to zero, and the material properties derived via the inverse method matched the material properties of Table 1 without displaying any error. This indicates that the material property inversion method implemented in this study was successfully executed.

4.2 Application to Cantilevered CFRP Beam

To evaluate the practical applicability of the proposed finite element model update method, the inverse operation was performed to

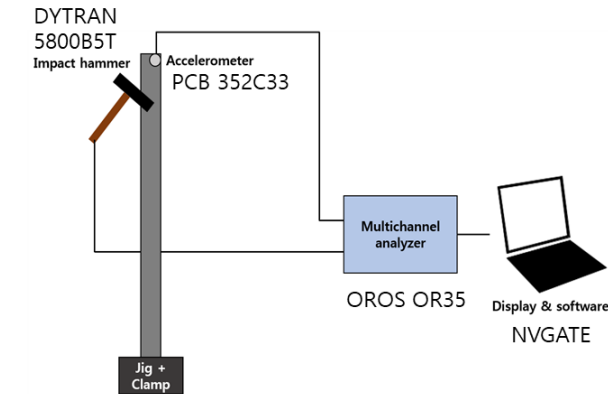
Table 4 Material property ranges and indiscrete genetic algorithm parameters of cantilevered CFRP beam

Parameter name	Value
Elastic modulus (N/m ²)	E_{11} 1.000E+11~4.150E+11 (6-bit)
	E_{22} 2.000E+09~2.000E+11 (5-bit)
Poisson's ratio	ν_{12} 0.28
Shear modulus (N/m ²)	G_{12} 1.000E+09~8.000E+09 (3-bit)
	G_{13} 1.000E+09~8.000E+09 (3-bit)
	G_{23} 1.000E+09~8.000E+09 (3-bit)
Density (kg/m ³)	ρ 1,590
Number of population, N_{pop}	40
Probability of crossover	0.9
Probability of mutation	0.1
convergence criteria	1E-6
Max. number of iteration	50

calculate the material properties of a random composite beam. The target structure was a unidirectional CFRP specimen together with the cantilevered CFRP beams used in the study conducted by Hwang et al. (2018). The specimen's specifications and fixing methods are similar to those used in numerical analysis model presented in Section 4.1.

As shown in Fig. 10, the natural frequencies of the target structure corresponding to the exact solution were calculated via a modal test using an impact hammer. The natural frequencies obtained from the first to fourth generations were 50.87 Hz (1st vertical bending), 255.30 Hz (1st twisting), 273.72 Hz (1st lateral bending), and 326.65 Hz (2nd vertical bending), respectively (Hwang et al., 2018).

Elastic moduli, E_{11} , and E_{22} , and shear moduli, G_{12} , G_{13} , and G_{23} , were selected as optimization parameters. Table 4 summarizes the ranges of the material properties, as well as those of the discrete genetic algorithm parameters. As a reference, the number of discrete data for the elastic moduli, E_{11} and E_{22} , was set to 64 (6-bit) and 32 (5-bit), respectively, and the number of discrete data for the shear



(a) Modal test configuration



(b) Clamped specimen

Fig. 10 Modal test of the cantilevered CFRP beam (Hwang et al., 2018)

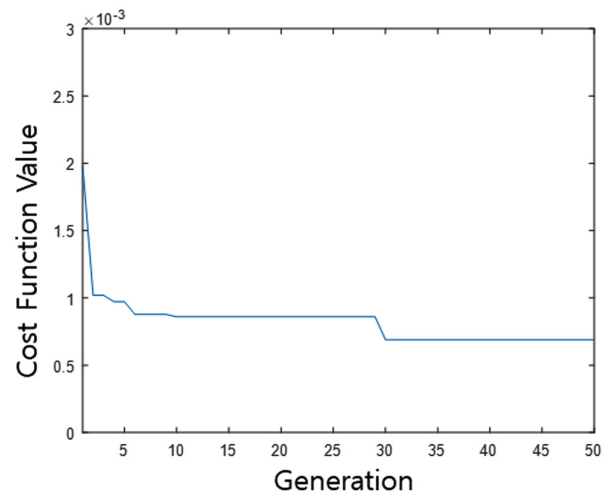


Fig. 11 Convergence plot (cantilevered CFRP beam): generation vs. cost function value

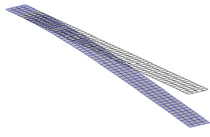
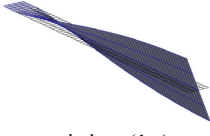
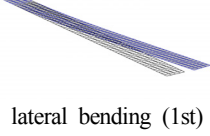
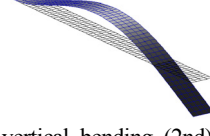
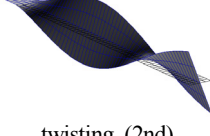
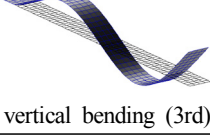
Table 5 Estimated material properties of the cantilevered CFRP beam

Optimization parameter		Final value
Elastic modulus (N/m ²)	E_{11}	3.3E+11
	E_{22}	4.0E+10
	G_{12}	4.0E+09
Shear modulus (N/m ²)	G_{13}	8.0E+09
	G_{23}	7.0E+09

moduli was set to 8 (3-bit). However, the number of individuals for each generation was set to 40, and the probabilities of crossover and mutation were set to 0.9 and 0.1, respectively, same as that of the previous section. The convergence criteria were established by setting 1E-6 as the required cost and 50 as the maximum number of iterations.

Fig. 11 presents a convergence plot graph showing the function values of the minimum cost for each generation in the optimization process. As illustrated, the required cost was not fulfilled until the

Table 6 Modal frequencies and shapes of the cantilevered CFRP beam

Order	Natural frequency (Hz)		Mode Shape
	Experiment	Numerical	
1	50.87	51.05	 vertical bending (1st)
2	255.30	256.52	 twisting (1st)
3	273.72	272.44	 lateral bending (1st)
4	326.65	318.43	 vertical bending (2nd)
5	-	812.75	 twisting (2nd)
6	-	882.51	 vertical bending (3rd)

maximum number of iterations. The final cost function value obtained is 6.904E-4 and Table 5 summarizes the final material properties of the orthotropic beam, which are the target optimization parameters.

Table 6 summarizes the comparison of natural frequencies measured via the modal test on the target orthotropic beam model, as well as the natural frequencies obtained from the updated finite element model. Additionally, the table presents the fifth and sixth natural frequencies obtained using the finite element model, as well as the first to sixth mode shapes. As presented in Table 7, the results obtained from the experiment and numerical estimation agreed optimally. Accordingly, via the updated finite element model, auxiliary information, such as high-order natural frequencies and mode shapes, can be estimated, as well as the material properties of the target structure.

5. Conclusions

This study proposed a finite element model update method, comprising processes of optimization parameter selection, finite element model development, and finite element model update, which was adopted to calculate the equivalent material properties of a target structure via the natural frequencies of a CFRP ship or structure. Additionally, an optimization technique was applied, in which the material properties of the target structure were iteratively updated such that the finite element model yielded natural frequencies of the pre-analysis or actual-measured values. A discrete genetic algorithm was utilized as the optimization technique. After which, a numerical analysis was conducted on a hypothetical cantilevered orthotropic beam structure to evaluate the validity of the proposed update on the finite element model. Consequently, it was inferred that the estimated material properties were consistent with the measured material properties of the target structure. Furthermore, a finite element model that yields values similar to that of the actual-measured natural frequencies was derived by performing numerical analysis on the cantilevered CFRP beam with unknown material properties. Finally, the feasibility of the proposed update on the finite element model was verified by estimating the high-order natural frequencies and mode shapes using the derived finite element model.

References

Chen, N.Z. Sun, H.H., & Carlos G.S. (2003). Reliability Analysis of a Ship Hull in Composite Material. *Composite Structures*, 62, 59-66. [https://doi.org/10.1016/S0263-8223\(03\)00084-9](https://doi.org/10.1016/S0263-8223(03)00084-9)

JASTRA Channel. (2020). Digital Twin for Ship Structures. Retrieved May 2020 from <https://www.youtube.com/watch?v=ICZ2faRyfA8>

Giagopoulos, D., Ntotsios, E., Papadimitriou, E., & Natsiavas, S. (2009). Finite Element Model Updating of an Experimental Vehicle Model Using Measured Modal Characteristics. *Proceedings of 2nd ECCOMAS Thematic Conference on Computational Methods in Structural Dynamics and Earthquake*

- Engineering (COMPDYN 2009), Rhodes, Greece, 768-780. <https://hdl.handle.net/2134/10772>
- Hofmeister, B., Bruns, M., & Rolfes, M. (2019). Finite Element Model Updating Using Deterministic Optimisation: A Global Pattern Search Approach. *Engineering Structures*, 195, 373-381. <https://doi.org/10.1016/j.engstruct.2019.05.047>
- Hwang, J.Y., Kim, K., Lee, K.H., Cho, D.S., Choi, T., Kim, J.H., & Shin, S.Y. (2018). Modal Property Evaluation of Cantilever CFRP Beams with Different Lay-up Orientation. *Proceedings of KAOSTS 2018*, Jeju, South Korea, 772-775.
- Lee, H.S., Song, M.C., Suh, J.C., & Chang, B.J. (2014). Hydro-elastic Analysis of Marine Propellers Based on a BEM-FEM Coupled FSI Algorithm. *International Journal of Naval Architecture and Ocean Engineering*, 6(3), 562-577. <https://doi.org/10.2478/IJNAOE-2013-0198>
- Oh, D.K. Lee, C.W. Jeong, U.C., & Ryu, C.H. (2013). A Study on the Basic Design and its Characteristics of 50 ft-class CFRP Cruise Boat. *Journal of the Korean Society of Marine Environment and Safety*, 19(6), 674-680. <https://doi.org/10.7837/kosomes.2013.19.6.674>
- Weitzenböck, J.R., Hayman, B., Hersvik, G., McGeorge, D., Noury, P., Hill, D.M., & Echtermeyer, A. (2010). Application of Composites in Ships and Offshore - A Review and Outlook. In *Royal Institution of Naval Architects - International Conference on Marine and Offshore Composites 2010*, London, United Kingdom, 1-39.
- Zahari, S.N., Zakaria, A.A.R., Sani, M.S.M., & Zaman, I. (2016). A Review on Model Updating of Joint Structure for Dynamic Analysis Purpose. *The 3rd International Conference on Mechanical Engineering Research (ICMER 2015)*, 74, 00023. <https://doi.org/10.1051/mateconf/20167400023>

Author ORCIDs

Author name	ORCID
Kim, Kookhyun	0000-0002-4214-4673
Park, Sungju	0000-0002-7129-8567
Lee, Sangjoong	0000-0001-9844-8556
Hwang, Seongjun	0000-0003-2942-9671
Kim, Sumin	0000-0002-2119-1796
Lee, Yonghee	0000-0002-4578-0229

Instructions for Authors

General information

To submit a manuscript to the Journal of Ocean Engineering and Technology (JOET), it is advised to first carefully read the aims and the scope section of this journal, as it provides information on the editorial policy and the category of papers it accepts. Unlike many regular journals, JOET usually has no lag in acceptance of a manuscript and its publication. Authors that find a match with the aims and the scope of JOET are encouraged to submit as we publish works from all over the world. JOET adheres completely to guidelines and best practices published by professional organizations, including Principles of Transparency and Best Practice in Scholarly Publishing (joint statement by COPE, DOAJ, WAME, and OASPA (<http://doaj.org/bestpractice>) if otherwise not described below. As such, JOET would like to keep the principles and policies of those professional organizations during editing and the publication process.

Research and publication ethics

Details on publication ethics are found in <http://joet.org/authors/ethics.php>. For the policies on research and publication ethics not stated in the Instructions, Guidelines on Good Publication (<http://publicationethics.org/>) can be applied.

Requirement for membership

One of the authors who submits a paper or papers should be member of the Korean Society of Ocean Engineers (KSOE), except a case that editorial board provides special admission of submission.

Publication type

Article types include scholarly monographs (original research articles), technical articles (technical reports and data), and review articles. The paper should have not been submitted to other academic journal. When part or whole of a manuscript was already published to conference papers, research reports, and dissertations, then the corresponding author should note it clearly in the manuscript.

Copyright

After published to JOET, the copyright of manuscripts should belong to KSOE. A transfer of copyright (publishing agreement) form can be found in submission website (<http://www.joet.org>).

Manuscript submission

Manuscript should be submitted through the on-line submission website (<http://www.joet.org>). The date that manuscript was received through on-line website is the official date of receipt. Other correspondences can be sent by an email to the Editor in Chief or secretariat. The manuscript must be accompanied by a signed statement that it has been neither published nor currently submitted for publication elsewhere. The manuscript should be written in English or Korean. Ensure that online submission are in a standard word processing format. Corresponding author must write the manuscript using the JOET template provided in Hangul or MS Word format. Ensure that graphics are high-resolution.

Be sure all necessary files have been uploaded/ attached.

Authors' checklist

Please refer to "Authors' Checklist" for details.

Article structure

Manuscript must be edited in the following order: (1) Title, (2) Authors' names and affiliations, (3) Keywords, (4) Abstract, (5) Nomenclature (optional), (6) Introduction, (7) Main body (analyses, tests, results, and discussions), (8) Conclusions, (9) Conflict of interest (optional), (10) Funding (optional), (11) Acknowledgements (optional), (12) References, (13) Appendices (optional), (14) Author's ORCIDs.

Abstract

A concise and factual abstract is required. The abstract should state briefly the background, purpose and methods of the research, the principal results and conclusions. An abstract should be written in around 300 words. References are not cited in abstract whenever possible. Also, non-standard or uncommon abbreviations should be avoided, but if essential they must be defined at their first mention in the abstract itself.

Keywords

Immediately after the abstract, provide a maximum of 5 or 6 keywords.

Unit

Use the international system units(SI). If other units are mentioned, please give their equivalent in SI.

Equations

All mathematical equations should be clearly printed/typed using well accepted explanation. Superscripts and subscripts should be typed clearly above or below the base line. Equation numbers should be given in Arabic numerals enclosed in parentheses on the right-hand margin.

Tables

Tables should be numbered consecutively with Arabic numerals. Each table should be fully titled. All tables should be referred to in the texts.

Figures

Figures should be numbered consecutively with Arabic numerals. Each figure should be fully titled. All figures should be referred to in the texts. All the illustrations should be of high quality meeting with the publishing requirement with legible symbols and legends.

Conflict of interest

It should be disclosed here according to the statement in the Research and publication ethics regardless of existence of conflict of interest. If the authors have nothing to disclose, please state: "No potential

conflict of interest relevant to this article was reported.”

Funding

Funding to the research should be provided here. Providing a FundRef ID is recommended including the name of the funding agency, country and if available, the number of the grant provided by the funding agency. If the funding agency does not have a FundRef ID, please ask that agency to contact the FundRef registry (e-mail: fundref.registry@crossref.org). Additional detailed policy of FundRef description is available from <http://www.crossref.org/fundref/>. Example of a funding description is as follows: The study is supported by the Inha University research fund (FundRef ID: 10.13039/501100002632), and the Korea Health Personnel Licensing Examination Institute research fund (FundRef ID: 10.13039/501100003647).

Acknowledgments

Any persons that contributed to the study or the manuscript, but not meeting the requirements of an authorship could be placed here. For mentioning any persons or any organizations in this section, there should be a written permission from them.

References in text

References in texts follow the APA style. Authors can also see how references appear in manuscript text through the ‘Template’.

Reference list

Reference list follows the APA style. Authors can see how references should be given in reference section through the ‘Template’.

Appendices

The appendix is an optional section that can contain details and data supplemental to the main text. If there is more than an appendix, they should be identified as A, B, C, etc. Formulae and equations in appendices should be given separate numbering: Eq. (A1), Eq. (A2), etc.; in a subsequent appendix, Eq. (B1) and so on. Similarly for tables and figures: Table A1; Fig. A1, etc.

ORCID (Open Researcher and Contributor ID)

All authors are recommended to provide an ORCID. To obtain an ORCID, authors should register in the ORCID web site: <http://orcid.org>. Registration is free to every researcher in the world. Example of ORCID description is as follows:

Joonmo Chung: <https://orcid.org/0000-0003-1407-9031>

Peer review and publication process

The peer review process can be broadly summarized into three groups: author process, review process, and publishing process for accepted submissions. General scheme is presented in Figure 1.

Check-in process for review

If the manuscript does not fit the aims and scope of the Journal or does not adhere to the Instructions to Authors, it may be rejected immediately after receipt and without a review. Before reviewing, all submitted manuscripts are inspected by Similarity Check powered by iThenticate (<https://www.crossref.org/services/similarity-check/>), a plagiarism-screening tool. If a too high degree of similarity score is found, the Editorial Board will do a more profound content screening.

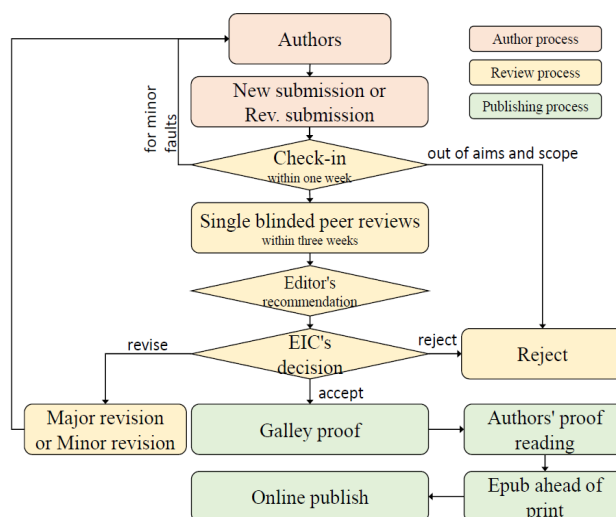


Figure 1 Flow chart of the peer review and publication process of JOET

The criterion for similarity rate for further screening is usually 15%; however, rather than the similarity rate, the Editorial Board focuses on cases where specific sentences or phrases are similar. The settings for Similarity Check screening are as follows: It excludes quotes, bibliography, small matches of 6 words, small sources of 1%, and the Methods section.

Number of reviewers

Reviewers will be selected from the list of reviewers. Manuscripts are then peer reviewed by at least 2 experts in the corresponding field, usually by 2.

Peer review process and the author response to the reviewer comments
JOET adopts single blind review, which means that the authors do not know the identity of the reviews. All papers, including those invited by the Editor, are subject to peer review.

The review period is 4 weeks. Usually the first decision is made within a week after completion of the review. The Editorial Board's decision after the review will be one of followings: Accept, Minor revision, Major revision, or Rejection. The Editorial Board may request the authors to revise the manuscript according to the reviewers' comments. If there are any requests for revision of the manuscript by the reviewers, the authors should do their best to revise the manuscript. If the reviewer's opinion is not acceptable or is believed to misinterpret the data, the author should reasonably indicate that. After revising the manuscript, the author should upload the revised files with a separate response sheet to each item of the reviewer's commentary. The author's revisions should be completed within 3 months after the request. If it is not received by the due date, the Editorial Board will notify the author. To extend the revision period beyond 3 months, the author should negotiate that with the Editorial Board. The manuscript review process can be provided for up two rounds. If the authors wish further review, the Editorial Board may consider it. The Editorial Board will make a final decision on the approval of the submitted manuscript for publication and can request any further corrections, revisions, and deletions of the article text if necessary. Statistical editing is also performed if the data requires professional statistical review by a statistician.

Processing after acceptance

If the manuscript is finally accepted, the galley proof will be sent to the corresponding author after professional manuscript editing and English proofreading. Proofreading should be performed for any misspellings or errors by the authors. Proofreading manuscript for publication is provided to the corresponding author, and the corresponding author must review the proofreading manuscript. Corresponding authors are responsible for the content of the proofreading manuscript and any errors. After final proofreading, the manuscript may appear at the journal homepage as an article in press with a unique DOI number for rapid communication. All published articles will be replaced by the replacement XML file and a final PDF.

Feedback after publication

If the authors or readers find any errors, or contents that should be revised, it can be requested from the Editorial Board. The Editorial Board may consider erratum, corrigendum or a retraction. If there are any revisions to the article, there will be a CrossMark description to announce the final draft. If there is a reader's opinion on the published article with the form of Letter to the editor, it will be forwarded to the authors. The authors can reply to the reader's letter. Letter to the editor and the author's reply may be also published.

How the journal handle complaints and appeals

The policy of JOET is primarily aimed at protecting the authors, reviewers, editors, and the publisher of the journal. If not described below, the process of handling complaints and appeals follows the guidelines of the Committee of Publication Ethics available from: <https://publicationethics.org/appeals>

- Who complains or makes an appeal?

Submitters, authors, reviewers, and readers may register complaints and appeals in a variety of cases as follows: falsification, fabrication, plagiarism, duplicate publication, authorship dispute, conflict of interest, ethical treatment of animals, informed consent, bias or unfair/inappropriate competitive acts, copyright, stolen data, defamation, and legal problem. If any individuals or institutions want to inform the cases, they can send a letter via the contact page on

our website: <https://www.joet.org/about/contact.php>. For the complaints or appeals, concrete data with answers to all factual questions (who, when, where, what, how, why) should be provided.

- Who is responsible to resolve and handle complaints and appeals?

The Editorial Board or Editorial Office is responsible for them. A legal consultant or ethics editor may be able to help with the decision making.

- What may be the consequence of remedy?

It depends on the type or degree of misconduct. The consequence of resolution will follow the guidelines of the Committee of Publication Ethics (COPE).

Article processing charge

Payment due

Article processing charge (APC) covers the range of publishing services JOET provides. This includes provision of online tools for editors and authors, article production and hosting, and customer services. Upon editorial acceptance of an article for the regular review service and upon submission of an article for the fast review service, the corresponding author will be notified that payment is due.

APC

The APC up to 6 pages is ₩200,000 (or \$200) and ₩550,000 (or \$550) for the for the regular and fast review services, respectively. An extra APC of \$50 per page is charged for papers longer than 6 pages. No taxes are included in this charge. For the fast review service, an advance fee of ₩250,000 (\$250) should be paid on submission.

Payment methods

Credit card payment can be made online using a secure payment form as soon as the manuscript has been editorially accepted. We will we send a receipt by email once payment has been processed. Please note that payment by credit card carries a surcharge of 10% of the total APC.

Invoice payment is due within 7 days of the manuscript receiving editorial acceptance. Receipts are available on request.



Original Research Article, Technical Article, Review Article, etc

Title of Article

Firstname Lastname¹, Firstname Lastname² and Firstname Lastname³

¹Professor, Department of OO, OO School, OO University, Busan, Korea

²Graduate Student, Department of OO, OO University, Seoul, Korea

³Senior Researcher, Department of OO, OO Engineering. Corp., Seoul, Korea

KEY WORDS: Lumped mass line model, Explicit method, Steel lazy wave riser (Immediately after the abstract, provide a maximum of 5 or 6 keywords.)

ABSTRACT: A concise and factual abstract is required. The abstract should state briefly the purpose of the research, the principal results and major conclusions. An abstract should be written in around 300 words and is often presented separately from the article, so it must be able to stand alone. For this reason, References should be avoided, but if essential, then cite the author(s) and year(s). Also, non-standard or uncommon abbreviations should be avoided, but if essential they must be defined at their first mention in the abstract itself.

Nomenclature

<i>I</i> TOC	Increment of total operating cost (\$/yr)
<i>L</i> HV	Lower heating value (kJ/kg)
<i>P</i> w	Power (kW)
<i>T</i>	Temperature (K)
<i>V</i>	Volume (m ³)
ρ	Density (kg/m ³)

1. Introduction

The introduction should briefly place the study in a broad context and highlight why it is important. It should define the purpose of the work and its significance. The current state of the research field should be reviewed carefully and key publications cited. Please highlight controversial and diverging hypotheses when necessary. Finally, briefly mention the main aim of the work and highlight the principal conclusions. As far as possible, please keep the introduction comprehensible to scientists outside your particular field of research.

2. General Information for Authors

2.1 Requirement for Membership

One of the authors who submits a paper or papers should be member of

The Korea Society of Ocean Engineers (KSOE), except a case that editorial board provides special admission of submission.

2.2 Publication type

Manuscript is made up of scholarly monographs, technical reports and data. The paper should have not been submitted to other academic journal. Conference papers, research reports, dissertations and review articles can be submitted to Journal Of Ocean Engineering and Technology (JOET). When part or whole of a paper was already published to conference papers, research reports, dissertations, and review articles, then corresponding author should note it clearly in the manuscript. After published to JOET, the copyright of manuscript belongs to KSOE.

(example) It is noted that this paper is revised edition based on proceedings of KAOST 2100 in Jeju.

2.3 Manuscript submission

Manuscript should be submitted through the on-line manuscript website (<http://www.joet.org>). The date that corresponding author submits a paper through on-line website is official date of submission. Other correspondences can be sent by an email to the Editor in Chief. The manuscript must be accompanied by a signed statement that it has been neither published nor currently submitted for publication elsewhere. The manuscript should be written in English or Korean and a

Received 00 February 2100, revised 00 October 2100, accepted 00 October 2100

Corresponding author Firstname Lastname: +82-51-759-0656, e-mail@e-mail.com

It is a recommended paper from the proceedings of 2019 spring symposium of the Korea Marine Robot Technology (KMRTS).

© 2100, The Korean Society of Ocean Engineers

This is an open access article distributed under the terms of the creative commons attribution non-commercial license (<http://creativecommons.org/licenses/by-nc/4.0>) which permits unrestricted non-commercial use, distribution, and reproduction in any medium, provided the original work is properly cited.

minimum standard of the proficiency in the English or Korean language should be met before submission to the editorial office.

Ensure that online submission or submission by e-mail text files are in a standard word processing format (Hangul or MS Word are preferred). Ensure that graphics are high-resolution. Be sure all necessary files have been uploaded/attached.

2.3.1 Author's checklist and Transfer of copyright

Author's checklist and Transfer of copyright can be found in submission homepage (<http://www.joet.org>).

2.4 Research and Publication Ethics

Authorship should be limited to those who have made a significant contribution to the conception, design, execution, or interpretation of the reported study. All those who have made significant contributions should be listed as co-authors. Where there are others who have participated in certain substantive aspects of the research project, they should be acknowledged or listed as contributors.

The corresponding author should ensure that all appropriate co-authors and no inappropriate co-authors are included on the paper, and that all co-authors have seen and approved the final version of the paper and have agreed to its submission for publication.

Details on publication ethics are found in the journal's website (<http://joet.org/authors/ethics.php>). For the policies on research and publication ethics not stated in the Instructions, Guidelines on Good Publication (<http://publicationethics.org/>) can be applied.

3. Manuscript

Manuscript must consist of as follow: (1) Title, (2) Author's information (include title), (3) Key word, (4) Abstract, (5) Nomenclature description, (6) Introduction, (7) Body (analysis, test, results and discussion, (8) Conclusion, (9) Acknowledgements, (10) Reference, (11) Appendix, etc.

3.1 Unit

Use the international system units(SI). If other units are mentioned, please give their equivalent in SI.

3.2 Equations

All mathematical equations should be clearly printed/typed using well accepted explanation. Superscripts and subscripts should be typed clearly above or below the base line. Equation numbers should be given in Arabic numerals enclosed in parentheses on the right-hand margin. They should be cited in the text as, for example, Eq. (1), or Eqs. (1)-(3).

$$G_{GEV}(x;\mu,\sigma,\xi) = \begin{cases} \exp[-(1+\xi(x-\mu)/\sigma)^{-1/\xi}] & \xi \neq 0 \\ \exp[-\exp(-(x-\mu)/\sigma)] & \xi = 0 \end{cases} \quad (1)$$

in which μ , σ , and ξ represent the location ("Shift" in figures), scale, and shape parameters, respectively.

3.3 Tables

Tables should be numbered consecutively with Arabic numerals. Each table should be typed on a separate sheet of paper and be fully titled. All tables should be referred to in the text.

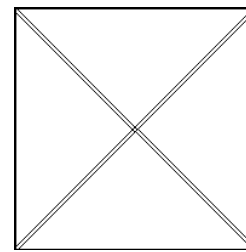
Table 1 Tables should be placed in the main text near to the first time they are cited

Item	Buoyancy riser
Segment length ¹ (m)	370
Outer diameter (m)	1.137
Inner diameter (m)	0.406
Dry weight (kg/m)	697
Bending rigidity (N·m ²)	1.66E8
Axial stiffness (N)	7.098E9
Inner flow density (kg·m ³)	881
Seabed stiffness (N/m ²)	6,000

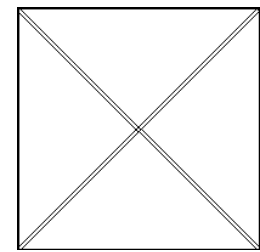
¹Tables may have a footer.

3.4 Figures

All the illustrations should be of high quality meeting with the publishing requirement with legible symbols and legends. In preparing the illustrations, authors should consider a size reduction during the printing process to have acceptable line clarity and character sizes. All figures should have captions. They should be referred to in the text as, for example, Fig. 1, or Figs. 1-3.



(a) Description of what is contained in the first panel



(b) Description of what is contained in the second panel

Fig. 1 Schemes follow the same formatting. If there are multiple panels, they should be listed as: (a) Description of what is contained in the first panel; (b) Description of what is contained in the second panel. Figures should be placed in the main text near to the first time they are cited

3.5 How to describe the references in main texts

All references should be listed at the end of the manuscripts, arranged in order of Alphabet. References in texts follow the American Psychological Association (APA) style. The exemplary form of listed references is as follows:

Single author: (Kim, 1998) or Kim (1998)

Two authors: (Kim and Lee, 2000) or Kim and Lee (2000)

Three or more authors: (Kim et al., 1997) or Kim et al. (1997)

Two or more papers: (Lee, 1995a; Lee, 1995b; Ryu et al., 1998)

Year unknown: (Kim, n.d.) or Kim (n.d.)

4. Results

This section may be divided by subheadings. It should provide a concise and precise description of the experimental results, their interpretation as well as the experimental conclusions that can be drawn. Tables and figures are recommended to present the results more rapidly and easily. Do not duplicate the content of a table or a figure with in the Results section. Briefly describe the core results related to the conclusion in the text when data are provided in tables or in figures. Supplementary results can be placed in the Appendix.

5. Discussion

Authors should discuss the results and how they can be interpreted in perspective of previous studies and of the working hypotheses. The findings and their implications should be discussed in the broadest context possible. Future research directions may also be highlighted

6. Conclusions

This section can be added to the manuscript.

Funding

Please add: “This research was funded by Name of Funder, grant number XXX” and “The OOO was funded by XXX”. Check carefully that the details given are accurate and use the standard spelling of funding agency names at <https://search.crossref.org/funding>

Acknowledgments

In this section you can acknowledge any support given which is not covered by the author contribution or funding sections. This may include administrative and technical support, or donations in kind (e.g., materials used for experiments). For mentioning any persons or any organizations in this section, there should be a written permission from them.

Conflict of interest

It should be disclosed here according to the statement in the Research and publication ethics regardless of existence of conflict of interest. If the authors have nothing to disclose, please state: “No potential conflict of interest relevant to this article was reported.”

References

- Journal name should not be abbreviated.
- A private report with limited access or download availability can not be a reference.
- Include the digital object identifier DOI or URL for all references

where available.

- Reference list follows the American Psychological Association (APA) style.

Referring to journal publications:

- Author, A.A., Author, B.B., & Author, C.C. (Year). Title of Article. Journal Title, vol(no), pp-pp. <https://doi.org/xx.xxxx/xxxxxx>
- Author, A.A., Author, B.B., Author, C.C. (accepted; in press). Title of Article. Title of Periodical. Retrieved from <http://xx.xxx/x.pdf>
- Lee, T.K., Kim, T.W., Rim, C.W., & Kim, S.C. (2013). A Study on Calculation of Local Ice Pressures for ARAON Based on Data Measured at Arctic Sea. Journal of Ocean Engineering and Technology, 27(5), 88-92. <https://doi.org/10.5574/KSOE.2013.27.5.088>
- Lee, T.K., Kim, T.W., Rim, C.W., & Kim, S.C. (accepted; in press). A Study on Calculation of Local Ice Pressures for ARAON Based on Data Measured at Arctic Sea. Journal of Ocean Engineering and Technology, Retrieved from <http://xxx.xxx/xxx.pdf>

Referring to conference proceedings:

- Author, A.A., Author, B.B., & Author, C.C. (Year). Title of Article. Proceeding Title, City, Country, pp-pp. <https://doi.org/xx.xxxx>
- Aoki, S., Liu, H., & Sawaragi, T. (1994). Wave Transformation and Wave Forces on Submerged Vertical Membrane. Proceedings of International Symposium Waves - Physical and Numerical Modeling, Vancouver, Canada, 1287-1296.
- Tsukamoto, C.L., Lee, W., Yuh, J., Choi, S.K., & Lorentz, J. (1997). Comparison Study on Advanced Thruster Control of Underwater Robots. Proceedings of International Conference on Robotics and Automation, 1845-1850. <https://doi.org/110.1109/ROBOT.1997.619056>

Referring to books:

- Author, A.A. (Year). Title of Book (xx ed.). Location: Publisher.
- Strunk, W., & White, E.B. (2000). The Elements of Style (4th ed.). New York, USA: Longman.
- Schlichting, H. (1968). Boundary Layer Theory (6th ed.). New York, USA: McGraw-Hill.

Referring to theses or dissertations:

- Author, A.A. (Year). Title of Doctoral Dissertation or Master's thesis (Doctoral Dissertation or Master's thesis). Name of Institution, City, Country.
- Giovanni, I. (1998). Modelling and Identification of Underwater Robotic Systems (Ph.D. Thesis). University of Genova, Genova, Italy.

Referring to technical reports, rules, or guidelines:

- Author, A.A. (Year). Title of report (Reprot No. xxx), Location: Publisher.
- Likhomanov, V. (2010). Full-Scale Ice Trials of the Korean Research Icebreaker ARAON. Daejeon, Korea: Arctic and Antarctic Research Institute (AARI).
- ABS. (2011). Guide for Ice Loads Monitoring Systems. Houston, USA: American Bureau of Shipping.
- Lloyd's Register. (2011). FDA ICE Fatigue Induced by Ice Loading,

ShipRight Design and construction - Fatigue Design Assessment. London, United Kingdom: Lloyd's Register.

Larson, M., & Kraus, N.C. (1989). SBEACH: Numerical Model for Simulating Storm-Induced Beach Change - Report 1 Empirical Foundation and Model Development (Technical Report CERC-89-9). Coastal Engineering research center Vicksburg Ms.

Referring to patents:

Rightholder, A.A. (Year). Title of Patent. Patent number, Patent office with country.

Dawoo Shipbuilding & Marine Engineering (DSME). (2013). Distance Length Standardization Method for Preventing Interference at the time of Uploading Cell Guide of Container Ship. Unexamined Patent Publication 1020130044635, Korean Intellectual Property Office.

Referring to websites:

Rightholder, A.A. (Year). Title of webpage. Retrieved Month Year from <http://xxxx>

International Association of Classification Societies (IACS). (2010a). Common Structural Rules for Bulk Carriers. Retrieved July 2010 from <http://www.iacs-data.org.uk>

US Congressional Hearing. (2009). Strategic Importance of the Arctic in Us Policy. Retrieved June 2019 from <https://fas.org/irp/arctic.pdf>

Dawoo Shipbuilding & Marine Engineering (DSME). (2013). Distance Length Standardization Method for Preventing Interference at the time of Uploading Cell Guide of Container Ship. Retrieved June 2019 from <https://patentimages.storage./pdfs/792.pdf>

Referring to software:

Rightholder, A.A. (Year). Title of Software. Downloaded Month Year from <http://xxxx>

Referring to some exceptional cases:

- when authors are missing, institution can replace authors

National Oceanic and Atmospheric Administration (NOAA). (2015). Deep-ocean Assessment and Reporting of Tsunamis (DART). Retrieved December 2019 from <https://nctr.pmel.noaa.gov/Dart/>

- when dates or years are missing, it is replaced with "n.d."

National Oceanic and Atmospheric Administration (NOAA). (n.d).

Deep-ocean Assessment and Reporting of Tsunamis (DART).

- when more than seven authors, first 6 authors ... last author.

Yeu, T., Choi, H.T., Lee, Y., Chae, J., Lee, Y., Kim, S.S., ... Lee, T.H. (2019). Development of Robot Platform for Autonomous Underwater Intervention. Journal of Ocean Engineering and Technology, 33(2), 168-177. <https://doi.org/10.26748/KSOE.2019.021>

Appendix

The appendix is an optional section that can contain details and data supplemental to the main text. For example, explanations of experimental details that would disrupt the flow of the main text, but nonetheless remain crucial to understanding and reproducing the research shown; figures of replicates for experiments of which representative data is shown in the main text can be added here if brief, or as Supplementary data. Mathematical proofs of results not central to the paper can be added as an appendix.

All appendix sections must be cited in the main text. In the appendixes, Figures, Tables, etc. should be labeled starting with 'A', e.g., Fig. A1, Fig. A2, etc.

Examples:

<https://doi.org/10.26748/KSOE.2019.022>

<https://doi.org/10.26748/KSOE.2018.4.32.2.095>

Author ORCIDs

All authors are recommended to provide an ORCID. To obtain an ORCID, authors should register in the ORCID web site: <http://orcid.org>. Registration is free to every researcher in the world. Example of ORCID description is as follows:

Author name	ORCID
So, Hee	0000-0000-000-00X
Park, Hye-Il	0000-0000-000-00X
Yoo, All	0000-0000-000-00X
Jung, Jewelry	0000-0000-000-00X

Authors' Checklist

The following list will be useful during the final checking of a manuscript prior to sending it to the journal for review. Please submit this checklist to the KSOE when you submit your article.

< Checklist for manuscript preparation >

- I checked my manuscript has been 'spell-checked' and 'grammar-checked'.
- One author has been designated as the corresponding author with contact details such as
 - E-mail address
 - Phone numbers
- I checked abstract 1) stated briefly the purpose of the research, the principal results and major conclusions, 2) was written in around 300 words, and 3) did not contain references (but if essential, then cite the author(s) and year(s)).
- I provided 5 or 6 keywords.
- I checked color figures were clearly marked as being intended for color reproduction on the Web and in print, or to be reproduced in color on the Web and in black-and-white in print.
- I checked all table and figure numbered consecutively in accordance with their appearance in the text.
- I checked abbreviations were defined at their first mention there and used with consistency throughout the article.
- I checked all references mentioned in the Reference list were cited in the text, and vice versa according to the APA style.
- I checked I used the international system units (SI) or SI-equivalent engineering units.

< Authorship checklist >

JOET considers individuals who meet all of the following criteria to be authors:

- Made a significant intellectual contribution to the theoretical development, system or experimental design, prototype development, and/or the analysis and interpretation of data associated with the work contained in the article.
- Contributed to drafting the article or reviewing and/or revising it for intellectual content.
- Approved the final version of the article as accepted for publication, including references.

< Checklist for publication ethics >

- I checked the work described has not been published previously (except in the form of an abstract or as a part of a published lecture or academic thesis).
- I checked when the work described has been published previously in other proceedings without copyright, it has clearly noted in the text.
- I checked permission has been obtained for use of copyrighted material from other sources including the Web.
- I have processed Plagiarism Prevention Check through reliable web sites such as www.kci.go.kr, <http://www.ithenticate.com/>, or <https://www.copykiller.org/> for my submission.
- I agree that final decision for my final manuscript can be changed according to results of Plagiarism Prevention Check by JOET administrator.
- I checked one author at least is member of the Korean Society of Ocean Engineers.
- I agreed all policies related to 'Research and Publication Ethics'
- I agreed to transfer copyright to the publisher as part of a journal publishing agreement and this article will not be published elsewhere including electronically in the same form, in English or in any other language, without the written consent of the copyright-holder.
- I made a payment for reviewing of the manuscript, and I will make a payment for publication on acceptance of the article.
- I have read and agree to the terms of Authors' Checklist.

Title of article :

Date of submission : DD/MM/YYYY

Corresponding author :

signature

Email address :

※ E-mail this with your signature to ksoehj@ksoe.or.kr

Publishing Agreement

ARTICLE DETAILS

Title of article :
Corresponding author :
E-mail address :
DOI : <https://doi.org/10.26748/KSOE.2XXX.XXX>

YOUR STATUS

I am one author signing on behalf of all co-authors of the manuscript.

ASSIGNMENT OF COPYRIGHT

I hereby assign to the Korean Society of Ocean Engineers, the copyright in the manuscript identified above and any tables, illustrations or other material submitted for publication as part of the manuscript (the "Article"). This assignment of rights means that I have granted to Korean Society of Ocean Engineers the exclusive right to publish and reproduce the Article, or any part of the Article, in print, electronic and all other media (whether now known or later developed), in any form, in all languages, throughout the world, for the full term of copyright, and the right to license others to do the same, effective when the Article is accepted for publication. This includes the right to enforce the rights granted hereunder against third parties.

SCHOLARLY COMMUNICATION RIGHTS

I understand that no rights in patents, trademarks or other intellectual property rights are transferred to the Journal owner. As the author of the Article, I understand that I shall have: (i) the same rights to reuse the Article as those allowed to third party users of the Article under the CC-BY-NC License, as well as (ii) the right to use the Article in a subsequent compilation of my works or to extend the Article to book length form, to include the Article in a thesis or

dissertation, or otherwise to use or re-use portions or excerpts in other works, for both commercial and non-commercial purposes. Except for such uses, I understand that the assignment of copyright to the Journal owner gives the Journal owner the exclusive right to make or sub-license commercial use.

USER RIGHTS

The publisher will apply the Creative Commons Attribution-Noncommercial Works 4.0 International License (CC-BY-NC) to the Article where it publishes the Article in the journal on its online platforms on an Open Access basis.

The CC-BY-NC license allows users to copy and distribute the Article, provided this is not done for commercial purposes and further does not permit distribution of the Article if it is changed or edited in any way, and provided the user gives appropriate credit (with a link to the formal publication through the relevant DOI), provides a link to the license, and that the licensor is not represented as endorsing the use made of the work. The full details of the license are available at <http://creativecommons.org/licenses/by-nc/4.0/legalcode>.

REVERSION OF RIGHTS

Articles may sometimes be accepted for publication but later rejected in the publication process, even in some cases after public posting in "Articles in Press" form, in which case all rights will revert to the author.

I have read and agree to the terms of the Journal Publishing Agreement.

Corresponding author:

name

signature

※ E-mail this with your signature to ksoehj@ksoe.or.kr (Papers will not be published unless this form is signed and returned)

Research and Publication Ethics

Journal of Ocean Engineering and Technology (JOET) adheres to the guidelines published by professional organizations, including Committee on Publication Ethics (COPE; <https://publicationethics.org/>)

1. Authorship

JOET considers individuals who meet all of the following criteria to be authors:

- 1) Made a significant intellectual contribution to the theoretical development, system or experimental design, prototype development, and/or the analysis and interpretation of data associated with the work contained in the article.
- 2) Contributed to drafting the article or reviewing and/or revising it for intellectual content.
- 3) Approved the final version of the article as accepted for publication, including references.

Contributors who do not meet all of the above criteria may be included in the Acknowledgment section of the article. Omitting an author who contributed to your article or including a person who did not fulfill all of the above requirements is considered a breach of publishing ethics.

Correction of authorship after publication: JOET does not correct authorship after publication unless a mistake has been made by the editorial staff.

2. Originality and Duplicate Publication

All submitted manuscripts should be original and should not be in consideration by other scientific journals for publication. Any part of the accepted manuscript should not be duplicated in any other scientific journal without permission of the Editorial Board, although the figures and tables can be used freely if the original source is verified according to the Creative Commons Attribution License (CC BY-NC). It is mandatory for all authors to resolve any copyright issues when citing a figure or table from other journal that is not open access.

3. Conflict-of-Interest Statement

Conflict of interest exists when an author or the author's institution, reviewer, or editor has financial or personal relationships that inappropriately influence or bias his or her actions. Such relationships are also known as dual commitments, competing interests, or competing loyalties. These relationships vary from being negligible to having a great potential for influencing judgment. Not all relationships represent true conflict of interest. On the other hand, the potential for conflict of interest can exist regardless of whether an individual believes that the relationship affects his or her scientific judgment. Financial relationships such as employment, consultancies, stock ownership, honoraria, and paid expert testimony are the most easily identifiable conflicts of interest and the most likely to undermine the credibility of the journal, the authors, or of the science itself. Conflicts can occur for other reasons as well, such as personal relationships, academic competition, and intellectual passion. If there are any conflicts of interest, authors should disclose them in the manuscript. The conflicts of interest may occur during the research process as well; however, it is important to provide disclosure. If there is a disclosure, editors, reviewers, and reader can approach the manuscript after understanding the situation and the background of the completed research.

4. Management Procedures for the Research and Publication Misconduct

When JOET faces suspected cases of research and publication misconduct such as a redundant (duplicate) publication, plagiarism, fabricated data, changes in authorship, undisclosed conflicts of interest, an ethical problem discovered with the submitted manuscript, a reviewer who has appropriated an author's idea or data, complaints against editors, and other issues, the resolving process will follow the flowchart provided by the Committee on Publication Ethics (<http://publicationethics.org/resources/flowcharts>). The Editorial Board of JOET will discuss the suspected cases and reach a decision. JOET will not hesitate to publish

errata, corrigenda, clarifications, retractions, and apologies when needed.

5. Editorial Responsibilities

The Editorial Board will continuously work to monitor and safeguard publication ethics: guidelines for retracting articles; maintenance of the integrity of the academic record; preclusion of business needs from compromising intellectual and ethical standards; publishing corrections, clarifications, retractions, and apologies when needed; and excluding plagiarism and fraudulent data. The editors maintain the following responsibilities: responsibility and authority to reject and accept articles; avoiding any conflict of interest with respect to articles they reject or accept; promoting publication of corrections or retractions when errors are found; and preservation of the anonymity of reviewers.

6. Hazards and human or animal subjects

If the work involves chemicals, procedures or equipment that have any unusual hazards inherent in their use, the author must clearly identify these in the manuscript. If the work involves the use of animal or human subjects, the author should ensure that the manuscript contains a statement that all procedures were performed in compliance with relevant laws and institutional guidelines and that the appropriate institutional committee(s) has approved them. Authors should include a statement in the manuscript that informed consent was obtained for experimentation with human subjects. The privacy rights of human subjects must always be observed.

Ensure correct use of the terms sex (when reporting biological factors) and gender (identity, psychosocial or cultural factors), and, unless inappropriate, report the sex and/or gender of study participants, the sex of animals or cells, and describe the methods used to determine sex and gender. If the study was done involving an exclusive population, for example in only one sex, authors should justify why, except in obvious cases. Authors should define how they determined race or ethnicity and justify their relevance.

7. Secondary publication

It is possible to republish manuscripts if the manuscripts satisfy the conditions of secondary publication. These are:

- The authors have received approval from the Editorial Board of both journals (the editor concerned with the secondary publication must have access to the primary version).
- The priority for the primary publication is respected by a publication interval negotiated by editors of both journals and the authors.
- The paper for secondary publication is intended for a different group of readers
- The secondary version faithfully reflects the data and interpretations of the primary version.
- The secondary version informs readers, peers, and documenting agencies that the paper has been published in whole or in part elsewhere, for example, with a note that might read, "This article is based on a study first reported in the [journal title, with full reference]"
- The title of the secondary publication should indicate that it is a secondary publication (complete or abridged republication or translation) of a primary publication.

8. Complaints and Appeals

The process of handling complaints and appeals follows the guidelines of the COPE available from: <https://publicationethics.org/appeals>

9. Post-publication discussions and corrections

The post-publication discussion is available through letter to editor. If any readers have a concern on any articles published, they can submit letter to editor on the articles. If there found any errors or mistakes in the article, it can be corrected through errata, corrigenda, or retraction.

2020년도 한 해 동안 한국해양공학회지에 투고된 원고를 심사하신 분들입니다.
심사위원 여러분께 감사드립니다.

강태순	(주)지오시스템리서치	박승민	(주)헤인이앤씨	이석진	경북대학교
강희진	KRISO	박원경	(주)대영엔지니어링	이세진	공주대학교
고대은	동의대학교	박일룡	한국해양대학교	이순섭	경상대학교
고동휘	KISOST	박종용	부경대학교	이용구	강원대학교
구본국	창원대학교	박종천	부산대학교	이우동	경상대학교
구원철	인하대학교	박준범	한국해양대학교	이용	한국과학기술원
권정일	한국기계연구원	박준수	경남대학교	이정훈	경상대학교
김경성	동명대학교	박철수	KRISO	이중현	제주대학교
김경환	KRISO	배윤혁	제주대학교	이주용	성균관대학교
김국현	동명대학교	백광준	인하대학교	이진학	KIOST
김도영	홍익대학교	부승환	원광대학교	이철진	중앙대학교
김동진	KRISO	서대원	한국선급	이철진	중앙대학교
김범일	한국선급	서민국	KRISO	이탁기	경상대학교
김병완	KRISO	서유택	서울대학교	장범선	서울대학교
김봉주	부산대학교	서정관	부산대학교	전명준	창원대
김상현	인하대학교	송창용	목포대학교	정광열	Nextfoam
김성재	인하대학교	신성철	부산대학교	정동호	KRISO
김신웅	한라대학교	신윤호	충북대학교	정성엽	KRISO
김연규	KRISO	신형철	동의대학교	정세민	조선대학교
김연중	인제대	심형원	KRISO	정재환	삼성중공업
김영식	KRISO	안진형	국방과학연구소	정준모	인하대학교
김영훈	경남대학교	양승호	울산과학대학교	조성필	KRISO
김유일	인하대학교	오승훈	KRISO	조영근	영남대학교
김준영	한국해양대학교	오정근	군산대학교	주문갑	부경대학교
김현석	KRISO	오태민	부산대학교	차주환	목포대학교
김현식	동명대학교	유병석	부경대학교	최형식	한국해양대학교
남보우	서울대학교	윤재선	한국농어촌공사	하윤진	KRISO
도기덕	한국해양대학교	윤현규	창원대학교	하태민	강원대학교
박동민	KRISO	이강수	KRISO	함승호	창원대학교
박동우	동명대학교	이광호	카톨릭관동대학교	홍성훈	계명대학교
박병재	KRISO	이근화	서울대학교	황성원	인하대학교
박선호	한국해양대학교	이동근	한국해양교통안전공단	황성철	KRISO
박성중	삼성중공업	이병혁	현대중공업		

(사)한국해양공학회 특별회원

한국해양공학회의 특별회원은 다음과 같으며, 귀사의 찬조에 진심으로 감사드립니다(순서: 입회순).

한국선급 / 현대중공업(주) / 대우조선해양(주) /
한국해양과학기술원 부설 선박해양플랜트연구소 / 삼성중공업(주) /
대양전기공업(주) / (주)대영엔지니어링 / 한국조선해양기자재연구원 /
한국조선해양플랜트협회 / (주)파나시아 / 한국가스공사 / 선보공업(주) /
(주)멀티스하이드로 / SK건설(주)



한국해양공학회의 특별회원 가입방법은 학회 홈페이지(www.ksoe.or.kr)의
입회안내를 참고하시고, 기타사항은 학회 사무국으로 연락주시기 바랍니다.



The Korean Society of Ocean Engineers